Universidade do Minho
Escola de Engenharia

Filipa Manuela Matos Oliveira

Development and optimization of a novel microcapsule polyamide platform and its application for the fabrication of high-performance magnetic, electro-shielding and high *k* thermoplastic composites

outubro de 2020

Development and optimization of a novel microcapsule polyamide platform and its application for the fabrication of high-performance magnetic, electro-shielding and high k thermoplastic composites

UMinho | 2020 Filipa Manuela Matos Oliveira

Universidade do Minho
Escola de Engenharia

Filipa Manuela Matos Oliveira

Development and optimization of a novel microcapsule polyamide platform and its application for the fabrication of high-performance magnetic, electro-shielding and high *k* thermoplastic composites

Tese de Doutoramento
Programa Doutoral em Materiais e
Processamento Avançados (AdvaMTech)

Trabalho efetuado sob orientação de
Professor Doutor Zlatan Zlatev Denchev
e
Doutora Maria Teresa Costanzo Nunes

outubro de 2020

ACKNOWLEDGMENTS

I would like to express my deep gratitude to all the persons who somehow contributed to the development of this work which could not have been without their support.

Firstly, I acknowledge the AdvaMTech Doctoral Program and Fundação para a Ciência e Tecnologia for the financial support in means of the doctoral scholarship PD/BD/114372/2016.

I earnestly express my sincere gratitude to my advisors Prof. Dr. Zlatan Denchev and Dr. Teresa Nunes for the opportunity to work with them and for all the support, knowledge and motivation provided.

I would like to express a special appreciation to Dr. Nadya Dencheva for her help and discussions on the practical and theoretical issues of this work.

To Prof. Dr. Senentxu Lanceros-Méndez and Dr. Pedro Libânio Martins for the scientific support and help during the electric measurements at the Electroactive Smart Materials Group.

To Prof. Dr. Tiberio Ezquerra for the kind reception at *Consejo Superior de Investigaciones Científicas* (CSIC), in Madrid, and all the scientific support during the time that I spent there.

To Prof. Dr. António Pontes for granting access to the equipment needed to perform the first tests on the EMI shielding studies, at the Department of Polymer Engineering (DEP).

To Prof. Dr. Nuno Borges de Carvalho for granting access to the laboratory facilities and equipment from the *Instituto de Telecomunicações*, in Aveiro, to perform the EMI shielding measurements. A special thanks to Eng. Hugo Mostardinha for the technical support and suggestions.

To Prof. Dr. Fernando Duarte for granting access to the laser cut machine at the DEP. A special thanks to Hector Oliveira for the sample preparation.

To technicians from the DEP, namely Eng. Maurício Malheiro, Francisco Mateus, Manuel Escourido and João Paulo.

To all my colleagues and friends from the DEP that somehow helped me during this important journey, namely, Joana, Raquel, Clara, Luís A., Paulo T., Helena, Henrique, Daniel, Ângela, Daniela, Paulo P., Palloma, Luís M., Gabriela, Duarte, Miguel, and Pedro.

I want to thank my closest friends Sofia S., Belinha, Maria, Elsa, Sandrine, Miguel, Adriana, Marina, Peixoto, Sofia E., I express my sincere gratitude for your friendship, love, motivation, advice, and all the moments we have been sharing.

I wish to thank my parents, my sister and my closest family for their love and support. I hope I made you proud. Last but not the least, I want to thank César for his friendship, love, patience, encouragement, and advice in all the course of action.

Thank you all for everything!

Filipa Oliveira

STATEMENT OF INTEGRITY

I hereby declare having conducted this academic work with integrity. I confirm that I have not used plagiarism or any form of undue use of information or falsification of results along the process leading to its elaboration.

I further declare that I have fully acknowledged the Code of Ethical Conduct of the University of Minho.

Desenvolvimento e otimização de uma plataforma original de microcápsulas de poliamida e a sua aplicação no fabrico de compósitos termoplásticos de elevado desempenho magnético de blindagem eletromagnética e de elevada constante dielétrica

RESUMO

A produção tradicional de compósitos avançados com propriedades de blindagem de interferência eletromagnética (IEM) e com elevada constante dielétrica não garante facilmente a dispersão desejada das cargas numa matriz polimérica. Com base em técnicas de processamento reativo, ainda não foi explorada a possibilidade de preparar materiais híbridos de poliamida 6 (PA6) contendo mais de uma carga na sua composição com propriedades eletromagnéticas e dielétricas adequadas. Como tal, nesta tese de doutoramento é estudada a possibilidade de produzir novos compósitos à base de PA6 com propriedades condutoras, dielétricas e de blindagem IEM adequadas implementando uma conhecida estratégia de microencapsulação reativa que inclui a síntese de microcápsulas híbridas de PA6 (MCPA) por polimerização aniónica ativada por abertura de anel de ε-caprolactama em solução e posterior moldação em materiais compósitos termoplásticos. Assim, foram sintetizadas MCPA com cargas duplas de metal/alótropo de carbono (alótropo-C), contendo cargas de Al, Cu, Fe ou Mg e nanotubos de carbono de paredes múltiplas (NTC) ou negro de fumo (NF). A partir da técnica de moldação por compressão, as MCPA foram transformadas em placas híbridas compósitas com cargas binárias metal/NTC (ou NF). Foram também preparados laminados reforçados com tecidos de fibra de carbono a partir da sua prensagem a quente com MCPA contendo partículas metálicas. Vários estudos morfológicos e estruturais foram realizados com as MCPA e os materiais compósitos produzidos, incluindo microscopia eletrónica de varrimento, calorimetria diferencial de varrimento e análise termogravimétrica. Análises de ressonância magnética nuclear no estado sólido foram realizadas com amostras de MCPA selecionadas. Também foram avaliadas as propriedades dielétricas e de condutividade elétrica de todos os compósitos, bem como as propriedades mecânicas em tensão. Em todas essas análises, as relações estrutura-propriedades foram estudadas em função do tipo e concentração de cargas de metal/alótropo-C. Por fim, foi utilizado um método validado para estudar de forma sistemática as propriedades de blindagem IEM dos compósitos binários de PA6/metal-NTC. Foi provado que o conceito de microencapsulação pode ser aplicado com sucesso na preparação de compósitos termoplásticos à base de PA6 com boas propriedades de blindagem IEM.

PALAVRAS-CHAVE: polimerização aniónica ativada, microcápsulas, compósitos poliméricos binários, compósitos conforme especificações, materiais de blindagem e absorção eletromagnética

Development and optimization of a novel microcapsule polyamide platform and its application for the fabrication of high-performance magnetic, electro-shielding and high *k* thermoplastic composites

ABSTRACT

The traditional production of advanced composites with electromagnetic interference (EMI) shielding and high k (HK) properties cannot ensure easily the desired good dispersion of the fillers in the polymer matrix. The possibility to prepare hybrid polyamide 6 (PA6) materials containing more than one filler with tailored electromagnetic and dielectric properties based on reactive processing techniques has not been explored so far. Therefore, this Ph.D. thesis studies the possibility to produce new PA6-based composites with tailored conductivity, dielectric and EMI shielding properties implementing the known reactive microencapsulation strategy that includes synthesis of hybrid PA6 microcapsule (PAMC) precursors by activated anionic ring-opening polymerization of ε-caprolactam in solution, and subsequent molding into PA6-based thermoplastic composite materials. Thus, PAMC with dual metal/carbon allotrope loads were synthesized, comprising Al, Cu, Fe, or Mg fillers and multi-walled carbon nanotubes (CNT), or carbon black (CB). By means of direct compression molding, the PAMC were transformed into composite plates with PA6 matrix and binary metal/CNT (or CB) loads. Carbon fiber textile reinforced laminates were also prepared by hot pressing them with metal-loaded PAMC. A number of morphological and structural studies were performed with both PAMC and the composite materials produced, including scanning electron microscopy, differential scanning calorimetry, and thermogravimetric analysis. Solid state NMR measurements were performed on selected PAMC samples. The dielectric and electric conductivity properties of all composites, as well as the mechanical properties in tension were also evaluated. In all these analyses the structure-properties relationships were studied as a function of the metal/C-allotrope fillers type and concentration. Lastly, a standard method was used to perform systematic studies on the EMI shielding properties of the binary metal/CNT PA6 composites. It was proved that the microencapsulation concept can be successfully applied for the preparation of PA6-based thermoplastic composites with good EMI shielding properties.

KEYWORDS: activated anionic polymerization, microcapsules, binary polymer composites, tailor-made composites, electro-shielding and absorbing materials

TABLE OF CONTENTS

^{13}C NMR	Carbon-13 nuclear magnetic resonance
^{1}H NMR	Hydrogen-1 nuclear magnetic resonance
AAROP	Activated anionic ring-opening polymerization
ABS	Acrylonitrile butadiene styrene
a.c.	Alternating current
ASTM	American standard test method
ATRP	Atom transfer radical polymerization
BDS	Broadband dielectric spectroscopy
C20	Bruggolen C20® – activator
C	Carbon nuclei
C-allotrope	Carbon allotrope
CB	Carbon black
CF	Carbon fibers
CFT	Carbon fiber textile
CNF	Carbon nanofibers
CNT	Carbon nanotubes
CM	Compression molding
CNT	Carbon nanotubes
CP	Cross polarization
dB	Decibel
d.c.	Direct current
dL	Deciliter
DL	Dilactamate® – initiator
DIN	Deutsches Institut für Normung
DM-samples	Dually loaded microcapsules
DP-samples	Dually loaded composite plates
DSC	Differential scanning calorimetry
ECL	ε-caprolactam
EDX	Energy-dispersive X-ray spectroscopy
EM	Electromagnetic

EMF	Electromagnetic field
EMI	Electromagnetic interference
EMI SE	Electromagnetic interference shielding effectiveness
EVA	Ethylene-vinyl acetate
FITC	Fluctuation-induced tunneling conduction
GHz	Gigahertz
Gr	Graphene
GR	Graphite
H-bonds	Hydrogen bonds
HK	High *k*
HPA6	Hydrolytic PA6
Hz	Hertz
IF	Improvement factor
IPC	Institute for Polymers and Composites
I-V	Current-Voltage
L-samples	CFT-metal hybrid laminates
MAS	Magic angle spinning
Me-PAMC	Metal-loaded PAMC
M-samples	PAMC with single load
MWCNT	Multi-wall CNT
MWS	Maxwell-Wagner-Sillars
NA	Natural abundance
NMR	Nuclear Magnetic Resonance
PA	Polyamide
PA6	Polyamide 6
PAMC	Polyamide 6 microcapsules
PC	Polycarbonate
PE	Polyethylene
PIEP	Pólo de Inovação em Engenharia de Polímeros
PMMA	Poly(methyl methacrylate)
PMC	Polymer matrix composites
PP	Polypropylene

ppm	Parts per million
PS	Polystyrene
P-samples	Hybrid plates
PVDF	Polyvinylidene fluoride
PY	Polymerization yield
RAM	Radar absorbing materials
RAFT	Reversible addition-fragmentation chain transfer
RL	Real load
RLM	Reflected light microscopy
RF	Radiofrequency
SE	Shielding effectiveness
SE_A	Shielding effectiveness by absorption
SE_M	Shielding effectiveness by multiple reflections
SE_R	Shielding effectiveness by reflection
SEM	Scanning electron microscopy
ssNMR	Solid-state nuclear magnetic resonance
SWCNT	Single-wall CNT
SE_T	Total SE
TGA	Thermogravimetric analysis
TOSM	Through-open-short-match
TPC	Thermoplastic polymer composites
UM	University of Minho
VNA	Vector network analyzer

LIST OF FIGURES

LIST OF TABLES

LATIN SYMBOLS

A	Absorption
	Area
a	Mark-Houwink constant
c	Speed of light
	Solution concentration
^{o}C	Celsius
C	Capacitance
C_0	Capacitance in free space
d	Thickness; distance
E	Young's moldulus
f	Frequency
h	Planck's constant, $h = 6,62607015 \cdot 10^{-34} J \cdot s$
i	Imaginary unit, $i = \sqrt{-1}$
k	Mark-Houwink constant
M_v	Average viscometric molecular weight
M_w	Molecular weight
Q	Charge
R	Reflection
	Resistance
t	Time
t_0	Time of the pure solvent
T	Temperature
T_c	Crystallization temperature
T_g	Glass transition temperature
T_m	Melting temperature
V	Volt

V_f	Volume fraction
X_c	Degree of crystallinity
Z	Impedance

GREEK SYMBOLS

α	Alpha crystalline phase of polyamide 6
γ	Gama crystalline phase of polyamide 6
	Gyromagnetic ratio
δ	Chemical shift
	Skin depth
ε_0	Dielectric permittivity of vacuum
ε^*	Complex dielectric permittivity
ε'	Real part of the dielectric permittivity or dielectric constant
ε''	Imaginary part of the dielectric permittivity
ε_e	Engineering strain
ε_{br}	Deformation at break
η_r	Relative viscosity
η_{sp}	Specific viscosity
η_{red}	Reduced viscosity
$[\eta]$	Intrinsic viscosity
η_{inh}	Inherent viscosity
σ	Electrical conductivity
σ^*	Complex electrical conductivity
σ'	ac conductivity
σ_{ac}	ac conductivity
σ_{dc}	dc conductivity
$\sigma_{\max}$	Maximum stress
σ_{br}	Stress at break
σ_e	Engineering stress

σ_{max}	Tensile strength
ρ	Resistivity
τ	Relaxation time
χ	Magnetic susceptibility
Ω	Ohm
ω	Angular frequency

CHAPTER 1

Polymer composites with electromagnetic interference shielding effect and high *k* properties based on a microencapsulation strategy – State of the art

1.1. Introduction

From the beginnings of humanity, the evolution of societies has been associated with their capacity to produce and transform materials that perform distinct tasks in satisfying specific needs. Indeed, the variety and quality of the available materials have been used as a measure of the degree of evolution of humanity. Moreover, various periods of the human history have been named after the predominant material employed, such as the Stone Age, Bronze Age or Iron Age [1].

Nowadays, the diversity of available materials with specific properties for certain applications is extraordinarily huge, trying to match the needs of a modern and demanding society. Investigation and development of new technologies face major challenges to produce multifunctional materials with tunable properties, but at the same time, with low cost and friendly for the user and environment.

Considering that we live now in the Information Age, investigations on electromagnetic interference (EMI) on electric or electronic devices and communications systems have gained increasing importance in academic and industrial areas. Any device with an electronic circuit integrated and exposed to electromagnetic fields (EMF) is susceptible to EMI. Moreover, all living organisms including humans are continually exposed to EMF caused by radiofrequency (RF) waves. Thus, understanding the EMI phenomenon and its effect in our daily life transits gradually from a purely scientific topic to a social issue.

In this context, the development of novel EMI shielding or radar absorbing materials (RAM) is expected to be important in the new era. Thus, materials working by reflection [2–4] or absorption [2, 3, 5] of EMI have been studied to avoid electronic systems´ damage or malfunction, as well as to hide the emitted electromagnetic (EM) waves. Several areas such as aerospace-aeronautics and military applications, object detection, electrical and electronic devices, communication systems, home appliances, and medical diagnostic equipment, exemplify how important is to produce materials with shielding properties [6–10]. The fact that EMI can not only affect the desired performance of the materials but also imply health hazards associated with the exposure to EMF [11–14] has also motivated investigations in this area.

Another class of materials emerging during the Information Age are those with high dielectric constant or high k (HK) materials. Dielectric materials have an important role in electronic utility devices, industry and transportation areas, as well as in various military applications. The demand for smaller and lighter capacitors with high storage capacity and low dielectric losses increases the importance of the HK materials [15–18].

Polymer-based composites have the potential to be useful in the resolution of all these challenges. These composites combine polymers´ low density, good processability and low cost with the conductive,

magnetic and/or dielectric properties of appropriate fillers. There exist many indications that polymer composites could be a proper approach in the development of cost-effective RAM and EMI shielding [7, 8, 19–21], and HK [15, 17, 22, 23] materials.

1.2. Polymer-based composites

A composite material is any material composed of two or more chemically and/or physically distinct immiscible components, with material properties that none of the components alone can achieve. Composites possess a matrix (called also continuous component) and reinforcement or filler component dispersed in the matrix. The continuous and dispersed components are separated by an interface, nevertheless, they should have appropriate adhesion to each other. Figure 1.1 illustrates the constituents of a composite material [24].

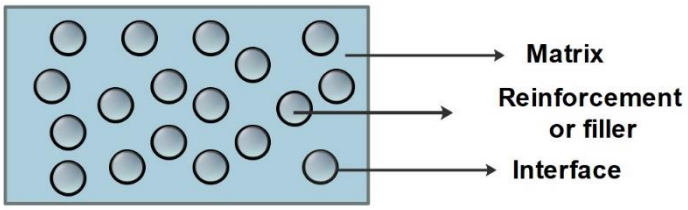

Figure 1.1 | Representation of the composition of a composite material.

The properties of the composite material depend on the matrix and reinforcing phase properties, and on the formation of an interface between them. The characteristics of the interface formed depend on the mechanical and thermal properties of the matrix and reinforcing components, the nature of the matrix and reinforcements or fillers, the physical and/or chemical interactions between the matrix and reinforcements, and the morphology of the reinforcing component [25].

The composite materials can be classified according to the type of matrix and reinforcements. The matrix can be polymeric, ceramic or metallic. Its role is to give shape to the composite, to keep the reinforcements in place and to transfer stress to them, as well as to protect them from the environmental factors, preventing chemical, mechanical or moisture damages.

Besides their low thermal resistance and a high coefficient of thermal expansion, several advantages of the polymer matrices make them more attractive in the development of advanced composite materials, namely low cost and density, good processability, high strength, stiffness, and fracture resistance, good abrasion and corrosion resistance, and sufficient impact resistance [26, 27].

Furthermore, the polymer matrix composites (PMC) can be classified as thermosetting or thermoplastic. The main advantages of the thermosetting materials are their heat resistance, structural stability, and good mechanical properties. However, the difficult processing procedures and the impossibility to recycle, make them less acceptable in this area. Epoxy or phenolic resins, polyesters, among others, are examples of thermosetting matrices. The thermoplastic matrices have significant advantages over thermosetting, such as increased toughness of the matrix, which increases the impact strength; the processing cycle is shorter, and the article can be re-melted and recycled. Thermoplastic matrices occupy an increasing place in the production of PMC. Polyamide (PA), polyethylene (PE), polypropylene (PP) are usual matrices used in the production of thermoplastic polymer composites (TPC).

The introduction of a reinforcement component or filler in the polymer matrix leads to the improvement of a specific property. In general, reinforcement components are used in structural applications to enhance the mechanical properties of the polymer composites. In composites with functional applications are used fillers to modify and improve the polymer matrix properties such as electrical and thermal properties. Therefore, particulate, fibrous or laminated fillers are incorporated into the polymer matrix. According to their shapes, the fillers can be one-dimensional (1D) e.g., a fiber, two-dimensional (2D) e.g., a textile structure or three-dimensional (3D) in the case of particles with different shapes and/or topography [28]. In Figure 1.2 are represented the different fillers that can be used in PMC.

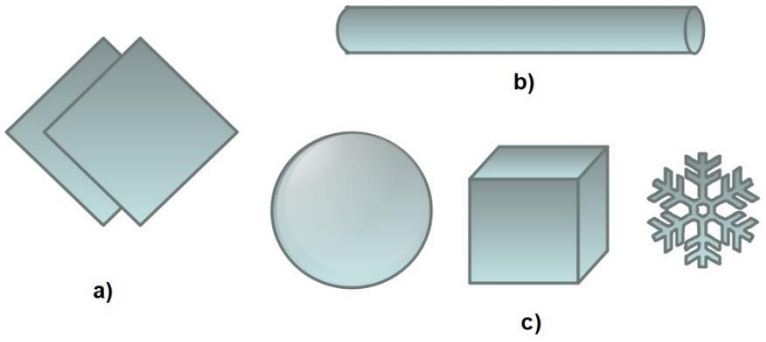

Figure 1.2 | Representation of the forms of the reinforcing phase: a) laminate type or 2D; b) fibers or 1D; c) particles or 3D. Adapted from [28].

The PMC can further be classified according to the size of the dispersed phase included in it: *i)* macrocomposite if the fillers comprise sizes above 0.1 mm; *ii)* microcomposites if their sizes are in the order of micrometers (μm); *iii)* nanocomposites if the filler has in one of its dimensions 100 nanometers

(nm) or less; *iv)* molecular composites, wherein the filler is constituted by macromolecules with diameters in the angstrom (Å) range [29].

In the development of new polymer-based composites, several fillers are dispersed in the polymer matrix, depending on the properties or final application intended. To produce PMC with EMI shielding effect and HK properties, carbon nanotubes (CNT) [2, 4, 8, 19, 23, 30] and carbon nanofibers (CNF) [8, 31] have been used as 1D fillers; graphene (Gr) [5, 8, 20, 30, 32] and graphite (GR) [8] are examples of 2D fillers; and carbon black (CB) [8], Fe [33], Fe oxide (Fe_2O_3) [8, 30] and Ag flakes [4] are possibilities for 3D particulate structures.

1.3. Polymer composite materials with EMI shielding effect and HK properties

1.3.1. Nature of the EMI shielding effect and HK properties

The origin of the EMI shielding effect and HK properties are related to the interaction of electric and magnetic fields and the formation of EM waves. The propagation of an EM wave is given by the fact that an electric field, $\vec{E}$, generates an induced magnetic field, $\vec{B}$, as a result of the movement of electric charges. Then, the $\vec{B}$ generates an $\vec{E}$ also induced, repeating this effect by itself through the direction of the EM wave propagation in free space [34].

The behavior of the EM waves is affected by the medium that they cross, in which the reflection, absorption, attenuation, or dissipation effects influence their propagation. The EM waves can be classified and arranged according to their wavelength, λ, and frequency, f in the EM spectrum, as shown in Figure 1.3 [35]. Since the EM waves travel in free space at the speed of light, c, the relation between λ and f is given by:

$$c = \lambda \cdot f \tag{1.1}$$

As previously mentioned, any device with an electronic circuit integrated and exposed to an EMF is susceptible to EMI. Subsequently, the EMI is related to the conducted and/or radiated EM signals emitted by the electronic circuit when it is switched on, perturbing the performance of surrounding electrical devices and systems concerned or causing radiative damage to living species [7, 36]. Therefore, the EMI shielding can be defined as a phenomenon in which the emission and propagation of the EM waves are minimized through reflection (R), absorption (A), and/or multiple reflection (M), mechanisms, acting as a shield against the radiation [6, 7, 36, 37].

In order to avoid undesirable transmission from the shielded device or system, the energy associated with the EM waves should be absorbed and stored into the respective material. This effect is

characteristic of dielectric materials with HK properties [15–17], the latter being influenced by their polarization capacity [38].

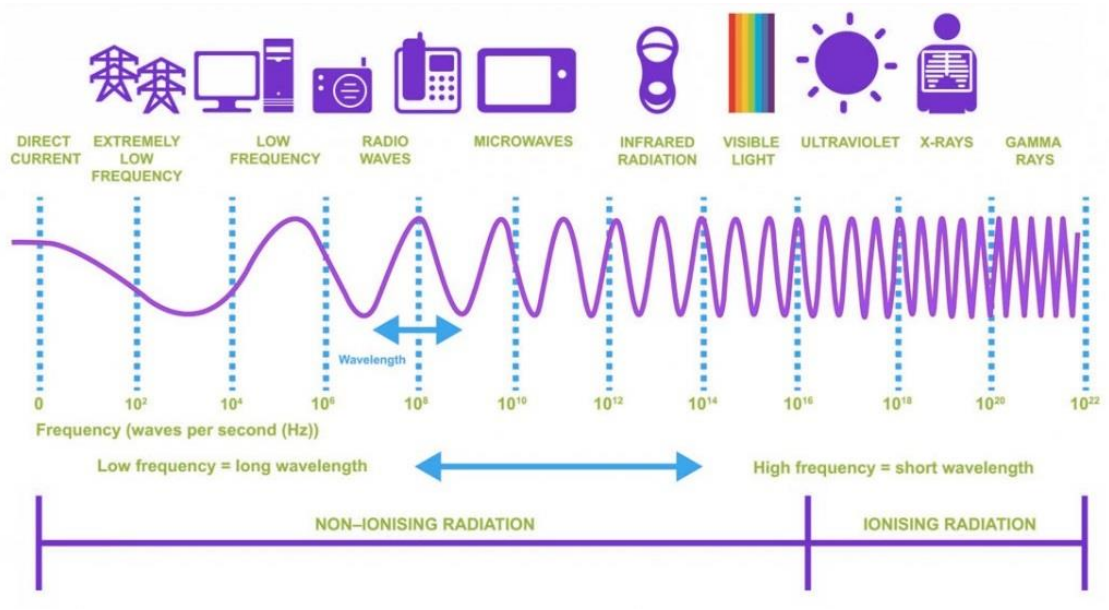

Figure 1.3 | Schematic illustration of the EM spectrum [35].

Different mechanisms can explain the phenomena associated with the EMI shielding effect and HK properties.

1.3.2. Mechanisms describing EMI shielding effect and HK properties

As mentioned above, three different mechanisms contribute to the EMI shielding properties of a certain material striked by EM waves. In Figure 1.4 there is a representation of the mechanisms that describe the EMI shielding effect.

The main shielding mechanism is by reflection, which is due to the impedance discrepancy between air and material subjected to EMI. Materials used for shielding by reflection comprise mobile charge carriers to interact with the EM field and to reflect or attenuate the radiation. Therefore, the shielding material should possess electric conductive properties. The absorption is the second shielding mechanism. It happens due to power dissipation while the EM waves interact with the dipoles of the material. Thus, dielectric and/or magnetic materials are required for the absorption mechanism. The third shielding mechanism is the multiple reflections resulting from the reflections by different surfaces or interfaces within the shielding material. The presence of a large surface and interfacial area, as well as porous topography, are needed for this mechanism to be effective [8, 36, 37].

Based on the shielding mechanisms described, the EMI shielding can be quantified through the measurement of the shielding effectiveness (SE). The overall SE of a material is defined by the capability to attenuate the EM waves passing through the material, as the ratio between the intensity of the EM waves before and after of the shielding mechanisms. Besides that, the SE can be characterized in relation to the reduction of the electric or magnetic field intensities induced by shielding.

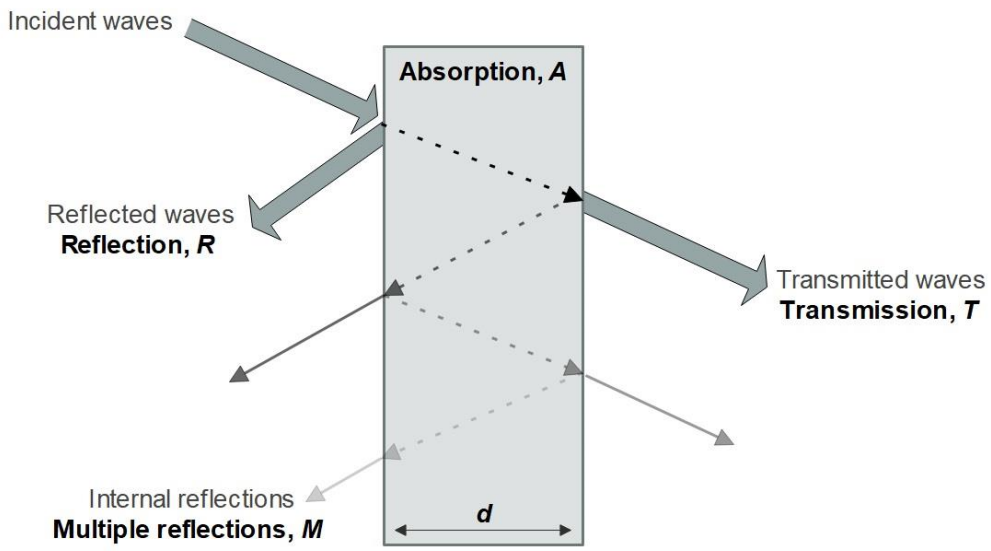

Figure 1.4 | Representation of the EMI shielding mechanisms. Adapted from [37].

Several factors influence the SE of a material with EMI shielding properties, in particular, the frequency of the incident EM field; the electric, permeability, and permittivity properties, as well as the thickness of the shield material; the type of EM field source; distance from the EM field source to the shield material; shielding degradation caused by any shield apertures and penetrations; and the quality of the preparation of the shield material [39].

Rigorous mathematical characterization of SE is presented in references [2, 39]. The overall SE can be expressed in decibels (dB) as the sum of the shielding mechanisms contribution, according to Equation 1.2:

$$SE(dB) = SE_R + SE_A + SE_M \tag{1.2}$$

The reflection loss or SE_R is expressed as:

$$SE_R(dB) = 39.5 + 10\log_{10}\left(\frac{\sigma}{2\pi f \mu}\right) \tag{1.3}$$

and the absorption loss SE_A is given by:

$$SE_A = 8.686 d \sqrt{\pi f \sigma \mu} \tag{1.4}$$

where d, μ and σ are, respectively, the thickness, magnetic permeability and electric conductivity of the shield material.

If the SE_A is higher than 10 dB, the multiple reflection SE_M can be neglected [2].

Additionally, the overall SE can also be determined from the power, P, electric, E, or magnetic field, H, intensities [40]:

$$SE(dB) = 10\log_{10}\left(\frac{P_I}{P_T}\right) = 20\log_{10}\left(\frac{E_I}{E_T}\right) = 20\log\left(\frac{H_I}{H_T}\right) \tag{1.5}$$

where P_I, E_I, H_I refers to the incident components, and P_T, E_T, H_T refers to the transmitted ones. The overall SE is measured as a function of the frequency, f.

With all these ideas in mind, in order to produce polymer-based composites with EMI shielding properties, the occurrence of EM reflection and/or absorption must be induced. Therefore, it will be important to tailor the composite's structure creating a balance between its dielectric and electric conductive properties.

A dielectric is an electrical insulator that when exposed to a high potential difference allows the flow of electric flux. The main feature of a dielectric is the polarization of its dipoles when subjected to an electric field. Therefore, there is an orientation of the positive charges in the direction of the field and the negative charges shift in the opposite direction. This separation of positive and negative charges and the resulted induced dipole moment are named polarization, as shown in Figure 1.5. Then, it is created an internal electric field, opposite to the external electric field, which causes the reduction of the overall electric field of the dielectric [41].

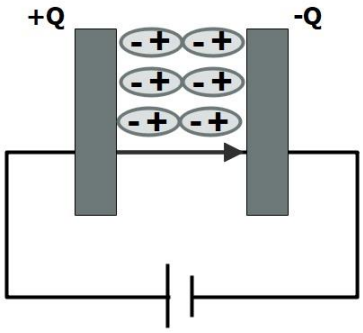

Figure 1.5 | Representation of the polarization phenomenon in a dielectric. Adapted from [41].

The more easily a dielectric is polarized, the greater the opposite electric field, which means a greater accumulation of electric charges to replace the initial external electric field. This is the capacitor's working principle.

The capacitors consist of two parallel conductive plates, usually a metal, separated by a dielectric. The ability of capacitors to store an electric charge is called capacitance. Thus, the capacitance of the parallel plate capacitor in free space, C_0 , is given by [38, 41]:

$$C_0 = \frac{Q_0}{\Delta V} \tag{1.6}$$

where Q_0 is the charge on the plates and ΔV is the potential difference applied between the plates. Figure 1.6a represents a parallel plate capacitor in free space.

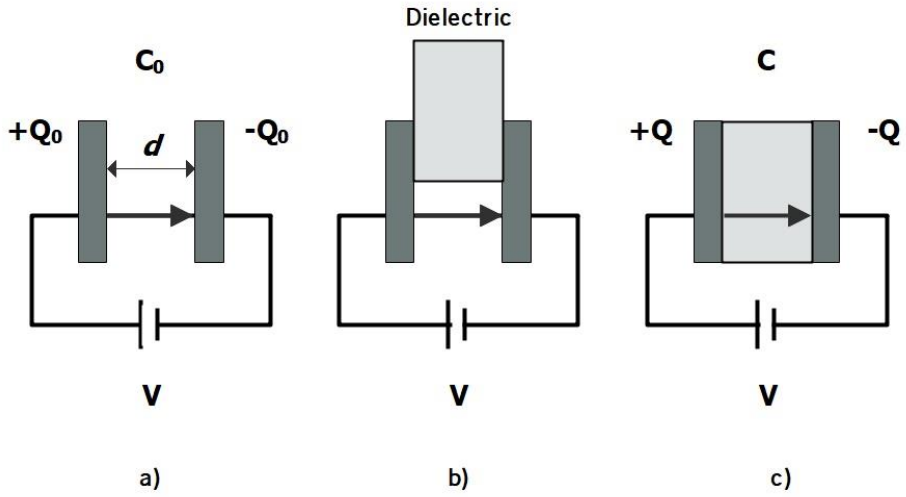

Figure 1.6 | Representation of a parallel plate capacitor: a) with free space between the plates; b) insertion of a dielectric material between the plates; c) with a dielectric material between the plates. Adapted from [41].

Moreover, a parallel-plate capacitor comprises two conducting plates with area, A , parallel to each other, and separated by a distance, d . Thus, the C_0 can be determined according to Equation 1.7:

$$C_0 = \frac{\varepsilon_0 A}{d} \tag{1.7}$$

where ε_0 is the dielectric permittivity in free space ($\varepsilon_0 = 8.854 \times 10^{-12} F \cdot m^{-1}$).[41]

If a dielectric material is inserted into the parallel plate capacitor, as represented in Fig. 1.6 b-c, the capacitance, C , is defined by [38, 41]:

$$C = \frac{\varepsilon' \cdot \varepsilon_0 \cdot A}{d} \tag{1.8}$$

where ε' represents the dielectric constant of the material. Then, the ε' can be directly determined according to Equation 1.9:

$$\varepsilon' = \frac{C \cdot d}{\varepsilon_0 \cdot A} \tag{1.9}$$

During the application of the electric field, in alternating current (a.c.), the electric dipoles are not able to suddenly follow the oscillation. The oscillating field and reorientation of the dipoles are out of phase, resulting in energy dissipation. This frequency-dependent phenomenon is known by dielectric relaxation, in which the total permittivity or dielectric constant of a material is defined by a complex function, as follow [38, 42]:

$$\varepsilon^*(\omega) = \varepsilon'(\omega) - i\varepsilon''(\omega) \tag{1.10}$$

where ε^* is the complex dielectric permittivity, ε' is the real component or dielectric constant, ε'' is the imaginary component or dielectric loss, and ω is the angular frequency of the external electric field ($\omega = 2\pi f$). The real component is related to the stored energy and it is defined by $\frac{Q}{Q_0}$. The imaginary component represents the polarization losses by the dielectric during the dipole's orientation, and its value is obtained from the loss factor, $\tan\delta$, according to Equation 1.11:

$$\tan\delta = \frac{\varepsilon''}{\varepsilon'} \tag{1.11}$$

It should be noted that ε^* is determined at a certain angular frequency, ω.

In Figure 1.7 is represented the frequency dependence of the real and imaginary parts of the permittivity, and its relaxation.

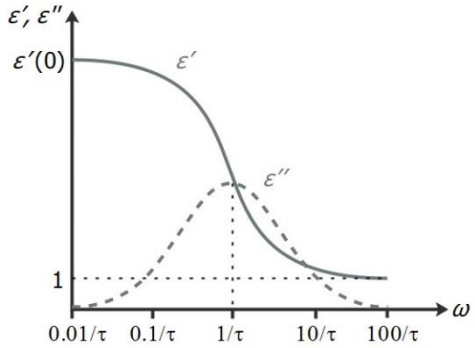

Figure 1.7 | Frequency dependence of the real and imaginary parts of the dielectric constant. Adapted from [41].

Frequency values are given as a function of the relaxation time, i.e. the average time a dipole needs to return to the starting position after the electric field is removed. The power dissipated by the dielectric reaches the maximum value when $\omega = 1/\tau$, the relaxation peak, which is at a frequency when the dipoles relaxations are at the exact rate for maximum power dissipation. The value $1/\tau$ depends on the material, but for a solid, usually it is in the gigahertz (GHz) range, i.e., at microwave frequencies. Moreover, besides of an orientational polarization, another polarization mechanism will occur since there are always electron clouds around individual atoms or in covalent bonds. Hence, the frequency dependence of the real and imaginary parts of the dielectric constant can also be represented according to the polarization mechanisms, as shown in Figure 1.8 [38, 41].

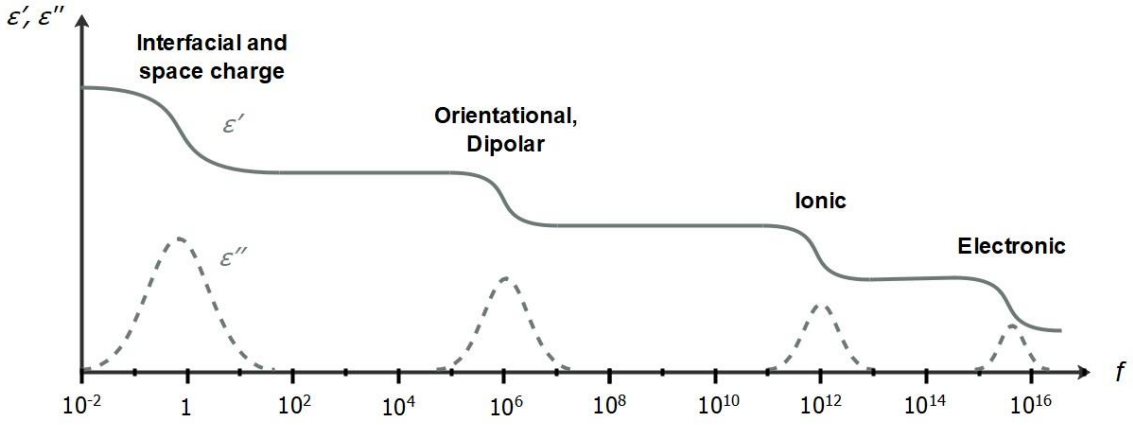

Figure 1.8 | Frequency dependence of the real and imaginary parts of the dielectric constant at different polarization mechanisms. Adapted from [41].

Each polarization mechanism has a different influence on the time response capability to a certain frequency, confirming the frequency dependence of the dielectric constant. Therefore, the dielectric constant decreases with the frequency increase, since the polarization phenomena are less effective.

Besides the influence of the frequency variation on the dielectric constant, ε', the electric conductivity, σ, is also affected, since the charge carriers reverse its direction whenever the polarity is reversed. The higher the frequency of polarity inversion is, the shorter becomes the distance traveled by the charge carriers in each direction. Consequently, they suffer fewer collisions, decreasing the resistance of the material and, as expected, the electric conductivity increases.

As implicit by Eq. 1.10, the dielectric response of a material subject to an a.c. field depends on ω. Further, the ε^* is related to complex conductivity, σ^*, by [38]:

$$\sigma^* = i\omega \cdot \varepsilon_0 \cdot \varepsilon^* + \varepsilon'' \cdot \omega \cdot \varepsilon_0 = i\sigma'' + \sigma' \quad (1.12)$$

Thereby, the a.c. electrical conductivity, σ' or σ_{ac}, can be obtained from the frequency dependence of the real part of the ε according to Equation 1.13:

$$\sigma_{ac} = \varepsilon'' \cdot \omega \cdot \varepsilon_0 \quad (1.13)$$

Based on this, it is verified that different mechanisms and parameters influence the EM shielding and dielectric properties of the materials. For EMI shielding properties, the SE below 20 dB is considered poor for a shielding material. The SE in the range of 20 – 40 dB is considered the minimum effective range of shielding for commercial applications, although the desirable SE value should be greater than 40 dB. If a material satisfies the 60 dB shielding requirement, it is considered an excellent EMI shielding material [7, 43, 44]. About the HK properties, the search for an HK ($\varepsilon' > 3.9$)[17, 45] conductor combined with very low dielectric losses ($\tan\delta \leq 1$)[23] in a single material has been a challenge in the development of advanced polymer composites.

1.3.3. Electric, magnetic and dielectric fillers with EMI shielding and HK properties in polymer composites

The mechanisms responsible for the EMI shielding phenomena or that confer HK properties to polymer composites are directly related to their conductive and dielectric properties being regulated by various fillers. In the first place come the metal fillers because of their high electric conductivity and their capacity to reflect and absorb EM waves. As noticed before, σ, μ and ε' influence the SE_R and SE_A mechanisms, and consequently the overall SE.

Thus, for an EMI shielding by a reflection mechanism, it is important to choose a metal with higher σ such as Al, Ag, Cu or Fe so that the mobile charge carriers could interact with the EM field. If the purpose is to obtain a material with a SE by absorption, metal fillers with high ε' or μ should be used, having in mind that the electric or magnetic dipoles interact with the EM field. Thus, the electric dipoles may be provided by dielectric fillers with a high $\varepsilon'$and the ones with a high value of μ, providing the magnetic dipoles. In these conditions, effective absorption of the transmitted EM radiation is achieved. Zinc oxide (ZnO), titanium oxide (TiO_2), and barium titanate ($BaTiO_3$) are examples of high ε' fillers, while carbonyl Fe, Ni, Co, or Fe_2O_3 are known by their high μ [8, 46, 47].

Carbon-based fillers such as CNT, CNF, Gr, GR or CB are another approach for providing EMI shielding properties to PMC. These fillers have widely been used in EMI shielding applications as a result

of their good electrical conductivity, providing mobile charge carriers to interact with the EM field, and ability to achieve low percolation thresholds through a conductive interconnected network [7, 8, 46–48].

For a broad spectrum of energy storage devices, the HK materials are highly important. In addition to a high ε', which is common to EMI shielding materials by SE_A mechanism, it is important to tailor the PMC constituents to ensure low dielectric losses, as mentioned above. Thus, the use of proper inorganic fillers like metal oxides, nitrides, and perovskites or selected organic fillers like carbon nanoparticles is a suitable path to improve the dielectric properties in PMC, since these loads have the ability to become polarized under an applied electric field [17, 49, 50].

Among the inorganic fillers used, nitrides and oxynitrides, tantalum oxide (Ta_2O_5), TiO_2, zirconium oxide (ZrO_2), $BaTiO_3$, barium zirconate titanate ($BaZrTiO_3$), aluminum oxide (Al_2O_3), are well known by their ability to improve the ε' of polymer-based composites [17, 22, 49, 50]. In Table 1.1 there are the ε' of the most used inorganic fillers in HK materials.

Table 1.1 | HK inorganic fillers commonly used in polymer-based composites [45]

Dielectric filler	ε'
$La_{1.8}Sr_{0.2}NiO_4$	≈ 100 000
$CaCu_3Ti_4O_{12}$	≈ 60 000
$SrTiO_3$	2 000
$BaTiO_3$	1 700
TiO_2	80
La_2O_3	30
ZrO_2	25
Ta_2O_5	22
$BaZrTiO_3$	17
Al_2O_3	9

The introduction of conductive carbon nanofillers into the polymer matrix can be useful in the fabrication of HK materials due to very low filler concentrations that are used to reach these properties, as noticed in the reparation of EMI shielding PMC [17, 23, 32]. Further, conductive fillers induce a strong interfacial polarization in conductive polymer composites, enough condition to improve the dielectric properties of such materials. CNT or Gr are possible choices of carbon nanofillers used to obtain HK

properties[17]. Values of ε' about up to 465 with multi-wall CNT (MWCNT) [23] or 14000 with Gr oxide [32] can be achieved depending on the intended application and frequency range to work it.

Knowing the phenomena associated with the effects of the EMI shielding effect and HK properties, as well as the type of fillers that can be used to induce the corresponding mechanisms, different analytical methods can be used in the study and characterization of materials with such properties.

1.3.4. Methods for studying the EMI shielding effect and HK properties

Experimentally, there are four test methods that can be used to measure the EM shielding properties of a material or even of an electronic device, namely Open Field of Free Space Method, Shielded Box Method, Shielded Room Method and Coaxial Transmission Line Method.

The Open Field or Free Space Method allows measuring the radiated emissions from an electronic device, its conductive emissions, and estimating the real SE of the normal use conditions of a complete electronic device. The setup requires the placement of the electronic device at 30 m from a receiving antenna and collecting data about the radiated emissions, as well as the conducted emissions transmitted. A noise level meter records the results, determining the level of EMI shielding obtained [37, 51].

For comparative studies of distinct shield materials, the Shielded Box Method is widely used. As the method name suggests, a metal box is used. Inside of it, there is an electrically tight seam fitted with a sample holder in one of the box walls, and a receiving antenna connected to it. Outside the box, there is a transmitting antenna that records the intensity of the signal with and without a sample. The adequate electrical contact between the samples and the shielded box, the restricted range of frequency of about 500 MHz, and the poor correlation between the results from different laboratories are limitations of this method [37, 51].

The disadvantages of the Shielded Box Method can be overcome by the Coaxial Transmission Line Method, whose setup is shown in Figure 1.9. The apparatus is composed by a specimen holder in the form of a coaxial transmission line connected to a pair of flanges in which the reference and load specimens are placed in it. The coaxial transmission line is connected to a vector network analyzer (VNA) by two ports (port-1 and port-2) which works as a signal generator and receiver. Coaxial cables and connectors and attenuators are included in that experimental configuration. The use of small specimens shaped as doughnuts, comparable results obtained in different laboratories, data obtained into reflected, absorbed and transmitted components, measurement of the signal attenuation as a direct measure of

the SE of the specimen, and the possibility to perform the measurements in a broad frequency range are important advantages of a coaxial transmission line [37, 51].

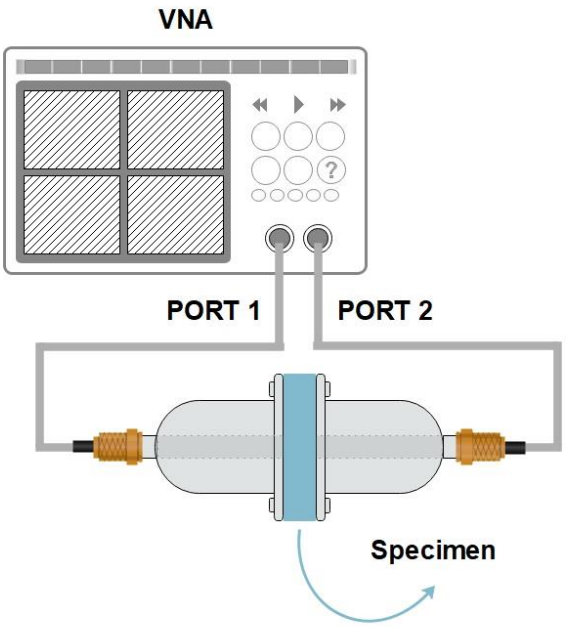

Figure 1.9 | Representation of the setup used in the Coaxial Transmission Line Method.

The most complex method is the Shielded Room Method. It was developed to overcome the disadvantages of the Shielded Box Method, and the general principle is the same. However, in the Shielded Room Method, components of the measuring system, signal generator, transmitting antenna, receiving antenna, and recorder are located in a separate room to eliminate the potential for any interference. Thus, the data reproducibility is ensured, and the frequency range can be extended. Though, compared to the other methods, the specimen size is of about 2.5 m^2, which requires specific laboratory installations to perform these tests [37, 51].

The dielectric properties of a material can be determined experimentally by five methods, such as Transmission Line Method, Coaxial Probe Method, Free Space Method, Resonant Cavity Method and Parallel Plate Method [52].

The Transmission Line Method allows measuring the dielectric properties of a material using a rectangular waveguide or a coaxial airline. The apparatus is connected to a VNA which works as a signal generator and receiver, measuring the reflected signal. The specimen should fit the cross-section of the

transmission line, without any gaps at fixture walls; smooth and homogeneous faces are also required. This method allows performing measurements in a broadband frequency range [52].

The Coaxial Probe Method has a similar operating mode to the Transmission Line Method, but it is used an open-ended coaxial probe, instead of coaxial airline. This cut off section is connected to the flat face of a solid specimen or immersed into a liquid, if the aim is to measure the dielectric properties of a liquid. Besides the proper cables and connectors, the coaxial probe is connected to a VNA or an impedance analyzer in order to measure the reflected signal. Moreover, the frequency dependence of temperature can also be determined, since proper temperature probes are used, which is a plus in the study of dielectric properties. However, the low-frequency range and the accuracy of the results are limitations if compared to other methods [52].

In the Free Space Method, the specimen is placed between a transmitting and receiving antennas, and the attenuation and phase shift of the signal are measured. Usually, this method is implemented for the performance control of industrial applications, and a wide and high-frequency range can be used. Materials under high temperatures and hostile environments can be studied provided that a suitable chamber is used.

The Resonant Cavity Method is frequently used for measuring the dielectric properties of low dielectric loss materials using small specimens. A rectangular or circular specimen is placed through the center of a waveguide (cavity), and the changes of the selected frequency and the stored energy are measured. The possibility to perform the measurements at only one or a few frequencies, and to adapt the setup to high or low temperatures are advantages of this method [52].

The Parallel Plate Method comprises placing a thin, flat and smooth sample between two electrodes to form a capacitor, as illustrated in Figure 1.10. Then, its capacitance is measured using an impedance analyzer or an Inductance-Capacitance-Resistance meter. The accuracy of this method is very high and usually is used for low-frequency measurements [52].

Apart from knowing well the different methods that can be used in the characterization of EMI shielding and HK materials, it is also very important to identify their specific composition, since the performance of these advanced materials is directly related to the concentrations of the conductive, magnetic or dielectric fillers. Some other factors related to the fillers such as the size, shape and its volume fraction are also significant. Thereby, different compositions and preparation methods can be found in the development of new TPC with EMI shielding and HK properties.

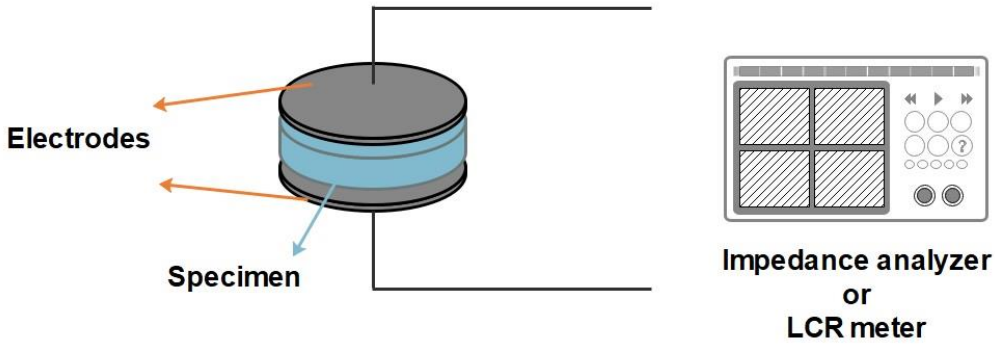

Figure 1.10 | Representation of the Parallel Plate Method.

1.4. Thermoplastic composites with EMI shielding effect and HK properties

1.4.1. Thermoplastic composites containing carbon fillers

The significant improvement of the electrical properties of a TPC when carbon allotropes are dispersed in its matrix is the main reason for the overall SE increase, often without looking for a greater contribution to a reflection or absorption mechanism. Thus, the type and size of the carbon allotrope´s particles, its aspect ratio and volume fraction have an important role in the EMI shielding effect.

Among the advances of TPC with EMI shielding properties, the use of GR had been studied due to its natural abundance and low cost. An overall SE value of 12 dB at a high graphite content of 26 vol.% in 3.2 mm thick polycarbonate (PC) composites was reported by Krueger et al. [53]. However, if a PA66 matrix is used, the SE values drop to 3 dB. High-density PE composites were prepared by Panwar and Mehra with different volume fractions of GR, achieving a SE value of 33 dB with 18.7 vol.% in a 3 mm thick sample [54]. Jiang et al. reported the preparation of 2.5 mm thick PE composites containing 7.05 vol.% GR without the use of any organic solvent with an excellent SE value of 51.6 dB [55].Different weight percentage of GR was used in the preparation of GR/acrylonitrile butadiene styrene (ABS) composites with thickness ~ 3 mm. The percolation threshold was reached at 3 wt.% of GR, resulting in an overall SE of 14 dB and TPC with a SE=60 dB were prepared using 15 wt.% of GR [56].

CNF or carbon fibers (CF) are considered appropriate fillers for TPC in EMI shielding due to their aspect ratio and electric conductivity. The effects of CF length and weight percentage upon the SE of PA66 composites were investigated by Jou et al. [57]. For 1.2 mm in thickness, 25 wt.% of longer CF, a SE value of 50 dB was obtained at 1 GHz. Krueger and King reported the preparation of PA66 and PC-based composites, in which an overall SE value of about 14–15 dB was attained with a CF content of 27 vol.%, introduced in PA66 or PC matrices [53]. An overall SE of about 24 dB was obtained for 2 mm thick

polystyrene (PS) composites with 7.5 vol.% of vacuum-grown CNF were produced by Al-Saleh et al. [58]. The authors also studied the influence of the CNF content on the EMI shielding effectiveness of ABS composites, achieving values of 35 dB by means of 15 wt.% CNF in 1.1 mm thick samples [59]. Nayak et al. presented the preparation of EMI shielding CNF-based polysulfone nanocomposites [60]. Different compositions were prepared containing 3–10 wt.% CNF. The composite with higher CNF wt.% and thickness of 1 mm achieved a SE value of 45 dB. Amelie et al. studied the effect of CF in PP foamed and solid composites with a thickness of 3.2 mm, up to a CF content of 10 vol.% [61]. The foamed composites showed the best EMI shielding properties with overall SE values of ca. 20 dB.

Due to the intrinsic high electrical conductivity and aspect ratio of CNT leading to low percolation thresholds, this carbon allotrope has been subject to much investigation resulting in the preparation of several TPC. Al-Saleh studied the shielding effect and mechanisms of CNT in PP [2] and ABS [59, 62]. For ABS nanocomposites the best overall SE value reported was 50 dB with 15 wt.% MWCNT [59], while 36.4 dB was the value obtained for a PP composite with 7.5 vol% MWCNT [2], both samples with a thickness of about 1 mm. Poly(trimethylene terephthalate) (PTT)/MWNT composites were prepared by melt-mixing varying the MWCNT from 0.24 to 4.76 vol.% [63]. The best EMI shielding performance was ~ 23 dB in a 2 mm thick composite at 4.76 vol.% MWCNT. A similar EMI shielding performance (EMI SE ~ 23.1 dB) was observed in 5.6 mm thick PC/MWCNT composites with 2 wt.% MWCNT and 70 wt.% PC beads [64]. Arjmand et al. compared the EMI shielding properties of injection molded versus compression-molded PS/MWCNT composites, and the injection-molded (MWCNT-aligned) samples showed lower EMI shielding properties than compression molding [65]. The EMI SE for the compression-molded samples with 2 mm in thickness and 5 and 20 wt.% of MWCNT was 15 and 30 dB, respectively. Nanocomposites based on an MWCNT-PP copolymer were prepared by micro- extrusion, and a SE value of 47 dB was reported for the system containing 4.6 vol.% MWCNT that showed also good mechanical and thermal properties [66]. The 2 mm thick samples for EMI tests were prepared by compression molding of the granulated form of the extruded nanocomposites. Jia et al. reported the effect of 1–5 wt.% CNT in a PE matrix, in which 5 wt.% CNT produced a SE of 46.2 dB in a molded sheet with 2.1 mm thickness [67]. For nanofibers mats of PA6/MWCNT with 0.1 mm in thickness and fabricated by electrospinning process, the reflection loss improved to 18 dB at 11.5 GHz with the content of 10 wt.% MWCNT [68]. Recently, the EMI shielding performance of PTT nanocomposites was evaluated through the dispersion of different wt.% of MWCNT and an overall SE value of about 38 dB was reached by means 3 wt.% MWCNT with a sample thickness of 2 mm [69].

CB is another carbon allotrope that is easily available and suitable in TPC requiring high electrical conductivity. Krueger et al. also studied the effect of CB dispersion in the PA66 and PC matrices, reporting SE values of about 22 dB for 6.6 vol.% in PA66 and 6.9 vol.% in PC [53]. The effect of two different types of CB admixed to acrylonitrile-butadiene copolymer (NBR), to ethylene-vinyl acetate copolymer (EVA) and their blends, was reported by Rahaman et al. [70]. SE values up to 60 dB were obtained in composites with segregated CB and a thickness of 4 cm. Furthermore, the same authors reported that NBR-based composites containing CB show improved EMI shielding properties as compared to composites with EVA matrix due to a better packing of the conductive network in the NBR matrix. Another study by Al Saleh et al., reported on composites with overall SE values of about 20 dB with 15 wt.% CB in 1.1 mm thick samples [56]. The shielding mechanisms in PP composite plates prepared with 10 vol.% CB with an SE values of 43 dB for a 2.8 mm thickness was also studied [71]. Conductive composites based on poly(styrene-b-ethylene-ran-butylene-b-styrene) and CB were prepared using a torque rheometer [72]. The effect of the filler loading on the electric properties and consequently on the EMI shielding was studied. For a 5 mm thick composite with 15 wt.% CB an overall SE value of 19 dB was obtained.

The use of Gr as a filler for EMI shielding has also attracted interest, as a result of its excellent thermal, mechanical and electric properties. There are indications that very low content of Gr is necessary to reach the percolation threshold. In the studies that employ thermoplastic matrices, functionalized Gr was used to prepare a polyvinylidene fluoride (PVDF) foam composite [73]. The effect of different loadings (0 – 7 wt.%) of Gr was evaluated and for the higher wt.% SE values of 28 dB measured in the 8 – 12 GHz range were obtained. Chen et al. also prepared Gr-foam composites with ~ 1 mm in thickness but using polydimethylsiloxane matrix, and overall SE values of 30 dB were obtained in the 30 MHz – 1.5 GHz frequency range [74]. The shielding properties of the composites with 3 mm thickness were improved up to an EMI SE of 21 dB with 0.8 wt.%. Gr-EVA composites with sandwich-like structures were prepared via wet casting using 10–60 vol.% Gr that resulted in an overall SE=16.5 dB at 12 GHz [75]. Biodegradable polylactide-Gr nanocomposites with 0–15 wt.% (0–9.1 vol%) of Gr were prepared via melt-blending and its EMI shielding properties were reported by Kashi et al. [76]. The best EMI shielding properties were achieved for the systems with the highest Gr content and 1.5 mm thickness reaching an overall SE values of 14.3 dB.

Despite its tendency toward agglomeration that can deteriorate the processability of PMC, the carbon-based fillers can suit the EMI shielding requirements if an appropriate optimization of the processing conditions is performed. It is confirmed that not only the nature of the electric conductive loads employed but also their granulometry, size, shape and aspect ratio, and consequently the volume

fraction used influence the desired properties. The use of nano-sized and/or higher aspect ratio loads decreases the volume fraction needed to obtain improved SE properties.

1.4.2. Thermoplastic composites containing metal fillers

The electrical conductivity of PA6/Al composites prepared by compression molding of a mixture of Al flakes and PA6 powder was investigated [77]. The effect of the filler size was evaluated, concluding that the percolation threshold is lower if bigger metal particles are used. The dielectric behavior of PVDF/Ni composites prepared with different Ni volume fractions was evaluated, and best values of $\varepsilon = 2050$ and $\tan\delta = 10$ were obtained [78]. Later, the EMI shielding properties of these composites were also investigated [79]. Besides their HK properties, the increase of the filler volume fraction led to the increase of the EMI SE values to 23 dB.

The use of Cu in electronic applications can be a proper path due to its superior electric properties. In the area of TPC materials, the preparation of Cu/PS composites was reported exhibiting an overall SE higher than 20 dB at 1.3 vol.% [80]. Yu et al. investigated the preparation of Ag/Polyvinyl alcohol composites with improved electric properties and EMI shielding [81]. Composite materials were also prepared with Co and PS, exploring the use of these composites as microwave absorbers when exposed to magnetic field [82]. The electric properties of Al/PE nanocomposites were reported by Huang et al., in which study the influence of the metal filler was evaluated in concentrations up to 48 wt.% [83]. The best dielectric properties were determined for the composite with 24 wt.% Al, indicating that the wt.% metal load affects the matrix polarization, and consequently its dielectric performance.

Efforts have also been made towards the preparation of TPC with ceramic fillers, e.g., $BaTiO_3$ combined with PVDF [22, 50, 84–87], PMMA [22, 50] or PS matrices [22, 50]. The intrinsic HK and ferroelectricity, and the different crystal phases of this metal filler allow obtaining different dielectric properties according to the intended final goal [88–90].

Some limitations of the use of metal or ferromagnetic loads may arise during the preparation of TPC with absorbing and HK properties. Generally, the high probability for oxidation during composite preparation, the extremely high density and hygroscopic properties of the metal fillers cause processing difficulties that obstruct their mass application for TPC preparation. As to the ceramic fillers, (e.g., $BaTiO_3$), high concentrations of them are needed, usually > 50 vol.% [22, 50, 91] which is considered costly.

1.4.3. Thermoplastic composites containing binary metal-carbon fillers

Very few works were found reporting the preparation of TPC composites with binary fillers, in order to overcome the limitations of the use of carbon- and metal fillers separately [92–97]. Metalization of carbon fillers, i.e., coating with metal layers is one possibility. Cu and Ni are among the main metals used to coat the carbonaceous fillers. Metal-coated carbon fillers are usually prepared by chemical vapor deposition [98], cementation, and electroless deposition techniques [93], or by electrochemical deposition [95], followed by melt mixing with the respective matrix polymer. A method to synthesize PS/Ni-MWCNT in the form of flexible composite film was reported by Srivastava [99]. Huang et al. produced PC/ABS blends with CF and Ni coated CF using extrusion for compounding, and compression molding to produce the molded composites [100]. PC/poly (styrene-co-acrylonitrile) blends loaded by MWCNT grafted Fe_3O_4 nanoparticles [101] and graphene sheets decorated with Ni nanoparticles [102] were prepared using a mini extruder. Zhang et al. prepared long-CF-reinforced PA6/Ni composites by the combination of melt blending and pultrusion processes [97]. Besides the reported improvements in the EMI shielding properties, with overall SE values varying between 15 and 60 dB [92–94, 96, 97, 100–102], materials as efficient EM absorbers with reflection losses up to 33 dB [99], or HK properties wherein values of ε' and tan δ up to 200 and 0.4, respectively, at 30 MHz were obtained [97]. It should be noted that the preparation of the respective conducting polymer hybrids by these methods includes various and relatively complex steps.

1.4.4. Importance of the dispersion homogeneity and its relation to EMI shielding and HK properties

Appropriate dispersion of fillers in a polymeric matrix, along with their intrinsic structures and physical properties, is considered the most critical factor affecting the properties and performance of the polymer composites, including electric, magnetic and dielectric properties. A good dispersion of the fillers in the polymer matrix is a major requirement in the development and production of high-performance polymer-based systems. Typical dispersion and distribution states of a filler in a polymeric matrix are illustrated in Figure 1.11 [49].

In an electric conductive material, the percolation threshold can be achieved if the conductive filler is dispersed and distributed as shown in Fig. 1.12b, thus obtaining a conductive network. On the other hand, to obtain a HK material, the aim is an uniform dispersion and distribution of the filler in the polymeric matrix, as shown in Fig. 1.12a, the same arrangement leading also to the improvement of the mechanical and thermal properties [49].

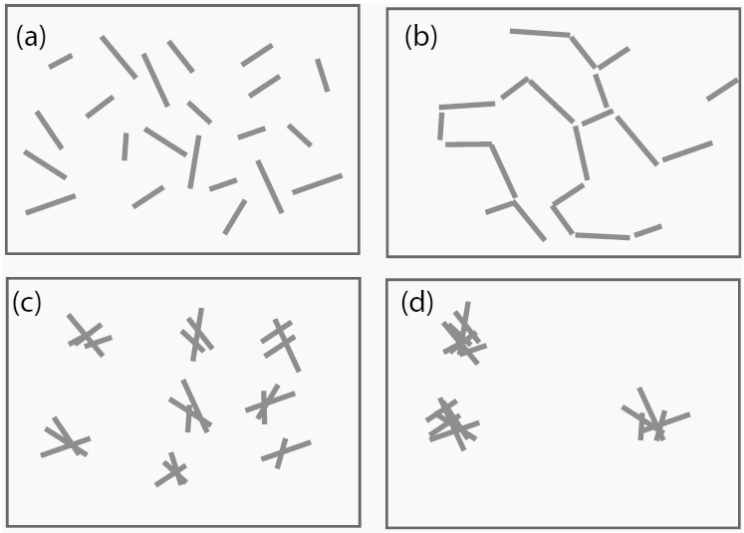

Figure 1.11 | Illustration of dispersion and distribution of states of filler in a polymeric matrix: a) uniform dispersion and uniform distribution; b) uniform dispersion and poor distribution; c) poor dispersion and uniform distribution; d) poor dispersion and poor distribution. Adapted from [49].

Unfortunately, conventional processing techniques such as extrusion or injection molding cannot provide easily the most advantageous state of distribution. Improving the dispersion by these two techniques passes through various high-temperature cycles at high processing pressures due to the elevated viscosity of the polymer matrix. The possibility of material degradation due to shear rates and temperatures applied is also present, and sometimes more than one melting/recrystallization cycle is required [103, 104]. The use of non-conventional processing machinery makes possible the production of parts with complex geometries and eliminates aesthetic and structural defects [105], however it is costly and with limited access [106].

Another possible pathway toward an optimal particle distribution is the chemical modification of the filler in order to enhance its miscibility with the polymer matrix. Thus, the poor dispersion of carbon allotropes affects quite negatively the mechanical and conductive properties of the final composite [107]. The dispersion can be improved by surface modification and covalent or non-covalent functionalization of the carbon filler. These approaches also enhance the adhesion between filler and polymer matrix [108]. It is important to note here that filler functionalization toward better miscibility is quite expensive and difficult to scale-up, limiting its use for high price applications only [109]. In addition to this, functionalization could deteriorate or even completely eliminate the useful properties of the functional filler, e.g. decreasing conductivity by creating the surface defects on the carbon filler [110, 111]. Ultimately, any attempt to use conventional processing with high loads (typically above 5 wt.%) of any filler in most of the cases leads to an agglomeration of the latter and inferior mechanical properties [28].

A recent approach toward polymer composite materials comprising various fillers/reinforcements whose electrical, dielectric and magnetic properties can be appropriately varied is related to the so-called micro- and nanoarchitecture strategy [22]. According to this methodology, each micro- or nanosized filler particle is first covered with selected polymers by grafting-from [112] or grafting-to techniques [113] thus forming core-shell particles. These are transformed into polymer composites by a conventional molding technique. This strategy offers several important advantages over the conventional melt mixing and solution mixing techniques for the preparation of polymer composites. It enables the synthesis of highly loaded composites with homogeneous filler dispersion [22]. Furthermore, the preparation of composites with tailored combinations of functional properties, such as EM and dielectric properties is made possible, i.e., such with suppressed dielectric loss at high ε' [112, 113]. At the same time, a possibility for fundamental insight on the role of the matrix-filler interfaces on the properties of the material appears [22, 114].

However, the analysis of the most common micro- and nanoarchitecture strategies reveals some important limitations. First, in most of the cases, the chemistries involved to produce the shell-core particles (e.g., click reactions, reversible addition/fragmentation chain transfer polymerization (RAFT) and atom transfer radical polymerization (ATRP) mechanisms) are relatively complex and hardly suitable for scale-up. Due to the complexity of the catalysts or reagents involved, RAFT and ATRP possess too many reaction variables affecting the characteristics of the final polymer [115]. Moreover, there seems to be still a problem to introduce into the same particle high loads of very different materials.

A way to overcome the above limitations and to extend the micro- and nanoarchitecture strategies toward the preparation of TPC with EMI shielding effect and HK properties can be the use of new microencapsulation strategies based on industry-relevant polymerization processes and polymer materials.

1.5. Polyamide-based composites

1.5.1. Importance of polyamide-matrix composites

The PA family of semi-crystalline polymers (called also nylons) is characterized by a relatively high service temperature and is widely used in the production of TPC. Polyamides possess good toughness, rigidity, a high degree of solvent/chemical resistance, thermal stability, resistance to wear, abrasion and friction, easy processing, and good surface appearance. Moreover, polyamides have low melt viscosity that facilitates processing and are also relatively low cost [116–118].

Among the different types of polyamides, polyamide 6 (PA6) is one the most widely used due to its toughness, strength, and thermal and chemical [119] e.g., in the automotive, construction, textile, and food industries. This semi-crystalline polymer is a versatile material that combines excellent properties and competitive cost with easy processability and aesthetic properties [120]. The chemical structure of PA6 is shown in Figure 1.12.

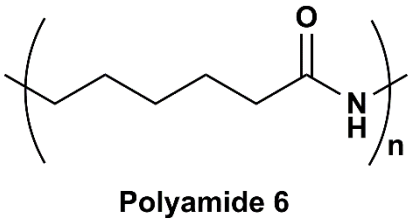

Figure 1.12 | Chemical structure of PA6.

1.5.2. Production of polyamide-based composites

PA-based composites can be prepared by conventional melt-blending techniques or by in situ reactive processing techniques.

1.5.2.1. Melt-blending techniques

Among the conventional melt-processing techniques, in which the fillers are mixed with a previously existing polymer matrix in the melt, processing techniques as extrusion [96, 121, 122], injection [53, 96, 123, 124] or microinjection [125] can be used in the fabrication of PA6-based composites. Nowadays all of these conventional processing techniques are widely applied in the transformation of PA6. However, along with their numerous advantages, traditional processing methods need relatively high processing temperatures, most frequently with the application of more than one melting/recrystallization cycle. This creates high possibility of material degradation due to shear forces and applied temperatures. Poor dispersion of particulate and fibrous loads with subsequent aggregate formation are other disadvantages of these methods [103, 104]. All these factors negatively influence the mechanical properties of the final product. Furthermore, melt-blending techniques are complicated with high amounts of fillers [28]. An alternative to overcome the limitations related to melt compounding would be to synthesize the polymer matrix in situ.

1.5.2.2. Reactive processing techniques

In reactive processing, the fillers are dispersed in a monomer or monomer solution and only afterwards the latter are transformed into a polymer in situ, employing for the purpose heat, radiation or suitable initiators [104]. The in situ polymerization allows a more homogeneous distribution of the fillers in the polymer matrix and the formation of a good matrix-load interface, fundamental aspects in the preparation of high-performance materials [104, 126].

PA6 can be obtained by hydrolytic polymerization of ε-caprolactam (ECL) [127], or by its anionic ring-opening polymerization (AROP) performed in solution [128] or in bulk [129].

The hydrolytic polymerization of ECL is very well studied theoretically and widely used in industry to produce neat PA6 because of its relative simplicity and low cost of the resulting granulate. Several disadvantages, however, characterize this polymerization. As the PA6 formation occurs in the melt, it requires high temperatures reaching 250–270°C that should be maintained for 12 or more hours. Moreover, in the final stages of the process, an effective elimination of the released H_2O is necessary [127, 130–132].

The AROP of lactams and the properties of the final polyamides have also been investigated in great detail. The first statement of anionic polymerization of ECL was made by Joyce in 1941 [133]. Then, Hanford [134], Šebenda [130, 135–137], Stehlíček [138] and Sekiguchi [131, 139] reported several contributions to this area. Moreover, the anionic mechanism has been extensively studied for ECL monomer since ECL is the most easily accessible and industrially produced lactam [140].

Comparing the two methods for PA6 synthesis shows that the AROP method has significant advantages namely: (i) the polymerization temperatures are by 70-100°C lower than in the hydrolytic process and (ii) the homogenization between the matrix and filers in case of in situ composites preparation by AROP may be better [140, 141].

The mechanism of anionic ROP of lactams is well-studied and understood. The rate-determining stage in ROP is the formation of an imide dimer with acyl-lactam structure. This is a very slow process leading to a long induction period. If the said acyl lactam is added in the beginning of the polymerization, a very fast and effective polymer-forming process is achieved, the process being denominated as “activated anionic ring-opening polymerization” (AAROP). The initiation step of the AAROP is schematized in Figure 1.13.

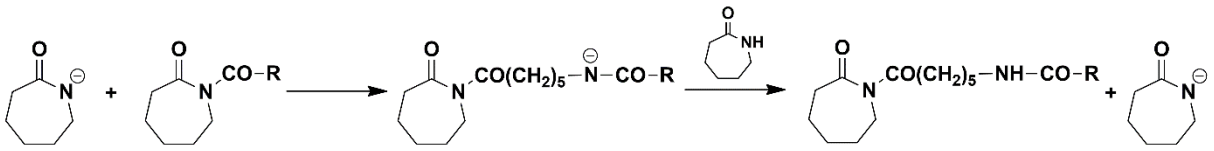

Figure 1.13 | Initiation step of the AAROP of ECL. Adapted from [132].

AAROP requires two active species: a lactam anion and a *N*-acyllactam, initiator and activator, respectively. Thus, the AAROP starts directly with the reaction between the acyl-lactam and the lactam anion followed by fast proton exchange with ECL monomer [132].

In the propagation step (Figure 1.14), a nucleophilic attack of the lactam anion on the endo-cyclic carbonyl group takes place, followed by rapid proton exchange with the monomer, thus regenerating the lactam anion and the propagating *N*-acyllactam. Theoretically, the polymerization ends with the monomer consumption. Thus, AAROP could occur as a "living" polymerization, provided that some side reactions do not occur. The latter normally lead to deactivation of both the lactam anion and the *N*-acyllactam active end [132].

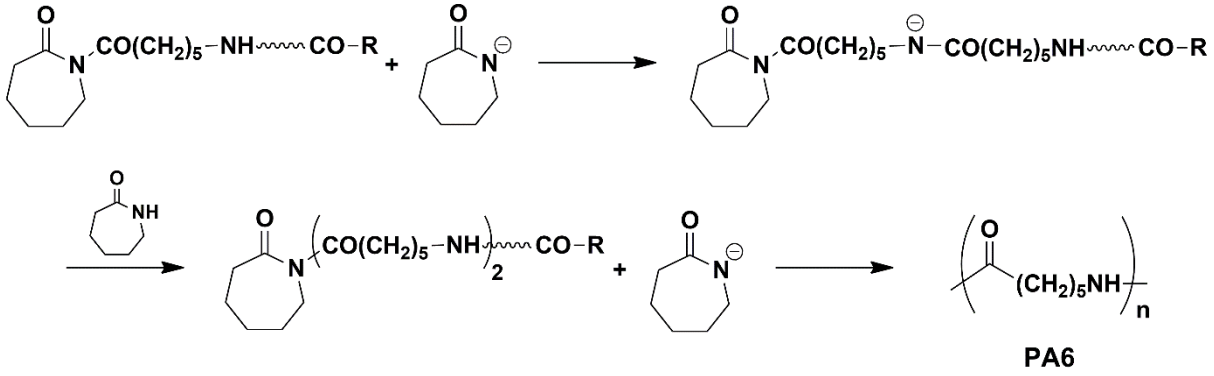

Figure 1.14 | Propagation step and final product of the AAROP of ECL. Adapted from [132].

The numerous studies about AAROP of ECL made clear the importance of the correct choice of the initiator and activator. Among the several initiators described in the literature, the most used are based on alkali metals [131], alkoxides [135], metal halides [142], and Grignard reagents [143]. As regards the activators, *N*-substituted lactams such as *N*-acyllactam [144, 145] or compounds containing carbamoyl groups with an electronegative substituent [143, 146, 147] are reported to be appropriate in AAROP. Silyl compounds have also been investigated as mild activators of the AAROP of ECL [148, 149].

In most of the cases the AAROP is performed in the bulk, producing highly crystalline materials called "cast polyamides" [150–152]. The castings are produced in large molds and subsequently

machined to final articles. The use of conventional polymer processing techniques such as extrusion or injection molding with cast polyamides is very difficult and costly, which is the basic limitation of these materials. The difficult agitation of the reactive system during the bulk AAROP is another inconvenience hindering the heat dissipation during the process that may result in inacceptable degradation rates, undesirable coloration, and mechanical properties degradation. The preparation of composite materials with particulate or fibrous reinforcements with good distribution by this method is not straightforward.

To overcome these shortcomings of the bulk process, AAROP in solution or suspension/emulsion has been suggested and well-studied by various authors [128, 153–157]. Reportedly, the AAROP in solution leads to the formation of a linear polymer with sufficient molecular weight and conversion degree, without the formation of undesired sub-products. Furthermore, the neat anionic PA is obtained in the form of a powder that can be easily shaped into final articles by traditional melt-processing techniques.

Very recently a new method for the preparation of differently loaded PA6 microcapsules (PAMC) by means of solution/precipitation AAROP and their subsequent transformation into thermoplastic PA6-based composite materials was filed for patenting [158]. The synthetic method applied was developed at the Institute for Polymers and Composites (IPC) of the University of Minho (UM), whereby the solution AAROP was adapted to be carried out in the presence of various organic and inorganic particulate solids. Thus, synthesis of micron-sized particles with porous PA6 shell and different micro- and nanosized core fillers was achieved that can be easily melt-processed to composite final articles by traditional processing methods [159]. Later, this fabrication concept permitted easy and simultaneous introduction into the PA6 matrix of organic or inorganic fillers in wide concentration ranges (up to 30-40 wt.%) and with controlled dispersion [159–162]. Considering the significant theoretical and practical experience about the PA6-microencapsulation existing in IPC-UM, there are all indications that this technology could be used to produce PA6-based composites with EMI shielding and HK properties.

1.5.3. Polyamide-based composites with EMI shielding effect and HK properties

There exist relatively few studies on the development and characterization of PA-based composites with relevant mechanical properties comprising conductive or dielectric fillers. Thus, the EMI shielding effectiveness of PA66 composites was studied considering the effects of CF length and weight percentage [57]. A SE value of 50 dB was obtained at 1 GHz for 1.2 mm thicker samples with 25 wt.% of longer CF. Krueger et al. reported on the EMI shielding performance of 3.2 mm thick PA66 composites loaded with different carbon allotropes [53]. PA66 composites containing single loads of CB, CF, GR, dually loaded with CB-GR, CB-CF, GR-CF and with a triple-load (CB-GR-CF) were prepared using different filler amounts.

All systems were produced by injection molding, after obtaining the pelletized compounds by extrusion. Overall SE values between 1.52 dB (PA66/30 wt.% GR) at 300 MHz and 42.23 dB (PA66/ 5-30-20 wt.% CB-GR-CF) at 800 MHz were obtained. Furthermore, the effect of the Al flakes content on the electric properties of PA6/Al composites was investigated, confirming its influence on the percolation threshold [77]. Yoo et al. used CF and GR coated with Ni, as well as CB, MWCNT, and TiO_2 in the fabrication of PA6 composites by extrusion and injection molding [96]. The EMI shielding properties were determined for systems with different compositions, in which the dually loaded PA6 containing 15 wt.% CF + 3 wt.% TiO_2 showed the best performance with 54.2 dB at 1 GHz and 2.0 mm in thickness. He et al. coated sisal fibers (SF) by CB and then different amounts of this mixture (up to 50 wt.%) were added to a PA6/PP blend to produce composites by extrusion [122]. At 16 GHz, overall SE values of 40.7 dB were obtained using 50 wt.% of fillers in 3 mm thick samples. Nasouri et al. produced nanofibers mats of PA6/MWCNT with 0.1 mm in thickness by electrospinning, and using 10 wt.% MWCNT the reflection loss improved to 18 dB at 11.5 GHz [68]. SE value of 36 dB was achieved at 3 GHz in 4 mm thick samples when 15 wt.% of CF and 10 wt.% of Ni powder were introduced within the PA6 matrix combining melt blending and pultrusion processes [97].

Regarding TPC with HK properties based on polyamides, only three relevant publications were found. Logakis et al. reported the effect of MWCNT on the dielectric relaxation of melt-processed PA6 composites, however the ε' and/or $\tan\delta$ were not determined [163]. K. Prashantha et al. reported the combination of polyamide 11 with natural halloysite nanotubes [124] performed by injection molding that produced composites with ε' values below 6.0 and $\tan\delta$ < 0.14. In the same investigation performed by Zhang et al. on long-CF-reinforced PA6/Ni composites, values of ε' and dielectric losses up to ca. 200 and 0.4 at 30 MHz, respectively, were obtained [97].

1.6. Thesis objectives and outline

Summarizing the available information, the few PA-based composites with EMI shielding and HK properties have been prepared by melt-processing techniques only. Bearing in mind the disadvantages of this processing method, the traditional production of advanced composites with EMI shielding and HK properties cannot ensure easily the desired good dispersion of the fillers in the polymer matrix. Furthermore, there are no reports on the possibility to prepare PA6 composites with tailored EM and dielectric properties based on the melt-processing of previously prepared dually loaded PAMC, comprising binary loads of both metals and carbon allotropes. The present thesis will target this particular niche.

Therefore, the main goal of this Ph.D. thesis is twofold:

i) Synthesis by reactive microencapsulation of particulate precursors and their transformation by compression molding in PA6-based thermoplastic composite materials with dual metal/carbon allotrope loads with tailored conductivity, magnetic and dielectric properties;

ii) Investigation of the structure-properties relationship in these composites using the information obtained for explanation of their EMI shielding and HK properties.

The microencapsulation technology for preparation of hybrid PA6 microcapsules based on AAROP of lactams in solution described in [158, 159] will be used to synthesize PAMC loaded with various particulate carbon allotropes and metals. These loaded PAMC will be transformed into composites by simple compression molding. These objectives will be achieved by:

i) Synthesis of PAMC with different loads at fixed polymerization conditions with evaluation of the influence of the type and amount of these loads (single or mixed) on the yield and granulometry of PAMC;

ii) Evaluation of the morphology, crystalline structure, mechanical and thermal properties of the PAMC and of the respective compression molded composites, as a function of the amount and type of the loads employed;

iii) Study the influence of the PAMC composition, structure and morphology on the dielectric and EM properties of the molded composite products;

iv) Demonstration of the ability to tailor the electrical and EM response of the PA6 composites by changing the payload amounts and type in PAMC, assessing the possibility to prepare EMI shielding and HK PA6-based composites.

Thus, the proposed methodology can be summarized as shown in Figure 1.15:

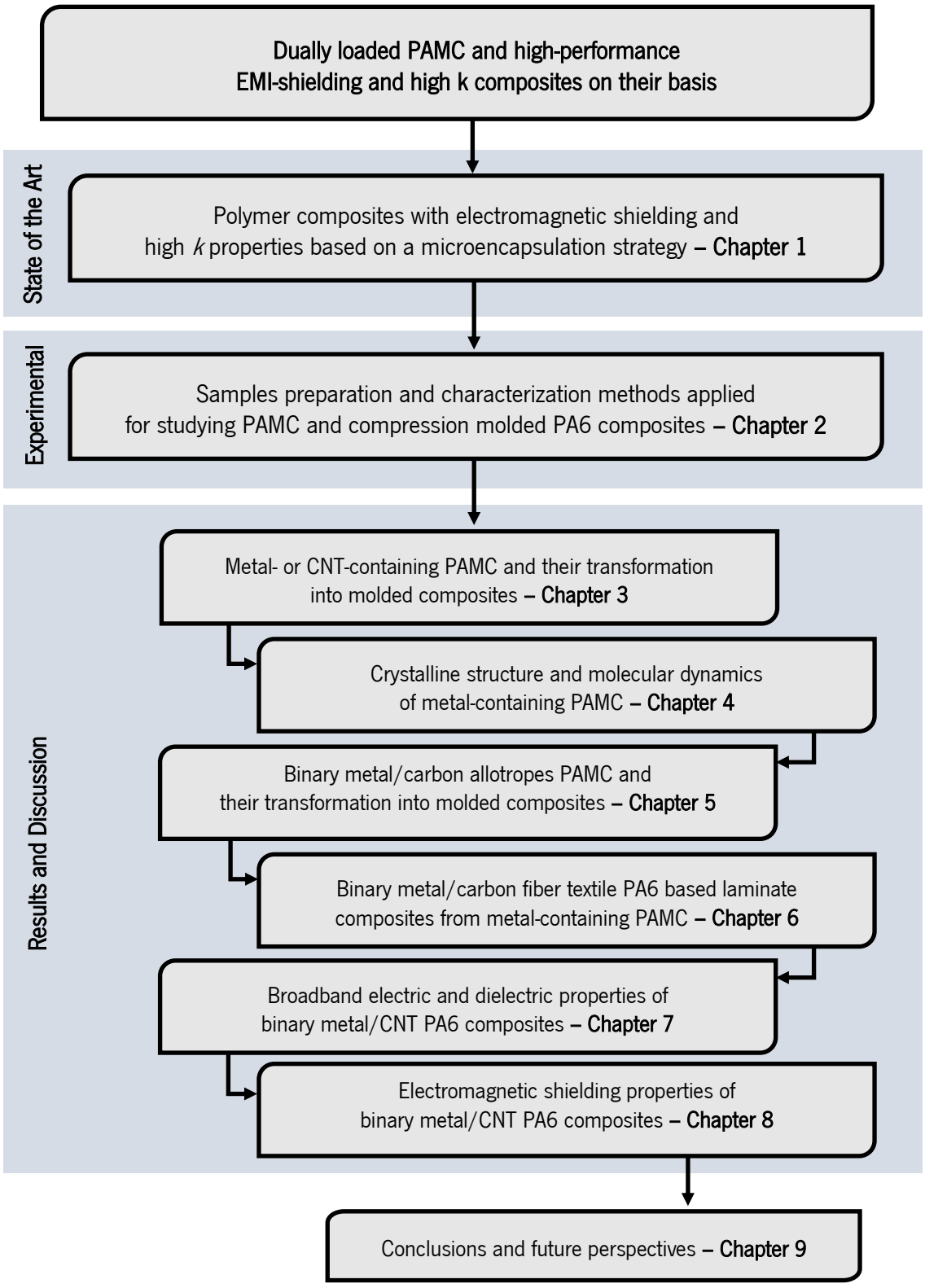

Figure 1.15| Structure and methodology of this Ph.D. thesis.

1.7. References

[1] Callister WD (2007) Introduction. In: Materials Science and Engineering: An Introduction, 7th ed. John Wiley & Sons, Inc, United States of America, p 2

[2] Al-Saleh MH, Sundararaj U (2009) Electromagnetic interference shielding mechanisms of CNT/polymer composites. *Carbon N Y*, 47:1738–1746. DOI: 10.1016/j.carbon.2009.02.030

[3] Lakshmi K, John H, Mathew KT, Joseph R, George KE (2009) Microwave absorption, reflection and EMI shielding of PU–PANI composite. *Acta Mater*, 57:371–375. DOI: 10.1016/j.actamat.2008.09.018

[4] Kwon S, Ma R, Kim U, Choi HR, Baik S (2014) Flexible electromagnetic interference shields made of silver flakes, carbon nanotubes and nitrile butadiene rubber. *Carbon N Y*, 68:118–124. DOI: 10.1016/j.carbon.2013.10.070

[5] Yan J, Huang Y, Wei C, Zhang N, Liu P (2017) Covalently bonded polyaniline/graphene composites as high-performance electromagnetic (EM) wave absorption materials. *Compos Part A Appl Sci Manuf*, 99:121–128. DOI: 10.1016/j.compositesa.2017.04.016

[6] Chung DDL (2001) Electromagnetic interference shielding effectiveness of carbon materials. *Carbon N Y*, 39:279–285. DOI: 10.1016/S0008-6223(00)00184-6

[7] Thomassin J-M, Jérôme C, Pardoen T, Bailly C, Huynen I, Detrembleur C (2013) Polymer/carbon based composites as electromagnetic interference (EMI) shielding materials. *Mater Sci Eng R Reports*, 74:211–232. DOI: 10.1016/j.mser.2013.06.001

[8] Sankaran S, Deshmukh K, Ahamed MB, Pasha SKK (2018) Recent advances in electromagnetic interference shielding properties of metal and carbon filler reinforced flexible polymer composites: A review. *Compos Part A Appl Sci Manuf*, 114:49–71. DOI: 10.1016/j.compositesa.2018.08.006

[9] Peng BJ, Walton JH, Cherry SR, Willig-Onwuachi J (2010) Studies of the interactions of an MRI system with the shielding in a combined PET/MRI scanner. *Phys Med Biol*, 55:265–280. DOI: 10.1088/0031-9155/55/1/016

[10] Peng BJ, Wu Y, Cherry SR, Walton JH (2014) New shielding configurations for a simultaneous PET/MRI scanner at 7T. *J Magn Reson*, 239:50–56. DOI: 10.1016/j.jmr.2013.10.027

[11] Hardell L, Koppel T, Carlberg M, Ahonen M, Hedendahl L (2016) Radiofrequency radiation at Stockholm Central Railway Station in Sweden and some medical aspects on public exposure to RF fields. *Int J Oncol*, 49:1315–1324. DOI: 10.3892/ijo.2016.3657

[12] Carlberg M, Hedendahl L, Ahonen M, Koppel T, Hardell L (2016) Increasing incidence of thyroid cancer in the Nordic countries with main focus on Swedish data. *BMC Cancer*, 16:426–440. DOI:

10.1186/s12885-016-2429-4

[13] Carlberg M, Koppel T, Ahonen M, Hardell L (2017) Case-control study on occupational exposure to extremely low-frequency electromagnetic fields and glioma risk. *Am J Ind Med*, 60:494–503. DOI: 10.1002/ajim.22707

[14] Aniołczyk H (2018) EM Noise and Its Impact on Human Health and Safety. In: Advanced Materials for Electromagnetic Shielding. John Wiley & Sons, Ltd, pp 11–33

[15] Chen Q, Shen Y, Zhang S, Zhang QM (2015) Polymer-Based Dielectrics with High Energy Storage Density. *Annu Rev Mater Res*, 45:433–458. DOI: 10.1146/annurev-matsci-070214-021017

[16] Li Q, Yao F-Z, Liu Y, Zhang G, Wang H, Wang Q (2018) High-Temperature Dielectric Materials for Electrical Energy Storage. *Annu Rev Mater Res*, 48:219–243. DOI: 10.1146/annurev-matsci-070317-124435

[17] Wang B, Huang W, Chi L, Al-Hashimi M, Marks TJ, Facchetti A (2018) High-k Gate Dielectrics for Emerging Flexible and Stretchable Electronics. *Chem Rev*, 118:5690–5754. DOI: 10.1021/acs.chemrev.8b00045

[18] Wallace RM (2017) Dielectric Materials for Microelectronics. In: Kasap S, Capper P (eds) Springer Handbook of Electronic and Photonic Materials, 2nd ed. Springer International Publishing, Cham, pp 615–644

[19] Bagotia N, Choudhary V, Sharma DK (2018) A review on the mechanical, electrical and EMI shielding properties of carbon nanotubes and graphene reinforced polycarbonate nanocomposites. *Polym Adv Technol*, 29:1547–1567. DOI: 10.1002/pat.4277

[20] Meng F, Wang H, Huang F, Guo Y, Wang Z, Hui D, Zhou Z (2018) Graphene-based microwave absorbing composites: A review and prospective. *Compos Part B Eng*, 137:260–277. DOI: 10.1016/j.compositesb.2017.11.023

[21] Huo J, Wang L, Yu H (2009) Polymeric nanocomposites for electromagnetic wave absorption. *J Mater Sci*, 44:3917–3927. DOI: 10.1007/s10853-009-3561-1

[22] Huang X, Jiang P (2015) Core–Shell Structured High-k Polymer Nanocomposites for Energy Storage and Dielectric Applications. *Adv Mater*, 27:546–554. DOI: 10.1002/adma.201401310

[23] Wang B, Liu L, Huang L, Chi L, Liang G, Yuan L, Gu A (2015) Fabrication and origin of high-k carbon nanotube/epoxy composites with low dielectric loss through layer-by-layer casting technique. *Carbon N Y*, 85:28–37. DOI: 10.1016/j.carbon.2014.12.062

[24] Groover MP (2010) Composite materials. In: Fundamentals of Modern Manufacturing: Materials, Processes and Systems, 4th ed. John Wiley & Sons, Inc, United States of America, p 192

[25] Chawla KK (1998) Interfaces. In: Chawla KK (ed) Composite Materials: Science and Engineering, 2nd ed. Springer Science & Business Media, New York, pp 101–129

[26] Chaurasia A, Sahoo NG, Wang M, He C, Mogal VT (2015) Fundamentals of Polymers and Polymer Composite. In: Nee AYC (ed) Handbook of Manufacturing Engineering and Technology. Springer London, London, England, pp 3–42

[27] Jose JP, Malhotra SK, Thomas S, Joseph K, Goda K, Sreekala MS (2012) Advances in Polymer Composites: Macro- and Microcomposites–State of the Art, New Challenges, and Opportunities. In: Thomas S, Joseph K, Malhotra SK, Goda K, Sreekala MS (eds) Polymer Composites, Macro- and Microcomposites - Volume 1, 1st ed. Wiley-VCH Verlag GmbH & Co. KGaA, Weinheim, Germany, pp 3–16

[28] Schadler LS (2003) Polymer-Based and Polymer-Filled Nanocomposites. In: Ajayan M, Schadler LS, Braun P V. (eds) Nanocomposite Science and Technology. Wiley-VCH Verlag GmbH & Co. KGaA, Weinheim, pp 77–153

[29] Denchev Z, Dencheva N (2012) Preparation, Mechanical Properties and Structural Characterization of Microfibrillar Composites Based on Polyethylene/Polyamide Blends. In: Bhattacharyya D, Fakirov S (eds) Synthetic Polymer–Polymer Composites. Hanser, pp 465–524

[30] Lee S-H, Kang D, Oh I-K (2017) Multilayered graphene-carbon nanotube-iron oxide three-dimensional heterostructure for flexible electromagnetic interference shielding film. *Carbon N Y*, 111:248–257. DOI: 10.1016/j.carbon.2016.10.003

[31] Zhong K, Li B (2017) Graphitic Nanomaterials and Their Polymer Nanocomposites for Dielectric Applications. In: Zhong W-H, Li B (eds) Polymer Nanocomposites for Dielectrics. Pan Stanford Publishing, pp 69–93

[32] Yousefi N, Sun X, Lin X, Shen X, Jia J, Zhang B, Tang B, Chan M, Kim J-K (2014) Highly Aligned Graphene/Polymer Nanocomposites with Excellent Dielectric Properties for High-Performance Electromagnetic Interference Shielding. *Adv Mater*, 26:5480–5487. DOI: 10.1002/adma.201305293

[33] Ji X, Lu M, Ye F, Zhou Q (2013) Electromagnetic Wave Absorption Properties of Coatings with Carbonyl-iron Particles coated by Silicon dioxide Nano-powders. *Adv Pure Appl Chem*, 1:111–115

[34] Coey JMD (2010) Magnetostatics. In: Magnetism and Magnetic Materials. Cambridge University Press, New York, United States of America, p 33

[35] London IC (2019) The Electromagnetic Spectrum. In: Study Cogn. Adolesc. Mob. Phones. http://www.scampstudy.org/the-science/#51f8b6924552de7d1d0df5573848424e_one.

Accessed 12 Jul 2019

[36] Aswathi MK, Rane A V., Ajitha AR, Thomas S, Jaroszewski4 M (2019) EMI Shielding Fundamentals. In: Jaroszewski M, Thomas S, Rane A V. (eds) Advanced Materials for Electromagnetic Shielding: Fundamentals, Properties, and Applications, 1st ed. John Wiley & Sons, Inc., USA, pp 1–9

[37] Daniel S, Thomas S (2019) Shielding Efficiency Measuring Methods and Systems. In: Jaroszewski M, Thomas S, Rane A V. (eds) Advanced Materials for Electromagnetic Shielding: Fundamentals, Properties, and Applications, 1st ed. John Wiley & Sons, Inc., USA, pp 61–87

[38] Li B, Zhong W-H (2017) Theoretical Analysis of Dielectric Relaxation in Polymer Nanocomposites. In: Zhong W-H, Li B (eds) Polymer Nanocomposites for Dielectrics, 1st ed. Pan Stanford Publishing, Singapore, pp 17–33

[39] Gooch JW, Daher JK (2007) Fundamentals of Electromagnetic Shielding. In: Electromagnetic Shielding and Corrosion Protection for Aerospace Vehicles. Springer New York, New York, pp 17–24

[40] Neelakanta PS (1995) Electromagnetic Shielding Materials. In: Handbook of Electromagnetic Materials, 1st ed. CRC-Press LLC, Florida, pp 447–490

[41] Kasap SO (2006) Dielectric Materials and Insulation. In: Principles of Electronic Materials and Devices, 3rd ed. McGraw-Hill, New York, pp 583–608

[42] Schönhals A, Kremer F (2003) Analysis of Dielectric Spectra. In: Kremer F, Schönhals A (eds) Broadband Dielectric Spectroscopy. Springer Berlin Heidelberg, Berlin, Heidelberg, pp 59–98

[43] (1987) Shielding. In: Military Handbook - Grounding, bonding, and shielding for electronic equipments and facilities - Volume 1. US Department of Defense, pp 1–80

[44] Yan D-X, Pang H, Li B, Vajtai R, Xu L, Ren P-G, Wang J-H, Li Z-M (2015) Structured Reduced Graphene Oxide/Polymer Composites for Ultra-Efficient Electromagnetic Interference Shielding. *Adv Funct Mater*, 25:559–566. DOI: 10.1002/adfm.201403809

[45] Billah SMR (2018) Dielectric Polymers. In: Jafar Mazumder MA, Sheardown H, Al-Ahmed A (eds) Functional Polymers. Springer International Publishing, Cham, pp 1–49

[46] Koo CM, Shahzad F, Kumar P, Yu S, Lee SH, Hong JP (2019) Polymer-Based EMI Shielding Materials. In: Jaroszewski M, Thomas S, Rane A V. (eds) Advanced Materials for Electromagnetic Shielding: Fundamentals, Properties, and Applications, 1st ed. John Wiley & Sons, Inc, pp 177–217

[47] Saini P, Arora M (2012) Microwave Absorption and EMI Shielding Behavior of Nanocomposites

Based on Intrinsically Conducting Polymers, Graphene and Carbon Nanotubes. In: Gomes ADS (ed) New Polymers for Special Applications. IntechOpen, pp 71–112

[48] Mishra RK, Dutta A, Mishra P, Thomas S (2019) Recent Progress in Electromagnetic Absorbing Materials. In: Jaroszewski M, Thomas S, Rane A V. (eds) Advanced Materials for Electromagnetic Shielding: Fundamentals, Properties, and Applications, 1st ed. John Wiley & Sons, Inc., USA, pp 147–166

[49] Li B, Zhong W-H (2017) Basics of Polymers and Polymer Nanocomposites as Dielectric Materials. In: Zhong W-H, Li B (eds) Polymer Nanocomposites for Dielectrics, 1st ed. Pan Stanford Publishing, Singapore, pp 1–15

[50] Li B, Zhong W-H (2017) Perovskite Ceramics and Their Polymer Nanocomposites. In: Zhong W-H, Li B (eds) Polymer Nanocomposites for Dielectrics, 1st ed. Pan Stanford Publishing Pte. Ltd., USA, pp 35–68

[51] Geetha S, Satheesh Kumar KK, Rao CRK, Vijayan M, Trivedi DC (2009) EMI shielding: Methods and materials—A review. *J Appl Polym Sci*, 112:2073–2086. DOI: 10.1002/app.29812

[52] Basics of Measuring the Dielectric Properties of Materials. Keysight Technologies, USA

[53] Krueger QJ, King JA (2003) Synergistic effects of carbon fillers on shielding effectiveness in conductive nylon 6,6- and polycarbonate-based resins. *Adv Polym Technol*, 22:96–111. DOI: 10.1002/adv.10040

[54] Panwar V, Mehra RM (2008) Analysis of electrical, dielectric, and electromagnetic interference shielding behavior of graphite filled high density polyethylene composites. *Polym Eng Sci*, 48:2178–2187. DOI: 10.1002/pen.21163

[55] Jiang X, Yan D-X, Bao Y, Pang H, Ji X, Li Z-M (2015) Facile, green and affordable strategy for structuring natural graphite/polymer composite with efficient electromagnetic interference shielding. *RSC Adv*, 5:22587–22592. DOI: 10.1039/C4RA11332B

[56] Sachdev VK, Patel K, Bhattacharya S, Tandon RP (2011) Electromagnetic interference shielding of graphite/acrylonitrile butadiene styrene composites. *J Appl Polym Sci*, 120:1100–1105. DOI: 10.1002/app.33248

[57] Jou WS, Wu TL, Chiu SK, Cheng WH (2001) Electromagnetic shielding of nylon-66 composites applied to laser modules. *J Electron Mater*, 30:1287–1293. DOI: 10.1007/s11664-001-0113-0

[58] Al-Saleh MH, Sundararaj U (2013) Morphological, electrical and electromagnetic interference shielding characterization of vapor grown carbon nanofiber/polystyrene nanocomposites. *Polym Int*, 62:601–607. DOI: 10.1002/pi.4317

[59] Al-Saleh MH, Saadeh WH, Sundararaj U (2013) EMI shielding effectiveness of carbon based nanostructured polymeric materials: A comparative study. *Carbon N Y*, 60:146–156. DOI: 10.1016/j.carbon.2013.04.008

[60] Nayak L, Khastgir D, Chaki TK (2013) A mechanistic study on electromagnetic shielding effectiveness of polysulfone/carbon nanofibers nanocomposites. *J Mater Sci*, 48:1492–1502. DOI: 10.1007/s10853-012-6904-2

[61] Ameli A. A4 - Jung, P.U. A4 - Park, C.B. AA-A (2013) Electrical properties and electromagnetic interference shielding effectiveness of polypropylene/carbon fiber composite foams. *Carbon N Y*, 60:379–391. DOI: 10.1016/j.carbon.2013.04.050

[62] Al-Saleh MH, Sundararaj U (2012) Microstructure, electrical, and electromagnetic interference shielding properties of carbon nanotube/acrylonitrile–butadiene–styrene nanocomposites. *J Polym Sci Part B Polym Phys*, 50:1356–1362. DOI: 10.1002/polb.23129

[63] Gupta A, Choudhary V (2011) Electrical conductivity and shielding effectiveness of poly(trimethylene terephthalate)/multiwalled carbon nanotube composites. *J Mater Sci*, 46:6416–6423. DOI: 10.1007/s10853-011-5591-8

[64] Maiti S, Suin S, Shrivastava NK, Khatua BB (2014) A strategy to achieve high electromagnetic interference shielding and ultra low percolation in multiwall carbon nanotube–polycarbonate composites through selective localization of carbon nanotubes. *RSC Adv*, 4:7979–7990. DOI: 10.1039/C3RA46480F

[65] Arjmand M, Apperley T, Okoniewski M, Sundararaj U (2012) Comparative study of electromagnetic interference shielding properties of injection molded versus compression molded multi-walled carbon nanotube/polystyrene composites. *Carbon N Y*, 50:5126–5134. DOI: 10.1016/j.carbon.2012.06.053

[66] Verma P, Saini P, Malik RS, Choudhary V (2015) Excellent electromagnetic interference shielding and mechanical properties of high loading carbon-nanotubes/polymer composites designed using melt recirculation equipped twin-screw extruder. *Carbon N Y*, 89:308–317. DOI: 10.1016/j.carbon.2015.03.063

[67] Jia L-C, Yan D-X, Cui C-H, Jiang X, Ji X, Li Z-M (2015) Electrically conductive and electromagnetic interference shielding of polyethylene composites with devisable carbon nanotube networks. *J Mater Chem C*, 3:9369–9378. DOI: 10.1039/C5TC01822F

[68] Nasouri K, Valipour P (2015) Fabrication of polyamide 6/carbon nanotubes composite electrospun nanofibers for microwave absorption application. *Polym Sci Ser A*, 57:359–364. DOI:

10.1134/S0965545X15030098

[69] Kunjappan AM, Poothanari MA, Ramachandran AA, Padmanabhan M, Mathew L, Thomas S (2019) High-performance electromagnetic interference shielding material based on an effective mixing protocol. *Polym Int*, 68:637–647. DOI: 10.1002/pi.5751

[70] Rahaman M, Chaki TK, Khastgir D (2011) Development of high performance EMI shielding material from EVA, NBR, and their blends: effect of carbon black structure. *J Mater Sci*, 46:3989–3999. DOI: 10.1007/s10853-011-5326-x

[71] Al-Saleh MH, Sundararaj U (2012) X-band {EMI} shielding mechanisms and shielding effectiveness of high structure carbon black/polypropylene composites. *J Phys D Appl Phys*, 46:35304. DOI: 10.1088/0022-3727/46/3/035304

[72] Kuester S, Merlini C, Barra GMO, Ferreira JC, Lucas A, de Souza AC, Soares BG (2016) Processing and characterization of conductive composites based on poly(styrene-b-ethylene-ran-butylene-b-styrene) (SEBS) and carbon additives: A comparative study of expanded graphite and carbon black. *Compos Part B Eng*, 84:236–247. DOI: 10.1016/j.compositesb.2015.09.001

[73] Eswaraiah V, Sankaranarayanan V, Ramaprabhu S (2011) Functionalized Graphene–PVDF Foam Composites for EMI Shielding. *Macromol Mater Eng*, 296:894–898. DOI: 10.1002/mame.201100035

[74] Chen Z, Xu C, Ma C, Ren W, Cheng H-M (2013) Lightweight and Flexible Graphene Foam Composites for High-Performance Electromagnetic Interference Shielding. *Adv Mater*, 25:1296–1300. DOI: 10.1002/adma.201204196

[75] Song W-L, Cao M-S, Lu M-M, Bi S, Wang C-Y, Liu J, Yuan J, Fan L-Z (2014) Flexible graphene/polymer composite films in sandwich structures for effective electromagnetic interference shielding. *Carbon N Y*, 66:67–76. DOI: 10.1016/j.carbon.2013.08.043

[76] Kashi S, Gupta RK, Baum T, Kao N, Bhattacharya SN (2016) Morphology, electromagnetic properties and electromagnetic interference shielding performance of poly lactide/graphene nanoplatelet nanocomposites. *Mater Des*, 95:119–126. DOI: 10.1016/j.matdes.2016.01.086

[77] Gabriel P, Ana J (2004) Conducting aluminum-filled nylon 6 composites. *Polym Compos*, 22:65–70. DOI: 10.1002/pc.10517

[78] Panda M, Srinivas V, Thakur AK (2008) On the question of percolation threshold in polyvinylidene fluoride/nanocrystalline nickel composites. *Appl Phys Lett*, 92:132905. DOI: 10.1063/1.2900710

[79] Gargama H, Thakur AK, Chaturvedi SK (2015) Polyvinylidene fluoride/nickel composite materials

for charge storing, electromagnetic interference absorption, and shielding applications. *J Appl Phys*, 117:224903. DOI: 10.1063/1.4922411

[80] Gelves GA, Al-Saleh MH, Sundararaj U (2011) Highly electrically conductive and high performance EMI shielding nanowire/polymer nanocomposites by miscible mixing and precipitation. *J Mater Chem*, 21:829–836. DOI: 10.1039/C0JM02546A

[81] Yu Y-H, Ma C-CM, Teng C-C, Huang Y-L, Lee S-H, Wang I, Wei M-H (2012) Electrical, morphological, and electromagnetic interference shielding properties of silver nanowires and nanoparticles conductive composites. *Mater Chem Phys*, 136:334–340. DOI: 10.1016/j.matchemphys.2012.05.024

[82] Chalapat K, Timonen JVI, Huuppola M, Koponen L, Johans C, Ras RHA, Ikkala O, Oksanen MA, Seppälä E, Paraoanu GS (2014) Ferromagnetic resonance in ϵ-Co magnetic composites. *Nanotechnology*, 25:485707. DOI: 10.1088/0957-4484/25/48/485707

[83] Huang XY, Jiang PK, Kim CU (2007) Electrical properties of polyethylene/aluminum nanocomposites. *J Appl Phys*, 102:124103. DOI: 10.1063/1.2822336

[84] Dang Z-M, Wang H-Y, Zhang Y-H, Qi J-Q (2005) Morphology and Dielectric Property of Homogenous $BaTiO_3$/PVDF Nanocomposites Prepared via the Natural Adsorption Action of Nanosized BaTiO3. *Macromol Rapid Commun*, 26:1185–1189. DOI: 10.1002/marc.200500137

[85] Dang Z-M, Wang H-Y, Peng B, Nan C-W (2008) Effect of $BaTiO_3$ size on dielectric property of BaTiO3/PVDF composites. *J Electroceramics*, 21:381–384. DOI: 10.1007/s10832-007-9201-8

[86] Gregorio R, Cestari M, Bernardino FE (1996) Dielectric behaviour of thin films of β-PVDF/PZT and β-PVDF/$BaTiO_3$ composites. *J Mater Sci*, 31:2925–2930. DOI: 10.1007/BF00356003

[87] Dang Z-M, Wang H-Y, Xu H-P (2006) Influence of silane coupling agent on morphology and dielectric property in $BaTiO_3$/polyvinylidene fluoride composites. *Appl Phys Lett*, 89:112902. DOI: 10.1063/1.2338529

[88] Megaw HD (1952) Origin of ferroelectricity in barium titanate and other perovskite-type crystals. *Acta Crystallogr*, 5:739–749. DOI: 10.1107/S0365110X52002069

[89] Benlahrache MT, Benhamla N, Achour S (2004) Dielectric properties of $BaTiO_3$–$NaNbO_3$ composites. *J Eur Ceram Soc*, 24:1493–1496. DOI: 10.1016/S0955-2219(03)00577-6

[90] Köferstein R, Jäger L, Zenkner M, Ebbinghaus SG (2010) Phase transition and dielectric properties of $BaTiO_3$ ceramics containing 10mol% BaGeO3. *Mater Chem Phys*, 119:118–122. DOI: 10.1016/j.matchemphys.2009.08.026

[91] Shen Y, Lin Y, Li M, Nan C-W (2007) High Dielectric Performance of Polymer Composite Films

Induced by a Percolating Interparticle Barrier Layer. *Adv Mater*, 19:1418–1422. DOI: 10.1002/adma.200602097

[92] Huang C-Y, Mo W-W, Roan M-L (2004) Studies on the influence of double-layer electroless metal deposition on the electromagnetic interference shielding effectiveness of carbon fiber/ABS composites. *Surf Coatings Technol*, 184:163–169. DOI: 10.1016/j.surfcoat.2003.11.010

[93] Tzeng S-S, Chang F-Y (2001) EMI shielding effectiveness of metal-coated carbon fiber-reinforced ABS composites. *Mater Sci Eng A*, 302:258–267. DOI: 10.1016/S0921-5093(00)01824-4

[94] Yang SY, Chen CY, Parng SH (2002) Effects of conductive fibers and processing conditions on the electromagnetic shielding effectiveness of injection molded composites. *Polym Compos*, 23:1003–1013. DOI: 10.1002/pc.10496

[95] Pierozynski B (2015) Electrodeposition of Nickel onto 12K Carbon Fibre Tow in a Continuous Manner. *Croat Chem Acta*, 85:1–8. DOI: 10.5562/cca1743

[96] Yoo TW, Lee YK, Lim SJ, Yoon HG, Kim WN (2014) Effects of hybrid fillers on the electromagnetic interference shielding effectiveness of polyamide 6/conductive filler composites. *J Mater Sci*, 49:1701–1708. DOI: 10.1007/s10853-013-7855-y

[97] Zhang S, Wang X, Wu D (2016) Design and fabrication of long-carbon-fiber-reinforced polyamide-6/nickel powder composites for electromagnetic interference shielding and high mechanical performance. *Polym Compos*, 37:2705–2718. DOI: 10.1002/pc.23465

[98] Ogawa F, Masuda C, Fujii H (2018) In situ chemical vapor deposition of metals on vapor-grown carbon fibers and fabrication of aluminum-matrix composites reinforced by coated fibers. *J Mater Sci*, 53:5036–5050. DOI: 10.1007/s10853-017-1921-9

[99] Kumar Srivastava R, Narayanan TN, Reena Mary AP, Anantharaman MR, Srivastava A, Vajtai R, Ajayan PM (2011) Ni filled flexible multi-walled carbon nanotube–polystyrene composite films as efficient microwave absorbers. *Appl Phys Lett*, 99:113116. DOI: 10.1063/1.3638462

[100] Huang C-Y, Wu C-C (2000) The EMI shielding effectiveness of PC/ABS/nickel-coated-carbon-fibre composites. *Eur Polym J*, 36:2729–2737. DOI: 10.1016/S0014-3057(00)00039-2

[101] Pawar SP, Marathe DA, Pattabhi K, Bose S (2015) Electromagnetic interference shielding through MWNT grafted Fe_3O_4 nanoparticles in PC/SAN blends. *J Mater Chem A*, 3:656–669. DOI: 10.1039/C4TA04559A

[102] Pawar SP, Stephen S, Bose S, Mittal V (2015) Tailored electrical conductivity, electromagnetic shielding and thermal transport in polymeric blends with graphene sheets decorated with nickel nanoparticles. *Phys Chem Chem Phys*, 17:14922–14930. DOI: 10.1039/C5CP00899A

[103] Schaefer DW, Justice RS (2007) How Nano are nano-composites? *Macromolecules*, 40:8501–8517. DOI: 10.1021/ma070356w

[104] Ojijo V, Ray SS (2013) Processing strategies in bionanocomposites. *Prog Polym Sci*, 38:1543–1589. DOI: 10.1016/j.progpolymsci.2013.05.011

[105] Cunha AM, Pontes AJ (2009) Non-Conventional Injection Molds. In: Kamal MR, Isayev A, Liu S-H (eds) Injection Molding Technology and Fundamentals. Carl Hanser Verlag GmbH & Co. KG, Munich, pp 171–194

[106] Gates BD, Xu Q, Stewart M, Ryan D, Willson CG, Whitesides GM (2005) New approaches to nanofabrication: molding, printing, and other techniques. *Chem Rev*, 105:1171–1196. DOI: 10.1021/cr030076o

[107] Linares A, Canalda JC, Cagiao ME, García-Gutiérrez MC, Nogales A, Martín-Gullón I, Vera J, Ezquerra TA (2008) Broad-Band Electrical Conductivity of High Density Polyethylene Nanocomposites with Carbon Nanoadditives: Multiwall Carbon Nanotubes and Carbon Nanofibers. *Macromolecules*, 41:7090–7097. DOI: 10.1021/ma801410j

[108] Mitchell CA, Bahr JL, Arepalli S, Tour JM, Krishnamoorti R (2002) Dispersion of Functionalized Carbon Nanotubes in Polystyrene. *Macromolecules*, 35:8825–8830. DOI: 10.1021/ma020890y

[109] Socher R, Krause B, Hermasch S, Wursche R, Pötschke P (2011) Electrical and thermal properties of polyamide 12 composites with hybrid fillers systems of multiwalled carbon nanotubes and carbon black. *Compos Sci Technol*, 71:1053–1059. DOI: 10.1016/j.compscitech.2011.03.004

[110] Bahr JL, Tour JM (2002) Covalent chemistry of single-wall carbon nanotubes. *J Mater Chem*, 12:1952–1958. DOI: 10.1039/B201013P

[111] Dyke CA, Tour JM (2003) Solvent-Free Functionalization of Carbon Nanotubes. *J Am Chem Soc*, 125:1156–1157. DOI: 10.1021/ja0289806

[112] Yang K, Huang X, Xie L, Wu C, Jiang P, Tanaka T (2012) Core–Shell Structured Polystyrene/BaTiO 3 Hybrid Nanodielectrics Prepared by In Situ RAFT Polymerization: A Route to High Dielectric Constant and Low Loss Materials with Weak Frequency Dependence. *Macromol Rapid Commun*, 33:1921–1926. DOI: 10.1002/marc.201200361

[113] Yang K, Huang X, Zhu M, Xie L, Tanaka T, Jiang P (2014) Combining RAFT Polymerization and Thiol–Ene Click Reaction for Core–Shell Structured Polymer@$BaTiO_3$ Nanodielectrics with High Dielectric Constant, Low Dielectric Loss, and High Energy Storage Capability. *ACS Appl Mater Interfaces*, 6:1812–1822. DOI: 10.1021/am4048267

[114] Siddabattuni S, Schuman TP, Dogan F (2013) Dielectric Properties of Polymer–Particle

Nanocomposites Influenced by Electronic Nature of Filler Surfaces. *Appl Mater Interfaces*, 5:1917–1927. DOI: 10.1021/am3030239

[115] Sigma-Aldrich Co. (2012) Controlled Radical Polymerization Guide - ATRP, RAFT, NMP. https://www.sigmaaldrich.com/technical-documents/articles/crp-guide.html. Accessed 13 Feb 2020

[116] Peters EN (2017) 1 - Engineering Thermoplastics—Materials, Properties, Trends. In: Kutz M (ed) Applied Plastics Engineering Handbook (Second Edition), Second Edi. William Andrew Publishing, pp 3–26

[117] Sibikin I, Karger-Kocsis J (2018) Toward industrial use of anionically activated lactam polymers: Past, present and future. *Adv Ind Eng Polym Res*, 1:48–60. DOI: 10.1016/j.aiepr.2018.06.003

[118] Friedrich K (2018) Polymer composites for tribological applications. *Adv Ind Eng Polym Res*, 1:3–39. DOI: 10.1016/j.aiepr.2018.05.001

[119] Tomasini A, León-Santiesteban HH (2015) 12 - Nylon uses in biotechnology. In: Misra M, Pandey JK, Mohanty AK (eds) Biocomposites. Woodhead Publishing, pp 319–346

[120] Page IB (2000) Polyamides as Engineering Thermoplastic Materials, 1st ed. iSmithers Rapra Publishing, United Kingdom

[121] Santos PA, Spinacé MAS, Fermoselli KKG, Paoli M-A De (2007) Polyamide-6/vegetal fiber composite prepared by extrusion and injection molding. *Compos Part A Appl Sci Manuf*, 38:2404–2411. DOI: 10.1016/j.compositesa.2007.08.011

[122] He H, Cheng S, Lian Y, Xing Y, He G, Huang Z, Wu M (2015) Electrical conductivity and electromagnetic interference shielding effectiveness of carbon black/sisal fiber/polyamide/polypropylene composites. *J Appl Polym Sci*, 132:42801. DOI: 10.1002/app.42801

[123] Hassan A, Hassan AA, Rafiq MIM (2011) Impact properties of injection molded glass fiber/polyamide-6 composites: effect of testing parameters. *J Reinf Plast Compos*, 30:889–898. DOI: 10.1177/0731684411412226

[124] Prashantha K, Lacrampe M-F, Krawczak P (2013) Highly dispersed polyamide-11/halloysite nanocomposites: Thermal, rheological, optical, dielectric, and mechanical properties. *J Appl Polym Sci*, 130:313–321. DOI: 10.1002/app.39160

[125] Ferreira T, Paiva MC, Pontes AJ (2013) Dispersion of carbon nanotubes in polyamide 6 for microinjection moulding. *J Polym Res*, 20:301. DOI: 10.1007/s10965-013-0301-7

[126] Hussain F, Hojjati M, Okamoto M, Gorga RE (2006) Polymer-matrix nanocomposites, processing,

manufacturing and application: An overview. *J Compos Mater*, 40:1511–1575. DOI: 10.1177/0021998306067321

[127] Korshak V V, Kudryavtsev R V, Sergeev VA, Intsikson LB (**1962**) A study of the mechanism of the hydrolytic polymerization of ε-caprolactam in the presence of water with a heavy oxygen isotope. *Bull Acad Sci USSR, Div Chem Sci*, 11:1378–1380. DOI: 10.1007/BF00907991

[128] Ricco L, Monticelli O, Russo S, Paglianti A, Mariani A (**2002**) Fast-activated anionic polymerization of ε-caprolactam in suspension, 1. Role of the continuous phase on characteristics and properties of powdered PA6. *Macromol Chem Phys*, 203:1436–1444. DOI: 10.1002/1521-3935(200207)203:10/11<1436::AID-MACP1436>3.0.CO;2-V

[129] Barhoumi N, Maazouz A, Jaziri M, Abdelhedi R (**2013**) Polyamide from lactams by reactive rotational molding via anionic ring-opening polymerization: Optimization of processing parameters. *eXPRESS Polym Lett*, 7:76–87

[130] Šebenda J (**1978**) Recent progress in the polymerization of lactams. *Prog Polym Sci*, 6:123–167. DOI: 10.1016/0079-6700(78)90006-0

[131] Sekiguchi H (**1984**) Lactam and Cyclic Imides. In: Ivin KJ, Saegusa T (eds) Ring-opening polymerization. Elseview Applied Science Publishers Ltd, London, pp 809–918

[132] Odian G (**2004**) Principles of Polimerization, 4th ed. John Wiley & Sons, Inc, New Jersey, pp 569-577

[133] Joyce PM, Ritter DM (**1941**) Process for Making Polymeric Materials

[134] Hanford WE, Joyce RM (**1948**) Polymeric amides from epsilon-caprolactam. *J Polym Sci*, 3:167–172. DOI: 10.1002/pol.1948.120030203

[135] Šebenda J (**1972**) Lactam Polymerization. *J Macromol Sci Part A - Chem*, 6:1145–1199. DOI: 10.1080/10601327208056889

[136] Šebenda J (**1976**) Polymerizability of Lactams. *Pure Appl Chem*, 48:329–334. DOI: 10.1351/pac197648030329

[137] Šebenda J (**1989**) Anionic Ring-opening Polymerization: Lactams. In: Allen G, Bevington JC (eds) Comprehensive Polymer Science and Supplements. Pergamon, Amsterdam, pp 511–530

[138] Stehlíček J, Šebenda T (**1986**) Anionic polymerization of 6-caprolactam—LVIII. The relative rates of elementary reactions in the activated anionic polymerization of ϵ-caprolactam in tetrahydrofuran. *Eur Polym J*, 22:5–11. DOI: 10.1016/0014-3057(86)90206-5

[139] Sekiguchi H, Coutin B (**1973**) Polymerizability and related problems in the anionic polymerization of lactams. *J Polym Sci Polym Chem Ed*, 11:1601–1614. DOI: 10.1002/pol.1973.170110710

[140] Roda J (2009) Polyamides. In: Dubois P, Coulembier O, Raquez J-M (eds) Handbook of Ring-Opening Polymerization. John Wiley & Sons, Ltd, Weinheim, pp 165–195

[141] van Rijswijk K, Bersee HEN (2007) Reactive processing of textile fiber-reinforced thermoplastic composites – An overview. *Compos Part A Appl Sci Manuf*, 38:666–681. DOI: 10.1016/j.compositesa.2006.05.007

[142] Šittler E, Šebenda J (1968) Alkaline polymerization of 6-caprolactam. XXXII. The kinetics of polymerization activated by N,N,N',N'-tetraacetylhexamethylenediamine. *Collect Czechoslov Chem Commun*, 33:270–277. DOI: 10.1135/cccc19680270

[143] Russo S, Biagini E, Bonta G (1991) Novel synthetic approaches to poly(ε-caprolactam)-based materials. *Makromol Chemie Macromol Symp*, 48–49:31–46. DOI: 10.1002/masy.19910480106

[144] Petit D, Jerome R, Teyssie P (1979) Anionic block copolymerization of ϵ-caprolactam. *J Polym Sci Polym Chem Ed*, 17:2903–2916. DOI: 10.1002/pol.1979.170170926

[145] Ricco L, Russo S, Orefice G, Riva F (2001) Caprolactam-Laurolactam Copolymers: Fast Activated Anionic Synthesis, Thermal Properties and Structural Investigations. *Macromol Chem Phys*, 202:2114–2121. DOI: 10.1002/1521-3935(20010601)202:10<2114::AID-MACP2114>3.0.CO;2-F

[146] Mateva R, Dencheva N (1992) On the behavior of organophosphorus lactam derivatives during anionic polymerization of ε-caprolactam. *J Polym Sci Part A Polym Chem*, 30:1449–1462. DOI: 10.1002/pola.1992.080300725

[147] Ricco L, Russo S, Orefice G, Riva F (1999) Anionic Poly(ε-caprolactam): Relationships among Conditions of Synthesis, Chain Regularity, Reticular Order, and Polymorphism. *Macromolecules*, 32:7726–7731. DOI: 10.1021/ma9909004

[148] Mateva R, Mateev M, Delev O (1996) Structure and properties of polyamide 6 modified by N-trialkylsilylcaprolactam. *Acta Polym*, 47:188–192. DOI: 10.1002/actp.1996.010470408

[149] Mateva RP, Delev ON, Dimanov SP, Nescheva GD (1990) N-substituted lactam derivatives as activators and co-monomers for the activated anionic polymerisation of lactams, Patent EP0387895A2

[150] Kohan MI (1995) Nylon Plastics Handbook, 1st ed. Hanser/Gardner Publications, Munich, Germany

[151] Kircher K (1987) Chemical Reactions in Plastics Processing, 1st ed. Hanser Publishers, Munich, Germany

[152] Rusu M, Constanta I, Murariu M, Sorin B, Elena A (1998) Centrifugal Casting of Polyamide 6 I. Influence of Thermal Treatment. *Polym Polym Compos*, 6:143–146

[153] Vasiliu-Oprea C, Dan F (1996) On the relation between synthesis parameters and morphology of anionic polycaproamide obtained in organic media. I. Influence of the $Na[O(CH_2)_2OCH_3]_2AlH_2$/isophorone diisocyanate catalytic system. *J Appl Polym Sci*, 62:1517–1527. DOI: 10.1002/(SICI)1097-4628(19961205)62:10<1517::AID-APP4>3.0.CO;2-R

[154] Dan F, Vasiliu-Oprea C (1998) Anionic polimerization of caprolactama in organic media. Morphological aspects. *Colloid Polym Sci*, 276:483–495. DOI: 10.1007/s003960050270

[155] Vasiliu-Oprea C, Dan F (1997) On the relation between synthesis parameters and morphology of anionic polycaproamide obtained in organic media. II. Influence of the $Na[O(CH_2)_2OCH_3]_2AlH_2$/aliphatic diisocyanates catalytic systems. *J Appl Polym Sci*, 64:2575–2583. DOI: 10.1002/(SICI)1097-4628(19970627)64:13<2575::AID-APP11>3.0.CO;2-Z

[156] Dan F, Vasiliu-Oprea C (1998) On the relationship between synthesis parameters and morphology of the anionic polycaproamide obtained in organic media. III. Macroporous powders obtained using CO2 and carbodiimides as activating compounds. *J Appl Polym Sci*, 67:231–243. DOI: 10.1002/(SICI)1097-4628(19980110)67:2<231::AID-APP5>3.0.CO;2-V

[157] Crespy D, Landfester K (2005) Anionic polymerization of ε-Caprolactam in miniemulsion: synthesis and characterization of polyamide-6 nanoparticles. *Macromolecules*, 38:6882–6887. DOI: 10.1021/ma050616e

[158] Denchev Z, Dencheva N (2015) Polyamide Microcapsules and Method to Produce the Same, Portuguese patent PT 107679 A, filled 03.06.2014, published 03.12.2015, C08G 69/18

[159] Dencheva N, Denchev Z, Lanceros-Méndez S, Ezquerra Sanz T (2016) One-step in situ synthesis of polyamide microcapsules with inorganic payload and their transformation into responsive thermoplastic composite materials. *Macromol Mater Eng*, 301:119–124. DOI: 10.1002/mame.201500194

[160] Oliveira F, Dencheva N, Martins P, Lanceros-Mendez S, Denchev Z (2016) Reactive microencapsulation of carbon allotropes in polyamide shell-core structures and their transformation in hybrid composites with tailored electrical properties. *eXPRESS Polym Lett*, 10:160–175. DOI: 10.3144/expresspolymlett.2016.15

[161] Brêda C, Dencheva N, Lanceros-Mendez S, Denchev Z (2016) Preparation and properties of metal-containing polyamide hybrid composites via reactive microencapsulation. *J Mater Sci*, 51:10534–10554. DOI: 10.1007/s10853-016-0274-0

[162] Dencheva NV, Vale DM, Denchev ZZ (2016) Dually reinforced all-polyamide laminate composites via microencapsulation strategy. *Polym Eng Sci*, 57:806–820. DOI: 10.1002/pen.24456

[163] Logakis E, Pandis C, Peoglos V, Pissis P, Pionteck J, Pötschke P, Mičušík M, Omastová M (2009) Electrical/dielectric properties and conduction mechanism in melt processed polyamide/multi-walled carbon nanotubes composites. *Polymer (Guildf)*, 50:5103–5111. DOI: 10.1016/j.polymer.2009.08.038

CHAPTER 2

Experimental methods

2.1. Introduction

Chapter 2 is composed of three parts. First, the chemical reagents, solvents, and payloads used to synthesize empty and loaded polyamide 6 (PA6) microcapsules (PAMC) are introduced. Then, a detailed description is given of all procedures for PAMC synthesis and their transformation into PA6 molded composites. Subsequently, the sample preparation, the characterization techniques and the conditions used for the respective evaluations are stated. The data treatment procedures are explained whenever needed.

2.2. Materials

The following materials were used in the activated anionic ring-opening polymerization (AAROP) of PAMC in this work:

a) **Monomer:** ε-caprolactam (ECL), AP-Nylon® Caprolactam, with reduced moisture content was purchased from Brüggemann Chemical, Germany;

b) **Activator:** the difunctional hexamethylene-1,6-dicarbamoyl-caprolactam, Bruggolen C20P® (C20), was purchased from Brüggemann Chemical, Germany. According to the manufacturer, it contains 17 wt. % of di-isocyanate blocked in ECL;

c) **Initiator:** the sodium dicaprolactamo-bis-(2-methoxyethoxo)-aluminate, Dilactamate® (DL), 80% in toluene solution, delivered by Katchem Co., Czech Republic;

d) **Carbon payloads:** the multi-walled carbon nanotubes (MWCNT, ≥ 98% carbon basis) with an outer diameter of 10 nm and length 3-6 μm were purchased from Sigma Aldrich (the MWCNT will be abbreviated as CNT in the following descriptions and along this thesis for simplification); the acetylene carbon black (CB) is a product of S.E.A Tudor, Spain; the plain-weave carbon fiber textile (CFT) structures with an area density of 195 g/m^2 was kindly donated by Pólo de Inovação em Engenharia de Polímeros (PIEP), Portugal;

e) **Metal payloads:** the powders of copper (Cu) (> 99.5 %, grain size < 40 μm), aluminum (Al) (> 93 %, grain size < 100 μm), and magnesium (Mg) (> 99.5 %, grain size < 100 μm) were supplied by Sigma Aldrich. The soft, non-insulated carbonyl Fe powder (> 99.5 %, average grain size 3–5 μm) was kindly donated by the BASF Group, Germany;

f) **Solvents:** the toluene and methanol are all "puriss" grade, and they were purchased from Sigma Aldrich.

All chemical reagents, solvents, and payloads were used as received, without further treatment.

2.3. Sample preparation

2.3.1. Synthesis of empty polyamide 6 microcapsules

The synthesis of the PAMC was carried out by AAROP of ECL in solution using the polymerization method presented broadly in section 1.5.2.2, Fig. 1.13-1.14 of Chapter 1. Figure 2.1 represents the concrete chemical reaction of PAMC synthesis applied in this work [1, 2].

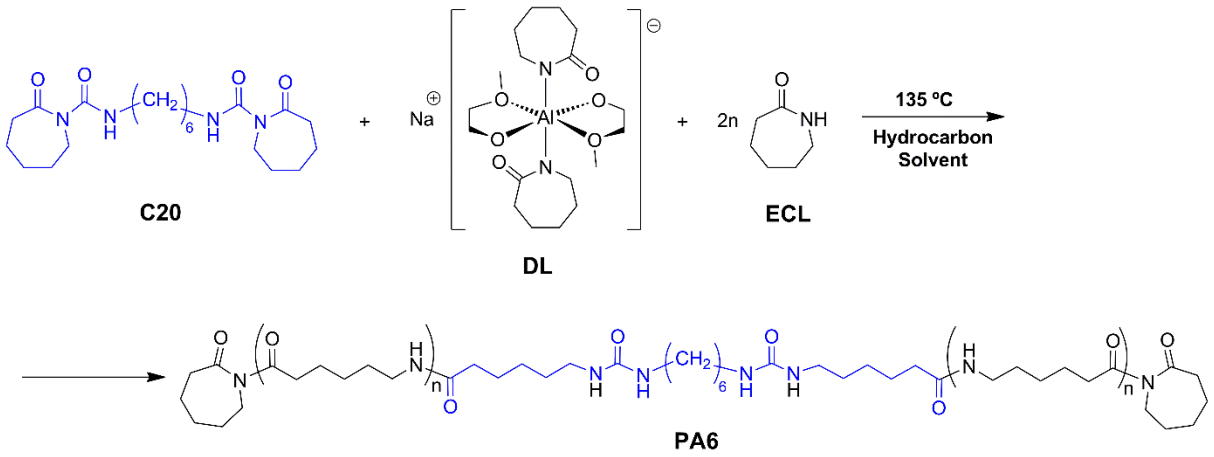

Figure 2.1 | Schematic representation of the PAMC synthesis in solution. Adapted from [2].

The synthesis was performed in a three-neck glass flask fitted with a thermometer, a magnetic stirrer, attachment for azeotropic distillation with reflux condenser, and an inlet for dry nitrogen. Thus, 56.5 g of ECL was added to 180 mL of toluene/xylene mixture while stirring, under N_2 atmosphere refluxing the mixture for 10–15 min up to stabilize it. Subsequently, 3 mol % of DL and 1.5 mol % of C20 were added at once. The polymerization time was about 2 h, from the point of catalytic system addition, maintaining the temperature in the 125–135°C range at a constant stirring rate of ca. 800 rpm. The empty PAMC formed as fine white powder and were separated from the reaction mixture by hot vacuum filtration, washed several times with methanol and dried for 4 h at 80 °C in a vacuum oven. The PAMC are stored in a desiccator.

2.3.2. Synthesis of hybrid polyamide 6 microcapsules with single load

The procedure described in [1, 2] was used for the preparation of hybrid PAMC. The desired amounts of metal particles (Al, Cu, Fe or Mg) or carbon allotropes (CNT or CB) were added to the reaction system. Metal and CB particles were added directly into the glass flask after the ECL introduction. Sonication of CNT in 100 mL of toluene/xylene mixture for 30 min was added to the protocol to prevent agglomeration. Then, the mixture was added to the ECL and the total solvent volume was increased to 180 mL. From this point on the AAROP was carried out as for the empty

microcapsules. The designation and composition of all the PAMC with single (or mono) loads were designated as M-samples. Their description is given in in Table 2.1.

Table 2.1 | Samples designation and composition of the M-samples – PAMC with mono load

Sample designation	Load, wt % [a]	Description
M-PA6	0	Non-loaded PA6 microcapsules
M-Al5	5	M-PA6 containing 5 wt% Al
M-Al10	10	M-PA6 containing 10 wt% Al
M-Cu5	5	M-PA6 containing 5 wt% Cu
M-Cu10	10	M-PA6 containing 10 wt% Cu
M-Fe5	5	M-PA6 containing 5 wt% Fe
M-Fe10	10	M-PA6 containing 10 wt% Fe
M-Mg5	5	M-PA6 containing 5 wt% Mg
M-Mg10	10	M-PA6 containing 10 wt% Mg
M-CNT3	3	M-PA6 containing 3 wt% CNT
M-CNT5	5	M-PA6 containing 5 wt% CNT
M-CNT7	7	M-PA6 containing 7 wt% CNT

[a] Percentage based on the weight of the ECL monomer in the starting AAROP mixture.

2.3.3. Synthesis of polyamide 6 microcapsules with dual load

Dual-loaded PAMC (DM-samples) were synthesized by introducing into the polymerization medium of a mixture comprising (i) the desired amounts of metal particles (Al, Cu, Fe or Mg) and (ii) carbon allotropes (CNT or CB). Such as in 2.3.2, a sonication process was carried out during 30 min with the mixtures of metal particles and CNT. Then, the procedure was executed as described previously in [1, 2]. The designation and composition of all the DM–samples synthesized are presented in Table 2.2. All PAMC types were used in the subsequent phase of compression molding (CM).

Table 2.2 | Sample designations and composition of the DM-samples – dually loaded PAMC

Sample designation	Load, wt % [a)]	Description
DM-Al3-CNT7	3 + 7	DM-PA6 with 3 wt% Al and 7 wt% CNT
DM-Al5-CNT5	5 + 5	DM-PA6 with 5 wt% Al and 5 wt% CNT
DM-Al7-CNT3	7 + 3	DM-PA6 with 7 wt% Al and 3 wt% CNT
DM-Al5-CB5	5 + 5	DM-PA6 with 5 wt% Al and 5 wt% CB
DM-Cu5-CNT5	5 + 5	DM-PA6 with 5 wt% Cu and 5 wt% CNT
DM-Fe5-CNT5	5 + 5	DM-PA6 with 5 wt% Fe and 5 wt% CNT
DM-Mg5-CNT5	5 + 5	DM-PA6 with 5 wt% Mg and 5 wt% CNT

a) Percentage based on the weight of the ECL monomer in the starting AAROP mixture.

2.3.4. Preparation of polyamide 6 composites

2.3.4.1. Polyamide 6 composites

The CM of the PA6 hybrid plates (P-samples) was performed in a 25-ton Moore Hydraulic Hot Press, England, using molds with dimensions 70 x 70 x 2 mm and 85 x 75 x 1 mm. The amount of each M-sample deposited into the mold was previously calculated considering the mold volume, the density of the PA6, and payload dispersed in it. A pressure of about 3-4 MPa was applied for 8 min at 230 °C. Then, the molded plates were cooled down to 80 °C. The designation and composition of all the P-samples prepared by CM of the respective M-samples are presented in Table 2.3. Figure 2.2 shows the visual aspect of these materials.

Figure 2.2| Visual aspect of the materials prepared: a) M-samples containing CNT; b) M-samples containing metal particles; c) P-samples from respective M-samples containing metal particles, from left to right: P-PA6, P-Al10, P-Cu10, P-Mg10, P-Fe10.

Table 2.3 | Sample designations and composition of the P-samples

Sample designation	Composition, vol.% [a]		Description
	Load	PA6	
P-PA6	0	100.0	PA6 matrix plate based on M-PA6
P-Al5	4.18	95.8	Composite plate based on M-Al5
P-Al10	9.15	90.8	Composite plate based on M-Al10
P-Cu5	1.33	98.7	Composite plate based on M-Cu5
P-Cu10	2.62	97.4	Composite plate based on M-Cu10
P-Fe5	1.06	98.9	Composite plate based on M-Fe5
P-Fe10	2.18	97.8	Composite plate based on M-Fe10
P-Mg5	6.54	93.5	Composite plate based on M-Mg5
P-Mg10	8.82	91.2	Composite plate based on M-Mg10
P-CNT3	2.65	97.4	Composite plate based on M-CNT3
P-CNT5	4.45	95.6	Composite plate based on M-CNT5
P-CNT7	6.72	93.3	Composite plate based on M-CNT7

[a] Represents the relation between the volumes of load (metal or CNT) and PA6 in the respective M sample.

The same procedure was applied to produce dually loaded composite plates (DP-samples) by CM of the respective DM samples. The designation and composition of all the DP-samples prepared are presented in Table 2.4. Figure 2.3 shows the visual aspect of some of the dual-loaded materials.

Table 2.4 | Sample designations and composition of the DP-samples

Sample designation	Composition, vol. % [a]			Description
	Metal	Carbon	PA6	
DP-Al3-CNT7	1.96	5.71	92.3	Composite plate based on DM-Al3-CNT7
DP-Al5-CNT5	3.84	4.80	91.4	Composite plate based on DM-Al5-CNT5
DP-Al7-CNT3	4.68	2.51	92.8	Composite plate based on DM-Al7-CNT3
DP-Al5-CB5	3.41	5.11	91.5	Composite plate based on DM-Al5-CB5
DP-Cu5-CNT5	1.03	4.29	94.7	Composite plate based on DM-Cu5-CNT5
DP-Fe5-CNT5	0.93	3.38	95.7	Composite plate based on DM-Fe5-CNT5
DP-Mg5-CNT5	5.15	4.15	90.7	Composite plate based on DM-Mg5-CNT5

[a] Represents the relation between the volumes of metal, carbon filler and PA6 in the respective DM-sample.

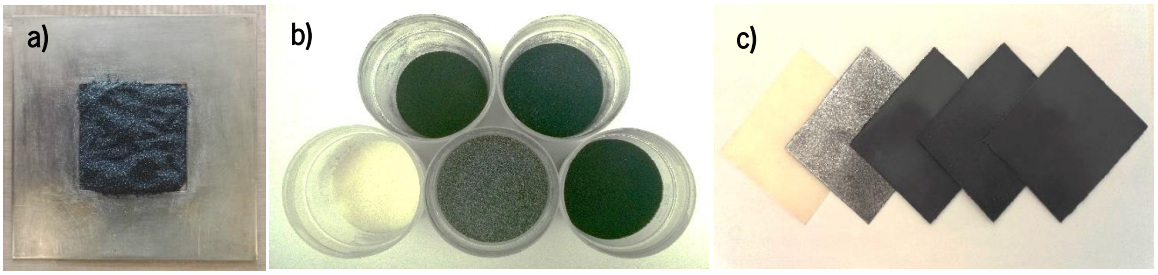

Figure 2.3| Visual aspect of the some of the dual-loaded materials prepared: a) DM-Al5-CNT5 deposited into mold used in CM process; b) DM-samples containing metal particles and CNT; c) DP-samples from respective DP-samples containing metal particles and CNT, from left to right: P-PA6, DP-Al5-CNT5, DP-Cu5-CNT5, DP-Mg5-CNT5, DP-Fe5-CNT5.

2.3.4.2. Polyamide 6 composite laminates

PA6 composite laminates dually reinforced by metal payloads and CFT (L-samples) were prepared by CM. Such as in the section 2.2.4.1., the CM was performed in a manual 25 Ton Moore Hydraulic Hot Press, England, using a square mold with dimensions 70 x 70 x 2 mm.

Two different volume fractions, V_f, of the CFT reinforcement, i.e., 0.25 and 0.50, were used to prepare the L-samples. To determine the number of CFT plies necessary to obtain the corresponding V_f values, it was applied Equation 2.1:

$$V_f = \frac{A_w \cdot n}{\rho_f \cdot t} \tag{2.1}$$

where A_w is the area density (g/m²) of the CFT used, n is the number of CFT plies, ρ_f is the density of the carbon fibers (g/m³) and t is the laminate thickness [3]. All CFT structures were cut to the shape of the mold and they were stacked unidirectionally.

The amount of each M-sample necessary to prepare the L-samples was previously calculated considering the V_f established (0.25 and 0.50), and the mold volume, the density of the CFT, and the density of the PA6 and metal payload dispersed in it. These amounts were then divided into $n+1$ equal portions and stacked with n CFT plies, n being calculated from Eq. 2.1. Then, the ply stacks were consolidated in a hot press applying a pressure of 3-4 MPa for 10 min at 230 °C. Subsequently, the molded laminates were cooled down to 80 °C. The designation and composition of all the L-samples prepared are presented in Table 2.5. Figure 2.4 shows the visual aspect of those materials.

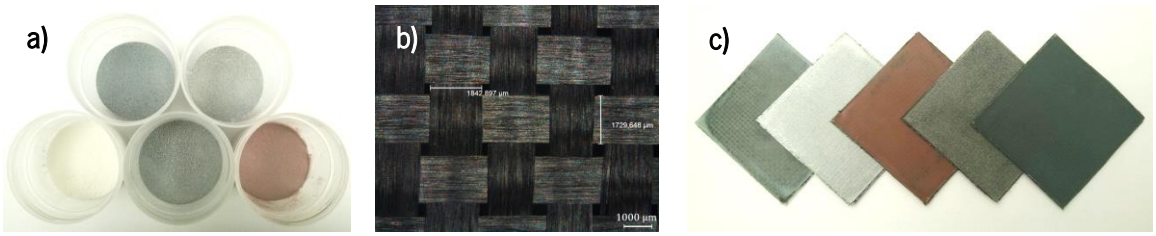

Figure 2.4 | Visual aspect of the materials used in the preparation of L-samples: a) M-samples containing 10 wt.% of metal particles; b) stereoscopic image of a plain-wave CFT ply; c) L-samples, from the left to right: L-PA6-25, L-Al-25, L-Cu-25, L-Mg-25 and L-Fe-25.

Table 2.5 | Sample designations and composition of L-samples

Sample designation	No. CFT plies	Volume fraction, V_f [a]			Description
		Metal	CFT	PA6	
L-PA6-25	4	0	0.24	0.76	Laminate based on M-PA6 and 0.25 V_f of CFT
L-PA6-50	9	0	0.42	0.58	Laminate based on M-PA6 and 0.50 V_f of CFT
L-Al-25	4	0.07	0.27	0.66	Laminate based on M-Al10 and 0.25 V_f of CFT
L-Al-50	9	0.05	0.45	0.50	Laminate based on M-Al10 and 0.50 V_f of CFT
L-Cu-25	4	0.02	0.27	0.71	Laminate based on M-Cu10 and 0.25 V_f of CFT
L-Cu-50	9	0.01	0.47	0.52	Laminate based on M-Cu10 and 0.50 V_f of CFT
L-Fe-25	4	0.02	0.26	0.72	Laminate based on M-Fe10 and 0.25 V_f of CFT
L-Fe-50	9	0.01	0.44	0.55	Laminate based on M-Fe10 and 0.50 V_f of CFT
L-Mg-25	4	0.07	0.25	0.68	Laminate based on M-Mg10 and 0.25 V_f of CFT
L-Mg-50	9	0.05	0.44	0.51	Laminate based on M-Mg10 and 0.50 V_f of CFT

[a] Represents the relation between the volume fractions of metal, CFT, and PA6 in the respective L sample.

2.4. Morphological and structural characterization

Various characterization techniques were implemented for a detailed morphological and structural characterization of the samples produced.

2.4.1. Viscosimetry

Capillary viscosimetry measures the time, t, required for a specified volume of the polymer solution to flow through a capillary tube comparing it to the flow time of the pure solvent, t_0 [4]. The ratio between t and t_0 defines the relative viscosity, η_r:

$$\eta_r = \frac{\eta}{\eta_0} = \frac{t}{t_0} \tag{2.2}$$

where η and η_0 are, respectively, the polymer solution viscosity and viscosity of the pure solvent.

From Eq. 2.2, the specific viscosity, η_{sp}, is determined by means of Equation 2.3:

$$\eta_{sp} = \eta_r - 1 = \frac{\eta - \eta_0}{\eta_0} = \frac{t - t_0}{t_0} \tag{2.3}$$

Knowing the η_{sp} value and using the polymer solution concentration, c, it is determined the reduced viscosity, η_{red}, according to Equation 2.4:

$$\eta_{red} = \frac{\eta_{sp}}{c} \tag{2.4}$$

Further, an inherent viscosity, η_{inh}, can be determined, applying the natural logarithm of the η_r, and the η and η_0 values, by means:

$$\eta_{inh} = \frac{\ln \eta_r}{c} \tag{2.5}$$

The η_{red} and η_{inh} viscosity can be plotted as a function of the solution concentration in order to determine the intrinsic viscosity, $[\eta]$. In this work $[\eta]$ was calculated using the following Equation 2.6 [5]:

$$[\eta] = 0,55 \cdot \frac{\eta_{sp}}{c} + 0,44 \tag{2.6}$$

Then, a correlation between $[\eta]$ and molecular weight can be made from the empirical Mark-Houwink equation, allowing the determination of the average viscometric molecular weight, $\overline{M_v}$, as:

$$\eta = k\overline{M_v}^{\alpha} \tag{2.7}$$

where k and α are constants that depend on the polymer-solvent system used, their values being 5.066x10^{-4} and 0.74074, respectively [6].

In this work, the M_v of the neat PA6 was determined at 25 °C in 97 % sulfuric acid (95-98%, Sigma-Aldrich), with a polymer concentration of 0.2 g/dL using a Ubbelohde viscometer. At least five runs were made to determine t and t_0.

2.4.2. Scanning electron microscopy

Scanning electron microscopy (SEM) enables direct observation of the size, shape, and porosity of the PAMC, and permits to assess the distribution of the payloads within the polymer matrix of the final composites. The interface between the matrix and the payload(s) used can also be investigated by SEM.

The SEM analysis required some pretreatment of the samples. Selected P-, DP- and L-samples were cryo-fractured and the sections obtained were sputter-coated with a gold-palladium (Au-Pd) alloy, 80–20 wt.%, with a thickness of about 8 nm using a 208 HR equipment of Cressington Scientific Instruments (Watford, UK) with high-resolution thickness control. Selected M- and DM-samples were observed after sputter-coating, as described above. The studies were performed in a NanoSEM-200 apparatus of FEI Nova (Hillsboro, USA) using mixed secondary electron/back-scattered electron in-lens detection.

2.4.3. Optical microscopy

Reflected light microscopy (RLM) is useful to observe opaque specimens comprising, for instance, metal particles [7]. In this work, the RLM study was performed in an Olympus BH-2 microscope (Olympus Corp. Japan) equipped with a Leica DFC200 (Leica Microsystems, Germany) digital camera. The samples were embedded in epoxy resin suitable for light microscopy. After curing, the surface of the embedded samples was polished in a Minitech 233 manual polishing machine (Presi, France) using wet sandpapers with different grit sizes to obtain a transparent and glossy surface without scratches.

2.4.4. Solid-state NMR spectroscopy

The crystalline structure and molecular dynamics in semi-crystalline polymers can be successfully studied by high-resolution solid-state nuclear magnetic resonance (ssNMR) [8]. Besides the application of ssNMR to study the interaction between filler(s) and polymeric matrix, this non-destructive method can be used to perform radiofrequency (RF) shielding studies, since a loss of NMR signal of the matrix is expected whenever fillers with paramagnetic or conductive properties are used [9].

In this work, the crystalline structure and molecular dynamics of M-samples comprising metal particles were analyzed. The RF shielding studies were performed with M-samples and DM-samples. All the ssNMR spectra were acquired using a Tecmag Redstone/Bruker 300WB spectrometer. The conditions used for each experiment are described in detail below. All the experiments were carried out at room temperature.

2.4.4.1. Magic angle spinning (MAS) and cross-polarization/MAS

M-samples (about 200 mg) were packed into 7 mm o.d. zirconia rotors, equipped with Kel-F caps. Carbon 13 (^{13}C) nucleus spectra were acquired at 75.49 MHz with a spinning rate of about 3 kHz and 90° RF pulses of 4 μs (i) or 4.5 μs (ii) using two different RF sequences: **i)** one pulse (Bloch decay) with 1 s relaxation delay and **ii)** cross-polarization/MAS (CP/MAS) spectra with a relaxation delay of 10 s, a contact time of 2 ms and a frequency field of 62.5 kHz for the spin-lock field B_1. ^{13}C chemical shifts were obtained using the glycine as an external reference, which was set at 176.03 ppm (^{13}CO signal). The pulse sequences used in the experiments (a) and (b) are illustrated, respectively, in Fig. 2.5a and Fig. 2.5b. From experiments (i) and (ii) the amorphous and crystalline PA6 matrix components were distinguished and characterized. The degree of crystallinity, X_c, of all the samples

was determined from the ^{13}C CP/MAS spectra. Gaussian functions were chosen to deconvolute the carbon (C) signals using PeakFit© commercial software. Calculations were made on the area of the crystalline and amorphous peaks of the respective aliphatic groups of all PAMC analyzed, using the C signals with the same multiplicity, according to Equation 2.8:

$$X_c{}^{ssNMR}{}_{partial} = \frac{\sum A_c}{\sum A_c + \sum A_a}, \% \quad (2.8)$$

where A_c is the sum of the areas of the crystalline phase signals and A_a is the sum of the areas of the amorphous phase signals. Applying the Eq. 2.8 to the empty and metal-loaded PAMC, the partial crystallinity index $X_c{}^{ssNMR}{}_{partial}$ was calculated considering the two groups of nuclei (C4, C2 + C3) and (C5, C1). Then, the total crystallinity index $X_c{}^{ssNMR}{}_{total}$ was also calculated based on the total sum of the area of the crystalline peaks according to Equation 2.9:

$$X_c{}^{ssNMR}{}_{total} = \sum A(C_4, C_2 + C_3)_c + \sum A(C_5, C_1)_c \quad (2.9)$$

2.4.4.2. Relaxation times

The influence of metal payloads on the molecular dynamics of the polymer matrix was performed by measuring different relaxation times at different frequencies. M-samples (about 200 mg) were packed into 7 mm o.d. zirconia rotors, equipped with Kel-F caps. The carbon spin-lattice relaxation time ($^{C}T_1$) and the carbon spin-lattice relaxation time in the rotating frame ($^{C}T_{1\rho}$) were measured using ^{13}C CP/MAS experiments.

$^{C}T_1$ was obtained in the MHz range by recording the intensity of the carbon signals as a function of the variable time delay, τ, in the TORCHIA sequence schematically shown in Fig. 2.5c [10]. Were selected either 14 values (0.5 s, 1 s, 2 s, 3 s, 4 s, 8 s, 10 s, 12 s, 16 s, 20 s, 25 s, 30 s, 35 s, 40 s) or 10 values (0.5 s, 1 s, 2 s, 3 s, 4 s, 8 s, 10 s, 12 s, 16 s, 20 s, 25 s), depending on the sample type (non-loaded or loaded M-samples, respectively). The number of scans was always higher than 120. The magnetization recorded from each C species was plotted against τ. The data were analyzed by a nonlinear least-squares fit of mono- or double-exponential functions.

$^{C}T_{1\rho}$ data were measured by recording the ^{13}C signal as a function of the ^{13}C spin-locking time, τ, immediately after a CP period of 2 ms; τ was selected between 0.5 s and 25 s (12 values: 0.5 s,

1 s, 2 s, 3 s, 4 s, 6 s, 8 s, 10 s, 12 s, 16 s, 20 s, 25 s). The frequency field of the spin-locking field B_1 was kept at 62.5 kHz and the recycle delay was 5 s.

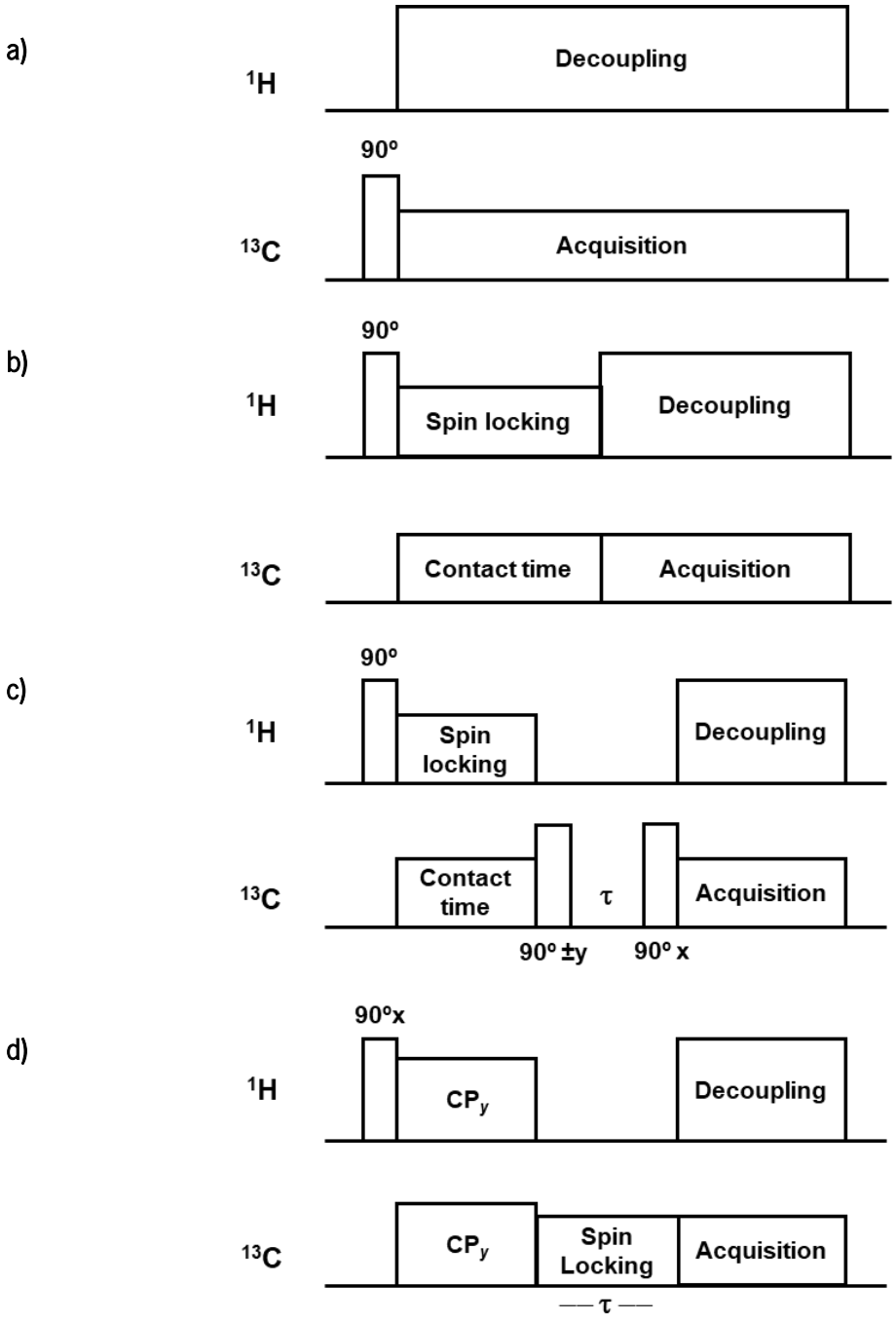

Figure 2.5 | ssNMR pulse sequences used: a) one pulse (Bloch decay); b) CP-MAS c) TORCHIA sequence for ${}^{C}T_1$ determination with CP/MAS; d) sequence for ${}^{C}T_{1\rho}$ measurement with CP/MAS.

$^{C}T_1$ data were obtained using Equations 2.10 or 2.11 (mono- or double-exponential decays, respectively) and $^{C}T_{1\rho}$ values were the time constants from mono-exponential decays (similar to Eq. 2.10):

$$y = I_0[\exp(-\tau / {}^{C}T_1] \tag{2.10}$$

$$y = I_0 + I_1[\exp(-\tau / ({}^{C}T_1)_1)] + I_2[\exp(-\tau / ({}^{C}T_1)_2)] \tag{2.11}$$

Eq. 2.10 or 2.11 were fitted to the experimental data (signal intensity as a function of τ), using the least-squares method. Relaxation data were always measured at about 20°C.

The pulse sequences used in molecular dynamic studies related to $^{C}T_1$ and $^{C}T_{1\rho}$ are illustrated, respectively, in Fig. 2.5c and Fig. 2.5d.

2.4.4.3. Radiofrequency shielding studies

The qualitative evaluation of the electromagnetic shielding properties of selected M- and DM-samples was carried out by ssNMR measurements. ^{13}C nucleus spectra were acquired at 75.49 MHz to evaluate the loss of the ^{13}C polyamide signal using zirconia rotors (7 mm o. d. and 18 mm long) packed with the M- or DM-sample under study. The volume filled in with each PAMC sample was 481 mm^3, the total volume of the container. The standard CP/MAS RF sequence was used for the spectrum acquisition, selecting the following parameters: 3.3 kHz spinning rate, 2 ms contact time, 10 s recycling delay and a number of scans between 100 and 400. ^{13}C chemical shifts were obtained using the glycine as an external reference, which was set at 176.03 ppm (^{13}CO signal).

2.5. Thermal characterization

2.5.1. Differential scanning calorimetry

Differential scanning calorimetry (DSC) measurements allow the direct determination of characteristic temperatures in a polymer material, such as the melting temperature, T_m, the crystallization temperature, T_c, and the glass transition temperature, T_g. Besides that, the degree of crystallinity, X_c , of the polymer matrix can be determined according to Equation 2.12:

$$X_c = \frac{\Delta H_m^i}{w \cdot \Delta H_m^0}, \% \tag{2.12}$$

where ΔH_m^i is the registered melting enthalpy of the current sample, w is the weight fraction of the polymer present in the sample and ΔH_m^o is the melting enthalpy of a 100 % crystalline sample.

In this work, the DSC measurements were carried out in a 200 F3 equipment of Netzsch (Selb, Germany) at a heating rate of 10 °C/min under N_2 purge. The typical sample weights were in the 10-15 mg range. The X_c of the PA6 matrix was calculated according to Eq. 2.12 and the ΔH_m^o value for a 100 % crystalline PA6 is 190 J/g [11]. All the PAMC synthesized and their respective molded composites were analyzed.

2.5.2. Thermogravimetric analysis

Generally, thermogravimetric analysis (TGA) was used to evaluate the loss of mass of all sample types of this work during a linear increase of the temperature, as a function of sample composition. In M- and DM-samples, TGA was used also to determine the effective real load (RL). A Q500 TGA equipment (TA Instruments, USA) was employed, heating the samples from 40 to 600°C at 10 °C/min in a N_2 atmosphere. The typical sample weights were in the 10-20 mg range. The R_L value in PAMC was calculated according to Equation 2.13:

$$RL = R_f - R_{PA6}, \% \tag{2.13}$$

where R_{PA6} is the carbonized residue at 600 °C of empty PAMC and R_f represents the carbonized residue of the respective loaded PAMC measured by TGA. All the PAMC synthesized and their respective molded composites were analyzed.

2.6. Mechanical characterization – Tensile tests

Tensile tests were performed according to ASTM standard D 638-03 using two testing machines: DP-samples were tested on an Instron 5969 testing machine (USA) at 23 ± 2 °C with a standard load cell of 50 kN at a constant crosshead speed of 50 mm/min; P- and L-samples were tested on a Shimadzu Autograph AGS-X Series (Japan) at 23 ± 2 °C with a standard load cell of 50 kN at a constant crosshead speed of 50 mm/min. From the P-, DP- and L-samples, standard specimens were cut out according to DIN standard 53504-S3A. At least five specimens of each sample were studied to calculate the average and standard deviation values of the tensile properties. Prior to tensile tests, all the samples were stored for ca. 30 days at 23 °C and 65 % relative humidity.

The engineering stress, σ_e, was determined as a ratio of the tensile force and the initial cross-section of the sample. The engineering strain, ε_e, was determined as a ratio of the sample gauge length at any time during drawing and that prior to drawing. The Young's modulus, E, values were obtained from the initial slope of the strain-stress curves up to 1% strain (secant modulus).

In order to determine the improvement of the tensile properties of the composites comparing with the neat PA6 matrix, the improvement factor (IF) was calculated for E, maximum stress, $\sigma_{\max}$, and stress at break, σ_{br}, values according to Equation 2.14:

$$IF = \frac{P_c - P_{PA6}}{P_{PA6}}, \% \tag{2.14}$$

where P_c and P_{PA6} are the parameter of the PA6 composite and the same parameter of the neat PA6 matrix, respectively.

2.7. Electric and dielectric characterization

2.7.1. Bulk resistivity

Bulk resistivity, ρ, is an intrinsic electrical property of the materials and it is related to the number of free carriers and their ability to move in the lattice when an electric field is applied [12]. A way to determine ρ is from the measurement of the voltage (V) through which a direct current (I) flows. Therefore, ρ can be viewed as the normalization of the bulk resistance, R, by its geometrical dimension, as illustrated in Figure 2.6. Thus, ρ is determined by means:

$$\rho = \frac{RA}{L} \tag{2.15}$$

where A is the cross-sectional area of the sample and L is the distance between the contacts. [12]

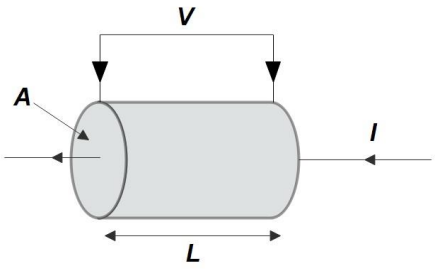

Figure 2.6 | Representation of the bulk resistance measurement.

In this work, electrical current/voltage measurements were performed in a Keithley 487 Pico-Ammeter/Voltage Source (Keithley Instruments Inc., Cleveland, USA) between ± 10 V using increasing and/or decreasing modes at room temperature and pressure. To rule out interferences due to the external electric field, all measurements were performed in a Faraday cage. A standard procedure was followed in which the current-voltage (I–V) dependences for all materials were determined and analyzed. From the slope of the graphs (straight lines for Ohmic materials) the resistance, $R(\Omega)$, was determined, from which the electric conductivity or direct current (d.c.) electric conductivity, $\sigma_{dc}(S \cdot m)$, were calculated according to Equation 2.16:

$$\sigma_{dc} = \frac{1}{\rho} = \frac{1}{R \cdot \frac{A}{d}} \tag{2.16}$$

where A is the area of the circular gold electrodes (5 mm in diameter) deposited on both the sample's surface and d the thickness of the samples (of about 600 μm). Four measurements in different parts of each molded sample were performed taking the arithmetical mean as a final value of conductivity.

2.7.2. Dielectric spectroscopy

As mentioned in section 1.3.2 of Chapter 1, the ability of a material to polarize with respect to an applied external electric field is measured as a function of frequency, which can be expressed as relative permittivity or dielectric constant, ε' [13, 14].

In the studies performed on this thesis, the dielectric properties were obtained by dielectric spectroscopy from the geometry of the samples in the shape of a parallel plate capacitor (circular electrodes of 5 mm diameter were deposited on both surfaces and the sample average thickness is of about 600 μm). The measurements were performed with a QuadTech (Marlborough, USA) model 1920 Precision Inductance-Capacitance-Resistance Meter at room temperature and pressure, over a frequency window of $10^2 < f$ (Hz) $< 10^6$. The ε' and dielectric losses, $\tan\delta$, of P-, DP- and L-samples were determined, respectively, according to Equations 1.9 and 1.11 enunciated in section 1.3.2 of Chapter 1.

2.7.3. Broadband electric conductivity

In order to obtain a detailed profile of the temperature and frequency-dependent electrical properties, broadband dielectric spectroscopy (BDS) measurements were performed in selected P- and DP-samples with sputtered gold electrodes (20 mm in diameter) deposited on both surfaces. The BDS

measurements were performed over a frequency window of $10^{-1} < f$ (Hz) $< 10^{6}$ and a temperature range of -150 °C < T (°C) < 100. To cover the said frequency range, a Novocontrol system integrating an ALPHA dielectric interface was employed. The control of the temperature during every single frequency sweep was secured by N_2 gas jet system (QUATRO Cryosystem from Novocontrol) with a temperature error of ± 0.1 °C. The AC electrical conductivity, σ_{ac}, was derived from Eq. 1.13 presented in section 1.3.2 of Chapter 1.

2.8. High-frequency shielding characterization

To measure the electromagnetic interference (EMI) shielding effectiveness (SE) of composite materials, several methods can be used, as described in section 1.3.4 of Chapter 1. Among them, the transmission coaxial line method is a suitable alternative to obtain the reflected, absorbed and transmitted components, besides of the EMI SE quantification [15, 16].

Experimentally, the shielding by reflection, SE_R, and the shielding by absorption, SE_A, can be determined by using the following equations [15]:

$$SE_R(dB) = -10\log_{10}(1-R) \tag{2.17}$$

$$SE_A(dB) = -10\log_{10}\left(\frac{T}{1-R}\right) \tag{2.18}$$

where the reflection, R, and transmission, T, coefficients are directly determined as followed:

$$R = |S_{11}|^2 = |S_{22}|^2 \tag{2.19}$$

$$T = |S_{12}|^2 = |S_{21}|^2 \tag{2.20}$$

in which S represents the scattering parameters through the coaxial transmission line, since the transmission/reflection waves are collected in both directions, as sketched in Figure 2.7.

Then, the relationship among SE_R and SE_A allows calculating the overall SE by using Equation 2.21:

$$SE_T(dB) = SE_R + SE_A \tag{2.21}$$

The shielding measurements are performed as a function of frequency, f.

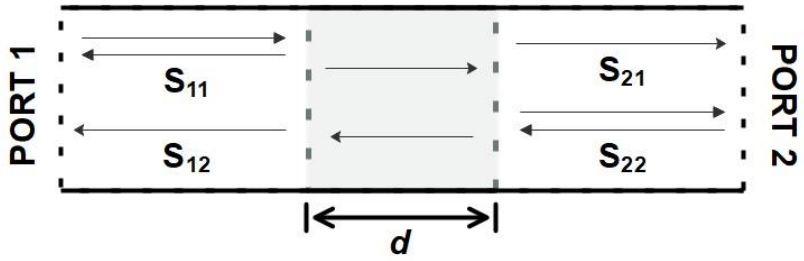

Figure 2.7 | Representation of the S-parameters through the coaxial transmission line; *d* – sample thickness.

Thus, inspired by the procedure of ASTM standard D4935-99 at room temperature [17], the EMI data of our plate materials were measured over a frequency range of 30 MHz to 3 GHz by means of Setup 1. For this measurement a ZVL3-75 Network Analyzer (Rohde & Schwarz, Germany) was employed in such frequency range, using a flanged coaxial line sample holder connected to the VNA by coaxial cables and connectors with 50 Ω characteristic impedance, and 10 dB attenuators fixed on each end of the sample holder. Additional EMI shielding measurements were made in the 3–12.4 GHz frequency range by means of Setup 2. It was used a N5242A PNA-X Network Analyzer (Agilent Technologies, USA), a flanged coaxial line sample holder connected to the VNA by coaxial cables and connectors with 50 Ω characteristic impedance, and 10 dB attenuators fixed on each end of the sample holder. Figure 2.8 shows the setup 2 apparatus used.

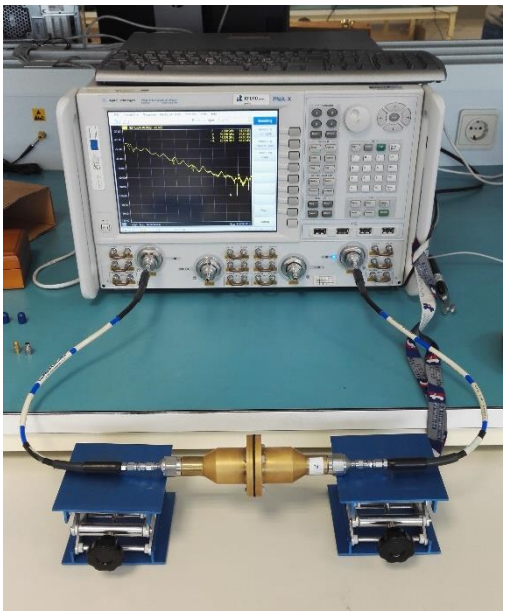

Figure 2.8 | Apparatus of the setup 2 used in the high-frequency shielding measurements.

For EMI shielding measurements, the ASTM standard D4935-99 requires a reference and load specimens with the same thickness for each composition analysis. Thus, the reference and load specimens were cut using a laser cutting machine LightCut 6090 (G-Weike, China), as shown in Figure 2.9. The reference specimen has a 60 mm outer diameter, 23 mm inner diameter, and it is still composed of a disk with a 10 mm diameter that matching with the internal conductor of the sample holder. The load specimen has 60 mm in diameter. P- and DP-samples (load and respective reference) with 1 and 2 mm were cut.

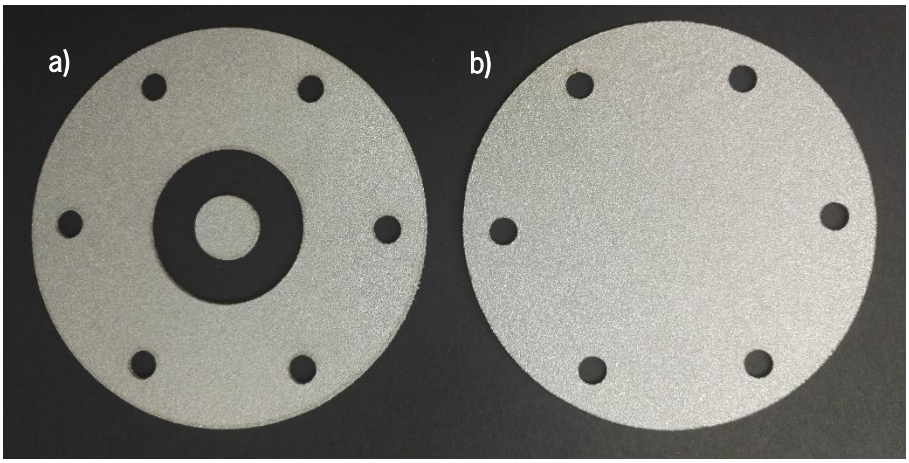

Figure 2.9 | Reference (a) and load (b) specimens of the P-Al5 sample.

Thereby, the overall SE was determined for the P-, DP-samples by measuring the ratio of the incident to transmitted electric field with both reference, E_R, and load, E_L, specimens by means:

$$SE(dB) = 20\log_{10}\left(\frac{E_R}{E_L}\right) \tag{2.22}$$

The SE_R and SE_A were calculated according to Eq. 2.17 and Eq. 2.18.

Before starting the SE measurements, both setups were properly calibrated. A through-open-short-match (TOSM) calibration procedure was applied, using an 85521A OSLT Mechanical Calibration Kit. The calibration was made for each port.

2.9. References

[1] Denchev Z, Dencheva N (**2015**) Polyamide Microcapsules and Method to Produce the Same, Portuguese patent PT 107679 A, filled 03.06.2014, published 03.12.2015, C08G 69/18

[2] Dencheva N, Denchev Z, Lanceros-Méndez S, Ezquerra Sanz T (**2016**) One-step in situ synthesis

of polyamide microcapsules with inorganic payload and their transformation into responsive thermoplastic composite materials. *Macromol Mater Eng*, 301:119–124. DOI: 10.1002/mame.201500194

[3] Gürdal Z, Haftka RT, Hajela P (**1999**) Design and Optimization of Laminated Composite Materials. John Wiley & Sons, Inc., New York, pp 1-32

[4] Billmeyer JFW (**1984**) Measurement of molecular weight and size. In: Textbook of Polymer Science, 3rd ed. John Wiley & Sons, Inc., New York, pp 186–228

[5] Ivanova L, Kulichikhin S, Alkaeva O, Akimushkina N, Vyrsky U, Malkin A (**1978**) Determining of molecular characteristics of polycaproamide. *Vysok Soedin*, A20:2813–2816

[6] Ueda K, Nakai M, Hattori K, Yamada K, Tai K (**1997**) Synthesis of High Molecular Weight Nylon 6 by Anionic Polymerization of ε-Caprolactam: Evaluation of Molecular Weight and Molecular Weight Distribution. *Kōbunshi rombun shū*, 54:401–406. DOI: 10.1295/koron.54.401

[7] Nadeau JL, Davidson MW (**2012**) Optical Microscopy. In: Characterization of Materials. American Cancer Society, pp 1–22

[8] Kurosu H, Ando S, Yoshimizu H, Ando I (**1994**) NMR Studies of Higher-order Structures of Solid Polymers. In: Ando I, Webb GA (eds). Academic Press, pp 189–275

[9] Jouni M, Buzlukov A, Bardet M, Boisson F, Eddarir A, Massardier V, Boiteux G (**2014**) Skin effect of conductive polymer composites observed by high-resolution solid-state NMR. *Compos Sci Technol*, 104:104–110. DOI: 10.1016/j.compscitech.2014.08.031

[10] Torchia DA (**1978**) The measurement of proton-enhanced carbon-13 T_1 values by a method which suppresses artifacts. *J Magn Reson*, 30:613–616. DOI: 10.1016/0022-2364(78)90288-3

[11] Shan G-F, Yang W, Yang M, Xie B, Feng J, Fu Q (**2007**) Effect of temperature and strain rate on the tensile deformation of polyamide 6. *Polymer (Guildf)*, 48:2958–2968. DOI: 10.1016/j.polymer.2007.03.013

[12] Deen MJ, Pascal F (**2017**) Electrical Characterization of Semiconductor Materials and Devices. In: Kasap S, Capper P (eds) Springer Handbook of Electronic and Photonic Materials. Springer International Publishing, Cham, pp 453–481

[13] Kasap SO (**2006**) Dielectric Materials and Insulation. In: Principles of Electronic Materials and Devices, 3rd ed. McGraw-Hill, New York, pp 583–608

[14] Dissado L (**2017**) Dielectric Response. In: Kasap S, Capper P (eds) Springer Handbook of Electronic and Photonic Materials. Springer International Publishing, Cham, pp 219–245

[15] Daniel S, Thomas S (2019) Shielding Efficiency Measuring Methods and Systems. In: Jaroszewski M, Thomas S, Rane A V. (eds) Advanced Materials for Electromagnetic Shielding: Fundamentals, Properties, and Applications, 1st ed. John Wiley & Sons, Inc., USA, pp 61–87

[16] Geetha S, Satheesh Kumar KK, Rao CRK, Vijayan M, Trivedi DC (2009) EMI shielding: Methods and materials—A review. *J Appl Polym Sci*, 112:2073–2086. DOI: 10.1002/app.29812

[17] ASTM D4935-99 Standard Test Method for Measuring the Electromagnetic Shielding Effectiveness of Planar Materials

RESULTS AND DISCUSSION

CHAPTER 3

Synthesis and properties of polyamide 6 hybrid microcapsules and composites on their basis

3.1. Introduction

The bibliographical survey in Chapter 1 led to the conclusions that the preparation of advanced polyamide 6 (PA6) composites based on the reactive microencapsulation strategy through activated anionic ring-opening polymerization (AAROP) of ε-caprolactam (ECL) in solution is a possible pathway to overcome the limitations of the traditional melt-processing techniques for composite preparation. Chapter 3 reports on the in-situ synthesis of PA6 microcapsules (PAMC) with single loads (M-samples) comprising up to 20 wt.% of different metal particles (Al, Cu, Fe, or Mg) or carbon nanotubes (CNT) by AAROP in solution, and their compression molding to composite plates (P-samples). This chapter reproduces some previous results on metal- and CNT containing PAMC through AAROP [1, 2] establishing their concentration levels. The effect of the type and content of the filler on the structure, morphology, and thermal properties of the loaded PAMC and respective composites was evaluated. The mechanical properties in tension of such loaded P-samples, as well as their electric conductivity and dielectric properties were studied. Some conclusions about the applicability of the reactive microencapsulation/compression molding strategy for the preparation of composites with tailored properties are also presented.

3.2. Synthesis of loaded polyamide 6 microcapsules

The synthesis of empty, CNT- and metal-loaded PAMC was carried out via AAROP, following the procedure described in sections 2.3.1 and 2.3.2. of Chapter 2. Table 3.1 shows the designations of the PAMC samples produced, the respective polymerization yields, the filler content in respect to ECL monomer, and the volume percentage of the filler based on the volumes of metal or MWCNT fillers used in AAROP.

The mechanism of empty PA6 microparticles formation was postulated in the works of Vasiliu-Oprea and Dan [3, 4] and Rico et al. [5], and then extended to differently loaded PAMC [1]. According to this mechanism, rather early in the AAROP of the ECL in solution viscous low molecular weight PA6 particles are formed. The latter pass through macromolecular chain propagation, coalescence, and crystallization to form the final PAMC. If CNT or metal payloads are dispersed in the constantly stirred reaction medium, as the AAROP advances, they become entrapped into the viscous particles and nucleate the PA6 crystallization to PAMC [1].

According to the PAMC yields obtained in this thesis (Table 3.1), the conversion of ECL to PA6 is around 50 %, regardless of the load used. By obtaining yields analogous to those of the empty PAMC, it

is demonstrated that CNT or metal loads do not hinder or block the anionic polymerization process. It should be noted also that the fillers used are not organically modified.

Table 3.1 | PAMC: sample designations, composition and polymerization yield

Sample	Load, wt.% [a]	Composition, vol. % [b]		PAMC yield, % [c]	Real load, wt.% [d]
		Load	PA6		
M-PA6	0	0	100	56.2	0
M-Al5	5	4.18	95.8	45.9	9.4
M-Al10	10	9.15	90.8	45.1	19.4
M-Cu5	5	1.33	98.7	42.4	9.6
M-Cu10	10	2.62	97.4	48.6	17.6
M-Fe5	5	1.06	98.9	45.3	7.0
M-Fe10	10	2.18	97.8	49.2	13.4
M-Mg5	5	6.54	93.5	46.3	9.7
M-Mg10	10	8.82	91.2	48.9	13.0
M-CNT3	3	2.65	97.4	54.6	4.9
M-CNT5	5	4.45	95.6	53.2	8.2
M-CNT7	7	6.72	93.3	52.3	12.1

[a] Percentage based on the weight of the ECL monomer in the starting AAROP mixture;

[b] Represents the relation between the volumes of load (metal or CNT) and PA6 in the respective M-sample;

[c] With respect to the sum of the ECL plus filler weight. Calculated from the conversion of ECL into polymer;

[d] Determined by thermogravimetric analysis (TGA) according to Eq. 2.13 of Chapter 2.

The reason why the PAMC yields are around 50 % and not closing 98–99 % as in the bulk AAROP [6, 7] is related to the fast growth of the polymer chains in the respective viscous particles resulting in the crystallization and precipitation of the latter, which makes the access of monomer molecules to the growing anionic centers very difficult and consequently limits the chain propagation [8].

3.3. Characterization of polyamide 6 microcapsules and their composites

3.3.1. Molecular weight by viscosimetry

Based on the procedure described in section 2.3.1 of Chapter 2, the average viscometric molecular weight, M_v, of the empty PAMC was found to be 33 100 g/mol, which was by 10–15 % lower than the values of commercial hydrolytic PA6 brands, whose M_v was measured at the same conditions.

The M_v values of the loaded PAMC were not determined since the presence of reaction products between sulfuric acid and metals or CNT could obstruct the capillary of the viscometer. However, it can be expected that these values should be very similar to that of the empty PAMC since the load particles do not seem to affect the AAROP mechanism and the monomer conversion (See Table 3.1).

3.3.2. Morphological studies by SEM

The morphology of the prepared M- and that of the corresponding P-samples loaded with 5 wt.% of CNT and 10 wt.% of metal particles was analyzed by scanning electron microscopy (SEM), comparing to the empty PAMC. The selected SEM micrographs are displayed in Figures 3.1 – 3.4.

From Fig. 3.1a it can be seen that the empty PAMC are present in the form of aggregates of several, partially fused PA6 spheroids with typical diameters of 5–10 μm that form final particles with an average diameter of 20–30 μm. Larger magnification (Fig. 3.1b-c) shows that the empty PAMC is porous, with scaffold-like morphology, the observable pores sizes being typically in the 250–500 nm range. Each microcapsule seems to be formed by coalescence of several PA6 spheroids. These results agree with the coalescence-crystallization-precipitation mechanism of AAROP in solution for the formation either empty or loaded PAMC [1].

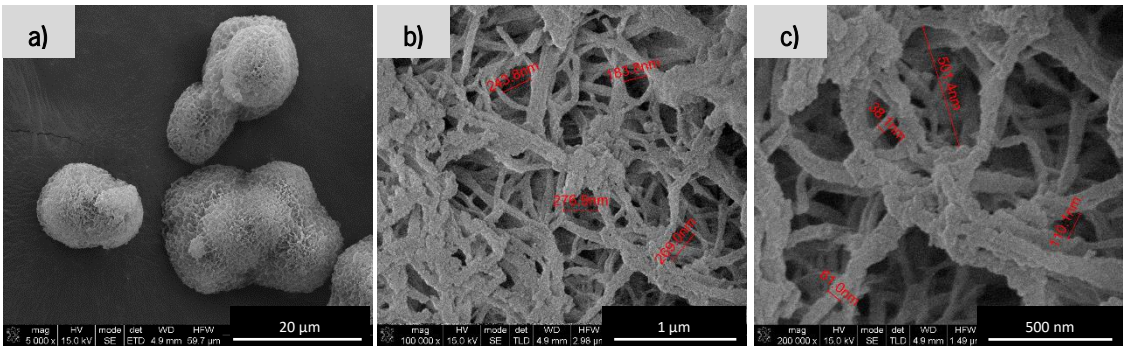

Figure 3.1 | Selected SEM micrographs of neat PAMC.

The SEM micrographs in Fig. 3.2. present information about the dispersion of CNT in the PA6 microparticles or in the composites obtained thereof.

The pure CNT filler (Fig. 3.2a) comprises 10 – 20 nm thick fibrils, with a tangled shape and a considerable length. Compared with the neat PA6, the topography of CNT-loaded PAMC (Fig. 3.2 b, c) is rather similar. The average visible pore diameter remains less than 500 nm (Fig. 3.2 b, c), maintaining a porous and scaffold-like topography such as the empty PAMC.

The morphological changes of M-CNT5 after their compression molding into P-CNT5 are shown in Fig. 3.2d-e. Thus, even with an 8.0 wt.% load of CNT that have the tendency to tangle and agglomerate, they seem to be finely dispersed within the PA6 matrix, their visible cross-sections being in the nanometer range. These observations confirm the utility of the transformation of loaded PAMC into composites, proving that this concept does not need chemical functionalization of the CNT to enhance its miscibility with the polymer matrix.

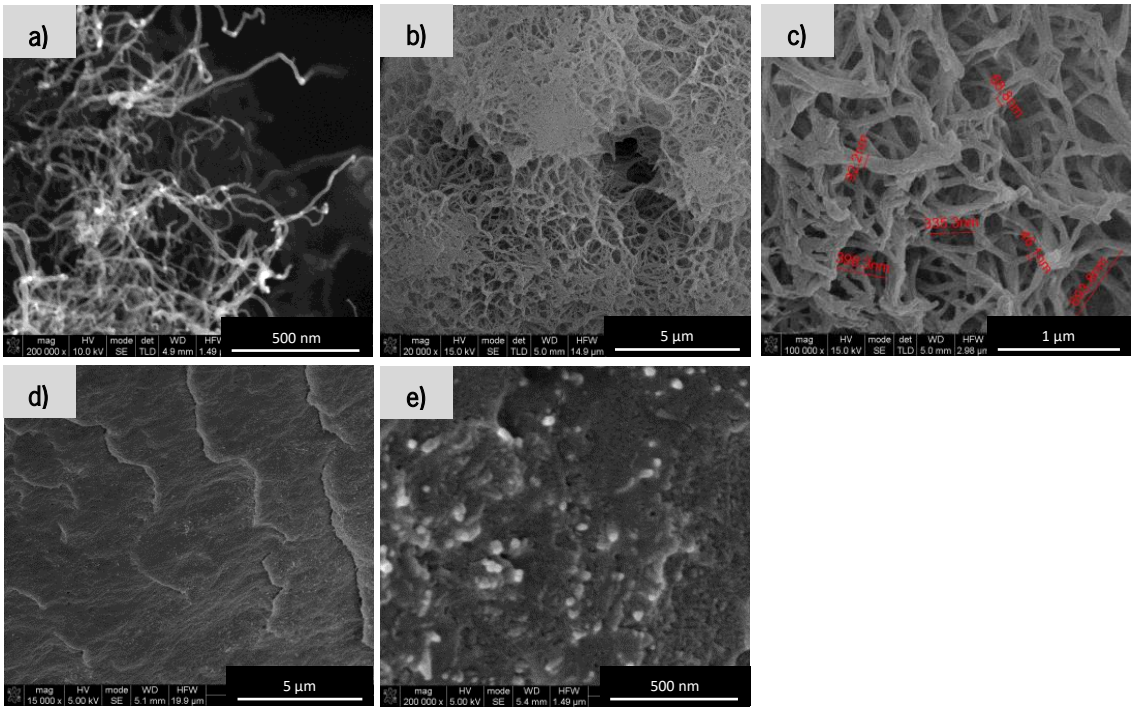

Figure 3.2| Selected SEM micrographs of neat CNT, CNT-loaded PAMC and respective molded composite: a) neat CNT; b) M-CNT5; c) close view of sample b); d) P-CNT5; e) close view of sample d) showing CNT.

The morphology of the metal loads in the M-samples loaded with metal particles is shown in Figure 3.3. SEM micrographs 3.3a-d visualize the neat metal particles of Al, Cu, Mg, and Fe loads. It

can be observed that the Al and Mg particles (Fig. 3.3a and Fig. 3.3c, respectively) are shaped as platelets with maximum sizes of 80–100 μm and thicknesses of 10–15 μm. Cu particles (Fig. 3.3b) display complex dendritic shapes with sizes in the 20–40 μm range, and the Fe particles (Fig. 3.3d) are strictly sphere-shaped with diameters between 1–5 μm.

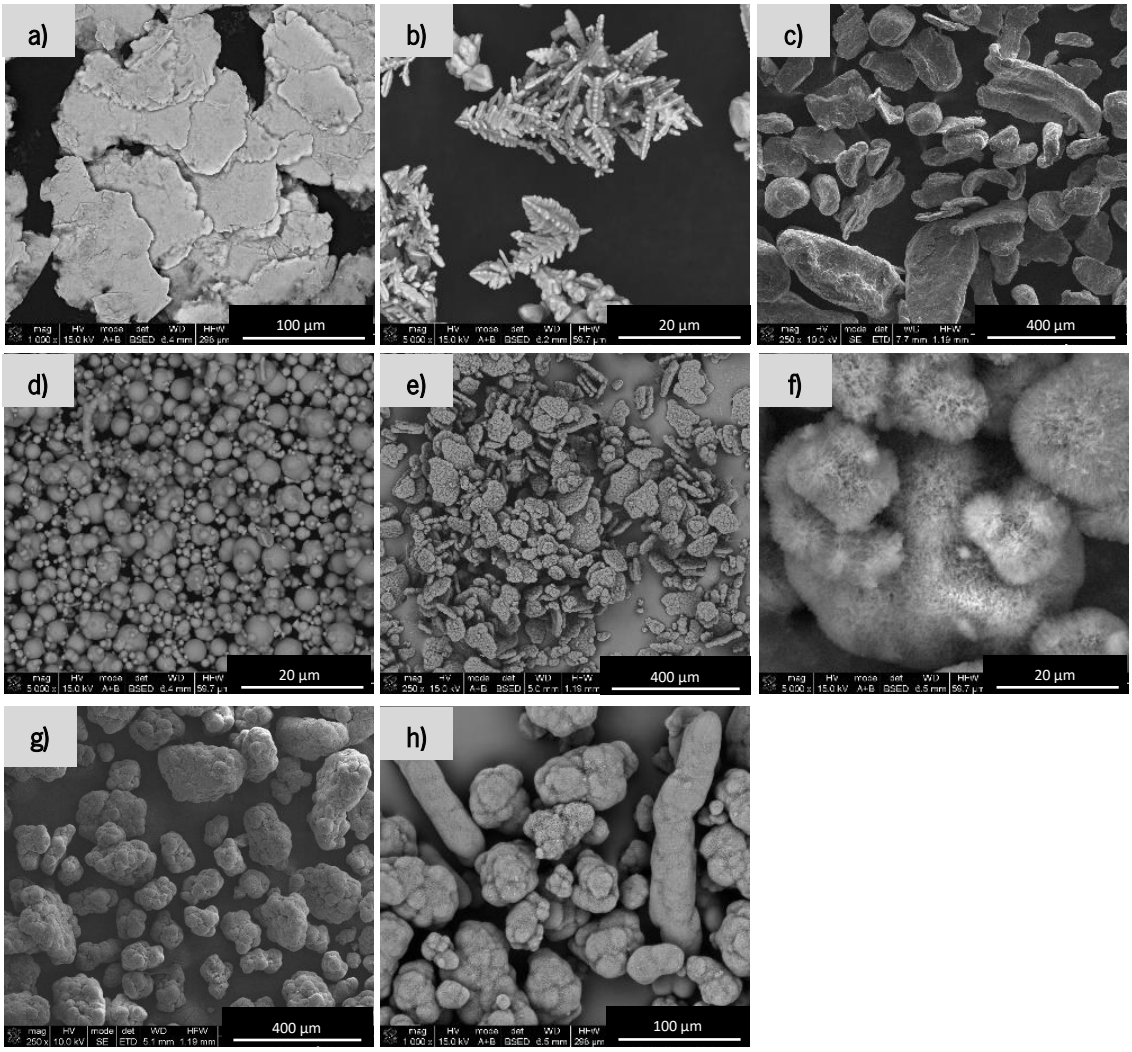

Figure 3.3 | Selected SEM micrographs of neat metal particles and metal-loaded PAMC: a) Al; b) Cu; c) Mg; d) Fe; e) M-Al10; f) M-Cu10; g) M-Mg10; h) M-Fe10.

As seen from Fig. 3.3, images e-h, the metal-loaded PAMC also show porosity. The Cu (Fig. 3.3f) and Fe (Fig. 3.3h) loaded PAMC represent aggregates of several, partially fused spheroids with typical diameters ≥10 μm. In the case of the M-Al10 sample (Fig. 3.3 e), most of the PAMC represent Al metal platelets coated by PA6, whereas M-Mg10 sample (image 3g) displays large irregular particles with a broad size distribution between 50–300 μm. In the case of M-Fe10, the formation of cylindrical

structures is observed, ascribed to auto-assembly of magnetized Fe spheres (the reaction media is stirred magnetically), covered by the in-situ forming PA6 [1]. Therefore, the size and shape of the PAMC are determined to a great extent by the morphology of the neat metal particles and their magnetic properties.

After compression molding of the metal-loaded PAMC into PA6 composites, morphological features can be observed in Figure 3.4. As seen in Fig. 3.4a-c, even at the high load of about 10 wt.%, the metal payloads are homogeneously dispersed within the PA6 matrix, without the need of functionalization or other additional treatment. Images d-f of the same figure show that, as expected, the morphology of the metal fillers (Fig. 3.4 d-f) is maintained in the molded composites.

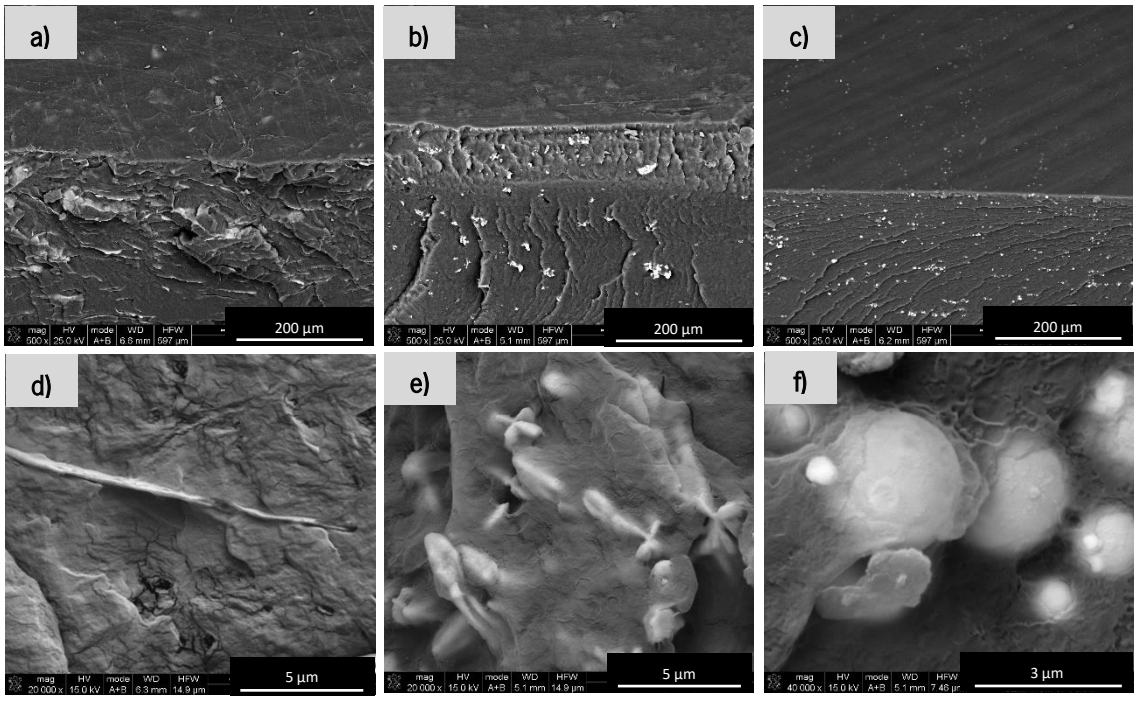

Figure 3.4 | Selected SEM micrographs of composites obtained from metal-loaded PAMC: a) P-Al10; b) P-Cu10; c) P-Fe10; d) magnification of a) showing Al particles; e) magnification of b) showing Cu particles; f) magnification of c) showing Fe particles.

3.4. Thermal properties of microcapsules and composites

3.4.1. By DSC

The results from the differential scanning calorimetry (DSC) measurements with 5 wt.% of CNT and 10 wt.% of metal loaded PAMC and of the respective molded composites are presented in Table

3.2. Figure 3.5 displays the respective DSC traces of the first heating scan (a), of the cooling (b) and during the second heating scan (c) for all samples.

Table 3.2 | DSC data comparison between M-samples and the respective compression-molded composites (P-samples)

Sample		First heating scan			Recrystallization [a]		Second heating scan			
		T_m, °C	ΔH, J/g	X_c, % [b]	T_c, °C	$-\Delta H$, J/g	T_g, °C	T_m, °C	ΔH, J/g	X_c, % [b]
M-	PA6	207.3	74.9	39.4	158.6	42.6	39.4	208.8	46.1	24.3
P-		209.8	72.3	38.1	162.1	54.9	47.5	211.1	56.5	29.7
M-	CNT5	209.0	82.0	46.9	177.4	60.1	45.6	212.0	60.2	34.4
P-		208.1	70.4	40.3	171.5	57.6	47.8	211.4	58.8	33.6
M-	Al10	206.6	84.6	52.2	161.0	40.9	39.8	209.8	41.7	25.7
P-		209.7	55.0	33.9	166.1	44.5	47.2	212.2	48.2	29.7
M-	Cu10	206.2	66.9	42.7	151.2	32.7	36.3	205.5	32.7	20.9
P-		209.8	42.2	27.0	156.4	49.9	44.6	210.8	49.4	31.6
M-	Fe10	206.8	74.2	45.1	157.7	39.2	35.4	206.2	40.3	24.5
P-		211.8	56.3	34.3	160.7	56.8	44.1	211.6	58.1	35.4
M-	Mg10	206.5	84.3	53.2	152.2	40.4	36.6	206.0	38.4	24.2
P-		208.8	49.5	31.2	164.0	44.8	46.7	210.8	49.5	31.2

[a] Determined after first DSC scan under fast cooling down;

[b] Determined according to Eq. 2.12 of Chapter 2.

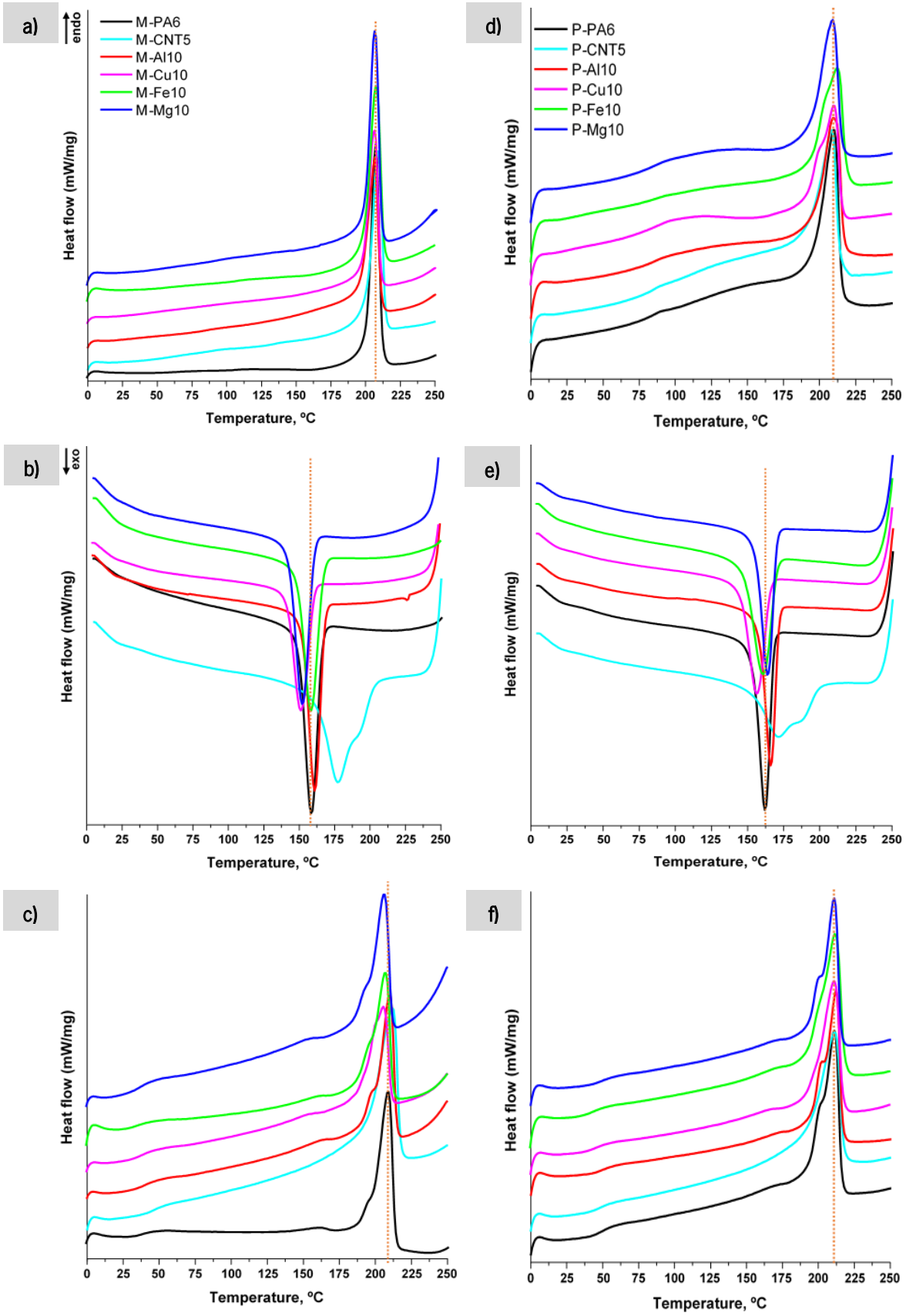

Figure 3.5 | DSC traces of CNT and metal-loaded PA6 systems: a, d) first heating scan; b, e) recrystallization from the melt; c, f) second heating scan. Left: M-samples; Right: P-samples produced from the respective M-samples by CM.

As seen from the results, all analyzed M-samples display a single melting peak (Fig. 3.5a) in the first heating scan typical of the predominant α-PA6 [9]. The CNT and metal-loaded PAMC show melting temperatures, T_m, in a narrow range between 206–209°C (Table 3.2), temperatures close to that of neat PA6 microparticles (207 °C). Apparently, the melting behavior in this scan is not affected significantly by the presence of the payloads. It should be noted, however, that the T_m of all M-samples is with 15–18°C lower than that of hydrolytic PA6 or anionic PA6 prepared by AAROP in bulk (~223 °C).

As regards the recrystallization in cooling mode of PAMC (Fig. 3.5b, Table 3.2), the melting behavior of the M-CNT5 sample is quite distinct. This is the only sample that displays a double exotherm in the 175–190 °C range, while the empty PAMC has a T_c = 157 °C. These findings can be explained by the strong nucleation effect of the CNT filler that enhances the crystallization at elevated temperature and the large interface between the nanosized CNT and the PA6 shell, enhanced by the high aspect ratio of the CNT [10, 11]. Co-existence of α- and γ-PA6 can be supposed in this case, too.

The metal-loaded PAMC display a single crystallization peak in the range of 151–161 °C. It is found that the M-Al10, and the empty PA6 PAMC follow a similar crystallization trend, their T_c being very close. In contrast, in the presence of Mg and Cu particles, T_c values are lower (Table 3.2), the difference reaching 7.5 °C for the M-Cu10 sample. These variances can be related to the different nature and morphology of the metal loads causing changes in the PA6 shell crystallization.

After the second heating scan of the M-samples (Fig. 3.5c), the temperature position of the main melting peak remains in the range of 206–210°C. However, all melting endotherms become broader, with a low-temperature shoulder, suggesting the presence of the γ-PA6 polymorph [9] with a lower melting point that co-exists with the predominant α-PA6. This behavior is evident in all metal-loaded PAMC.

The DSC traces of the P-samples are presented in Fig. 3.5 d-f. The first scan melting peaks become broader and with low-temperature shoulders, suggesting the coexistence of α- and γ-PA6 polymorphs [9, 12]. The first scan of the P-samples looks very much as the second scan of the respective M-samples, which was to be expected, since the composite P-samples were prepared by compression molding of the respective PAMC.

Comparisons of the X_c values of the M- and P-samples were made, the respective ΔH values being determined in the same temperature intervals (Table 3.2). With the M-samples, in the first heating scan, the presence of CNT leads to ~8 % difference as compared to the empty PAMC. With the

metal fillers, the inclusion of Al and Mg particles causes a higher X_c, the difference reaching 12 % and 14 % with Al and Mg particles, respectively. With the inclusion of Cu particles, a slight increase of the X_c in relation to the PA6 is observed. These findings indicate that the CNT, Al and Mg particles enhance the crystallization process, resulting in higher crystallinity index. It is also observed that the X_c of M-samples in the first heating scan is higher than that of the respective P-sample (Table 3.2). The difference depends on the filler and can reach 18–22 %, as in Al10 and Mg10 compositions. This difference decreases for all samples after the second scan. These results confirm the importance of the thermal history of PA6 when determining the X_c [9, 13]. The M-samples were synthesized and crystallized at isothermal conditions (~135 °C for 2 h) by AAROP, while the P-samples were obtained after melting of the respective PAMC at 230 °C and cooling down with ca. 20 °C/min to room temperature. For that reason, the difference between the X_c values of the first DSC scan of M- and P-samples is positive and can reach 20–22 %. Comparing these values after the second DSC scan, a lesser difference of 5–10 % is shown.

Another comparison based on the data in Table 3.2 can be made of about the glass transition temperatures, T_g, of loaded PAMC and their molded composites. In M-samples, the presence of CNT affects the segmental mobility of the PA6 chains since its T_g value is with 7 °C higher than that of the neat PA6. In the metal-loaded PAMC, marginal differences of less than 2–3 °C in the T_g values are observed (Table 3.2). However, after the CM process, all the P-samples show higher T_g values compared to the respective M-samples (Table 3.2), indicating that the segmental mobility of the amorphous PA6 chains in PAMC is much lower than in the molded composites. The differences can reach up to 10 °C and should be related to the pressure applied during the CM process, most probably leading to more compact and dense microstructures.

3.4.2. By TGA

M- and respective P-samples loaded with different amounts of CNT and 10 wt.% of metal particles were studied by TGA in order to establish the thermal stability of the samples as a function of the load type and amount and to determine the real amount of fillers. Table 3.3 summarizes the numerical data of the thermal degradation of all samples. Figures 3.6–3.7 display the TGA traces obtained. The determination of the real load content based on the carbonized residue at 600 °C according to Eq. 2.13 of Chapter 2 is shown in Table 3.3.

Table 3.3 | Numerical data from TGA analysis of metal and CNT loaded PAMC

Sample		T_{in} [a]	T_{max}, °C [b]		v_{max}, %/°C [c]		Residue at 600 °C, %	Real load, wt.%
			I	II	I	II		
M-	PA6	302.5	339.3	-	2.3	-	1.4	-
P-		312.9	354.0	-	3.7	-	1.1	-
M-	CNT3	274.2	321.7	-	1.8	-	6.3	4.9
P-		318.0	364.3	379.9	1.5	1.4	6.2	5.1
M-	CNT5	286.5	345.4	-	1.4	-	9.5	8.2
P-		324.0	368.6	401.3	0.9	0.9	9.4	8.3
M-	CNT7	292.7	348.0	-	1.3	-	13.5	12.1
P-		335.1	375.1	427.6	0.9	0.7	13.3	12.2
M-	Al10	330.9	358.5	-	1.7	-	20.8	19.4
P-		331.5	357.5	-	2.2	-	20.6	19.5
M-	Cu10	300.7	335.9	-	1.8	-	19.0	17.6
P-		301.2	321.5	344.5	1.6	1.7	18.8	17.7
M-	Fe10	300.2	334.3	-	1.9	-	14.8	13.4
P-		300.6	319.4	-	2.0	-	14.7	13.6
M-	Mg10	319.3	347.1	-	1.6	-	14.3	13.0
P-		310.8	345.6	-	2.3	-	13.7	12.7

[a] T_{in} = Temperature of initial degradation obtained from integral TGA curves;

[b] T_{max} = Maximum degradation temperature obtained from the 1st derivative of the TGA curves;

[c] Maximum degradation rate at T_{max} obtained from the first derivative of the TGA curves.

Table 3.3 and Fig. 3.6-3.7, images a-b, display data about the thermal stability of the loaded PAMC. In the empty PAMC, the temperature of initial degradation is T_{in} = 302.5 °C and the maximum degradation temperature is reached at T_{max} = 339.3 °C. With the incorporation of different amounts of CNT, the thermal degradation becomes more pronounced, whereby T_{in} is between T_{in} = 274.2 °C (M-CNT3) and T_{in} = 292.7 °C (M-CNT7). Although the CNT-loaded samples start to degrade earlier with respect to the M-PA6 sample, Table 3.3 shows that in the presence of CNT the degradation rate (v_{max}, %/°C) is slower. Moreover, the maximum degradation rate is reached at T_{max} = 354.0 °C in M-CNT5 and at T_{max} = 348.0 °C in M-CNT7, i.e., 9–14 °C higher than the empty PAMC.

In the respective P-samples (Fig. 3.6 c-d), the melting temperature is between T_{in} = 318.0 °C (P-CNT3) and T_{in} = 335.1 °C (P-CNT7), values that are higher than the neat PA6 (T_{in} = 312.9 °C). The thermal stability increases with increasing of the amount of CNT, as observed in the M-samples,

confirming that the CM process does not affect negatively the thermal stability of the molded plates. This effect agrees with the degradation rates determined from the first derivative curves (Table 3.3, Fig. 3.6d) since they decrease with increasing the amount of CNT. Further, in the presence of CNT two degradation steps are observed (Fig. 3.6d), being more pronounced in P-CNT5 and P-CNT7 samples. These findings suggest that the CNT load causes an efficient dissipation of the heat that can be related with the good dispersion of the carbon allotrope (see the SEM image in Fig. 3.2), with the high aspect ratio of the CNT and their good thermal stability. Increasing the real amount of CNT up to 12 wt.% improves the thermal stability of the CNT-loaded samples.

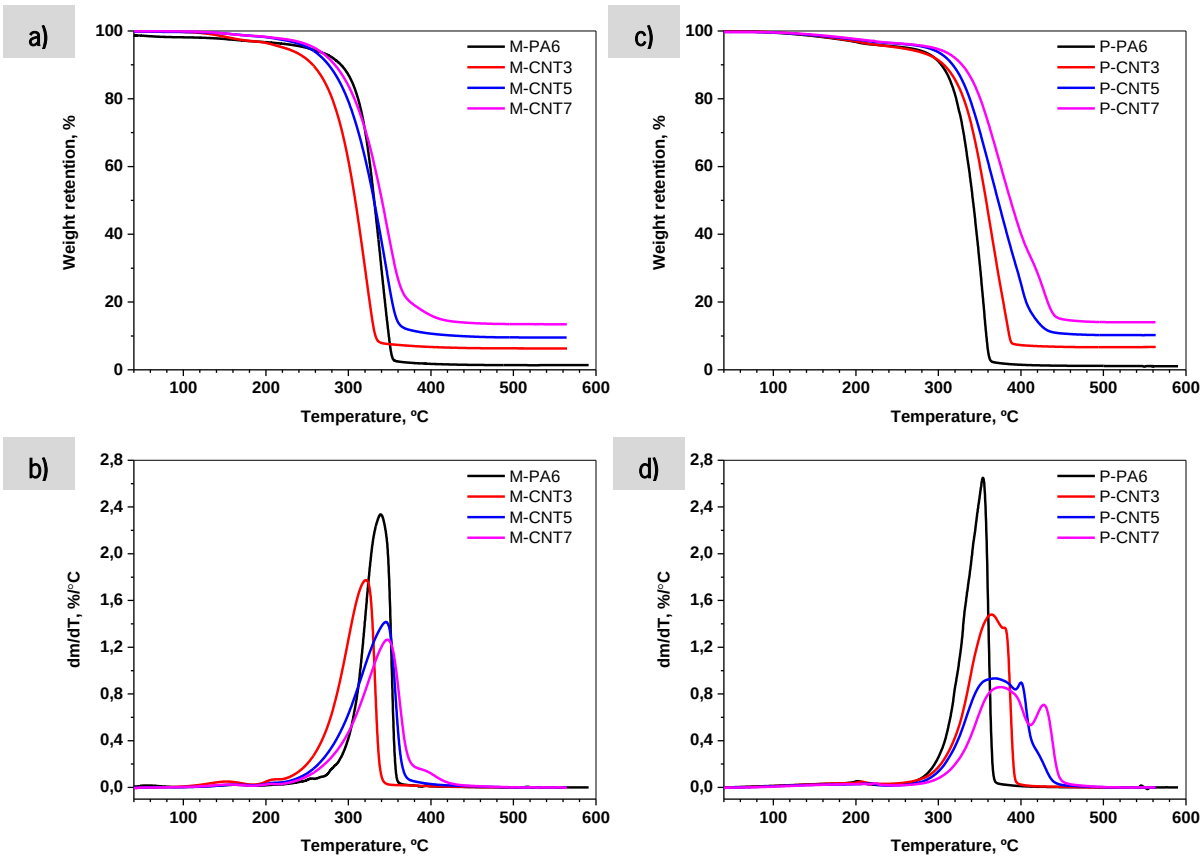

Figure 3.6 | TGA curves of CNT-loaded PA6 systems in N_2 atmosphere: **a**, **b)** M-samples; **c**, **d)** P-samples produced from the respective M-samples by CM. Top: Integral curves; bottom: first derivative curves.

The TGA curves and the results extracted from them obtained with the metal-containing M-samples and the respective molded plates containing real loads of 13–19 wt.% are shown in Table 3.3 and Fig. 3.7.

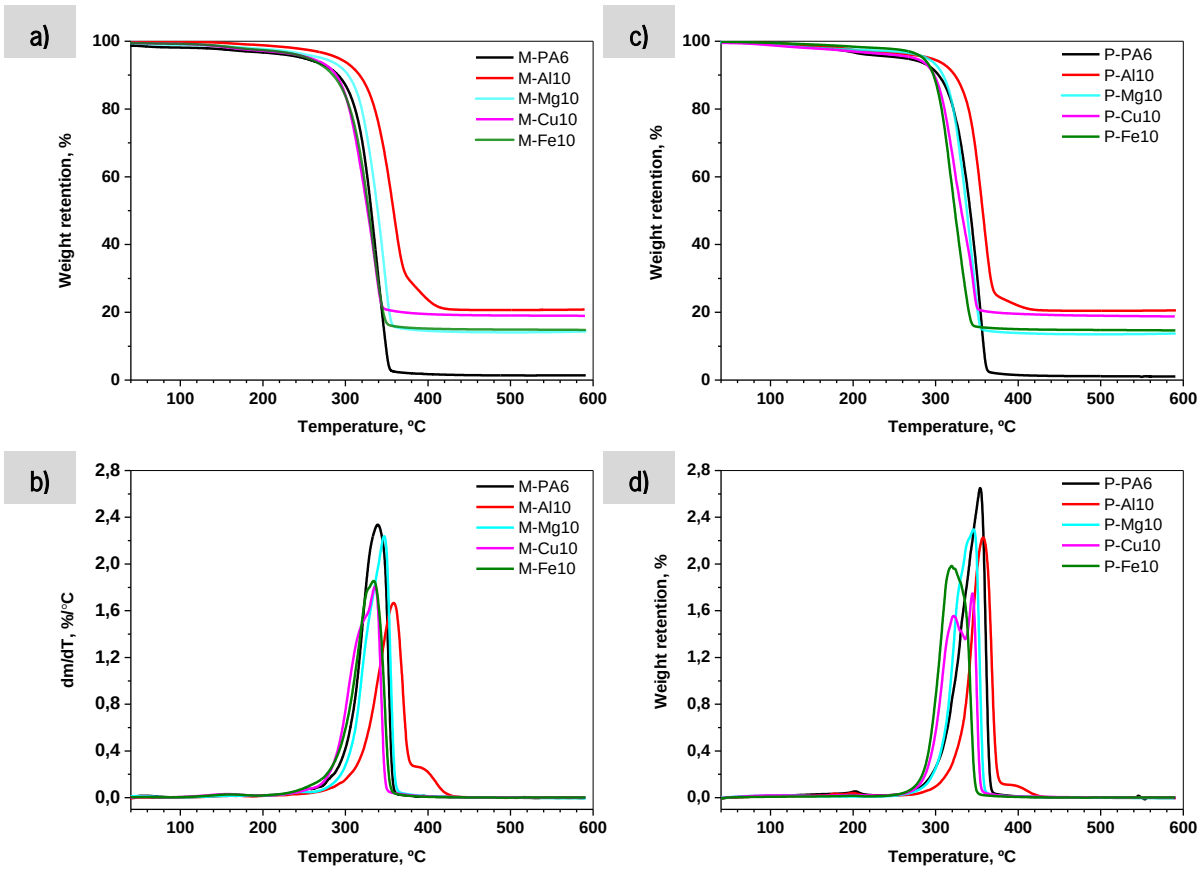

Figure 3.7 | TGA curves of metal-loaded PA6 systems in N_2 atmosphere: **a**, **b)** M-samples; **c**, **d)** P-samples produced from the respective M-samples by CM. Top: Integral curves; bottom: first derivative curves.

Judging from the T_{in} and $T_{\max}$ in Table 3.3, stability improvement is observed in the systems comprising the large and less dense Al and Mg particles, whose temperature of initial degradation is T_{in} = 330.9 °C (M-Al10) and T_{in} = 319.3 °C (M-Mg10) and the maximum degradation rate is reached at $T_{\max}$ = 358.5 °C (M-Al10) and $T_{\max}$ = 347.1 °C (M-Mg10). At the same time, in the Cu- and Fe-containing PAMC the thermal degradation is similar to that of the neat PAMC (Table 3.3). However, after the transformation of the M-Cu10 into molded plates, two degradation steps are observed in the P-Cu10 sample (Table 3.3, Fig. 3.6d). This observation can be due to the dendritic shape of Cu particles (Fig. 3.3b) which apparently dissipate better the heat as compared to the spherical Fe particles (Fig. 3.3d). The better thermal stability of Al and Mg-loaded samples can be explained with the dense packing of these metal particles within the PA6 matrix, that touch to one another as visualized in the SEM micrographs in Fig. 3.3. This most probably leads to an easier dissipation of the heat during the

TGA experiment and, consequently, to higher degradation temperatures. On the contrary, loading the PA6 matrix with lower volume fractions of the smaller Cu and Fe particles that remain separated by large PA6 islands seems to increase the degradation due to local overheating and bad heat transport.

3.5. Mechanical properties in tension

Representative stress-strain curves of the composites produced from PAMC loaded with CNT and metal fillers compared with that of the neat PA6 from empty PAMC are presented in Figure 3.8. Table 3.4 shows the data of the Young' modulus, E, maximum stress, $\sigma_{\max}$, stress at break, σ_{br}, and deformation at break, ε_{br}, extracted from the stress-strain curves of all samples, as well as the improvement factors (IF) for the E and σ_{br} values.

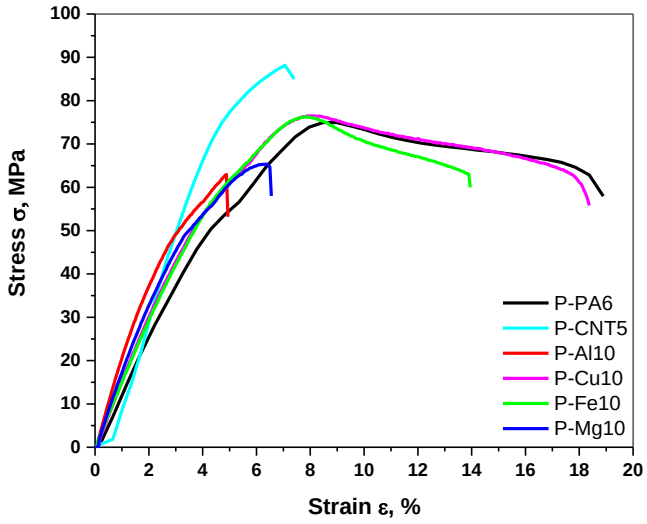

Figure 3.8| Representative stress-strain curves of P-samples molded from CNT and metal-loaded PAMC.

All composites display higher E values (Table 3.4). The IF calculated is always positive and increases up to 84 % for CNT loaded composite and 17–57 % for samples with metal fillers. The stress-strain curves of plates produced from empty PAMC and from Cu- and Fe-loaded PAMC (Fig. 3.8, samples P-PA6, P-Cu10, P-Fe10) display clear Hookean elasticity regions followed by a ductile behavior with well-expressed yield point at $\sigma_{\max}$ = 70–75 MPa and ε = 8–9 % strain, the ε_{br} reaching 17–20 %. The Young´s moduli calculated for the two metal-containing samples of 1.47 GPa are slightly higher than that of the neat PA6 (1.25 GPa) (Table 3.4). Further, these three samples display curves with a

plateau typical of cold flow with neck formation in the test samples. At the same time, no cold flow is observed in the hybrid plates denoted as P-CNT5, P-Al10, and P-Mg10. They show Hookean elasticity and a brittle fracture with ε_{br} values of 4–7 %, about three times less than the ε_{br} of the pure matrix, and $\sigma_{br} = \sigma_{\max}$ of 87 MPa in P-CNT 5 sample and 58–66 MPa in the presence of Al and Mg particles.

Table 3.4 | Mechanical properties of P-samples molded from CNT and metal-loaded PAMC

Sample	Young's modulus, E (GPa)	IF (%) [a]	Tensile strength, $\sigma_{\max}$ (MPa)	IF (%) [a]	Stress at break, σ_{br} (MPa)	IF (%) [a]	Deformation at break, ε_{br} (%)
P-PA6	1.25 ± 0.07	-	75.84 ± 0.75	-	63.68 ± 4.95	-	20.46 ± 4.60
P-CNT5	2.31 ± 0.10	84.4	87.20 ± 4.90	15.0	87.20 ± 4.90	36.9	6.19 ± 1.29
P-Al10	1.96 ± 0.08	56.9	58.27 ± 3.91	-23.1	58.27 ± 3.91	-8.5	4.73 ± 0.38
P-Cu10	1.47 ± 0.01	17.8	72.47 ± 0.79	-4.4	55.09 ± 2.19	-13.5	19.70 ± 1.96
P-Fe10	1.47 ± 0.03	17.2	75.75 ± 0.70	0.0	65.40 ± 1.58	2.7	13.89 ± 1.18
P-Mg10	1.78 ± 0.03	42.1	66.08 ± 1.53	-12.8	66.08 ± 1.53	3.8	6.27 ± 0.34

[a] In respect to neat anionic PA6 plate obtained from empty PAMC, calculated according to Eq. 2.14 of Chapter 2.

The improvements in the E and σ values of the P-CNT5 sample in respect to the P-PA6 reference can be associated with the high aspect ratio of the nanotubes and their good dispersion within the PA6 matrix due to the use of the M-CNT5 precursor. In metal-loaded P-samples, the results can be related with the sizes of the metal particles used: it is observed that high *E*-values are caused by the larger and most densely packed Al and Mg particles, whereas the smaller Cu and especially Fe particles do not change the stress-strain profile and increase only slightly the Young´s modulus. The lower density of the Al and Mg particles determines a higher volume fraction of these fillers in the respective composites, leading to brittle behavior in tension. On the opposite, the neck formation during the tensile tests of the Cu- and Fe-loaded samples results in tensile strength values similar to that of the neat matrix (Table 3.4), since these two metals are quite dense and their volume fraction in the composite is less.

3.6. Electrical conductivity and dielectric properties

The d.c. electrical conductivity, σ_{dc}, dielectric constant, ε', and the loss factor, $\tan\delta$, were determined for all composites produced from respective CNT and metal-loaded PAMC, and the data obtained are summarized in Table 3.6. Figure 3.9 displays the semi-logarithmic plots of the ε' and $\tan\delta$ as a function of frequency for such P-samples.

Table 3.5 | Electrical properties of P-samples prepared from CNT and metal-loaded PAMC

Sample	Conductivity, σ_{dc} (S/m)	Dielectric constant [a], ε'	Loss factor [a], $\tan\delta$
P-PA6	5.22E-10 ± 1.40E-11	6.64 ± 0.20	0.05 ± 0.00
P-CNT5	1.26E-01 ± 1.11E-02	393.00 ± 9.80	119.00 ± 0.37
P-Al10	3.50E-09 ± 1.70E-10	22.90 ± 2.55	1.09 ± 0.13
P-Cu10	1.56E-09 ± 1.76E-10	24.00 ± 1.41	1.08 ± 0.10
P-Fe10	2.52E-09 ± 3.82E-10	24.50 ± 0.35	1.27 ± 0.08
P-Mg10	4.78E-09 ± 3.78E-10	23.60 ± 1.48	1.29 ± 0.08

[a] Values obtained at 1 MHz.

As expected, neat PA6 is an insulator with σ_{dc} values of above 10^{-10} S/m. The well-dispersed CNT nanofiller (Fig. 3.2d, e) with 5 wt.% result in a notable growth of σ_{dc} with 9 decades reaching values characteristic of semiconductor materials. Relating these results to the morphology of CNT (Fig. 3.2), it can be inferred that the nanometric size of this C-allotrope and their homogeneous distribution within the PA6 matrix are important factors enhancing the electrical conductivity. Further, the aspect ratio of the CNT seems also to contribute to the increase of σ_{dc}, building a conductive network with effective charge transfer. As regards the ε' and $\tan\delta$ values (Fig. 3.9, Table 3.6), it is observed a combination of high conductivity and high permittivity compared to neat PA6. However, the presence of CNT induces a loss factor $\tan\delta$ being 100 times higher. The higher dielectric losses of the P-CNT5 sample can be attributed to the conductive network produced in this sample. The charge carriers lead to the leakage current increase through the conductive network in the composite – a property that is not desired in an HK material [14]. However, these results indicate that adjustments can be made on the electrical properties depending on the intended application: a composite with high dielectric absorption, and, simultaneously, high dielectric losses can be obtained.

About the effect of metal fillers within the PA6 matrix, the data in Table 3.6 reveal that such systems maintain the electrical insulating properties of the neat PA6 matrix showing σ_{dc} values in the range of 10^{-9} S/m, as determined by Brêda et. al [2]. The reason is that the filler particles are always completely enclosed by the non-conductive matrix polymer, which impedes the free movement of charges. As seen from the SEM studies in Fig. 3.4d-f, complete enclosure of the metal particles in the PA6 matrix material is observed in the PA6-metal hybrids.

Analyzing the dielectric properties (Table 3.6, Fig. 3.9), improvements on the dielectric properties are observed in P-samples loaded with metal fillers comparing to the P-PA6 reference sample.

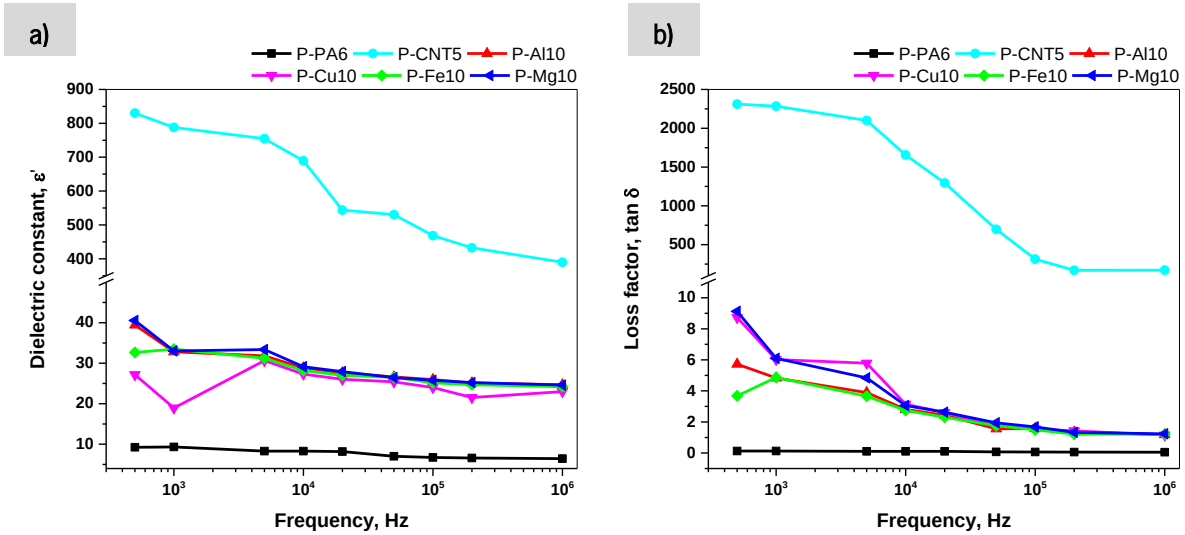

Figure 3.9| Dielectric constant **(a)** and dielectric loss **(b)** as a function of frequency for P-samples prepared from CNT and metal-loaded PAMC.

At lower frequencies, the PA6-metal hybrids produce higher ε' values but, as expected, the ε' decreases with increasing frequency, since the dipoles in the polymer matrix cannot reorient fast enough and therefore, the ε' decreases [15]. This effect is noticed in Fig. 3.9a in which an important contribution to the increase of the ε' is also related to increasing energy dissipation (and not just to increase in energy storage ability) as shown by the dielectric losses (Fig. 3.9b). Thus, the composites with the highest ε' are also the ones with the higher dielectric loss. Further, the hybrids containing 13–19 wt.% metal display $\tan\delta$ values within the entire frequency range varying from 9 to 1. These low $\tan\delta$ values associated with the enhanced ε' compared to the neat matrix suggest the ability of the PA6-metal hybrids to store electric energy.

3.7. Summary

A series of CNT and metal-containing PA6 composites were prepared by a two-stage method including (i) microencapsulation strategy for the synthesis of particulate PA6 hybrid precursors, and (ii) transformation of the latter into PA6 composites by compression molding. It was observed that the presence of CNT and metal particles improves the thermal, and mechanical properties of the composite materials produced. The best electric conductivity values of 1.26E-01 S/m were obtained with 5 wt.% of CNT, showing d.c. conductivity 9 decades higher than the neat PA6. In the presence of metal loads the insulating properties of the hybrids are maintained, whereby percolation between the metal particles was not achieved within the concentration range studied.

3.8. References

[1] Dencheva N, Denchev Z, Lanceros-Méndez S, Ezquerra Sanz T (2016) One-step in situ synthesis of polyamide microcapsules with inorganic payload and their transformation into responsive thermoplastic composite materials. *Macromol Mater Eng*, 301:119–124. DOI: 10.1002/mame.201500194

[2] Brêda C, Dencheva N, Lanceros-Mendez S, Denchev Z (2016) Preparation and properties of metal-containing polyamide hybrid composites via reactive microencapsulation. *J Mater Sci*, 51:10534–10554. DOI: 10.1007/s10853-016-0274-0

[3] Dan F, Vasiliu-Oprea C (1998) Anionic polimerization of caprolactama in organic media. Morphological aspects. *Colloid Polym Sci*, 276:483–495. DOI: 10.1007/s003960050270

[4] Vasiliu-Oprea C, Dan F (1996) On the relation between synthesis parameters and morphology of anionic polycaproamide obtained in organic media. I. Influence of the $Na[O(CH_2)_2OCH_3]_2AlH_2$/isophorone diisocyanate catalytic system. *J Appl Polym Sci*, 62:1517–1527. DOI: 10.1002/(SICI)1097-4628(19961205)62:10<1517::AID-APP4>3.0.CO;2-R

[5] Ricco L, Monticelli O, Russo S, Paglianti A, Mariani A (2002) Fast-activated anionic polymerization of ε-caprolactam in suspension, 1. Role of the continuous phase on characteristics and properties of powdered PA6. *Macromol Chem Phys*, 203:1436–1444. DOI: 10.1002/1521-3935(200207)203:10/11<1436::AID-MACP1436>3.0.CO;2-V

[6] Ricco L, Russo S, Orefice G, Riva F (1999) Anionic Poly(ε-caprolactam): Relationships among Conditions of Synthesis, Chain Regularity, Reticular Order, and Polymorphism. *Macromolecules*, 32:7726–7731. DOI: 10.1021/ma9909004

[7] van Rijswijk K, Bersee HEN, Jager WF, Picken SJ (2006) Optimisation of anionic polyamide-6 for

vacuum infusion of thermoplastic composites: choice of activator and initiator. *Compos Part A Appl Sci Manuf*, 37:949–956. DOI: 10.1016/j.compositesa.2005.01.023

[8] Vasiliu-Oprea C, Dan F (1997) On the relation between synthesis parameters and morphology of anionic polycaproamide obtained in organic media. II. Influence of the $Na[O(CH_2)_2OCH_3]_2AlH_2$/aliphatic diisocyanates catalytic systems. *J Appl Polym Sci*, 64:2575–2583. DOI: 10.1002/(SICI)1097-4628(19970627)64:13<2575::AID-APP11>3.0.CO;2-Z

[9] Fornes TD, Paul DR (2003) Crystallization behavior of nylon 6 nanocomposites. *Polymer (Guildf)*, 44:3945–3961. DOI: 10.1016/S0032-3861(03)00344-6

[10] Phang IY, Ma J, Shen L, Liu T, Zhang W-D (2006) Crystallization and melting behavior of multi-walled carbon nanotube-reinforced nylon-6 composites. *Polym Int*, 55:71–79. DOI: 10.1002/pi.1920

[11] Brosse A-C, Tencé-Girault S, Piccione PM, Leibler L (2008) Effect of multi-walled carbon nanotubes on the lamellae morphology of polyamide-6. *Polymer (Guildf)*, 49:4680–4686. DOI: 10.1016/j.polymer.2008.08.003

[12] Li Y, Goddard WA (2002) Nylon 6 Crystal Structures, Folds, and Lamellae from Theory. *Macromolecules*, 35:8440–8455. DOI: 10.1021/ma020815n

[13] Pesetskii SS, Jurkowski B, Olkhov YA, Bogdanovich SP, Koval VN (2005) Influence of a cooling rate on a structure of PA6. *Eur Polym J*, 41:1380–1390. DOI: 10.1016/j.eurpolymj.2004.12.009

[14] Yang C, Lin Y, Nan CW (2009) Modified carbon nanotube composites with high dielectric constant, low dielectric loss and large energy density. *Carbon N Y*, 47:1096–1101. DOI: 10.1016/j.carbon.2008.12.037

[15] Chung DDL (2003) Composite materials for dielectric applications. In: Composite Materials: Functional Materials for Modern Technologies. Springer London, London, pp 125–166

CHAPTER 4

Crystalline structure and molecular dynamics of metal-containing polyamide 6 microcapsules by solid-state NMR

4.1. Introduction

Polyamide 6 (PA6) is a well-known semi-crystalline polymer used as an engineering material in a wide variety of applications. The first comprehensive structural studies by high-resolution solid-state nuclear magnetic resonance (ssNMR) on neat PA6 appeared in the late 1980s´ using Carbon-13 (^{13}C) [1–3] or Nitrogen-15 (^{15}N) [4, 5] nuclei. Since then, various ssNMR studies have been communicated on the structure of PA6 or some composites thereof, mostly comprising nanosized clays [6–14]. At the same time, no scientific communications focusing on the ssNMR characterization of PA6 composites loaded with metal fillers were found. Some scarce studies reporting on the structural characterization of polystyrene-titanate nanocomposites [15] and high-density polyethylene-based systems containing multi-wall carbon nanotubes (MWCNT) or Ag nanoparticles [16] are only available at this point. Therefore, the motivation of the studies in this chapter was to investigate by high-resolution ssNMR the influence of some metal particles (i.e., Al, Cu, Mg) on the crystalline structure and molecular dynamics of the PA6 matrix, in which the said metal fillers were dispersed by means of reactive microencapsulation by activated anionic ring-opening polymerization (AAROP) of ε-caprolactam (ECL). The intention was to further use these data in the explanation of the radar absorbing and electromagnetic interference shielding properties of the metal-containing PA6-based composites.

In the present study, metals with different magnetic properties were used as loading particles (Al, Mg, and Cu). Copper is diamagnetic (the electronic configuration in the gas phase is $1s^2 2s^2 2p^6 3s^2 3p^6 3d^{10} 4s^1$); the effective magnetic field within Cu particles is reduced because the created magnetic moments oppose H (Cu has a small negative magnetic susceptibility χ of -1.0×10^{-5} [17], where $\chi = M/H$, with M the magnetic moment per unit volume and H the applied magnetic field in ssNMR spectrum acquisitions). On the contrary, the effective magnetic fields within Al and Mg particles reinforce H because the polarization occurs in the H direction (Al and Mg have small magnetic dipole moments that partly line up with H because they have small positive χ: 2.2×10^{-5} and 1.2×10^{-5}, respectively [17]). Therefore, Al and Mg are both paramagnetic (the electronic configurations referring to the gas phase are $1s^2 2s^2 2p^6 3s^2 3p^1$ and $1s^2 2s^2 2p^6 3s^2$, respectively). Paramagnetism arises not only from unpaired electrons (Curie paramagnetism) but also from conduction electrons (hence, the interaction between the electron spins and the magnetic field H is known as Pauli paramagnetism) [18].

It is well known that the NMR spectra of paramagnetic materials in solution usually have signals that are not only shifted over a large frequency range but are also often broadened. This is the case, for example, when paramagnetic relaxation enhancement is used to study chelated paramagnetic metals by liquid-state NMR [19]. In the present study, because the metals are not chemically bonded to PA6, it can be anticipated

a small effect of the magnetic field created within the metal particles. Therefore, the influence on ^{13}C ssNMR resonances, if any, is expected to be restricted to the atoms close to filler particles: signal broadening, magnetic field shifts, and relaxation enhancement may be detected.

The response of the semi-crystalline PA6 matrix was recorded by means of conventional ^{13}C magic angle spinning (MAS) or ^{13}C cross-polarization (CP)/MAS pulse sequences. In the first case, the spectra were obtained under the conditions of Bloch decay with a short time between two consecutive scans (Experiment (i) described in section 2.3.4.1 of Chapter 2). This procedure shows only the signals of the amorphous PA6 fraction since the spin system of the crystalline domains does not have sufficient time for relaxation and normally are not revealed [7]. Alternatively, the spectra recorded by a combination of ^{13}C CP/MAS allowing sufficiently long times between two consecutive scans (i.e., Experiment (ii) described in section 2.3.4.1 of Chapter 2), reveal the resonance lines of the carbons from both crystalline and amorphous domains. By deconvolution of the spectral data obtained in MAS and CP/MAS experiments the NMR degree of crystallinity in all metal-loaded PA6 microcapsules (Me-PAMC) was calculated as a function of the metal type.

The ssNMR method enables also probing the molecular mobility in different frequency ranges, which are expected to occur in amorphous and crystalline PA6 regions. Motions in the kHz and MHz frequency scales influence, respectively, i) the spin-lattice relaxation time in the rotating frame, $T_{1\rho}$, characterized by slower motions; and ii) the spin-lattice relaxation time, T_1, sensitive to rapid molecular motions [20, 21]. Therefore, molecular dynamics studies in the PAMC with mono metal loads were also performed and reported in this chapter. It must be pointed out here that hydrogen relaxation times depend also on spin H-H diffusion, an energy conservative process that may mask mobility data [22]. This process is particularly relevant for hydrogen nuclei, due to both high isotopic natural abundance (NA about 100 %) and gyromagnetic ratio (γ =42.58 MHz/Tesla), and must be taken into account when long relaxation times are under measurement. Hence, relaxation data were obtained from carbon nuclei (NA about 1 % and γ=10.71 MHz/Tesla).

4.2. Sample preparation

The Me-PAMC were synthesized by the microencapsulation process based on AAROP of ECL described in Chapter 2, section, 2.3.2. The loaded PAMC containing 10 wt.% metal (Al, Cu, and Mg, the percentage in respect to the ECL) formed as a fine powder with metallic luster typical of the respective metal load. The yields of empty PAMC were 56 % and 45–49 % for the metal-loaded PAMC (Table 4.1). Table 4.1. presents all samples of this study with their designations, yields, and information about the real

metal content. For all samples, the real load was determined by thermogravimetric analysis (TGA) according to Eq. 2.13 of Chapter 2.

The pulverulent Me-PAMC samples were directly used in the ssNMR studies performed. Preliminary spectral observations on dually loaded PA6 samples were also performed. However, because the conductivity of these samples is high (see Table 5.5 in Chapter 5), either the signal to noise ratio was low or, in the limit, even no resonances were observed. Indeed, hardware problems (like probe head tuning and arcing) and poor MAS rate (due to Foucault currents) did not allow any correct spectrum acquisition.

Table 4.1 | PAMC: sample designations, composition and polymerization yield

Sample	Load, wt.% [a]	Composition, vol. % [b]		PAMC yield, % [c]	Real load, wt.% [d]
		Load	PA6		
M-PA6	0	0	100	56.2	0
M-Al10	10	9.15	90.8	45.1	19.4
M-Cu10	10	2.62	97.4	48.6	17.6
M-Mg10	10	8.82	91.2	48.9	13.0

[a] Percentage based on the weight of the ECL monomer in the starting AAROP mixture;

[b] Represents the relation between the volumes of metal and PA6 in the respective M-sample;

[c] With respect to the sum of the ECL plus filler weight;

[d] Determined by TGA according to Eq. 2.13 of Chapter 2.

4.3. ^{13}C Solid-state NMR spectra of metal-containing polyamide 6 microcapsules – general evaluation

ssNMR relies on the local environment and enables probing the order of a crystalline phase over distances not larger than 0.5-1 nm. Consequently, it is a suitable technique to evaluate the effect on the crystallinity of the PA6 material in close vicinity to the metal filler particles. As the first step in this determination, the overall ^{13}C MAS and ^{13}C CP/MAS spectra of Me-PAMC at room temperature were compared (Figure 4.1). The numeric data of chemical shifts are presented in Table 4.2.

From Figure 4.1a and 4.1b, it can be seen that the ^{13}C MAS and CP/MAS ssNMR spectra of PA6 consist of several signals attributable to C4, C2+C3, C5, and C1 methylene carbon nuclei and one peak of C6 carbonyl nucleus with chemical shifts being identical or close to those reported for PA6 earlier [1, 2]. As expected, the MAS spectra presented broader and less resolved peaks of the disordered PA6 phase, while the narrower lines in the CP-MAS spectra should be related to the sum of the amorphous and crystalline PA6 phases.

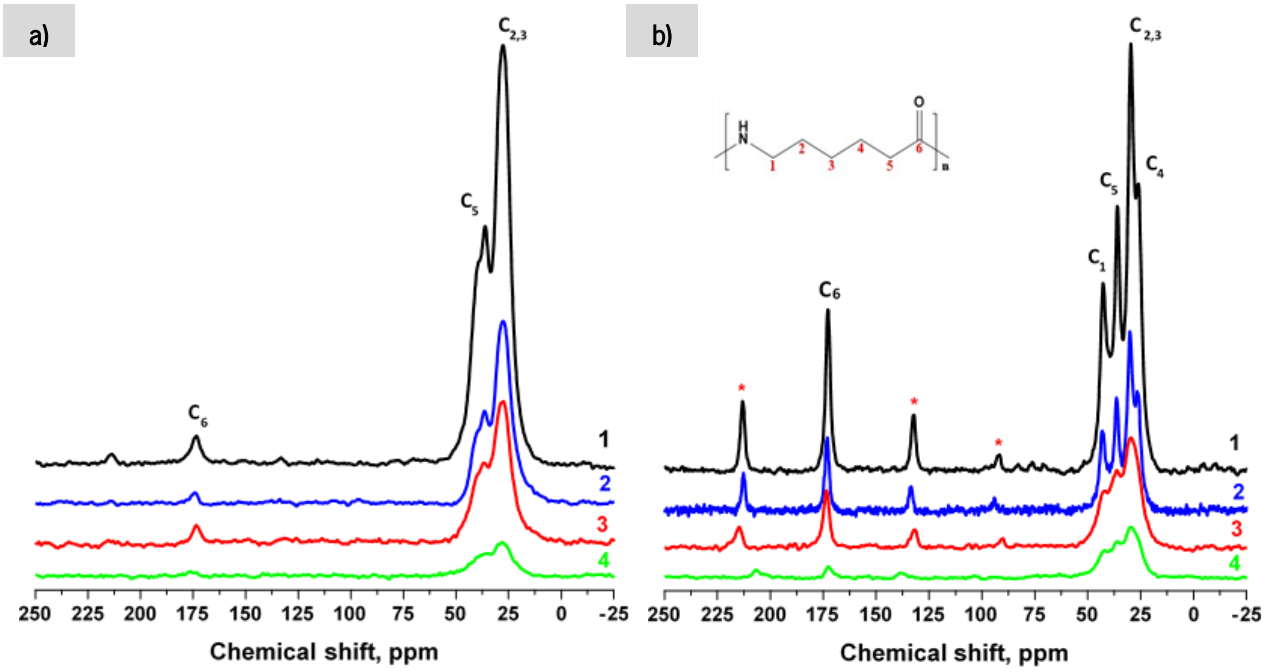

Figure 4.1 | ^{13}C MAS (a) and ^{13}C CP/MAS (b) and spectra comparison of M-PAMC at room temperature: 1 – M-PA6, 2 – M-Cu10, 3 – M-Al10, 4 – M-Mg10. Asterisks denote spinning sidebands. Chemical structure of PA6 is added in Fig. 4.1b.

Table 4.2 | ^{13}C MAS and ^{13}C CP/MAS chemical shifts (δ /ppm) of carbon nuclei (C) obtained from PAMC. The error to be assigned to the chemical shifts is 0.2 ppm

Sample and ssNMR experiment		Chemical shift δ , ppm				
		C1	C2,3	C4	C5	C6
M-PA6	MAS	-[a]	28.1	-[a]	36.4	173.9
	CP/MAS	42.7	29.7	26.4	36.2	173.2
M-Al10	MAS	-[a]	28.1	-[a]	37.1	174.7
	CP/MAS	42.7[b]	29.4[b]	-[a]	36.6[b]	174.1
M-Cu10	MAS	-[a]	27.9	-[a]	36.8	174.5
	CP/MAS	43.4	30.3	26.4	36.6	173.6
M-Mg10	MAS	-[a]	28.0	-[a]	35.6	173.5
	CP/MAS	42.5	29.7	-[a]	36.4	173.0

[a] Unresolved; [b] Broad signal; [c] Not detected (low signal/noise ratio).

The first comparison of the MAS and CP/MAS spectra of empty and Cu-loaded PAMC (curves 1 and 2) in Fig. 4.1a and 4.1b reveals the similarity of the PA6 resonance lines as far as peak position and resolution are concerned. Apparently, the diamagnetic Cu filler does not obstruct the observation of the NMR peaks. The intensity decrease of the signals in the presence of Cu has to be only correlated to radiofrequency absorption due to the so-called skin-effect [16]. When PAMC are loaded with Al or Mg particles (curves 2-4), line broadening and loss of peak resolution in both MAS and CP/MAS signals is observed. This is in good agreement with previous results on the effect of paramagnetic metals on the NMR signals´ intensity and width [23, 24].

Figure 4.2 focuses on the evolution of the C1-C5 signals' intensity and shape of the ^{13}C MAS and ^{13}C CP/MAS spectra of neat PAMC and such loaded with Al, Cu, and Mg. The evolution of the C6 signal intensity and the shape are displayed in Figure 4.3.

In the ^{13}C MAS spectra of neat PA6 (the methylene group region), the main peaks are centered at 40.0, 36.2 and 27.8 ppm (Fig. 4.2a). In the ^{13}C CP/MAS spectra of PA6, the main methylene C peaks are centered at 42.8, 38.8, 29.7 and 26.0 ppm (Fig. 4.2b). Regarding the C6 nucleus of the neat matrix (M-PA6 sample), its ^{13}C MAS peak appears at 173.5 ppm (Fig. 4.3a), and in ^{13}C CP/MAS the peak is centered at 172.8 ppm (Fig. 4.3b).

As seen from the ^{13}C MAS spectra in Fig. 4.2a, the incorporation of metal particles in PA6 leads to a general decrease in the intensity of the ssNMR signals and/or line broadening. The presence of diamagnetic Cu filler does not change the shape of the PA6 signal, only an intensity decrease is registered. The presence of paramagnetic Al and Mg causes a more significant intensity decrease, the methylene C signals becoming broader and less resolved. In the M-Mg10 sample (Fig. 4.3a), the C6 signal is split into two, whereby a second peak in weaker fields at ≈177 ppm appears. Analyzing the differences of the resonance lines of the aliphatic carbons in the ^{13}C CP/MAS experiment (Fig. 4.2b) reveals the same general trends as in MAS. In the carbonyl C region (Fig. 4.3b), the intensity decrease of C6 in the CP-MAS spectra for all samples strongly drops, best observed in the M-Mg10 sample. No splitting or shifting of the carbonyl nucleus peak of this sample was found, contrary to the MAS experiment.

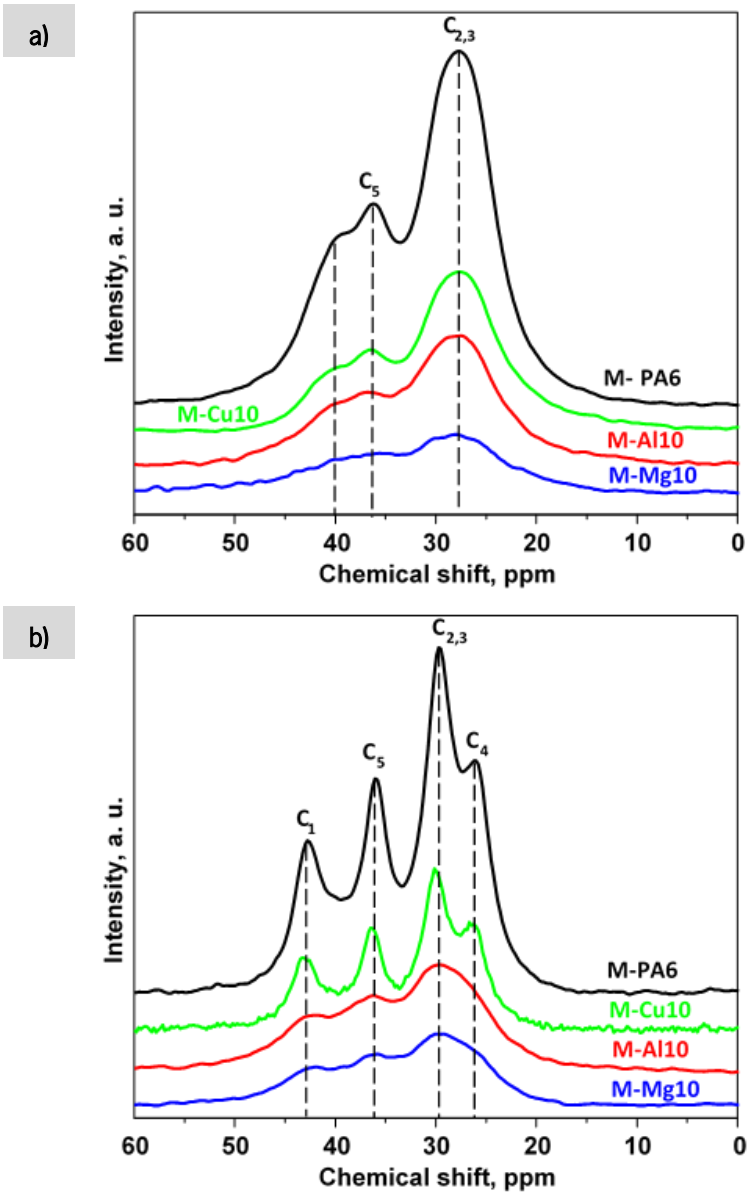

Figure 4.2 | Evolution of the C1-C5 signals and shape of the spectra in (a) ^{13}C MAS and (b) ^{13}C CP/MAS experiments with neat and Me-PAMC. The curves are displaced along the Y-axis for better visibility, whereby each set of curves has the same scaling of the intensity.

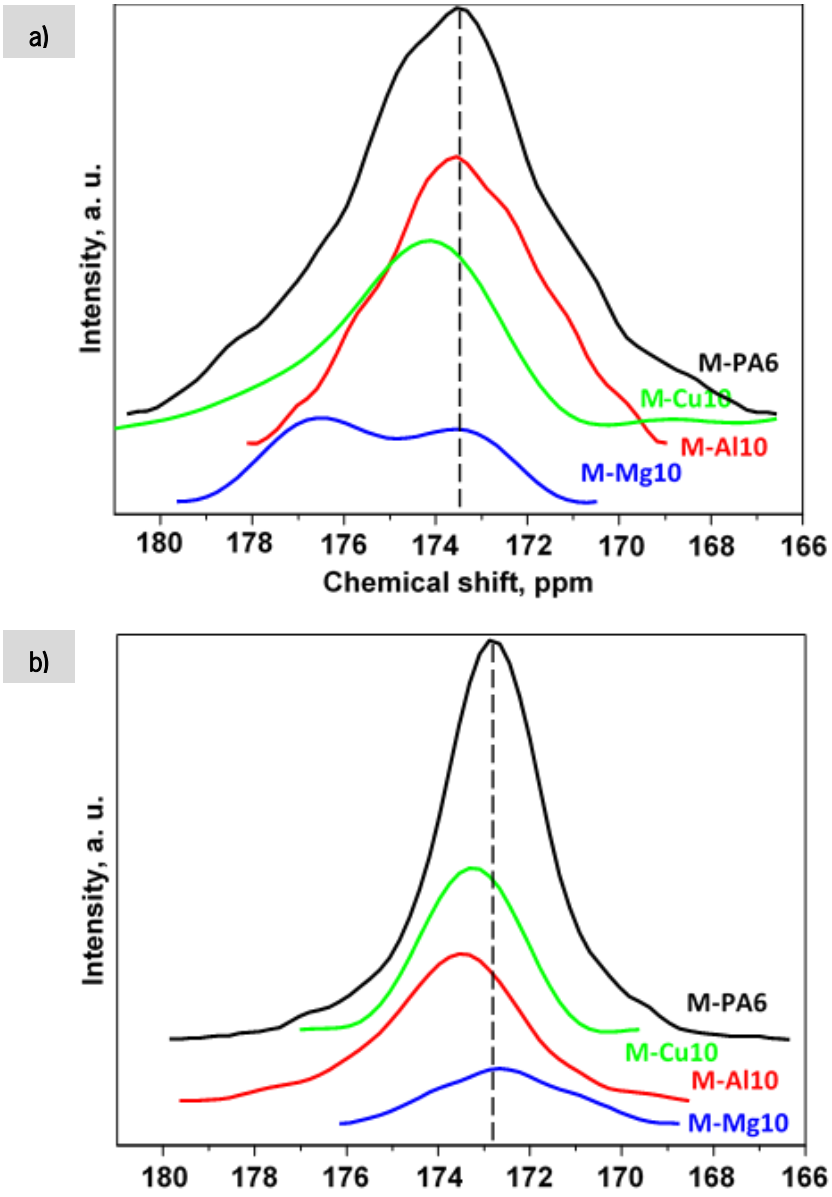

Figure 4.3 | Evolution of the C6 signal and shape of the spectra in **(a)** ^{13}C MAS and **(b)** ^{13}C CP/MAS experiments with neat and Me-PAMC. The curves are displaced along the Y-axis for better visibility, whereby each set of curves has the same scaling of the intensity. The dashed line in (a) and (b) corresponds to the center of the C6 signal in the neat PA6, at 173.5 and 172.8 ppm, respectively.

4.4. Influence of metal on the crystalline structure of the polyamide 6 matrix

The second step in the evaluation of the PA6 crystalline structure in the M-PAMC series by ssNMR was the determination of their NMR degree of crystallinity, X_c^{ssNMR}. To do that, first, the ^{13}C MAS spectra were deconvoluted obtaining only the response of the amorphous PA6 domains. Then, the ^{13}C CP/MAS spectra were deconvoluted placing the amorphous peaks known for MAS and adding then the respective

crystalline peaks. Gaussian functions were chosen to fit both ^{13}C MAS and ^{13}C CP-MAS spectral lines. Apart from calculating X_c^{ssNMR}, the deconvolution data from MAS and CP/MAS were used to quantify the effect of the metal particles on the width and the chemical shift of the signals of the PA6 matrix. Figures 4.4 and 4.5 show the aliphatic methylene regions of the experimental MAS and CP-MAS spectra fitted by Gaussian curves, and the resulting reconstructed spectra (the green solid lines). The respective numeric data obtained from the fits of all PAMC samples studied are displayed in Tables 4.3 and 4.4.

Table 4.3 | ^{13}C MAS results of the PAMC obtained by peak fitting of ssNMR data for the aliphatic region

Sample (Fitting coef.)	Carbon	Chemical shift, ppm		Var. chem. shift, ppm	FWHM, ppm	Var. FWHM, ppm	Area, %	Var. area, %
	C4, C2 +C3	27.87	± 0.03	-	8.01	-	68.11	-
M-PA6	**C5** [a]	**35.75**	**± 0.41**	**-**	**3.88**	**-**	**10.01**	-
(0.9986)	C1, C5	39.25	± 0.18	-	6.12	-	17.54	-
	C1 [b]	**41.63**	**± 0.21**	**-**	**5.36**	**-**	**4.34**	-
	C4, C2 +C3	28.15	± 0.05	0.28	9.15	1.14	67.48	-0.63
M-Al10	**C5** [a]	**36.12**	**± 0.11**	**0.37**	**3.75**	**-0.13**	**3.32**	**-6.69**
(0.9986)	C1, C5	39.33	± 0.27	0.08	8.42	2.30	27.72	10.18
	C1 [b]	**46.68**	**± 0.24**	**5.05**	**4.01**	**-1.35**	**1.48**	**-2.86**
	C4, C2 +C3	27.85	± 0.04	-0.02	8.86	0.85	72.35	4.24
M-Cu10	**C5** [a]	**36.09**	**± 0.30**	**0.34**	**3.40**	**-0.48**	**6.46**	**-3.55**
(0.9965)	C1, C5	39.37	± 1.41	0.12	6.53	0.41	18.15	-0.61
	C1 [b]	**42.36**	**± 0.23**	**0.73**	**5.48**	**0.12**	**3.04**	**-1.30**
	C4, C2 +C3	28.27	± 0.06	0.40	11.72	3.71	72.44	4.33
M-Mg10	**C5** [a]	**35.87**	**± 0.32**	**0.12**	**3.29**	**-0.59**	**4.18**	**-5.83**
(0.9918)	C1, C5	39.31	± 0.57	0.06	5.76	-0.36	13.85	-3.69
	C1 [b]	**43.77**	**± 0.46**	**2.14**	**7.99**	**2.63**	**9.53**	**5.19**

[a] C5 nucleus in close vicinity to C=O in more ordered PA6 domains;

[b] C1 nucleus in close vicinity to NH in more ordered domains.

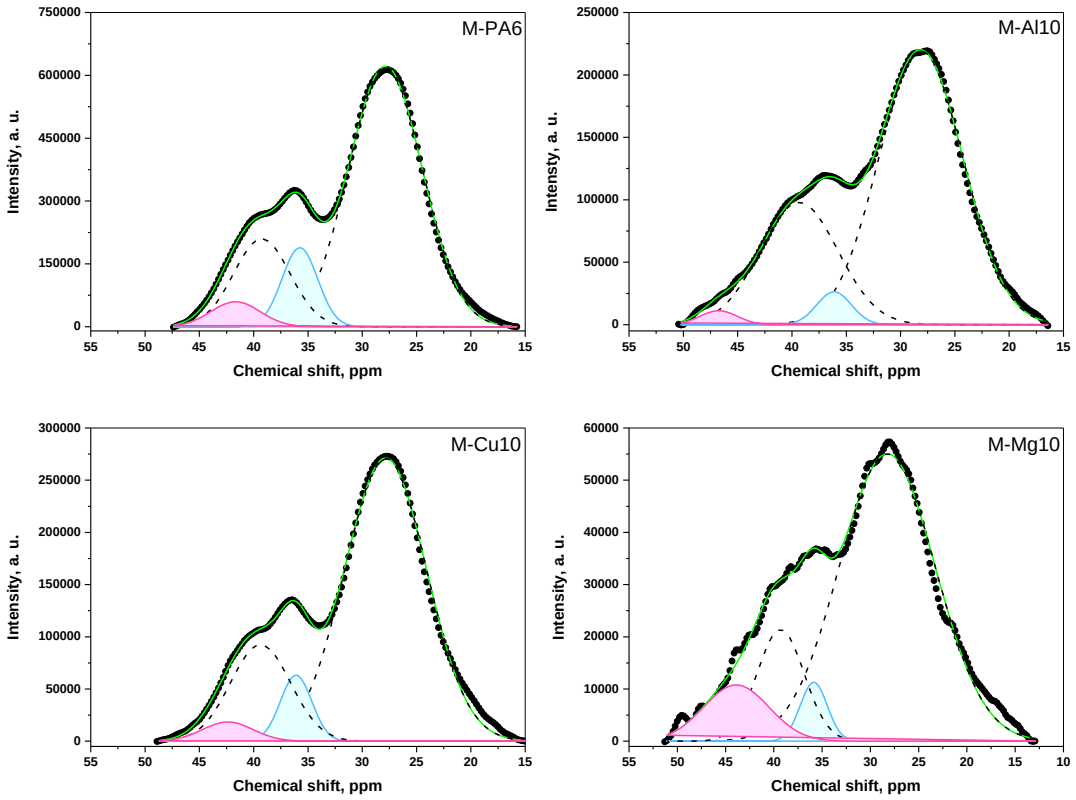

Figure 4.4| Aliphatic region of the ^{13}C MAS spectra of neat and Me-PAMC: experimental (black dots) and computed (green line). The two dashed curves present the combination of the amorphous resonances (C4, C2+C3) and (C1+C5). The peaks shaded in blue and pink areas represent the C5 and C1 signals, respectively, located in more ordered domains. The chemical shifts of all resonance lines are given in Table 4.3.

The first conclusion from Fig. 4.4 and Table 4.3 is that the merged amorphous resonance peak of (C1+C5) in all studied samples is centered at ca. 39.3 ppm, i.e., downfield shifted in respect to the (C4, C2+C3) peak appearing at ca. 28 ppm. The shift of the peak related to the (C1+C5) nuclei to lower fields is due to lesser electron shielding of these nuclei caused by the presence in their close vicinity of NH and C=O groups, respectively. Weak but observable downfield shifts of up to 0.12-0.40 ppm are observed with these two amorphous peaks in the presence of metal particles, the larger being reached with the (C4, C2+C3) combined resonance. This means that the metal particles in the amorphous PA6 phase interact only slightly with the CH_2 groups of the PA6, not causing significant redistribution of the electron density of the respective C-atoms.

It should be noted that the ^{13}C MAS spectra in Fig. 4.4. cannot be fitted without introducing of two additional narrow peaks (i.e., related to PA6 phase with some order) at ca. 36 ppm and in the 42-47 ppm interval, attributable to C5 and C1 resonances, respectively. The physical meaning of these two peaks is explained as follows. In all samples studied, including the neat PA6, the C5 nucleus is found in close vicinity to the C=O and the C1 next to the NH groups of the amide moiety. Having in mind that hydrogen bonds (H-bonds) are established between carbonyl and secondary amine groups, as a result of their formation redistribution of the electron density around C5 and C6 nuclei occurs resulting in a downfield shift of C5. The same tendency is observed in C1 resonance since the C1 nucleus is in close vicinity to the hydrogen-bonded N-H group. On the other hand, the formation of multiple intra- and intermolecular H-bonds should result in some densification of the amorphous fraction forming some quasi-ordered (or rigid amorphous) PA6 phase [25]. The latter produces the relatively narrow C1 and C5 peaks that can be revealed in a ^{13}C MAS ssNMR experiment.

The introduction of Al and Mg particles results in a significant downfield shift of the C1 signal by 5.05 and 2.14 ppm, while in the presence of Cu the shift is less than 1 ppm (Table 4.3). With all M-PAMC samples, the shift of the C5 signal in respect to that of the neat PA6 is much weaker, being in the range of 0.1-0.4 ppm. This would mean that the Al and Mg particles are somehow closer to the NH groups of the PA6 phase than the Cu particles. One of the possible reasons could be the fact that Cu has diamagnetic, while Mg and Al – paramagnetic properties. On the other hand, the proper morphology of the metal particles could also contribute to that different behavior. The Cu particles exhibit dendritic shapes with average sizes in the 20-40 μm range (Figure 3.3b of Chapter 3), whereas the Mg filler (Fig. 3.3c of Chapter 3) and the Al filler (Fig. 3.3a of Chapter 3) represent platelets larger than 100 μm and thicknesses of 10-15 μm.

Summarizing the results from the MAS experiment, it seems that the metal particles are located within the amorphous domains of the PA6 matrix and affect differently the H-bond formation. In all samples, including the neat PA6, these H-bonds cause some densification and ordering of the amorphous PA6 matrix most probably forming a rigid amorphous phase.

Table 4.3 contains information about the FWHM of all peaks in the ^{13}C MAS experiment. Most of them become broader in the presence of Al and Mg particles, although these data should be treated with caution due to the possibility of signal overlapping that is difficult to account for in the deconvolution procedure applied.

The deconvolution of the ^{13}C CP/MAS spectra (Fig. 4.5, Table 4.4) allows the distinction between the large peaks of the amorphous PA6 (the dashed lines in the plots) and the crystalline peaks that are shaded in pink. As a whole, the M-PA6 and M-Cu10 samples produced narrow crystalline peaks with similar shapes

and positions for all methylene carbons. For the other two samples with paramagnetic Al and Mg fillers, the peaks related to the ordered PA6 are much broader. As seen in Table 4.4, the metal particles influence FWHM in two different ways. On the one hand, it grows for both amorphous and crystalline signals in the presence of paramagnetic Al and Mg. This growth is larger for the crystalline peaks (being between 0.66 ppm and 3.85 ppm), while it keeps around 1 ppm for the amorphous methylene C signals. This means that both Al and Mg particles influence stronger the C signals in the crystalline phase. Also, the variation of the FWHM of the crystalline C1 and C5 is higher than that of the crystalline C4, and C2+C4 signals.

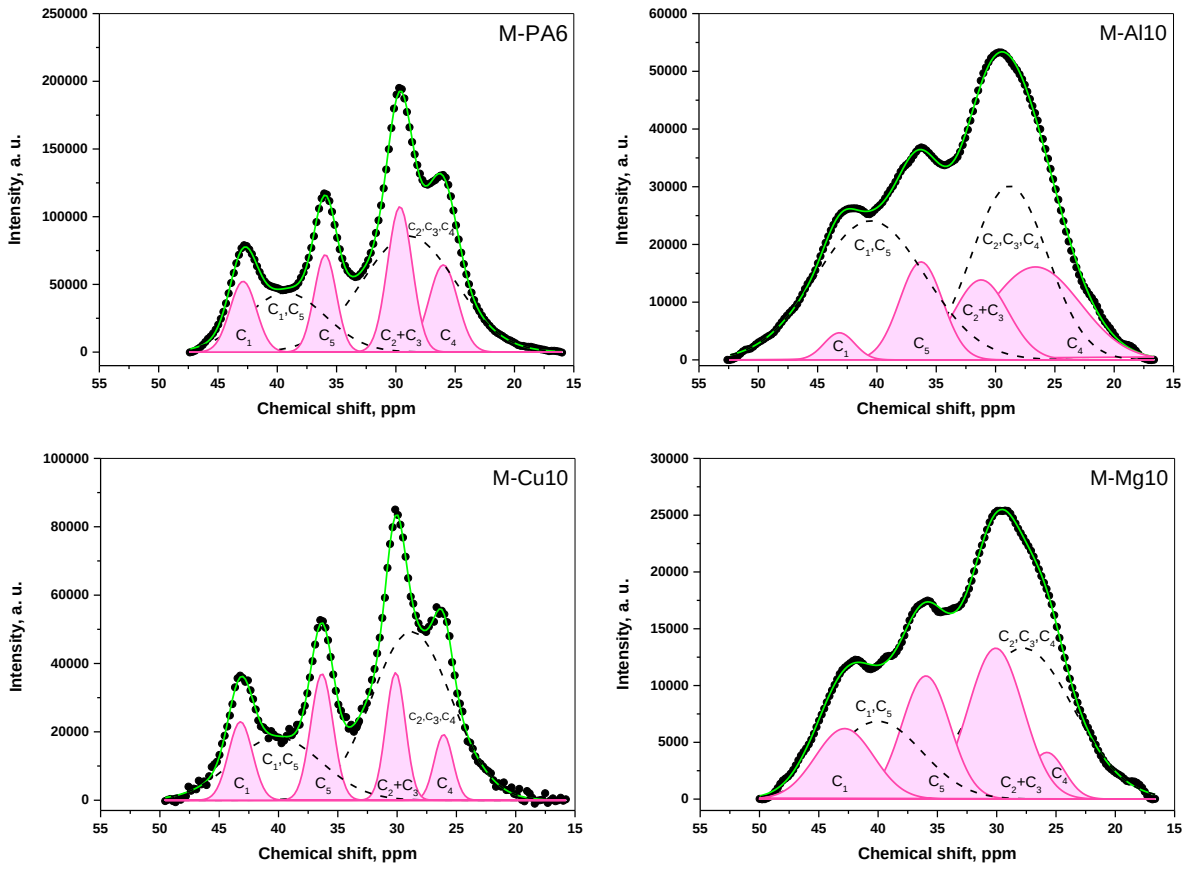

Figure 4.5| Aliphatic region of the ^{13}C-CP/MAS spectra of the neat and Me-containing PAMC: experimental (black dots) and computed (green line) spectra; the pink-shaded Gaussians represent the crystalline peaks of the indicated carbons, and the black dashed lines - the amorphous resonances used in the deconvolution. Table 4.4 contains identification and quantification of all resonance lines.

The increase in M-Al10 is in the range of 1.20 ppm (C1) to 3.85 ppm (C5), and between 3.16 ppm (C1) and 2.59 ppm (C5) for Mg10. Therefore, it can be deduced that the Al and Mg particles are located closer to the ordered regions than the Cu particles. On the other hand, the FWHM is either unchanged or slightly decreases in the presence of Cu particles, which was also observed in the ^{13}C MAS spectra of the disordered PA6 phase. Thus, the suggested effect of paramagnetic Al and Mg and diamagnetic Cu on the FWHM evolution in ^{13}C CP/MAS spectra will be the same as in the MAS technique.

The numeric data in Table 4.4 allow the comparison of the parameters extracted from the ^{13}C CP/MAS experiment related to the crystalline structure of the samples, including two partial (calculated on the basis of C2+C3+C4 and C1+C5 signals, respectively) and one total crystallinity index considering the areas of all crystalline and amorphous peaks. The values of the differential scanning calorimetry (DSC) crystallinity indices of the respective samples (presented initially in Chapter 3, Table 3.2) are also shown to enable comparison.

Analyzing the results of Table 4.4 about the two partial X_c^{ssNMR} values for all samples, it can be concluded that the one resulting from the three "middle" methylene carbons (i.e., C2+C3+C4) is always lower than that based on the C1+C5 carbons. This might be an indication that the C1 and C5 carbons located next to the NH and C=O groups participating in the H-bond formation are a part of a more ordered PA6 phase, while the C2-C4 carbons are located in the more disordered domains.

The total X_c^{ssNMR} for all samples is in between the two partial values. It was interesting to compare the total ssNMR crystallinity index with that from the DSC measurements, X_c^{DSC}. For the neat M-PA6, the two values completely coincide. In the presence of metal particles such as Al10 and Cu10, the X_c^{DSC} values of 43-53% become closer to the partial X_c^{ssNMR} based on the C1-C5 varying between 46-54%. At the same time, the X-ray crystallinities of the M-PA6, Al10 and Cu10 samples are in the same range of ca. 50% [26]. In the case of M-Mg10, the X_c^{DSC} is again closer to the C1-C5 NMR value, but the X-ray crystallinity of 45.6% almost coincides with the total X_c^{ssNMR} of 47.7%. Of course, a total coincidence between the crystallinities determined by X-ray, ssNMR, and DSC should not be expected since the principles behind these three methods are different. However, the presence of some relations between them is an indirect indication for the correctness of the ssNMR deconvolution procedure employed.

Table 4.4 | ^{13}C – CP/MAS results for the aliphatic region. The carbons in boldface are of the crystalline PA6 phase

Sample (Fitting coef.)	Carbon	Chemical shift, ppm		Var. chemical shift, ppm	FWHM, ppm	Var. FWHM, ppm	Area, %	$X_c^{ssNMR}{}_{partial}$, % [a]	$X_c^{ssNMR}{}_{total}$, % [b]	X_c^{DSC}, % [c]	X_c^{XRD}, % [d]
M-PA6 (0.9995)	**C4**	**26.00**	**± 0.02**	**-**	**2.83**	**-**	**9.70**		**39.4**	**39.4**	**49.5**
	C2, C3, C4	28.92	± 0.14	-	9.29	-	42.38	35.86			
	C2 + C3	**29.66**	**± 0.01**	**-**	**2.45**	**-**	**14.00**				
	C5	**35.96**	**± 0.01**	**-**	**2.19**	**-**	**8.39**				
	C1, C5	39.21	± 0.25	-	7.87	-	18.22	46.29			
	C1	**42.88**	**± 0.02**	**-**	**2.63**	**-**	**7.31**				
M-Al10 (0.9996)	**C4**	**27.51**	**± 0.84**	**1.51**	**5.73**	**2.90**	**15.38**		**50.0**	**52.2**	**50.7**
	C2, C3, C4	28.26	± 5.63	-0.67	10.6	1.27	29.99	46.45			
	C2 + C3	**30.77**	**± 0.26**	**1.11**	**4.18**	**1.72**	10.63				
	C5	**36.30**	**± 0.83**	**0.34**	**6.05**	**3.85**	**20.13**				
	C1, C5	42.33	± 2.71	3.12	9.41	1.54	20.11	54.29			
	C1	**42.75**	**± 0.22**	**-0.13**	**3.83**	**1.20**	**3.76**				
M-Cu10 (0.9980)	**C4**	**26.08**	**± 0.03**	**0.08**	**1.84**	**-0.99**	**4.44**		**30.7**	**42.7**	**49.5**
	C2, C3, C4	28.79	± 0.08	-0.13	7.92	-1.37	49.10	21.55			
	C2 + C3	**30.12**	**± 0.02**	**0.46**	**1.93**	**-0.52**	**9.04**				
	C5	**36.34**	**± 0.01**	**0.38**	**2.21**	**0.02**	**10.29**				
	C1, C5	40.07	± 0.39	0.86	8.82	0.95	20.25	45.87			
	C1	**43.21**	**± 0.03**	**0.33**	**2.28**	**-0.25**	**6.87**				
M-Mg10 (0.9993)	**C4**	**25.77**	**± 0.27**	**-0.23**	**3.49**	**0.66**	**3.92**		**47.7**	**53.2**	**45.6**
	C2, C3, C4	27.83	± 4.74	-1.09	9.94	0.65	35.96	39.78			
	C2 + C3	**30.08**	**± 1.05**	**0.42**	**5.47**	**3.02**	**19.84**				
	C5	**35.97**	**± 0.43**	**0.01**	**4.78**	**2.59**	**14.15**				
	C1, C5	39.97	± 3.42	0.76	8.77	0.91	16.36	59.40			
	C1	**42.81**	**± 3.76**	**-0.07**	**5.79**	**3.16**	**9.78**				

[a] Calculated according to Eq. 2.8 of Chapter 2; [b] Calculated according to Eq. 2.9 of Chapter 2; [c] Determined according to Eq. 2.12 of Chapter 2; [d] According to ref. [26].

4.5. Molecular dynamics

In addition to the information on Me-PAMC morphology, ssNMR was used to produce time-dependence data suitable to study molecular dynamics. In a solid, shielding anisotropy and dipolar coupling to the magnetic nuclei of neighboring atoms are the most important contributions to the local magnetic field of an excited nucleus. NMR relaxation depends on local magnetic field fluctuations mostly caused by molecular motion. ^{13}C relaxation measurements enable probing the mobility of chemically inequivalent carbon atoms. Although the distinction between mobile and rigid PA6 components appears to be best achieved by using $^{C}T_{1\rho}$ [25], this study also reports on $^{C}T_{1}$ evaluation. The $^{C}T_{1\rho}$ (ms) and $^{C}T_{1}$ (s) of the C1-C6 nuclei are shown in Figure 4.6. Table 4.5 includes the corresponding data.

Spin-lattice relaxation times in the rotating frame obtained for neat PA6 (Fig. 4.6, Table 4.5) allow some conclusions to be made: a) $^{C}T_{1\rho}$ data were obtained from mono-exponential fitting functions, in agreement with amorphous and rigid domains presenting similar mobility in the kHz frequency ranges; b) all the aliphatic carbons are characterized by $^{C}T_{1\rho}$ of about 5 ms and a longer relaxation time is observed for carbonyl (about 42 ms), which is characteristic of a rigid phase [25]. The large difference between aliphatic and carbonyl data is due to C-H dipole-dipole interaction being the driving process for relaxation. This is a trough-space interaction which depends on r^{3} [27] (r is the C-H internuclear distance) and therefore is mainly dominant for ^{13}C in methylene groups. On the other hand, carbonyl groups participate directly in H-bonds and ^{13}C has a large shielding anisotropy which also contributes for the nucleus relaxation (easily detected by the presence of spinning sidebands at low MAS rate, not completing averaging out that interaction, as shown in Fig. 4.1). Hence, $^{C}T_{1\rho}$ of $^{13}C{=}O$ (C6) is strongly dependent on molecular motion, which is related to the presence of H-bonds and to the shielding anisotropy of carbon nuclei. NMR investigations of orientational and structural changes in PA6 by drawing reported about 55 ms and 3 ms on $^{C}T_{1\rho}$ of ^{13}CO in rigid and mobile phases, respectively, at a draw ratio of 1 [25]. Comparing the $^{C}T_{1\rho}$ results from unloaded and loaded PA6 (Fig. 4.6a, Table 4.5), there are two trends to be noticed. First, the $^{C}T_{1\rho}$ for the aliphatic nuclei of neat PA6 and Cu10 are in the same range: 5.05 ± 0.11 ms for neat PA6 and, slightly lower, 4.67 ± 0.08 ms for the M-Cu10. Therefore, for both samples, all aliphatic nuclei have similar mobility. Further, the $^{C}T_{1\rho}$ of C6 in these two samples is much higher, in the range from 40.47 ± 1.44 (M-Cu10) to 42.11 ± 1.68 ms (M-PA6).

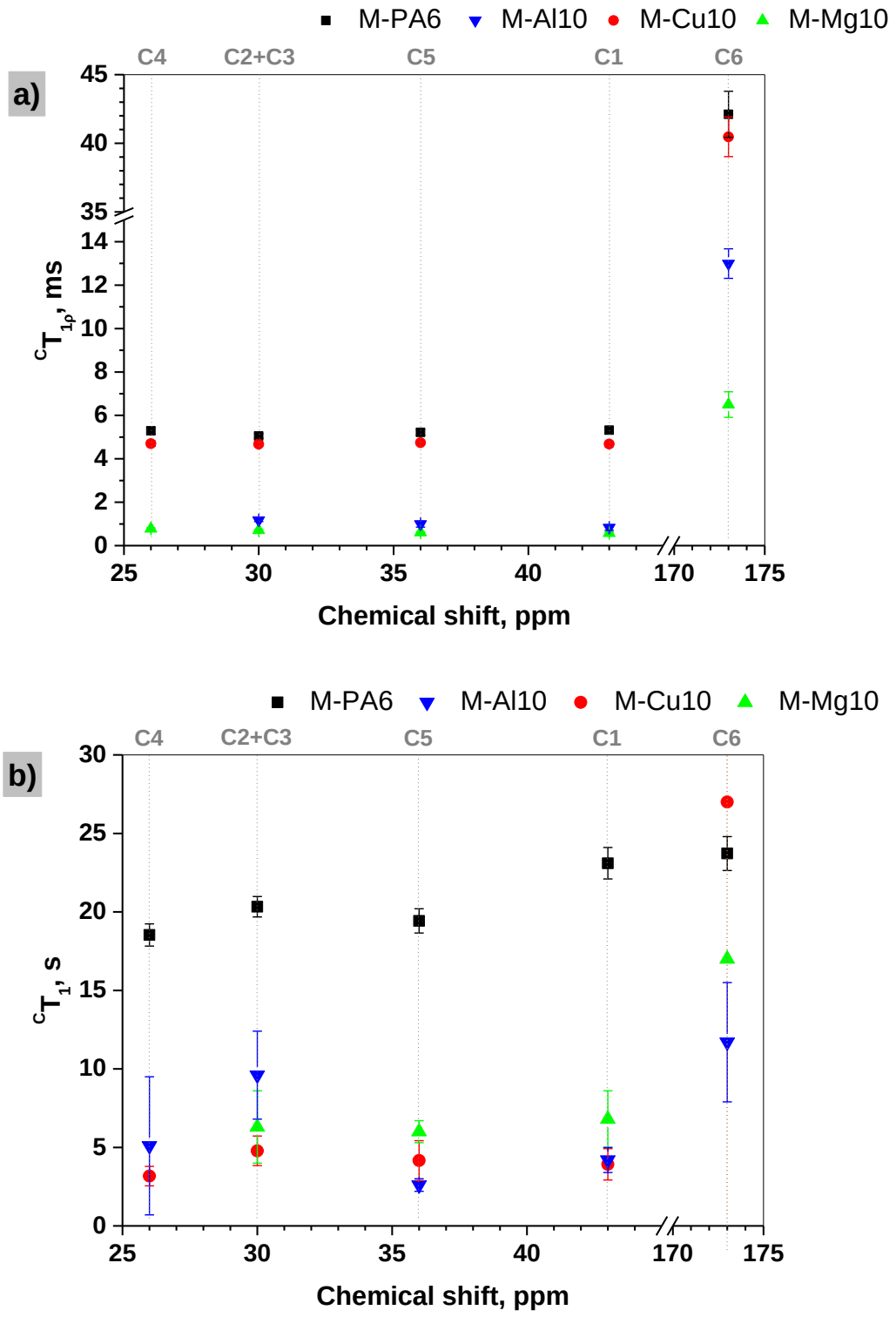

Figure 4.6 | a) $^{C}T_{1\rho}$ and b) $^{C}T_{1}$ of the carbon nuclei in empty and Me-PAMC.

Table 4.5 | $^{C}T_{1\rho}$ (ms) and $^{C}T_{1}$ (s) of the empty and Me-PAMC; the relaxation times were obtained by fitting the experimental data with mono-exponential functions (Equation 2.11 of Chapter 2) unless specified otherwise

	$^{C}T_{1\rho}$				$^{C}T_{1}$			
Carbon	**M-PA6**	**M-Al10**	**M-Cu10**	**M-Mg10**	**M-PA6**	**M-Al10** [c]	**M-Cu10**	**M-Mg10** [c]
C1	5.32 ± 0.11	0.83 ± 0.13	4.68 ± 0.12	0.58 ± 0.05	23.10 ± 1.00 0.69 ± 0.81 (28%)[a] 27.8 ± 12.5 (72%)[a]	4.2 ± 0.8	3.92 ± 1.00	6.8 ± 1.8
C2,3	5.05 ± 0.11	1.17 ± 0.06	4.67 ± 0.08	0.71 ± 0.04	20.33 ± 0.65 2.32 ± 0.36 (33%)[a] ~49 (67%)[a,b]	9.6 ± 2.8	4.78 ± 0.94 1.10 ± 0.31 (38%)[a] 19.6 ± 11.0 (62%)[a]	6.3 ± 2.3
C4	5.29 ± 0.15	-	4.70 ± 0.13	0.78 ± 0.04	18.53 ± 0.71 0.95 ± 0.21 (48%)[a] 28.0 ± 7.7 (52%)[a]	5.1 ± 4.4	3.17 ± 0.62 0.93 ± 0.27 (52%)[a] 14.5 ± 9.1 (48%)[a]	-
C5	5.22 ± 0.13	0.99 ± 0.14	4.74 ± 0.01	0.61 ± 0.03	19.43 ± 0.77 2.24 ± 0.75 (39%)[a] 28 ± 15 (61%)[a]	2.6 ± 0.4	4.16 ± 1.27 0.84 ± 1.28 (44%)[a] ~11 (56%)[a,b]	6.0 ± 0.7
C6	42.11 ± 1.68	12.99 ± 0.68	40.47 ± 1.44	6.50 ± 0.59	23.72 ± 1.08 3.01 ± 3.05 (25%)[a] ~38 (75%)[a,b]	11.7 ± 3.8	~27[b]	~17[b]

[a] Using Equation 2.12 of Chapter 2 to fit the experimental data;

[b] Rough estimate (large fitting error);

[c] Low signal to noise ratio.

The second trend refers to the M-Al10 and M-Mg10 samples, where it is noticed higher mobility for the aliphatic nuclei with $^{C}T_{1\rho}$ values in the range of 0.58 – 0.99 ms and 6.50 – 12.99 ms for carbonyl group. These findings suggest that the Al and Mg particles are closer to carbon nuclei due their sizes > 100 μm (Fig. 3.3a and Fig. 3.3c of Chapter 3), decreasing their respective $^{C}T_{1\rho}$ not only due to the proximity of paramagnetic particles [28] to carbon nuclei but also because metal particles, by imposing restrictions to the presence of polymeric ordered domains, facilitate the mobility of C atoms. These results agree with the line-shape of the respective ^{13}C MAS and ^{13}C CP/MAS spectra where broader signals and low resolution were observed [23, 29].

Data from $^{C}T_{1}$ measurements (Fig. 4.6, Table 4.5) show that the presence of metal particles decreases the $^{C}T_{1}$ of the aliphatic nuclei comparing with neat PA6. In M-PA6 sample, the $^{C}T_{1}$ values of the aliphatic C (from mono-exponential fitting functions) are from about 18.53 ± 0.71 s (C4) to 23.10 ± 1.00 s (C1), while in Me-PAMC, such values are notably lower, from about 2.6 ± 0.4 s (C5 of Al10) to 9.6 ± 2.8 s (C2,3 of Al10). These results suggest that the presence of metal particles affect the segmental motion of the PA6 chains, intensifying the spin-lattice relaxation of the aliphatic C, independently on the loaded metal. The similarity between the aliphatic $^{C}T_{1}$ values in Me-PAMC can be due to the effects of spin-diffusion [27], which can hide other properties of the materials under study. Table 4.5 also presents M-PA6 and M-Cu10 $^{C}T_{1}$ data obtained from double-exponential fitting functions (Equation 2.12, Chapter 2), as should be expected for a semi-crystalline polymer like PA6. Although some values need to be considered as rough estimates, due to large associated fitting errors, it is worth mentioning the similar behavior of M-PA6 and M-Cu10.

Concerning C6 nucleus (Table 4.5), as stated in the analysis of the $^{C}T_{1\rho}$, it is visible the effect of the carbonyl group on the spin-lattice relaxation, decreasing the mobility of that nucleus. However, differences can be observed between the analyzed samples. It should be noted that long T_1 is related to the crystalline phase [30], and it agrees well with the line narrowing of the ^{13}C CP/MAS spectra of the empty and Cu-loaded PAMC (Fig. 4.1a). On the other hand, broader signals indicate the predominance of the amorphous phase and consequently lower T_1 values, which match with the $^{C}T_{1}$ values obtained for C6 in Al- and Mg-loaded PAMC (Table 4.5) and the respective ^{13}C CP/MAS spectra (Fig. 4.1a) [30]. Thus, it can be concluded that the hydrogen bonding that is characteristic for the formation of PA6

crystallinity is somehow absent in the M-Al10 and M-Mg10 samples, with the consequent increase of the carbonyl mobility, resulting in the lower ${}^{C}T_1$ values of the C6.

4.6. Summary

After obtaining empty and Me-PAMC carrying 10–20 wt.% of different metal fillers (Al, Cu, Mg) via AAROP of ECL in solution, the effect of the well-dispersed payloads on the PA6 structure and its molecular dynamics was evaluated by solid-state ^{13}C NMR. ^{13}C MAS and ^{13}C CP/MAS experiments revealed a spectral similarity between neat PA6 and M-Cu10 on one hand, and between M-Al10 and M-Mg10 compositions, on the other. The spectra of the Al- and Mg-loaded PAMC have line broadening and low peak resolution due to their paramagnetic properties. These broader peaks and resolution loss are not observed in the M-Cu10 sample, indicating that the dispersion of Cu particles in the polymer matrix and its diamagnetic properties did not affect the C resonances. From the study of the PA6's crystalline structure, it was observed that the size and morphology of the dispersed metal fillers affect its X_c. Mg and Al particles act as nucleating agents, as opposed to the Cu particles which reduce the crystalline mass fraction. These results agree with the X_c determined by DSC since the M-Al10 and Mg10 samples present higher crystallinity. In the molecular dynamics study, it was found out that the local mobility of each C is influenced by the presence of metal particles. The paramagnetic properties of the Al and Mg particles lower both ${}^{C}T_{1\rho}$ and ${}^{C}T_1$ spin-lattice relaxation times of either aliphatic and carbonyl carbon nuclei, meaning intensified local motion. At the same time, the dendritic-shaped, diamagnetic Cu particles do not change the relaxation times i.e., in their presence the local motion of nuclei is the same as in the neat PA6.

4.7. References

[1] Weeding TL, Veeman WS, Gaur HA, Huysmans WGB (1988) Structural investigation of polyamide-6 and polyamide-6 composites using carbon-13 cross polarization/magic angle spinning NMR. Macromolecules 21:2028–2032. DOI: 10.1021/ma00185a024

[2] Kubo K, Yamanobe T, Komoto T, Ando I, Shiibashi T (1989) Nylon 6 structure in solid state as studied by high-resolution ^{13}C-NMR spectroscopy. J Polym Sci Part B Polym Phys 27:929–937. DOI: 10.1002/polb.1989.090270416

[3] Kubo K, Ando I, Shiibashi T, Yamanobe T, Komoto T (1991) Conformations and ^{13}C NMR chemical shifts of some polyamides in the solid state as studied by high-resolution ^{13}C NMR spectroscopy.

J Polym Sci Part B Polym Phys 29:57–66. DOI: 10.1002/polb.1991.090290108

[4] Mathias LJ, Powell DG, Autran J-P, Porter RS (1990) Solid state ^{15}N nuclear magnetic resonance of ^{15}N-labeled nylon 6 and nylon 11: Observation of multiple crystalline forms and amorphous regions. Mater Sci Eng A 126:253–263. DOI: 10.1016/0921-5093(90)90131-L

[5] Powell DG, Mathias LJ (1990) Characterization of nylon 6 by nitrogen-15 solid-state nuclear magnetic resonance. J Am Chem Soc 112:669–675. DOI: 10.1021/ja00158a027

[6] Powell DG, Sikes AM, Mathias LJ (1988) Nitrogen-15 solid state NMR characterization of aramid-containing nylon-6 by in situ polymerization with benzoyl caprolactam derivatives. Macromolecules 21:1533–1536. DOI: 10.1021/ma00183a054

[7] Mathias LJ, Davis RD, Jarrett WL (1999) Observation of α and γ Crystal Forms and Amorphous Regions of Nylon 6–Clay Nanocomposites Using Solid-State ^{15}N Nuclear Magnetic Resonance. Macromolecules 32:7958–7960. DOI: 10.1021/ma991307p

[8] Davis RD, Jarrett WL, Mathias LJ (2001) Solution and Solid-State NMR Spectroscopy of Nylon 6-Montmorillonite Clay Nanocomposites. In: Polymer Nanocomposites. pp 117–126

[9] VanderHart DL, Asano A, Gilman JW (2001) NMR Measurements Related to Clay-Dispersion Quality and Organic-Modifier Stability in Nylon-6/Clay Nanocomposites. Macromolecules 34:3819–3822. DOI: 10.1021/ma002089z

[10] VanderHart DL, Asano A, Gilman JW (2001) Solid-State NMR Investigation of Paramagnetic Nylon-6 Clay Nanocomposites. 1. Crystallinity, Morphology, and the Direct Influence of Fe3+ on Nuclear Spins. Chem Mater 13:3781–3795. DOI: 10.1021/cm0110775

[11] VanderHart DL, Asano A, Gilman JW (2001) Solid-State NMR Investigation of Paramagnetic Nylon-6 Clay Nanocomposites. 2. Measurement of Clay Dispersion, Crystal Stratification, and Stability of Organic Modifiers. Chem Mater 13:3796–3809. DOI: 10.1021/cm011078x

[12] Hatfield GR, Glans JH, Hammond WB (1990) Characterization of structure and morphology in nylon 6 by solid-state carbon-13 and nitrogen-15 NMR. Macromolecules 23:1654–1658. DOI: 10.1021/ma00208a016

[13] Konishi R, Ito M (2004) Relation between ductility and segmental mobility of nylon-6. Polymer (Guildf) 45:5191–5198. DOI: 10.1016/j.polymer.2004.04.034

[14] Dencheva N, Nunes T, Oliveira MJ, Denchev Z (2005) Microfibrillar composites based on polyamide/polyethylene blends. 1. Structure investigations in oriented and isotropic polyamide 6. Polymer (Guildf) 46:887–901. DOI: 10.1016/j.polymer.2004.11.105

[15] Umek P, Huskić M, Škapin AS, Florjančič U, Zupančič B, Emri I, Arčon D (2009) Structural and

mechanical properties of polystyrene nanocomposites with 1D titanate nanostructures prepared by an extrusion process. Polym Compos 30:1318–1325. DOI: 10.1002/pc.20697

[16] Jouni M, Buzlukov A, Bardet M, Boisson F, Eddarir A, Massardier V, Boiteux G (2014) Skin effect of conductive polymer composites observed by high-resolution solid-state NMR. Compos Sci Technol 104:104–110. DOI: 10.1016/j.compscitech.2014.08.031

[17] Young HD (1992) Sources of magnetic field. In: Young HD (ed) University Physics, 8th ed. Addison-Wesley Pub. Co, pp 804–836

[18] Morton JJ (2012) Magnetic properties of materials. https://www.ucl.ac.uk/quantum-spins/sites/quantum-spins/files/MPM-Part2.pdf. Accessed 17 Mar 2020

[19] Zangger K, Respondek M, Göbl C, Hohlweg W, Rasmussen K, Grampp G, Madl T (2009) Positioning of Micelle-Bound Peptides by Paramagnetic Relaxation Enhancements. J Phys Chem B 113:4400–4406. DOI: 10.1021/jp808501x

[20] Axelson DE, Russell KE (1985) Characterization of polymers by means of ^{13}C NMR spectroscopy: (a) Morphology by Solid-State NMR (b) End-Group Studies. Prog Polym Sci 11:221–282. DOI: 10.1016/0079-6700(85)90003-6

[21] Bovey FA, Jelinski LW (1985) The observation of chain motion in macromolecules by carbon-13 and deuterium nuclear magnetic resonance spectroscopy. J Phys Chem 89:571–583. DOI: 10.1021/j100250a006

[22] Koenig JL (1992) NMR Relaxation Spectroscopy of Polymers. In: Spectrosocpy of Polymers, 1st ed. American Chemical Society, Washington DC, p 267

[23] Apperley DC, Harris RK, Hodgkinson P (2012) Solid-State NMR: Basic Principles & Practice. Momentum Press, New York

[24] Pell AJ, Pintacuda G, Grey CP (2019) Paramagnetic NMR in solution and the solid state. Prog Nucl Magn Reson Spectrosc 111:1–271. DOI: 10.1016/j.pnmrs.2018.05.001

[25] Schreiber R, Veeman WS, Gabriëlse W, Arnauts J (1999) NMR Investigations of Orientational and Structural Changes in Polyamide-6 Yarns by Drawing. Macromolecules 32:4647–4657. DOI: 10.1021/ma9818679

[26] Brêda C, Dencheva N, Lanceros-Mendez S, Denchev Z (2016) Preparation and properties of metal-containing polyamide hybrid composites via reactive microencapsulation. J Mater Sci 51:10534–10554. DOI: 10.1007/s10853-016-0274-0

[27] Jelinski LW, Melchior MT (2004) High-Resolution NMR of Solids. Appl Spectrosc Rev 35:25–93. DOI: 10.1081/ASR-100101220

[28] Bertini I, Luchinat C, Parigi G (2001) Relaxation. In: Bertini I, Luchinat C, Parigi G (eds) Solution NMR of Paramagnetic Molecules. Elsevier, pp 75–118

[29] Swift TJ (1973) 2 - The Paramagnetic Linewidth. In: Mar GN La, Horrocks WD, Holm RH (eds) NMR of Paramagnetic Molecules, 1st ed. Academic Press, pp 53–83

[30] Bovey FA, Mirau PA (1996) The dynamics of macromolecules. In: Bovey FA, Mirau PA (eds) NMR of Polymers. Academic Press, San Diego, pp 353–453

CHAPTER 5

Synthesis and properties of binary polyamide 6 composites containing carbon allotropes and metal particles

This chapter is based on the article:

Oliveira, F.; Dencheva, N.; Lanceros-Méndez, S.; Nunes, T. G.; Denchev, Z. Binary Polyamide Hybrid Composites Containing Carbon Allotropes and Metal Particles with Radiofrequency Shielding Effect. *Polym. Compos.* 2019, *40*, E1338–E1352. DOI: 10.1002/pc.24993.

5.1. Introduction

According to the results obtained on single loaded polyamide 6 microcapsules (PAMC) – M-samples – and their respective molded plates (P-samples) reported in Chapter 3, all changes in thermal, mechanical, electric and dielectric properties depend on the filler type dispersed within the polyamide 6 (PA6) matrix. Chapter 5 reports on the possibility to develop PA6-based composite materials with tailored electrical conductivity, dielectric and mechanical properties based on PAMC with binary loads, that is, micro- and nanoparticles of both metals and C-allotropes. The motivation of this study is that the presence of two different, finely dispersed fillers in a PA6 matrix can be suitable for the development of novel radar absorbing materials (RAM) or in electromagnetic interferences (EMI) shielding materials. Effective RAM and EMI materials can cancel out by selective absorption or reflection both magnetic and electric components of the incident radiation. This effect is usually achieved by the simultaneous incorporation of conductive, magnetic and/or dielectric fillers into a matrix that can be also polymeric [1, 2]. Novel structural RAM or EMI materials are attracting increasing interest from academia and industry due to their diverse applications in military stealth technologies, in aircraft and ship transports as well as in television for image interference reduction [1–7], and in medical diagnostic equipment [8, 9], among others. In this chapter, carbon black (CB) and carbon nanotubes (CNT) were used as absorbers that depend on the ohmic loss of energy and can also provide mechanical reinforcement to the composite. Moreover, micron-sized powders of Al, Cu, Mg, and Fe were employed for tuning the electrical response of the composite, the latter being also a magnetic absorber. The structure, morphology, electrical conductivity, dielectric, and thermal properties and mechanical behavior of the novel composites were investigated. The RAM properties of selected compositions were demonstrated by means of solid-state nuclear magnetic resonance (ssNMR) spectroscopy.

5.2. Synthesis of binary metal/carbon allotropes polyamide 6 microcapsules

The dually loaded PAMC were produced by activated anionic ring-opening polymerization (AAROP) of ε-caprolactam (ECL) performed as described in section 2.3.3 of Chapter 2. The chemistry of the process is described in detail in previous works [10–13]. According to these studies, the loads are entrapped into the viscous droplets formed by growing PA6 polymer molecules during AAROP. After reaching some critical molecular mass and various acts of coalescence, the viscous PA6 droplets crystallize transforming into a porous PA6 shell that embeds the mixed payload particles. The dually loaded PAMC of this study were obtained at the conditions determined in [10], under which the AAROP

of ECL produced high yields of PAMC without the formation of lumps: stirring rate of ca. 800 rpm, temperature of AAROP close to 135 °C and time duration of the process 2 h.

Table 5.1 shows the designations of the loaded PAMC samples prepared, the respective polymerization yields and the metal-carbon filler contents. For all samples, the real load content (Table 5.1) was determined by thermogravimetric analysis (TGA) according to Eq. 2.13 of Chapter 2. Deviations between the real and theoretical loads up to 4–7 % are observed for all samples except for the DM-Fe5-CNT5 sample where it was around 2 %. The said deviation depends on the polymerization yields that were in the range of 52–63 %. Since during the preparation of the hybrid PAMC all filler particles are entrapped into PAMC, the lower the PAMC yield, calculated in relation to the initial ECL, the higher the percentage of the filler in the final PAMC.

Table 5.1 | PAMC: sample designations, composition and polymerization yield.

Sample	Load, wt.% [a]	Composition, vol.% [b]			PAMC yield, % [c]	Real load, wt.% [d]
		Metal	Carbon	PA6		
M-PA6	0	0	0	100	56.2	0
DM-Al3-CNT7	3 + 7	1.96	5.71	92.3	61.0	14.4
DM-Al5-CNT5	5 + 5	3.84	4.80	91.4	50.4	16.7
DM-Al7-CNT3	7 + 3	4.68	2.51	92.8	58.9	14.7
DM-Al5-CB5	5 + 5	3.41	5.11	91.5	60.4	15.1
DM-Cu5-CNT5	5 + 5	1.03	4.29	94.7	51.8	14.8
DM-Fe5-CNT5	5 + 5	0.93	3.38	95.7	63.0	11.9
DM-Mg5-CNT5	5 + 5	5.15	4.15	90.7	54.7	14.9

[a] Percentage based on the weight of the ECL monomer in the starting AAROP mixture;

[b] Represents the relation between the volumes of load (metal or metal + C-allotrope) and PA6 in the respective DM-sample;

[c] With respect to the sum of the ECL plus fillers' weight. Calculated from the conversion of ECL into polymer;

[d] Determined by TGA according to Eq. 2.13 of Chapter 2.

5.3. Morphological studies by SEM

To analyze the morphology of the prepared PAMC, scanning electron microscopy (SEM) studies were performed (Figures 5.1–5.3). The scanning electron micrographs in Figure 5.1 a-f present information about the size and shape of the Al, Mg, Cu and Fe loads. The Mg and Al particles (images

5.1 e and 5.1 c) are shaped as platelets with maximum sizes of 80–100 μm and thicknesses of 10–15 μm. Cu particles display complex dendritic shapes with sizes in the 20–40 μm range [12], and the Fe particles are strictly circular with sizes between 1–5 μm. On the other hand, as seen from images 5.1d and 5.1e respectively, the CNT filler comprises 10–20 nm thick fibrils and the CB displays particles with spherical morphology with diameters being in the 40–80 nm range.

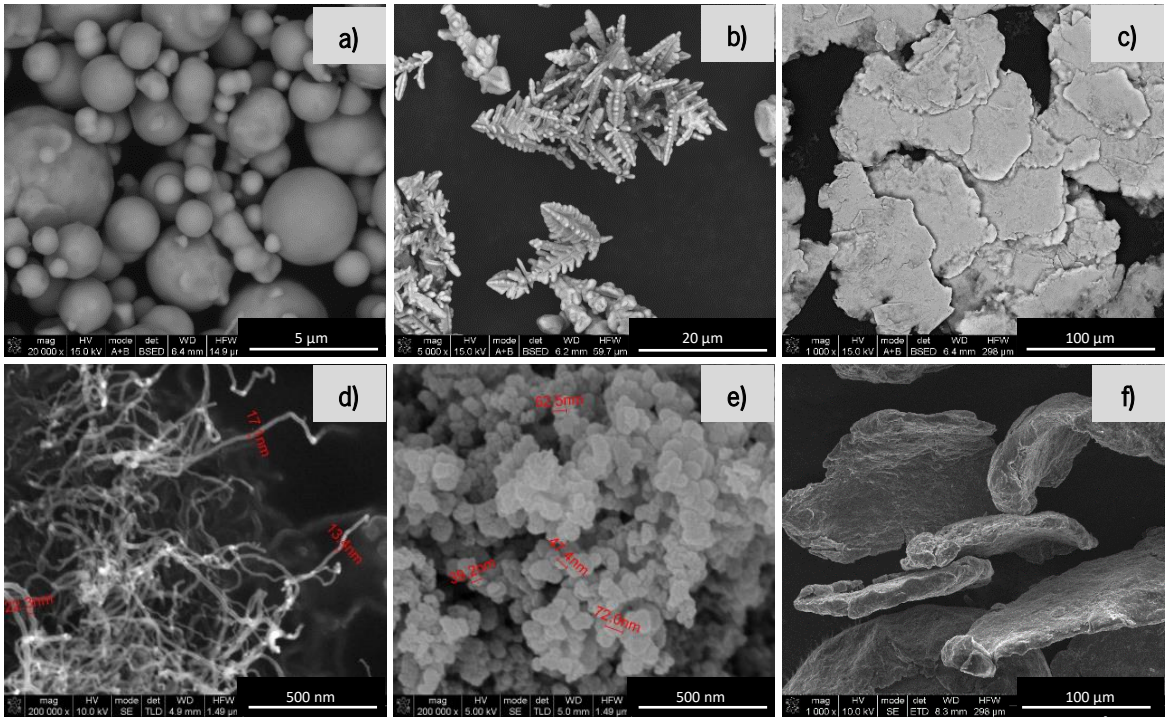

Figure 5.1 | SEM micrographs of filler particles: a) Fe; b) Cu; c) Al; d) CNT; e) CB; f) Mg.

The shape and size of the loaded PAMC visualized by SEM are presented in Figure 5.2. The empty PA6 microparticles (Fig. 5.2a) are present in the form of aggregates of several, partially fused PA6 spheres with typical diameters of 5–10 μm that form final particles of 20–30 μm. This observation is in agreement with the previously postulated effect of coalescence during the PAMC formation [14–16] confirmed later in [10–12]. Larger magnification (image 5.2i) shows that the empty PAMC are porous, with scaffold-like morphology, the pores sizes being typically in the 250–500 nm range.

The SEM images of PAMC carrying binary metal/carbon allotrope (C-allotrope) show a dependence between the size of the larger filler particles and that of the final loaded PAMC. Thus, the PAMC loaded with CNT/Fe (Fig. 5.2b) and CNT/Cu (5.2c) wherein the metal particles are in the 5–20 μm range are only slightly bigger than the empty PAMC. Notably, the surface texture of both PAMC with binary filler is visibly different as compared to Fig. 5.2a, most probably due to epitaxial crystallization of PA6 in the

presence of metal/C-allotrope binary fillers which is impossible in empty PAMC. At the same time, PAMC that contain Al platelets are either significantly larger and less spherical (e.g., DM-Al5-CNT5, image 5.2d), or embed metal platelets (sample DM-Al5-CB5, image 5.2e). In DM-Mg5-CNT5 sample predominate spherical particles with diameters of 20–30 μm (image 5.2f), which could be explained with some fragmentation of the initial Mg platelets during the AAROP due to the energetic stirring.

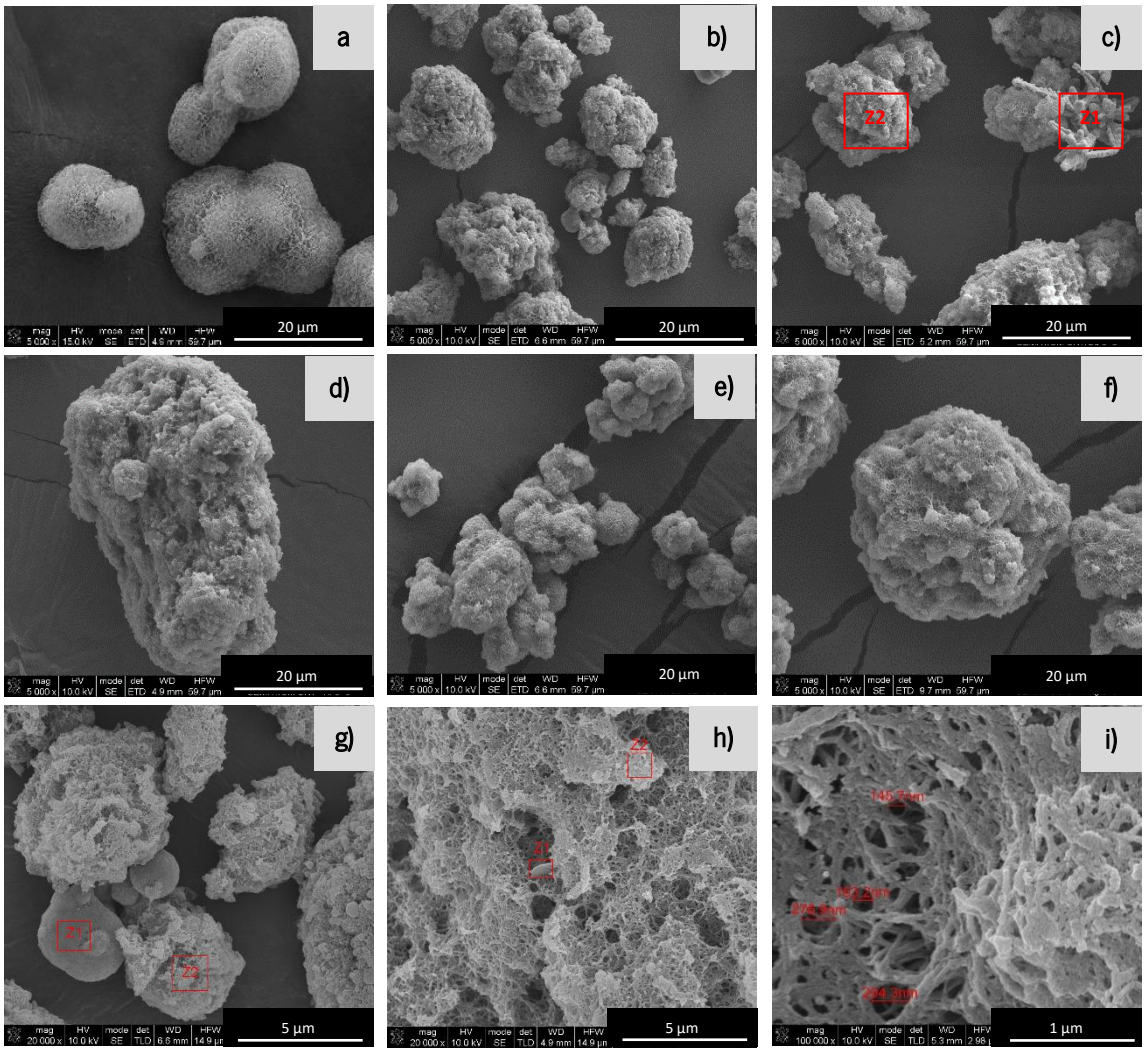

Figure 5.2 | Selected SEM micrographs of DM-samples: a) empty PA6 microcapsules b) DM-Fe5-CNT5; c) DM-Cu5-CNT5; d) DM-Al5-CNT5; e) DM-Al5-CB5; f) DM-Mg5-CNT5; g) same as b), magnified, EDX; h) same as d), magnified, EDX; i) same as a), magnified.

Generally, the metal particles are distributed in the core of PAMC and therefore not directly observable. In some cases, they can be seen close to the PAMC surface as in Fig. 5.2c that shows a PA6 covered Cu particle with its specific form (site Z1). Energy dispersive X-ray spectroscopy (EDX) in this site rendered 69 % of Cu versus 6.7 % in site Z2 where no Cu particle are directly observed. Analogously, the

DM-Al5-CNT5 sample (Fig. 5.2f) in sites Z1 (the supposed Al platelet) and Z2 (the PA6 matrix) renders Al contents of 81 % and 2.5 % respectively. Similar results were obtained in the DM-Fe5-CNT5 sample (Fig. 5.2g), in which Fe particles with different coating by PA6 were obtained containing 71 % Fe (Z1) and only 5.5 % Fe (Z2). In all of the samples in Fig. 5.2 it was not possible to visualize the CNT or CB fillers probably because of their nanometric size and their scattering properties that should be basically the same as of the PA6 matrix.

Figure 5.3 shows the SEM images of selected cryofractured molded plates produced from the respective DM-samples using a rectangular mold with dimensions 85 × 75 × 1 mm.

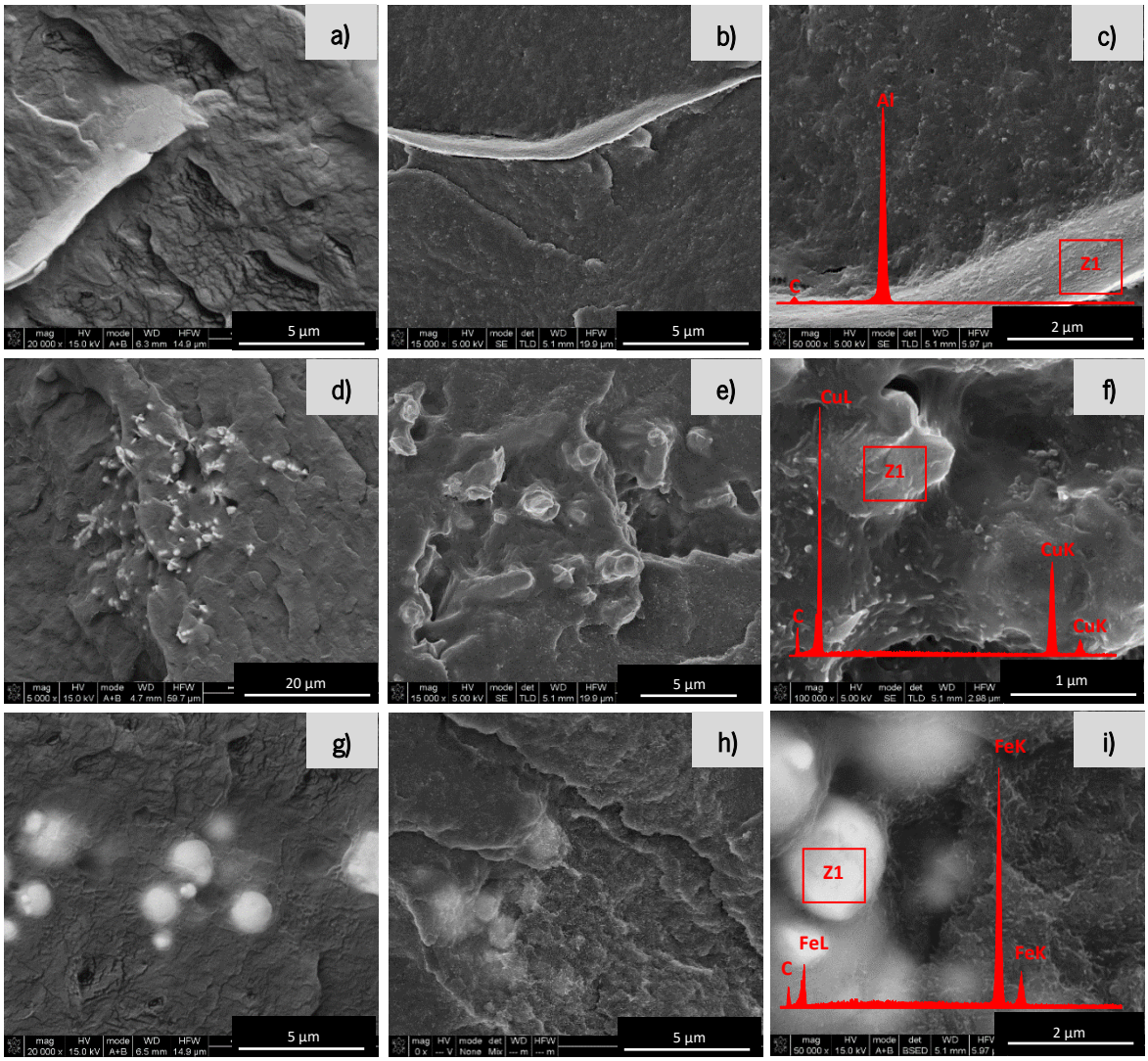

Figure 5.3 | Selected SEM micrographs of selected molded samples: a) P-Al5; b) DP-Al5-CNT5; c) same as c), magnified; d) P-Cu5; e) DP-Cu5-CNT5; f) same as e), magnified; g) P-Fe5; h) DP-Fe5-CNT5; i) same as h), magnified. The right-hand column of images contains the EDX peaks obtained in a certain location Z1.

The left-hand column with images 5.3a, 5.3d and 5.3g reflects the morphology of the PA6-metal composites, containing 5 wt.% of Al, Cu and Fe, respectively. The rest of the SEM images display the surface topography of the molded plates with binary CNT-metal load, 5 wt.% + 5 wt.%. As seen from the micrographs in the middle and especially on the right in Fig. 5.3, the CNT appear as bright nanometric dots being very well dispersed, with almost no aggregation, within the PA6 matrix, as well as on the top of the metal particles (Fig. 5.3c, 5.3f and 5.3i). The EDX curves in these last three images confirms the composition of the electron-rich bright metal particles.

5.4. Thermal properties of microcapsules and composites

5.4.1. By DSC

All samples were subjected to a differential scanning calorimetry (DSC) heating scan at in the 0 – 250 °C, followed by a cooling to 0 °C and a second heating to 250 °C, all scans being performed at a rate of 10 °C/min. Figure 5.4 displays some typical DSC curves of metal/C-allotrope composite systems in the form of either microcapsules or molded composite plates. All data extracted from the DSC curves of the PAMC samples and the respective compression molded plates are presented in Table 5.2.

As observed from the first heating scan of the PAMC samples (Fig. 5.3a, left-hand group of curves), the metal/CNT loaded PAMC display a single narrow melting endotherm at ca. 210 °C, approximately the same as the empty PAMC. This endotherm can be related to the melting of the predominant α-PA6 polymorph [13]. Apparently, the presence of metal and C-allotrope fillers in the loaded PAMC does not influence significantly the melting behavior in this scan. The broad peak centered at 85 °C in some samples of this series should be explained with evaporation of trace amounts of the solvents used in AAROP and the subsequent PAMC isolation. The samples dried for 1 h at 100 °C and immediately subjected to DSC (DM-Cu5-CNT5 and DM-Mg5-CNT5 in Fig. 5.4a) do not show such a peak.

The recrystallization study (Table 5.2, Fig. 5.4b) shows a double exotherm in the 170 – 200 °C, while the empty PAMC sample produces a sharp crystallization peak at 150 °C. This can be explained with two effects: (i) the strong heteronucleation effect of the metal/C-allotrope binary fillers that enhances the crystallizability at elevated temperatures and (ii) formation and coexistence in all loaded PAMC of both α and γ-polymorphs [17]. The lower crystallizing γ-phase in PAMC displays a peak with constant intensity, while the one at the higher temperature (typical for the α-PA6) seems to be slightly dependent on the metal particles type.

It is interesting to follow the effect of the CNT amount on the melting of the PAMC during the DSC scan. The recrystallization of the M-CNT5 sample discussed in Chapter 3 produced a double exotherm in

the 170–190 °C range (Fig. 3.5b). In dually metal-CNT PAMC with 5 % CNT (Fig. 5.4 b), the double exotherm also appears approximately in the same temperature range. At higher CNT content (the DM-Al3-CNT7 sample in Fig. 5.5a) the double exotherm shifts slightly to higher temperatures. Interestingly, the DM-Al5-CB5 sample in Fig. 5.5b containing CB instead of CNT displays one single crystallization peak at 180 °C. Most probably, these differences in the crystallization behavior of dually loaded PAMC, in which the carbon component is CB or CNT should be related to the different geometry of the C-allotrope nanosized fillers – spherical in CB and fibrillar with high aspect ratio in CNT.

Table 5.2 | DSC data comparison between PAMC and the respective compression-molded composites

Sample		First heating scan		Recrystallization [a]	Second heating scan	
		T_m, °C	X_c, [b] %	T_c, °C	T_g, °C	X_c, [b] %
M-	PA6	211.3	35.0	151.1	34.4	20.6
P-		212.8	24.2	159.7	46.8	21.8
DM-	Al3-CNT7	207.1	49.7	183.2	44.1	34.8
DP-		206.2	34.2	174.5	39.0	33.0
DM-	Al5-CNT5	211.8	49.2	176.3	47.6	32.7
DP-		215.2	42.5	177.0	44.6	36.0
DM-	Al7-CNT3	210.4	48.1	174.2	43.4	32.6
DP-		210.7	40.0	174.4	51.0	37.1
DM-	Al5-CB5	204.5	44.6	178.9	49.5	32.9
DP-		205.0	35.7	175.6	53.6	31.2
DM-	Cu5-CNT5	208.5	43.8	173.9	43.2	30.1
DP-		211.9	34.3	174.7	46.5	35.5
DM-	Fe5-CNT5	210.9	45.4	175.5	41.6	32.6
DP-		212.1	45.5	177.3	43.8	36.7
DM-	Mg5-CNT5	208.4	48.0	172.3	38.1	31.2
DP-		211.8	34.4	160.7	42.6	33.6

[a] Determined after first DSC scan under fast cooling down;

[b] Determined according to Eq. 2.12 of Chapter 2.

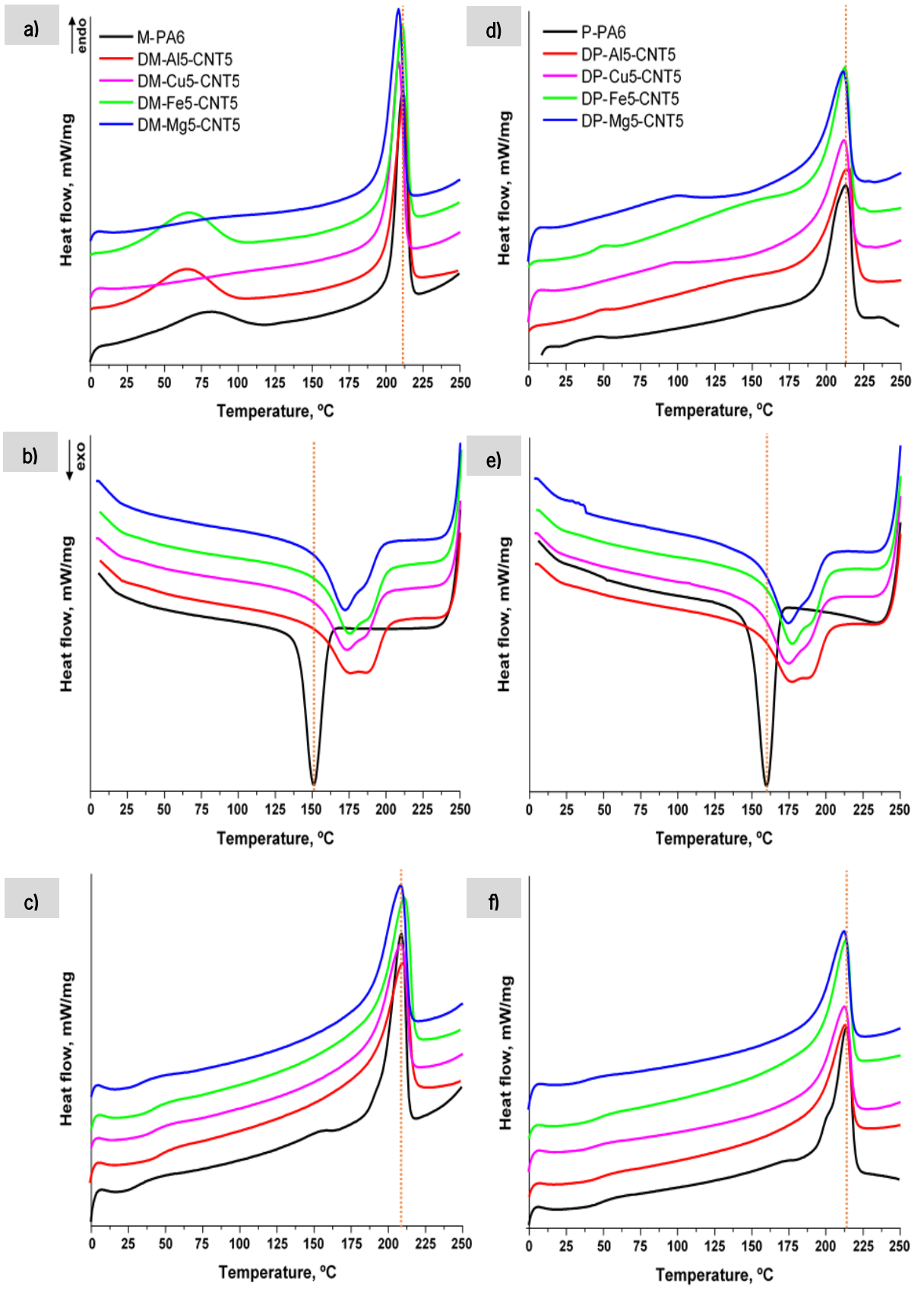

Figure 5.4 | Typical DSC traces of metal/CNT PA6 systems: a, d) first heating scan; b, e) recrystallization from the melt; c, f) second heating scan. Left: DM-samples; Right: DP-samples produced from the respective DM-samples by CM.

The second DSC scan of the PAMC (Fig. 5.4c) results in uniformization of the melting temperature for all samples, however all melting endotherms become broader indicating the presence of more γ-PA6 with lower melting point. The DSC traces (first and second scans, and recrystallization) of the molded composite plates (Fig. 5.4d-f) are similar to that of the respective PAMC. The only difference is that even during the first scan all composites show a mixture of the two PA6 polymorphs proved by the broader endotherms, i.e. the first DSC scan of the composites resembles the second scan of PAMC. This is to be expected since the composites were prepared by compression molding of the respective PAMC.

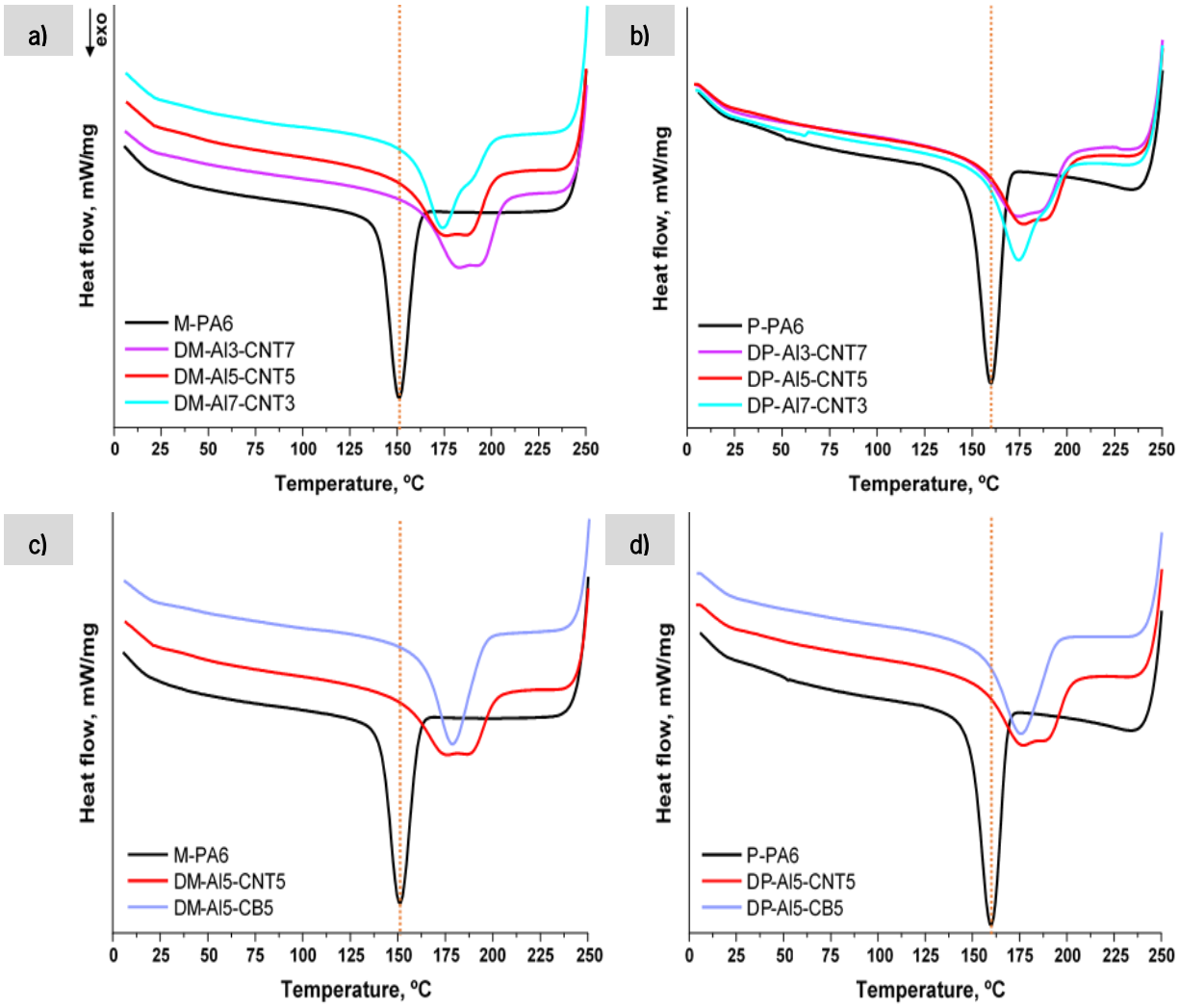

Figure 5.5 | Recrystallization from the melt of Al/C-allotrope PA6 systems: a, b) Al-CNT systems with total 10 wt.%; c, d) Al/C-allotrope systems 5/5 wt.%. Left: DM-samples; Right: DP-samples produced from the respective DM-samples by CM.

Table 5.2 shows that the values of the DSC crystallinity index, X_c, of all PAMC samples obtained during the first scan is always higher than those in the second scan. This can be related to the isothermal crystallization of PAMC during the AAROP carried out for 1 h at 120 – 130 °C that would produce larger and more perfect PA6 crystallites as compared to those obtained during the non-isothermic and much faster crystallization within the DSC equipment during the second scan. This observation confirms the previously established fact that the thermal history of the PA6 sample is of prime importance for its crystallinity index [18, 19].

Comparing the glass transition temperatures, T_g, of PAMC and molded plates allows the conclusion that the T_g of empty PAMC (34.4 °C) is significantly lower than in the neat PA6 plate sample (46.8 °C). This means that the segmental mobility of the amorphous PA6 chains in PAMC is much higher than in the molded PA6 plate which should be related with the pressure applied during the compression molding, leading to more compact and dense microstructures. According to Table 5.2, introducing the binary metal/C-allotrope filler into the amorphous regions of the matrix, as a rule, increases the T_g of PAMC, meaning lower segmental mobility of chains. Apparently, in the samples containing large metal particles (i.e., in the Al7-CNT3 and Al5-CB5) the drop of the segmental mobility in both PAMC and molded plates is the highest.

5.4.2. By TGA

All DM-samples and the respective molded composites were studied by TGA in order to establish the thermal stability of the samples as a function of the load type and amount and to determine the real amount of fillers. Figure 5.6 displays the TGA traces of selected composites. Table 5.3 summarizes the numerical data of the thermal degradation of all samples. The determination of the real load content on the basis of the carbonized residue at 600 °C is shown in Table 5.1. This method should account not only for the metal filler content but, as demonstrated in previous work [11], also for that of the C-allotropes.

As seen from Figure 5.6 and Table 5.3, the empty PAMC and the neat PA6 plate show their 10 % weight losses up to ca. 300°C ($T_{10\%}$). The data from the first derivative curves (Table 5.3) of these samples suggest a single degradation processes with temperatures of maximum degradation rate (T_{max}) of 340 °C and 354 °C, respectively. The samples with compositions Mg5-CNT5 and Cu5-CNT5 in either PAMC or molded plate produced $T_{10\%}$ and T_{max} being similar or even slightly below those of the respective PA6

counterparts. The microcapsules containing Mg and CNT display a second degradation process with T_{max} = 384 °C not present in the composite. The Al5-CNT5 and the Fe5-CNT5 samples show significantly higher values for $T_{10\%}$ (with 15-70°C) and for the first T_{max} with up to 25 – 30 °C. In both samples, a second degradation process appears with $T_{max\,II}$ values of up to 465 °C (Table 5.3). This means that the binary Al-CNT and Fe-CNT fillers can significantly improve the heat resistance of the PA6 matrix material at low and maximal degradation rate. The Al5-CB5 sample (PAMC and plate) show also a high degradation process at T_{max} > 400°C but its $T_{10\%}$ values are even lower than those of the PA6. Summarizing, in terms of heat resistance the Al-CNT composites in either particulate or molded forms containing equal weight amounts of Al and CNT seem to be with optimal thermal degradation properties, especially in the form of plate. Only with Al3-CNT7 compositions some weight loss below 200 °C was found, most probably due to the presence of oligomer products in the respective PAMC that are then transferred to the molded product (Table 5.3).

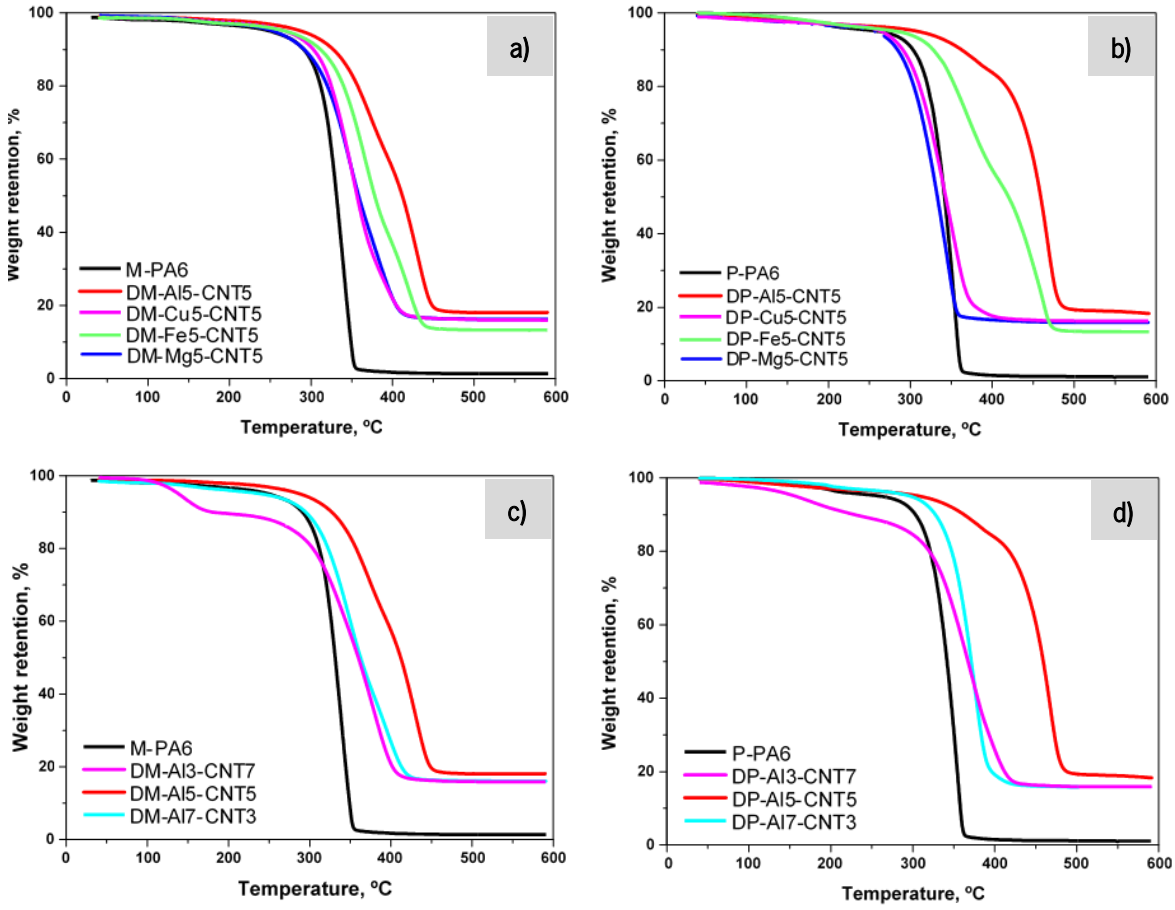

Figure 5.6 | Selected TGA integral curves of: (a, c) PAMC; (b, d) molded plates from respective PAMC.

Table 5.3 | Data from TGA about the thermal degradation of dually loaded DM- and DP-samples

Sample		$T_{10\%}$ [a]	T_{max}, °C [b]		Residue at 600 °C, %	Real load, wt.%
			I	II		
M-	PA6	295.4	339.3	-	1.4	-
P-		303.8	354.0	-	1.1	-
DM-	Al3-CNT7	205.0	146.2	376.9	15.8	14.4
DP-		252.1	373.8	-	15.9	14.9
DM-	Al5-CNT5	331.0	373.0	431.0	18.1	16.7
DP-		371.2	375.2	467.3	18.3	17.3
DM-	Al7-CNT3	301.3	348.3	395.4	16.1	14.7
DP-		328.1	375.1	-	15.9	14.8
DM-	Al5-CB5	282.0	367.7	392.0	16.5	15.1
DP-		301.5	382.9	415.6	16.2	15.2
DM-	Cu5-CNT5	306.8	351.1	-	16.1	14.8
DP-		294.1	352.0	-	16.3	15.2
DM-	Fe5-CNT5	319.1	366.1	419.5	13.3	11.9
DP-		328.5	371.5	461.6	13.3	12.3
DM-	Mg5-CNT5	294.9	347.0	384.0	16.3	14.9
DP-		286.6	345.9	-	15.9	14.9

[a] $T_{10\%}$ = Temperature of 10 % weight-loss;

[b] T_{max} = Maximum degradation temperature obtained from the 1st derivative of the TGA curves;

5.5. Mechanical properties in tension

Figure 5.7 shows representative stress-strain curves of the DP-samples produced by CM of respective binary loaded PAMC compared with that of the neat PA6. Table 5.4 presents the data about E, σ_{br}, and ε_{br}, extracted from the stress-strain curves, as well as the IF for the E and σ_{br} values. The neat PA6 displays ductile behavior with a well-expressed yield point at σ = 48 MPa and ε = 10 – 20 % strain and hardening region reaching the ε_{br} value at ca. 220 %. The E value of 1.59 GPa (Table 5.4)

is typical of anionic PA6 [20] and higher than that of hydrolytic non-oriented neat PA6, which was close to 1.0 GPa [21].

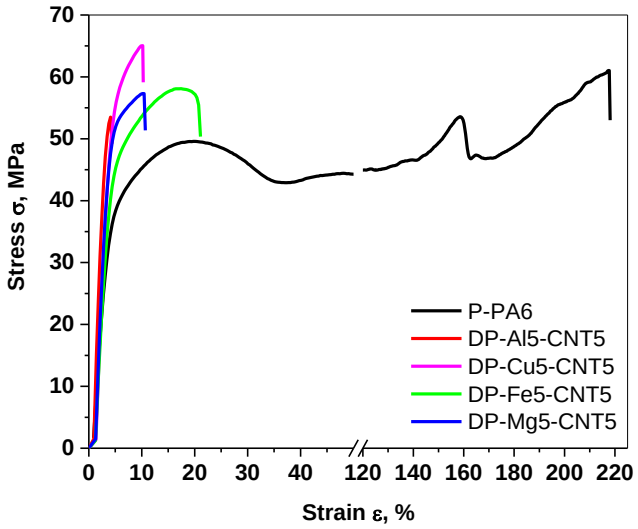

Figure 5.7 | Selected stress-strain curves of compression molded composite plates produced from loaded PAMC containing dual metal-CNT fillers (5/5 wt.%).

Table 5.4 | Mechanical properties of P-samples molded from CNT and metal-loaded PAMC

Sample	Young's modulus, E (GPa)	IF (%) [a]	Stress at break, σ_{br} (MPa)	IF (%) [a]	Deformation at break, ε_{br} (%)
P-PA6	1.59 ± 0.05	–	60.7 ± 3.9	–	218.3 ± 4.3
DP-Al3-CNT7	1.57 ± 0.01	-1.3	43.8 ± 1.5	-27.8	15.9 ± 1.3
DP-Al5-CNT5	2.53 ± 0.06	59.1	52.3 ± 2.2	-13.8	4.3 ± 0.6
DP-Al7-CNT3	2.33 ± 0.02	46.7	48.3 ± 1.5	-20.4	7.1 ± 1.2
DP-Al5-CB5	1.61 ± 0.04	1.8	38.2 ± 1.1	-37.1	10.4 ± 1.0
DP-Cu5-CNT5	2.08 ± 0.03	31.7	60.2 ± 6.9	0.0	12.7 ± 3.0
DP-Fe5-CNT5	1.86 ± 0.06	17.7	56.7 ± 1.7	- 6.6	21.5 ± 2.9
DP-Mg5-CNT5	2.12 ± 0.05	34.5	59.9 ± 9.0	- 1.3	10.7 ± 3.3

[a] In respect to neat anionic PA6 plate obtained from empty PAMC, calculated according to Eq. 2.14 of Chapter 2.

The binary metal-CNT molded composites in Fig. 5.7 display a fragile fracture with ε_{br} between 4 – 22 %, no yield point and a notable improvement of the E values of 18 – 59 % with respect to the matrix PA6. Interestingly, the highest E-values are observed whenever the C-allotrope is CNT (i.e.,

nanofibrils with high aspect ratio) and at weight ratio metal/CNT of 1:1. At the same time, the decrease of the σ_{br} values in these composites is in the 7 – 20 %. It should be noted that for all binary composites in Fig. 5.6 the σ_{br} values are higher than the yield point stress of neat PA6 which could be of importance for their further applications.

5.6. Electrical conductivity and dielectric properties

The d.c. electrical conductivity, σ_{dc}, dielectric constant, ε', and the loss factor, $\tan\delta$, were determined for all DP-samples produced from respective dually loaded PAMC, and the data obtained are summarized in Table 5.5.

First, the electrical properties of the binary metal-carbon composites (5/5 wt.%) were compared to composites comprising 5 wt.% of either one C-allotrope or one single metal load (Table 5.5). As demonstrated in an earlier publication on PA6-metal hybrids obtained via microencapsulation [12] such systems maintain the electrical insulating properties of the neat PA6 matrix showing σ values in the range of 10^{-10} to 10^{-9} S/m even in the metal concentration is raised up to 30 % by weight. This phenomenon is in a good agreement with the Maxwell–Wagner–Sillars (MWS) interfacial polarization theory. The MWS predicts no electrical conduction of a composite material containing conductive filler particles dispersed in an insulating matrix at any filler volume fraction [22]. The reason is that the filler particles are always completely enclosed by the non-conductive matrix polymer, which impedes the free movement of charges. As seen from the SEM studies in Fig. 5.3 (images a, d, and g), complete enclosure of the metal particles in the PA6 matrix material is observed in the PA6-metal hybrids. On the contrary, the P-CNT5 or P-CB5 composites obtained earlier by microencapsulation [11] show a seven and eight order of magnitude improvement of the electrical conductivity, that is, from 10^{-10} to 10^{-2} S/m. These results were obtained with 5–8 wt.% of CNT or CB meaning that these concentrations are above the percolation threshold and a conductive network was built with effective charge transfer.

For the samples of the present study containing different amounts of a combined Al–CNT filler (Table 5.5), σ values of up to $3 - 4 \times 10^{-1}$ S/m were measured being ca. three to four times higher than in a P-CNT5 sample (Table 5.5). Comparing the DP-Al5–CB5 sample and the P-CB5 samples shows more than 10 times higher conductivity. It seems that if a PA6 insulating matrix embeds both well-dispersed metal microparticles and a conductive network of CNT or CB nanoparticles, the MWS polarization is not only eliminated but, in some cases, a synergetic effect of significant conductivity increase is produced.

Evidently, the co-presence in the PA6 matrix of a sufficient amount of nanosized CNT or CB and conductive metal particles promotes the charge mobility at the metal-polymer matrix interface.

Table 5.5 | Electrical properties of PA6 hybrid plates obtained by CM of loaded PAMC

Sample	Conductivity, σ_{dc} (S/m)	Dielectric constant [a], ε'	Loss factor [a], $\tan\delta$
P-PA6	6.21E-10 ± 1.53E-11	6.50E+00 ± 7.00E-02	5.31E-02 ± 1.90E-03
P-CNT5	1.26E-01 ± 1.11E-02	3.93E+02 ± 9.80E+00	1.19E+02 ± 3.70E-01
P-CB5	2.02E-02 ± 1.02E-03	5.32E+02 ± 2.65E+00	1.97E+00 ± 3.40E-03
P-Al5	9.10E-09 ± 3.91E-10	5.01E+00 ± 8.70E-01	1.73E-04 ± 9.63E-05
P-Cu5	2.80E-08 ± 1.35E-09	2.30E+01 ± 2.13E+00	5.02E-02 ± 2.48E-03
P-Fe5	9.63E-09 ± 6.12E-10	2.42E+01 ± 1.47E+00	5.00E-02 ± 3.56E-03
P-Mg5	6.13E-09 ± 1.64E-10	2.46E+01 ± 1.35E+00	5.01E-02 ± 2.21E-03
DP-Al3-CNT7	4.06E-01 ± 1.16E-02	1.36E+03 ± 1.26E+02	6.90E+01 ± 1.30E-01
DP-Al5-CNT5	3.31E-01 ± 1.40E-02	2.28E+02 ± 2.57E+01	4.08E-01 ± 2.00E-02
DP-Al7-CNT3	3.60E-03 ± 2.21E-04	7.41E+02 ± 3.14E+01	3.44E+03 ± 3.06E+02
DP-Al5-CB5	1.32E-01 ± 1.63E-02	2.13E+02 ± 2.61E+01	5.61E+00 ± 1.70E+00
DP-Cu5-CNT5	3.28E-02 ± 1.24E-03	2.74E+02 ± 5.31E+01	2.92E+01 ± 5.11E+00
DP-Fe5-CNT5	1.72E-02 ± 3.87E-03	6.77E+01 ± 3.99E+00	9.79E+00 ± 7.10E-01
DP-Mg5-CNT5	3.80E-02 ± 1.16E-03	4.06E+02 ± 2.61E+01	4.90E+01 ± 1.91E+01

[a] Values obtained at 1 MHz.

The conductive properties of the DP-Al5–CB5 binary composite indicate that the expensive CNT can be substituted by the much cheaper CB maintaining the electrical conductivity in the same range. This is important for the application of such binary PA6 hybrids. Moreover, the DP-Al5–CNT5 sample presents an interesting feature: together with good electrical conductivity, it displays also a low loss factor $\tan\delta$ (Table 5.5), while in most of the other samples the latter increases as the d.c. conductivity also increases. This means that the electric/dielectric properties of the binary composites of this study can be conveniently changed by variation of the metal/C-allotrope relation, the type of the metal or C-allotrope and their amount in the composite.

Figure 5.7a-c displays the semilogarithmic plots of ε' as a function of the frequency for the metal-CNT 5/5 wt.% composites. At 1 MHz, the composite DP-Fe5-CNT5 shows lower ε' (67.7) than the DP-Al5-, Mg5- and Cu5-CNT5 composites, with ε' values of ca. 100. Fig. 5.7c shows that the DP-Al5-CNT5 sample keeps almost constant values of the ε' (500–200) independently of the frequency which could be interesting in some applications. Once again, the use of various metals, C-allotropes in different concentrations or relations in the binary composites leads to tunable conductive and dielectric properties.

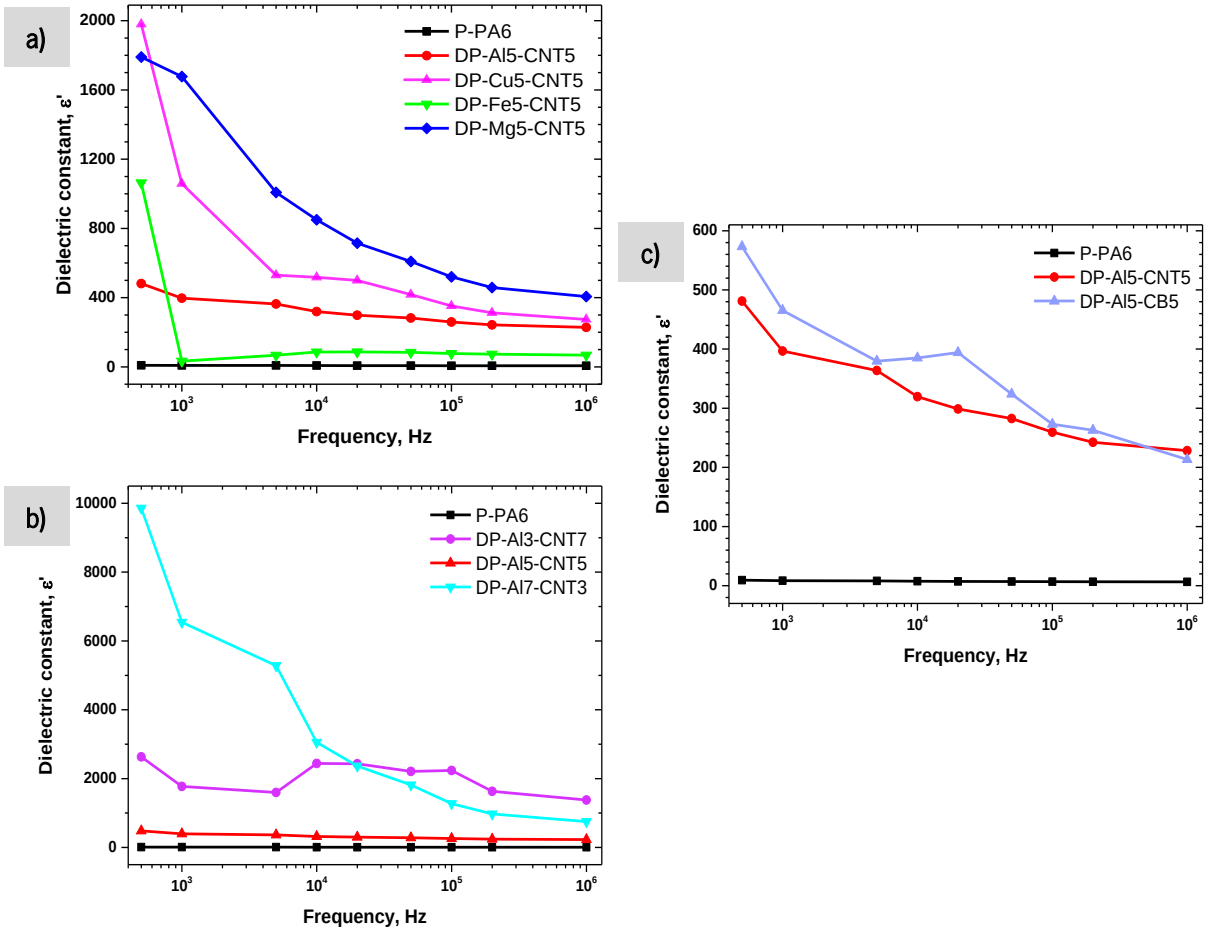

Figure 5.8 | Dielectric constant as a function of frequency for compression molded composite plates produced from loaded PAMC containing: a) metal-CNT 5/5 wt.%; b) Al-CNT with total 10 wt.%; c) Al-C allotrope 5/5 wt.%.

5.7. NMR studies of selected hybrid polyamide 6 microcapsules

ssNMR spectroscopy provides structural and molecular dynamic data obtained from the interaction between electromagnetic radiation and matter. This non-destructive method was used in the study of electrical and magnetic properties of the prepared materials. A loss of NMR signal was expected with

increasing amounts of fillers with paramagnetic or conductive properties, due to a skin effect caused by the conductive properties of fillers limiting the adsorption of radiofrequency [23]. First analyses were performed with PAMC of M-AI10, M-CNT5, DM-AI7–CNT3, and DM-AI3–CNT7 samples for the observation of ^{13}C resonances at 75 MHz. Figure 5.9 represents the CP-MAS ^{13}C ssNMR full-range spectra of the analyzed materials. In addition, the chemical structure of PA6 and the carbon numbering followed in this study is illustrated within Fig. 5.9. All spectra contain at least two spinning bands due to the chemical shift anisotropy of the carbonyl groups. Table 5.6 displays the ^{13}C chemical shifts obtained for the PAMC samples investigated.

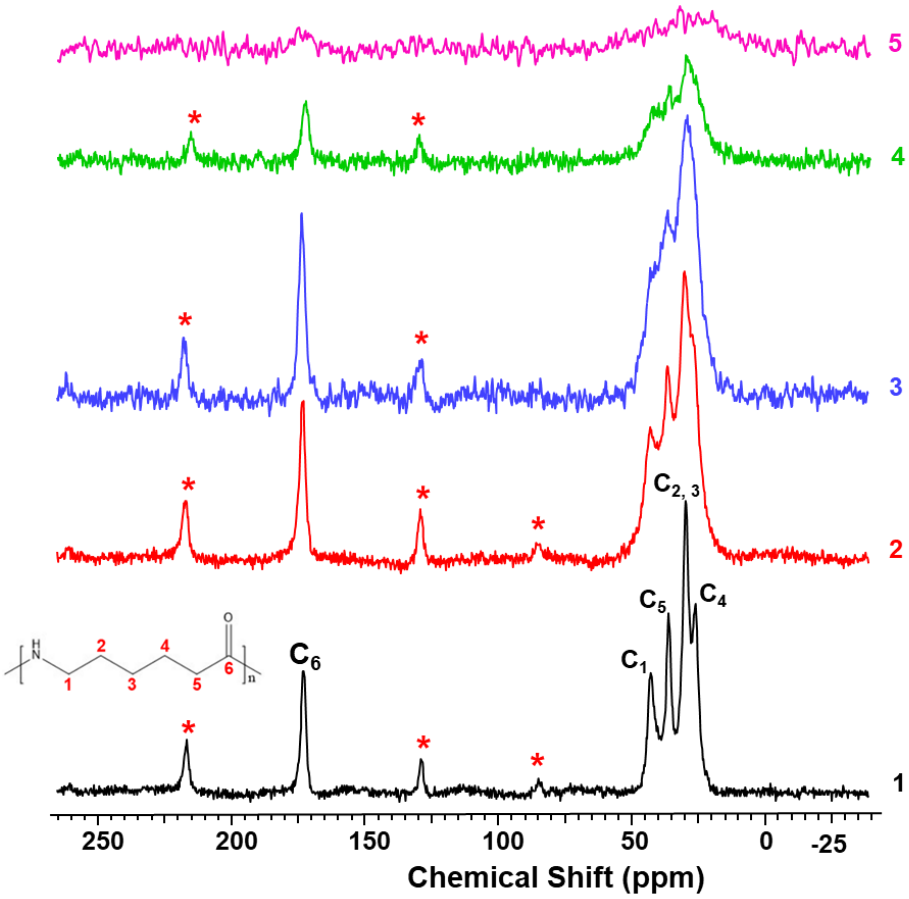

Figure 5.9 | ^{13}C CP-MAS spectra of PAMC: 1) M-PA6; 2) M-CNT5; 3) M-AI10; 4) DM-AI7-CNT3; 5) DM-AI3-CNT7. Asterisks denote spinning sidebands. The curves in this staked plot are with normalized intensities.

By comparing M-PA6 and M-CNT5 spectra (Fig. 5.9), it is noticed that the CNT loaded microcapsules cause a slight increase of peak width in the region of the aliphatic carbons which results on the following chemical shifts (carbon numbers within parentheses): 42.6 (C1), 30.2 (C2 + C3), 27.1

(C4), and 36.5 (C5). On the other hand, when Al is used as filler, the signal resolution strongly decreases and the resonance from C4 nucleus is not resolved. The resolution and the peak intensity decrease further on the binary Al–CNT 7/3 spectrum: the signal to noise ratio is low and, consequently, almost all the aliphatic carbon signals are unresolved. The effect of dispersion of conductive fillers on PA6 is well present on the binary Al–CNT 3/7 due to the nearly complete disappearance of the ssNMR peaks. This event suggests that the mixture of metal-carbon fillers has a shielding effect on the radiofrequency (RF) pulses used to irradiate the polymeric matrix at 75 and 300 MHz (see section 2.4.4 of Chapter 2 for details on the RF sequence). These preliminary results may be correlated with the electrical properties of the composites under study. Hence, they provide an indication about the capability of the binary composites containing C-allotropes and metal particles to be applied in RAM.

Table 5.6 | Chemical shifts registered for the carbons in ^{13}C ssNMR spectra of loaded PAMC

Sample	Chemical shifts of carbons, ppm				
	C1	C2+C3	C4	C5	C6
M-PA6	42.8	29.7	25.8	36.0	172.9
M-CNT5	42.6	30.2	27.1	36.5	173.3
M-Al10	41[a]	29.1	Unresolved	36.3	173.5
DM-Al7-CNT3	Unresolved	29.7	25[a]	35.8	172.0
DM-Al3-CNT7	Unresolved	Unresolved	Unresolved	Unresolved	Unresolved

[a] Not well resolved.

5.8. Summary

The solution/precipitation activated anionic polymerization of ECL in the presence of binary metal and C-allotrope fillers is a useful route for the preparation of PA6 microcapsules bearing two different payloads at the same time. The CM of these loaded microcapsules produces PA6-based composites with binary reinforcements. By appropriately changing the metal, the C-allotrope and their relation, composite plates with increased resistance to thermal degradation, high *E*-modulus and tailored electrical properties, with a strong increase of both electrical conductivity and dielectric response can be prepared. The best performing composite systems contain Al and CNT or CB. Varying the relation between Al and CNT molded composites has enabled reducing resonance signals nearly completely at the probed NMR frequencies. This last study exemplifies one of the possible applications of the novel binary metal/C-

allotrope PA6 hybrids, i.e., for radio wave absorbers. A factor of prime importance to get such unusual set of properties in the metal–CNT PA6 hybrids was the good distribution of high loads of metal microparticles and CNT/CB nanoparticles within the PA6 matrix successfully achieved by the microencapsulation-compression molding method used in this thesis.

5.9. References

[1] Al-Saleh MH, Saadeh WH, Sundararaj U (2013) EMI shielding effectiveness of carbon based nanostructured polymeric materials: A comparative study. *Carbon N Y*, 60:146–156. DOI: 10.1016/j.carbon.2013.04.008

[2] Thomassin J-M, Jérôme C, Pardoen T, Bailly C, Huynen I, Detrembleur C (2013) Polymer/carbon based composites as electromagnetic interference (EMI) shielding materials. *Mater Sci Eng R Reports*, 74:211–232. DOI: 10.1016/j.mser.2013.06.001

[3] Chen YJ, Gao P, Zhu CL, Wang RX, Wang LJ, Cao MS, Fang XY (2009) Synthesis, magnetic and electromagnetic wave absorption properties of porous Fe3O4/Fe/SiO2 core/shell nanorods. *J Appl Phys*, 106:054303. DOI: 10.1063/1.3204958

[4] Liu P-B, Huang Y, Sun X (2013) Excellent Electromagnetic Absorption Properties of Poly(3,4-ethylenedioxythiophene)-Reduced Graphene Oxide–Co3O4 Composites Prepared by a Hydrothermal Method. *Appl Mater Interfaces*, 5:12355–12360. DOI: 10.1021/am404561c

[5] Vyas MK, Chandra A (2016) Ion–Electron-Conducting Polymer Composites: Promising Electromagnetic Interference Shielding Material. *Appl Mater Interfaces*, 8:18450–18461. DOI: 10.1021/acsami.6b05313

[6] Yan J, Huang Y, Wei C, Zhang N, Liu P (2017) Covalently bonded polyaniline/graphene composites as high-performance electromagnetic (EM) wave absorption materials. *Compos Part A Appl Sci Manuf*, 99:121–128. DOI: 10.1016/j.compositesa.2017.04.016

[7] Dar MA, Kotnala RK, Verma V, Shah J, Siddiqui WA, Alam M (2012) High Magneto-Crystalline Anisotropic Core–Shell Structured Mn0.5Zn0.5Fe2O4/Polyaniline Nanocomposites Prepared by in Situ Emulsion Polymerization. *J Phys Chem C*, 116:5277–5287. DOI: 10.1021/jp205652d

[8] Peng BJ, Walton JH, Cherry SR, Willig-Onwuachi J (2010) Studies of the interactions of an MRI system with the shielding in a combined PET/MRI scanner. *Phys Med Biol*, 55:265–280. DOI: 10.1088/0031-9155/55/1/016

[9] Peng BJ, Wu Y, Cherry SR, Walton JH (2014) New shielding configurations for a simultaneous PET/MRI scanner at 7T. *J Magn Reson*, 239:50–56. DOI: 10.1016/j.jmr.2013.10.027

[10] Dencheva N, Denchev Z, Lanceros-Méndez S, Ezquerra Sanz T (2016) One-step in situ synthesis of polyamide microcapsules with inorganic payload and their transformation into responsive thermoplastic composite materials. *Macromol Mater Eng*, 301:119–124. DOI: 10.1002/mame.201500194

[11] Oliveira F, Dencheva N, Martins P, Lanceros-Mendez S, Denchev Z (2016) Reactive microencapsulation of carbon allotropes in polyamide shell-core structures and their transformation in hybrid composites with tailored electrical properties. *eXPRESS Polym Lett*, 10:160–175. DOI: 10.3144/expresspolymlett.2016.15

[12] Brêda C, Dencheva N, Lanceros-Mendez S, Denchev Z (2016) Preparation and properties of metal-containing polyamide hybrid composites via reactive microencapsulation. *J Mater Sci*, 51:10534–10554. DOI: 10.1007/s10853-016-0274-0

[13] Dencheva NV, Vale DM, Denchev ZZ (2016) Dually reinforced all-polyamide laminate composites via microencapsulation strategy. *Polym Eng Sci*, 57:806–820. DOI: 10.1002/pen.24456

[14] Dan F, Vasiliu-Oprea C (1998) Anionic polimerization of caprolactama in organic media. Morphological aspects. *Colloid Polym Sci*, 276:483–495. DOI: 10.1007/s003960050270

[15] Vasiliu-Oprea C, Dan F (1997) On the relation between synthesis parameters and morphology of anionic polycaproamide obtained in organic media. II. Influence of the Na[O(CH2)2OCH3]2AlH2/aliphatic diisocyanates catalytic systems. *J Appl Polym Sci*, 64:2575–2583. DOI: 10.1002/(SICI)1097-4628(19970627)64:13<2575::AID-APP11>3.0.CO;2-Z

[16] Dan F, Vasiliu-Oprea C (1998) On the relationship between synthesis parameters and morphology of the anionic polycaproamide obtained in organic media. III. Macroporous powders obtained using CO2 and carbodiimides as activating compounds. *J Appl Polym Sci*, 67:231–243. DOI: 10.1002/(SICI)1097-4628(19980110)67:2<231::AID-APP5>3.0.CO;2-V

[17] Li Y, Goddard WA (2002) Nylon 6 Crystal Structures, Folds, and Lamellae from Theory. *Macromolecules*, 35:8440–8455. DOI: 10.1021/ma020815n

[18] Fornes TD, Paul DR (2003) Crystallization behavior of nylon 6 nanocomposites. *Polymer (Guildf)*, 44:3945–3961. DOI: 10.1016/S0032-3861(03)00344-6

[19] Pesetskii SS, Jurkowski B, Olkhov YA, Bogdanovich SP, Koval VN (2005) Influence of a cooling rate on a structure of PA6. *Eur Polym J*, 41:1380–1390. DOI: 10.1016/j.eurpolymj.2004.12.009

[20] Dencheva N, Denchev Z, Pouzada AS, Sampaio AS, Rocha AM (2013) Structure–properties relationship in single polymer composites based on polyamide 6 prepared by in-mold anionic polymerization. *J Mater Sci*, 48:7260–7273. DOI: 10.1007/s10853-013-7546-8

[21] Dencheva N, Denchev Z, Oliveira MJ, Funari SS (2007) Relationship between crystalline structure and mechanical behavior in isotropic and oriented polyamide 6. *J Appl Polym Sci*, 103:2242–2252. DOI: 10.1002/app.25250

[22] Steeman PAM, van Turnhout J (2003) Dielectric Properties of Inhomogeneous Media. In: Kremer F, Schönhals A (eds) Broadband Dielectric Spectroscopy. Springer Berlin Heidelberg, Berlin, Heidelberg, pp 495–522

[23] Jouni M, Buzlukov A, Bardet M, Boisson F, Eddarir A, Massardier V, Boiteux G (2014) Skin effect of conductive polymer composites observed by high-resolution solid-state NMR. *Compos Sci Technol*, 104:104–110. DOI: 10.1016/j.compscitech.2014.08.031

CHAPTER 6

Preparation and properties of binary metal/carbon fiber textile polyamide 6 laminate composites

This chapter is based on the article:

Oliveira, F.; Dencheva, N.; Martins, P.; Lanceros-Méndez, S.; Denchev, Z. A New Approach for Preparation of Metal-Containing Polyamide/Carbon Textile Laminate Composites with Tunable Electrical Conductivity. *J. Mater. Sci.* 2018, *53*, 11444–11459. DOI: 10.1007/s10853-018-2435-9.

6.1. Introduction

Polymer composites reinforced by carbon fibers or textiles thereof (CFT) are being used for more than four decades in a steadily increasing number of applications replacing metal-based structures in many industries. Traditional *thermoset* CFT composites based on epoxy, polyester or phenolic matrices deliver exceptional stiffness and strength, being at the same time very lightweight. The *thermoplastic* CFT polymer composites (TPC/CFT) possess some advantages as compared to their thermoset counterparts, such as higher toughness of the matrix, higher impact resistance at low temperature, and significantly shorter manufacturing cycles. In addition to being lightweight, TPC can be welded [1] and in some cases recycled by reprocessing [2], which is important in view of the rigorous requirements for environmental protection imposed in most industrialized countries.

Generally, fiber-reinforced TPC are manufactured by melt-processing of the polymer matrix and the mineral reinforcement [3–7]. The common shortcoming of the melt processing techniques is the high viscosity of the melted polymer matrix material and the related insufficient wetting of the reinforcement resulting in a weak matrix/reinforcement interface. An alternative way to produce TPC is by reactive processing techniques, where the TPC is obtained in situ, through polymerization of low-viscosity monomers or oligomers in the presence of the reinforcements [8–12].

A common disadvantage of the reactive processing methods is the inevitable formation of low molecular weight fraction during the polymerization stage. It is impossible to remove and leads to the deterioration of the mechanical properties of the finished composite part. An additional limitation of the CFT-reinforced thermosets and thermoplastics is the fact that the conventional matrix polymers are electric insulators that can be limiting for some applications. Diverse methods have been used to improve this material property using chemical vapor deposition of copper thin films for the metallization of the laminate [13–18]. All these procedures require expensive and specific equipment with high processing costs, the part sizes and shapes being limited to the equipment geometry.

This chapter suggests a novel two-stage process to produce TPC/CFT laminate composites based on polyamide 6 (PA6) that combines the advantages of the reactive processing and the carbon fiber metallization concept. First, metal-containing PA6 microcapsules (PAMC) are prepared via reactive microencapsulation process in which various types of finely divided metals are incorporated into PA6 particles formed during solution/precipitation activated anionic ring-opening polymerization (AAROP) of ε-caprolactam (ECL) monomer. Thus, pulverulent PA6 material free of low molecular weight fraction and optimal metal particles content and distribution can be produced. The latter is used in the second stage for powder-coating of CFT plies consolidated thereafter into polyamide TPC/CFT by compression

molding. The morphology of the resulting multiscale composites was explored by light and scanning electron microscopy (SEM) and correlated with their electrical conductivity, dielectric properties and mechanical properties in tension.

6.2. Sample preparation

The binary metal-carbon textile reinforced laminates were prepared through a two-stage process. First, metal-loaded PAMC precursors were produced that were then compression molded with carbon fiber textiles. The hybrid PAMC precursors were synthesized by a microencapsulation process as described in ref. [19–21] Details of the procedures can be found in Chapter 2, section, 2.3.2. The loaded PAMC containing 10 wt.% metal (Al, Cu, Fe, and Mg) formed as a fine powder with metallic luster typical of the respective metal load. The yields of empty PAMC were 56 % (in respect to ECL) and 45–49 % for the metal-loaded PAMC (Chapter 3, Table 3.1).

The PA6 laminate composites dually reinforced by metal and CFT (L-samples) were prepared by compression molding of the respective metal-loaded PAMC with two volume fractions of CFT V_f = 0.25 and 0.50. For more details see Chapter 2, section 2.3.4.2. Composites without CFT (P-samples) were prepared by compression molding (CM) of metal-containing PAMC at the same processing conditions and used as references.

Table 6.1. presents all samples of this study with their designations, as well as information about the real metal content, CFT volume fractions and the number of textile plies employed. For all samples, the real load (RL) was determined by thermogravimetric analysis (TGA) according to Eq. 2.13 of Chapter 2. Since the polymerization yields were in the range of 50 % in respect to ECL, the RL in PAMC were expected to be almost twice as high as in the starting reaction mixture. This was the case with the Al- and Cu-containing PAMC where RL values of 18–19 % were observed. The smaller RL in the Mg-loaded PAMC can be attributed to the very low density of the Mg particles resulting in their loss during AAROP that is performed under reflux and nitrogen flow. In the case of the PAMC containing Fe, a part of the metal particles gets stuck to the magnetic stirrer and is therefore not involved in microcapsules that resulted in lower RL.

Table 6.1 | Designation of all composite materials prepared by CM with and without CFT

Sample	Real load, wt.% [a]	CFT load, %	No. CFT plies
P-PA6	0	0	0
L-PA6-25	-	25	4
L-PA6-50	-	50	9
P-Al10	19.4	0	0
L-Al-25	-	25	4
L-Al-50	-	50	9
P-Cu10	17.6	0	0
L-Cu-25	-	25	4
L-Cu-50	-	50	9
P-Fe10	13.4	0	0
L-Fe-25	-	25	4
L-Fe-50	-	50	9
P-Mg10	13.0	0	0
L-Mg-25	-	25	4
L-Mg-50	-	50	9

a) Determined by TGA according to Eq. 2.13 of Chapter 2.

6.3. Microscopy studies

The scanning electron micrographs in Figure 6.1 present information about the size and shape of the used metal particles. The Al and Mg particles (images 6.1a and 6.1c) are shaped as platelets with maximum sizes of 100–350 μm and 300–400 μm respectively, and thicknesses of ca. 1–10 μm. The Cu particles (image 6.1b) display complex dendritic shapes with sizes in the 20–40 μm range, and the Fe particles (image 6.1d) are spherical with sizes between 1-5 μm.

The morphological characterization of neat PAMC and such loaded with up to 5–6 wt.% Al, Cu and Fe particles was reported in [20]. Figures 6.1e, 6.1f, 6.1g, and 6.1i represent similar PAMC but loaded with more than 3 times more metal of each type. With the exception of the PAMC containing Al, all other loaded and empty PAMC represent aggregates of several, partially fused spheres with typical diameters of 5-10 μm that form final particles of 20–30 μm (Fig. 6.1e, no metal load) to 80–90 μm for the M-Mg10 sample (Fig. 6.1h). This observation confirms the previously postulated effect of coalescence during the PAMC formation. In the case of the M-Al10 sample (Fig. 6.1f) the in-situ forming PA6 coats the metal platelets. It is to notice that the size and shape of the loaded PAMC is determined by the morphology of the initial metal particles. In the case of Fe-loaded PAMC (Fig. 6.1i) the formation

of cylindrical structures should be ascribed to auto-assembly of magnetized Fe-particles and their subsequent coating by anionic PA6 in the process of microencapsulation [20].

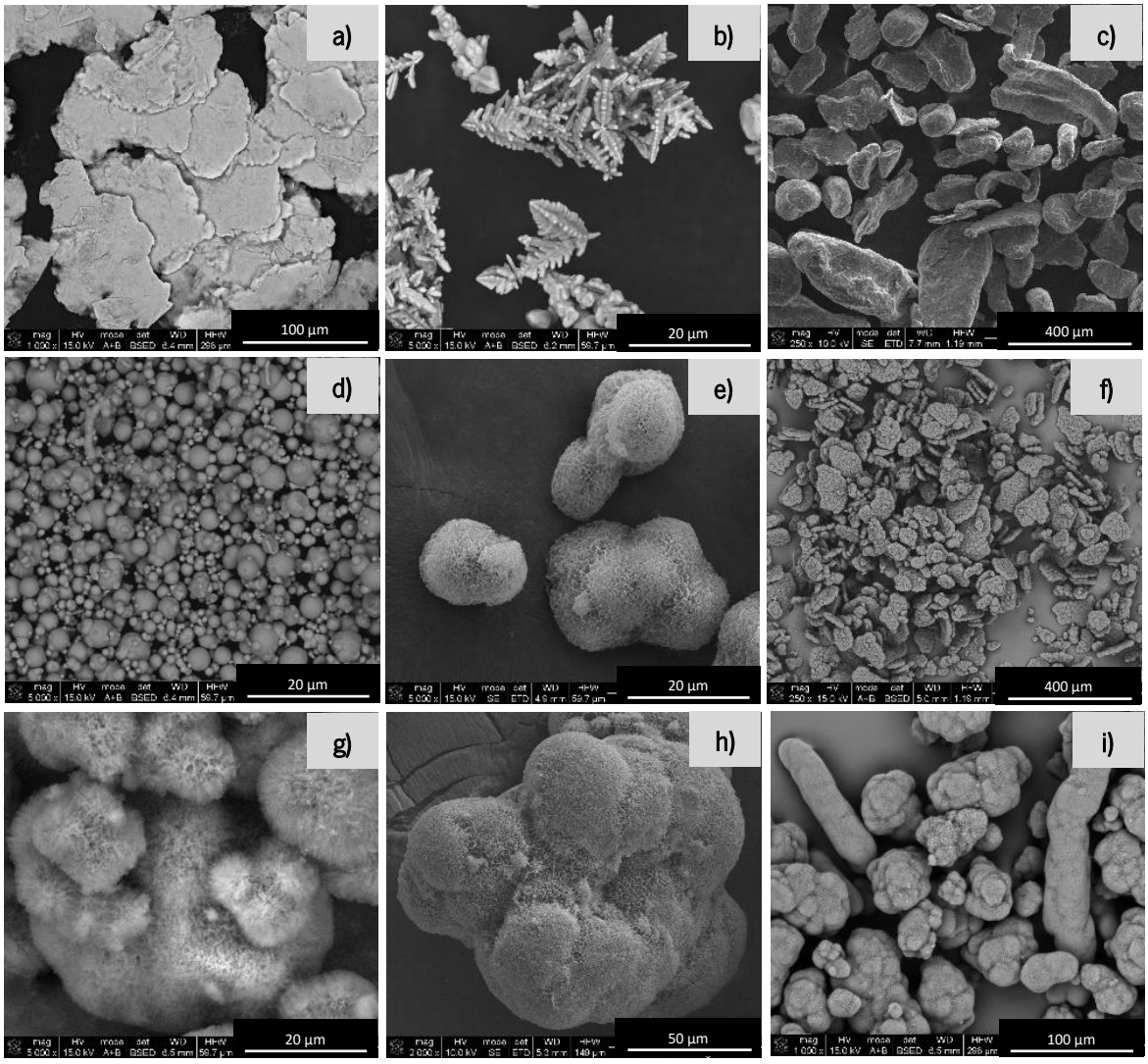

Figure 6.1 | Selected SEM micrographs of neat metal particles and metal-loaded PAMC: a) Al; b) Cu; c) Mg; d) Fe; e) empty PAMC; f) M-Al10; g) M-Cu10; h) M-Mg10; i) M-Fe10.

The stereoscopic image of the plain-weave CFT used in the production of L-samples, using a square mold with dimensions 70 x 70 x 2 mm (See section 2.3.4.2 of Chapter 2), shows the isotropic arrangement of the carbon filament bundles in two perpendicular directions (Figure 6.2a).

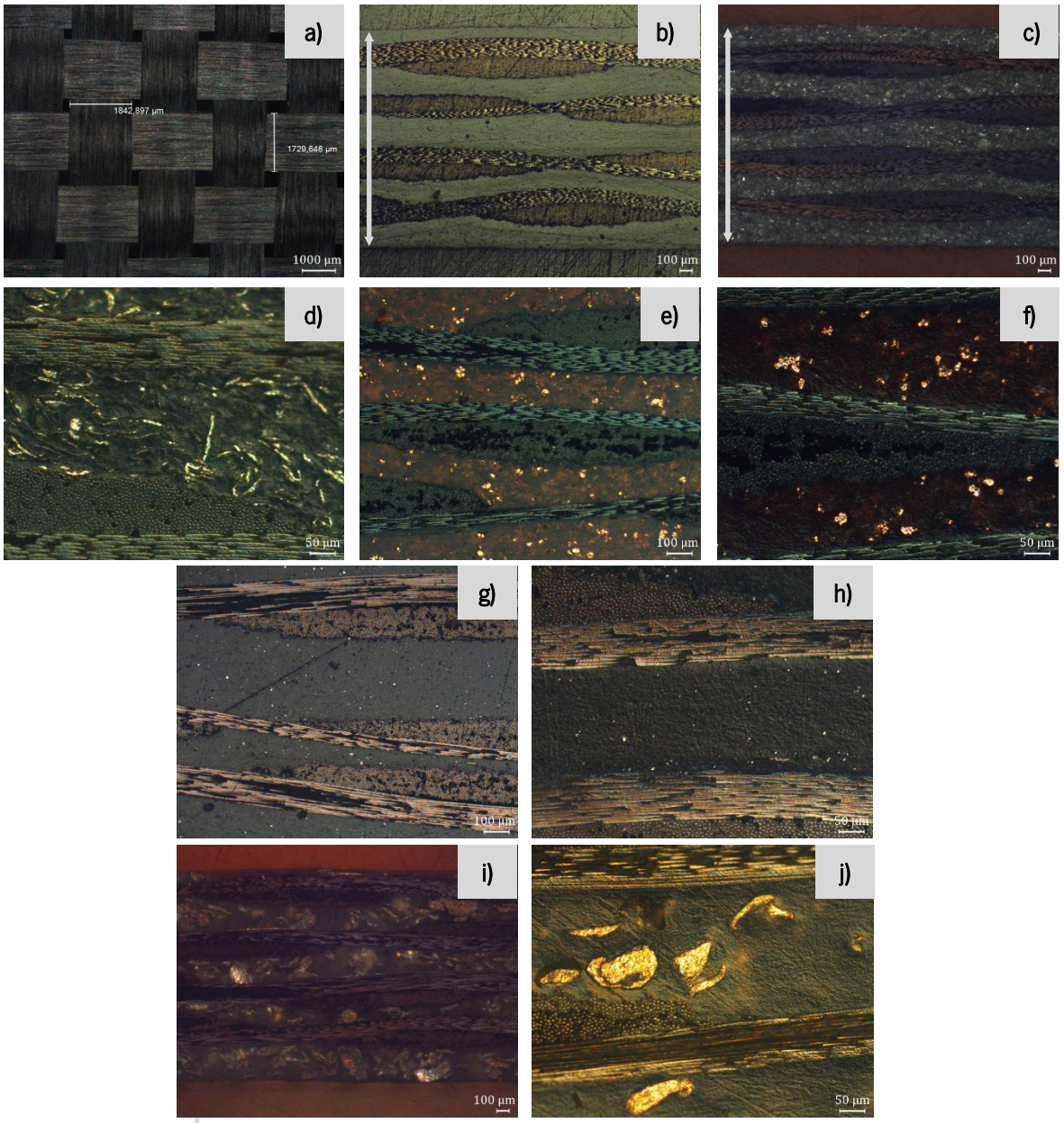

Figure 6.2 | Selected a) stereoscopic image of a plain-wave CFT ply; and RLM images of L-samples with V_f = 0.25: b) L-PA6-25; c) L-Al-25; d) close view of the distribution of Al particles in sample c; e) L-Cu-25; f) magnification of the sample e; g) L-Fe-25; h) magnification of sample g; i) L-Mg-25; j) close view of sample i. White arrows in images b, c and i are guides to delimit the thickness of molded laminates composites.

The reflected light microscopy (RLM) images of selected dually reinforced laminate composites prepared by the consolidation of metal-loaded PAMC and CFT in a volume fraction $V_f = 0.25$ are presented in Figure 6.2b-j. It can be observed that in all of these systems containing four CFT plies, a good distribution of the metal particles within the five PA6 matrix zones was achieved. The relatively low

density of the Al and Mg and the bigger sizes of these particles leads to the very dense packing of the PA6 matrix interlayers with metal (images 6.2c, 6.2d, and 6.2i, 6.2j, respectively). The heavier Cu and Fe particles are included in lower concentrations in the interlayers making them hardly visible in the latter case due to the smaller sizes of the Fe particles (3–5 μm), against the 20–25 μm size of Cu particles. A general feature of all images in Fig. 6.2 is that no damage of the CFT plies is caused during consolidation and that the well-distributed metal particles are also in good contact with the carbon filaments from CFT, especially in the Al- and Mg-containing laminates.

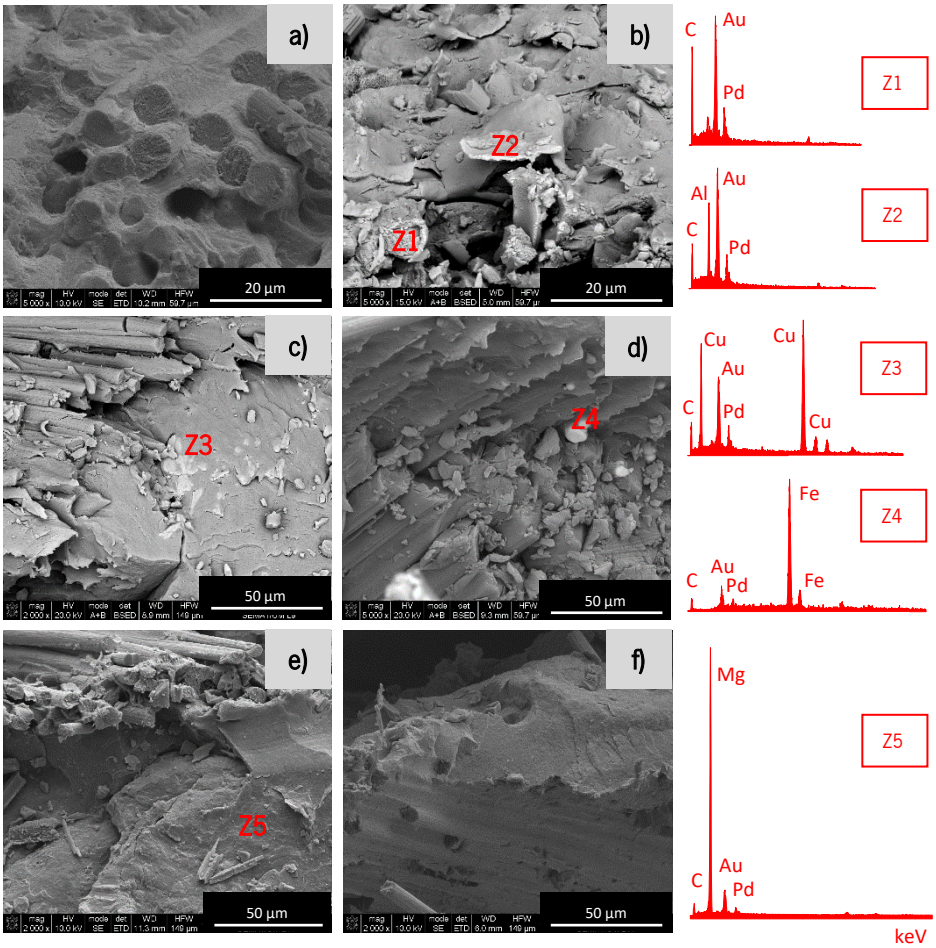

Figure 6.3| Selected SEM images of molded laminate composites prepared from metal-loaded PAMC: a) L-PA6-50; b) L-Al-50; c) L-Cu-50; d) L-Fe-25; e) L-Mg-25; f) L-Mg-50. For sample designation see Table 2.5 of Chapter 2. The graphs in the right column shows the EDX emission curves in the Z sites.

To visualize better the metal-loaded PA6 matrix/ interface in the same L-samples and the morphology of the CF, SEM studies were performed using cryofractured samples (Figure 6.3). In general, the micrographs provide proof for good and relatively homogeneous impregnation of the CFT

by the PA6 matrix material without metal load (Fig. 6.3a) or containing high metal loads (Fig. 6.3b–f). The latter five images display also carbon filaments from CFT with average diameters of 7.0–7.5 µm. In all metal-containing laminates, it was possible to identify by energy-dispersive X-ray spectroscopy (EDX) the specific emission peaks of the respective metal particles, well incrusted by matrix material in the interlayers between the CFT plies (Fig. 6.3).

6.4. Thermal properties by TGA

All metal-loaded PAMC and corresponding composites were analyzed by TGA. One of the purposes was the determination of the RL in either PAMC or the molded plates thereof taking in account the carbonized residue at 600 °C. As expected, the RL in PAMC and the respective molded plates are basically the same (Table 6.2). Small loss of metal during the compression molding was observed only in the Mg-containing plates.

Table 6.2 | Numerical data from TGA analysis of metal and CNT loaded PAMC

Sample		$T_{10\%}$ [a]	T_{max}, °C [b]	Residue at 600 °C, %	RL, wt.%
M-	PA6	295.4	339.3	1.4	-
P-		303.8	354.0	1.1	-
M-	Al10	317.0	358.5	20.8	19.4
P-		323.8	357.5	20.6	19.5
M-	Cu10	290.0	335.9	19.0	17.6
P-		300.9	321.5	18.8	17.7
M-	Fe10	286.7	334.3	14.8	13.4
P-		297.8	319.4	14.7	13.6
M-	Mg10	331.3	347.1	14.3	13.0
P-		309.7	345.6	13.7	12.7

[a] $T_{10\%}$ = Temperature of 10 % weight-loss;

[b] T_{max} = Maximum degradation temperature obtained from the 1st derivative of the TGA curves;

[c] Maximum degradation rate at T_{max} obtained from the first derivative of the TGA curves.

Figure 6.4 displays the weight retention TGA curves and Table 6.2 summarizes the numerical data of the thermal degradation derived from the TGA curves. The metal-loaded PAMC (Fig. 6.4a) and

the respective molded plates (Fig. 6.4b) display similar thermal stability as compared to the neat PA6 counterparts. Judging from the temperature of $T_{10\%}$ and that of the T_{max} in Table 6.2, some stability improvement is observed in the systems comprising the large and less dense Al and Mg particles. At the same time, in the Cu- and Fe-containing PAMC the thermal degradation is more pronounced, especially in the molded plates. This effect can be explained by the thicker packing of the PA6 matrix with touching to one another Al and Mg particles, that was visualized in the microscopic studies in Figure 6.2. This leads to an easier dissipation of the heat during the TGA experiment and, consequently in higher degradation temperatures. On the contrary, loading the PA6 matrix with lower volume fractions of the smaller Cu and Fe particles that remain isolated seems to have an opposite effect attributable to overheating localized around each metal particle.

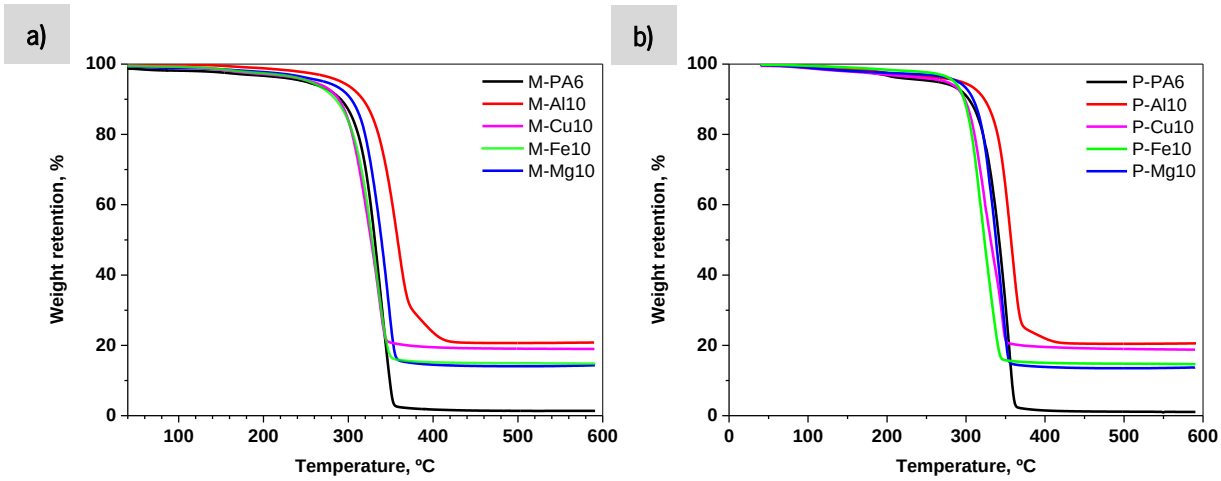

Figure 6.4 | Integral TGA curves of a) meal-loaded PAMC and b) molded plates thereof (P-samples) obtained in inert N_2 atmosphere.

6.5. Mechanical properties in tension

Representative stress-strain curves of the hybrid plates obtained from metal-loaded PAMC and of the dually reinforced laminates with CFT volume fraction V_f = 0.25 are presented in Figure 6.5a and 6.5b, respectively. Table 6.3 shows the data about E, σ_{br}, and ε_{br}, extracted from the stress-strain curves, as well as the IF for the E and σ_{br} values.

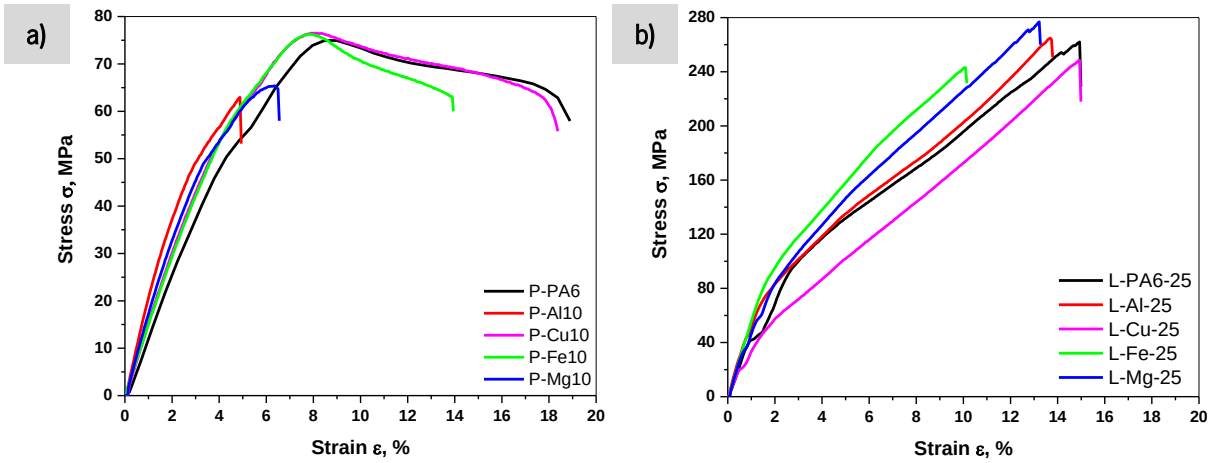

Figure 6.5 | Stress-strain curves from the tensile tests of: a) hybrid plates obtained from metal-loaded PAMC; b) dually reinforced laminate composites prepared with metal-loaded PAMC and V_f = 0.25 of CFT.

Table 6.3 | Results from the tensile strength experiments

Sample	Young's modulus, E (GPa)	IF (%) [a]	Stress at break, σ_{br} (MPa)	IF (%) [a]	Deformation at break, ε_{br} (%)
P-PA6	1.25 ± 0.07	-	63.7 ± 4.95	-	20.5 ± 4.60
P-Al10	1.96 ± 0.08	56.9	58.27 ± 3.91	-8.5	4.73 ± 0.38
P-Cu10	1.47 ± 0.01	17.8	55.09 ± 2.19	-13.5	19.70 ± 1.96
P-Fe10	1.47 ± 0.03	17.2	65.40 ± 1.58	2.7	13.89 ± 1.18
P-Mg10	1.78 ± 0.03	42.1	66.08 ± 1.53	3.8	6.27 ± 0.34
L-PA6-25	4.22 ± 0.24	238.0	251.17 ± 22.35	294.4	14.0 ± 2.01
L-Al-25	4.88 ± 0.10	290.5	271.88 ± 12.09	326.9	13.8 ± 0.86
L-Cu-25	4.45 ± 0.24	255.7	249.14 ± 21.25	291.2	11.3 ± 1.37
L-Fe-25	5.14± 0.37	311.1	239.03 ± 6.14	275.4	10.8 ± 0.48
L-Mg-25	4.76 ± 0.57	280.4	260.00 ± 14.19	308.3	13.0 ± 0.21

[a] In respect to neat anionic PA6 plate obtained from empty PAMC, calculated according to Eq. 2.14 of Chapter 2.

The stress-strain curves of plates produced from empty PAMC and Cu- and Fe-loaded PAMC (Fig. 6.5a, samples P-PA6, P-Cu10, P-Fe10) display very similar ductile behavior with well-expressed yield point at σ = 70-75 MPa and ε = 8–9 % strain, the deformation at break reaching 17–19 %. The

Young´s moduli calculated for the two metal-containing samples of 1.47 GPa are only slightly higher than that of the neat PA6 (Table 6.3). At the same time, the hybrid plates denoted as P-Al10 and P-Mg10 show brittle fracture with ε_{br} values of 6–7 % and σ_{br} below 65 MPa, i.e., lower than those of the neat PA6. The E-values of these two hybrids, however, are 57 % and 42 % higher than those of the matrix PA6. These results can be related with the sizes of the metal particles used: it is observed that high E-values are caused by the larger and most densely packed Al and Mg particles, whereas the smaller Cu and especially Fe particles do not change the stress-strain profile and increase only slightly the Young´s modulus.

As expected, the introduction of CFT plies significantly increases the E and σ_{br} values (in average by 280–327 %, Table 6.3) accompanied by the appearance of strain-hardening regions in all stress-strain curves (Fig. 6.5b). This behavior was expected as being typical for the textile-reinforced PA6-based TPC produced by AAROP [12, 22]. All metal-containing laminates in Table 6.3 show E-values being significantly better than the L-PA6-25 control sample, i.e., a synergetic effect between the CFT and metal powder reinforcements is observed. As regards the σ_{br}, the metal/CFT synergism is more evidenced in the Al- and Mg-containing laminates.

6.6. Electrical conductivity and dielectric properties

The d.c. electrical conductivity, σ_{dc}, dielectric constant ε', and the loss factor, $\tan\delta$, were determined for all composites produced by CM, and the data obtained are summarized in Tables 6.4 and 6.5.

The data in Table 6.4 confirm previous findings [21] reporting that metal-containing PA6 hybrids produced by molding of PAMC with real loads of metal microparticles in the range of 1–30 wt.% are still insulators with σ values in the range of 10^{-9} S/m, i.e., almost identical to that of the PA6 matrix. This effect was explained with an MWS type polarization typical for multiphase dielectrics, in which the resistivity of the phases is quite different [23, 24]. The presence of plain-weave CFT along with the Al, Cu, Fe and Mg content with effective loads up to 19 % (in respect to the PA6 matrix) apparently eliminates the polarization at the metal/PA6 interface. This causes a notable growth of the electrical conductivity σ in 7 orders of magnitude (Table 6.5). It should be noted that in the L-PA6-25 control laminate sample not containing metal particles this increase was reduced to 2 decades only. In view of this fact, the largely increased conductivity of the dually reinforced metal-CFT polyamide laminates should be assigned to the very good distribution of metal particles within the interlayer PA6 zones of the

laminates and the close contact of these particles with the carbon filaments of CFT observed in the RLM (Fig. 6.2) and SEM studies (Fig. 6.3). As seen from Table 6.5, increasing the CFT volume fraction in the laminates from 0.25 to 0.50 maintaining the metal concentration results in an increase of the conductivity, in particular in the Cu- and Al-containing laminates.

Table 6.4 | Electrical properties of P-samples prepared from metal-loaded PAMC

Sample	Conductivity, σ_{dc} (S/m) $\times 10^{-10}$	Dielectric constant [a], ε'	Loss factor [a], $\tan\delta$
P-PA6	5.22 ± 0.14	6.64 ± 0.20	0.05 ± 0.00
P-Al10	35.0 ± 1.70	22.90 ± 2.55	1.09 ± 0.13
P-Cu10	15.6 ± 1.76	24.00 ± 1.41	1.08 ± 0.10
P-Fe10	25.2 ± 3.82	24.50 ± 0.35	1.27 ± 0.08
P-Mg10	47.8 ± 3.78	23.60 ± 1.48	1.29 ± 0.08

[a] Values obtained at 1 MHz.

Table 6.5 | Electrical properties of dually reinforced laminate composites

Sample	Conductivity, σ_{dc} (S/m)	Dielectric constant [a], ε'	Loss factor [a], $\tan\delta$
P-PA6	5.22E-10 ± 1.40E-11	6.64E+00 ± 1.98E-01	5.26E-02 ± 7.78E-04
L-PA6-25	5.21E-08 ± 3.60E-09	1.74E+01 ± 4.24E-01	1.37E-02 ± 1.34E-03
L-Al-25	3.02E-07 ± 2.81E-08	1.77E+01 ± 9.19E-01	1.19E-02 ± 1.41E-04
L-Cu-25	2.08E-07 ± 1.51E-08	1.76E+01 ± 2.12E-01	1.56E-02 ± 9.19E-04
L-Fe-25	4.32E-03 ± 3.52E-04	1.67E+01 ± 2.83E-01	1.49E-02 ± 7.07E-04
L-Mg-25	3.21E-03 ± 1.29E-04	1.80E+01 ± 9.19E-01	9.77E-03 ± 1.46E-03
L-PA6-50	3.60E-07 ± 2.55E-08	2.14E+01 ± 7.07E-02	1.32E-02 ± 1.06E-03
L-Al-50	2.67E-03 ± 4.88E-04	2.04E+01 ± 4.24E-01	1.50E-02 ± 3.11E-03
L-Cu-50	2.93E-03 ± 3.96E-04	2.05E+01 ± 3.54E-01	1.00E-02 ± 2.52E-03
L-Fe-50	4.61E-03 ± 2.07E-04	2.08E+01 ± 7.07E-02	1.53E-02 ± 7.78E-04
L-Mg-50	4.37E-03 ± 1.04E-04	2.10E+01 ± 4.95E-01	1.46E-02 ± 2.83E-04

[a] Values obtained at 1 MHz.

Figure 6.6 displays the semi-logarithmic plots of the ε' and $\tan\delta$ as a function of frequency for the metal-loaded composites (Fig. 6.6a, b), L-samples with V_f = 0.25 (Fig. 6.6c, d) and V_f = 0.5 (Fig. 6.6e, f). At 1 MHz, the ε' of all L-samples displays similar values in the range of 17–21, which is almost independent on the CFT content, the values of the PA6 reference sample being 7–9 (Table 6.5). Changing the frequency in the 10^2–10^6 range produces relatively few changes. Apparently, at lower frequencies, the PA6-metal hybrids without CFT (P-samples, Fig. 6.5a) produce higher ε' values than their L-series counterparts. It is to notice in Fig. 6.6 that an important contribution to the increase of the ε' is also related to increasing energy dissipation (and not just to increase in energy storage ability) as shown by the dielectric losses. Thus, the composites with the highest ε' are also the ones with the higher dielectric loss, being also a direct correlation between the real part of the electrical conductivity, σ', and the dielectric loss by $\sigma' = \omega \cdot \varepsilon' \cdot \tan\delta$ [25].

As to the $\tan\delta$ values, the hybrids containing 13–19 % metal without CFT (Fig. 6.6b) display notably higher values within the entire frequency range varying from 9 to 1, as compared to the L25 and L50 laminates wherein the respective values are 10–100 times lower (Figs. 6.6d, f). The lower values of $\tan\delta$ in the latter case are related to the interfaces established between the metal particles and the CF. Apparently, these interfaces decrease the mobility of the charge carriers, maintaining them within those interfaces. The micrographs of the L-series obtained by RLM (Fig. 6.1) and SEM (Fig. 6.2) are in good agreement with these low losses, demonstrating once again a good impregnation of CFT with metal-enriched PA6 materials, i.e., a good affinity between fillers with different nature.

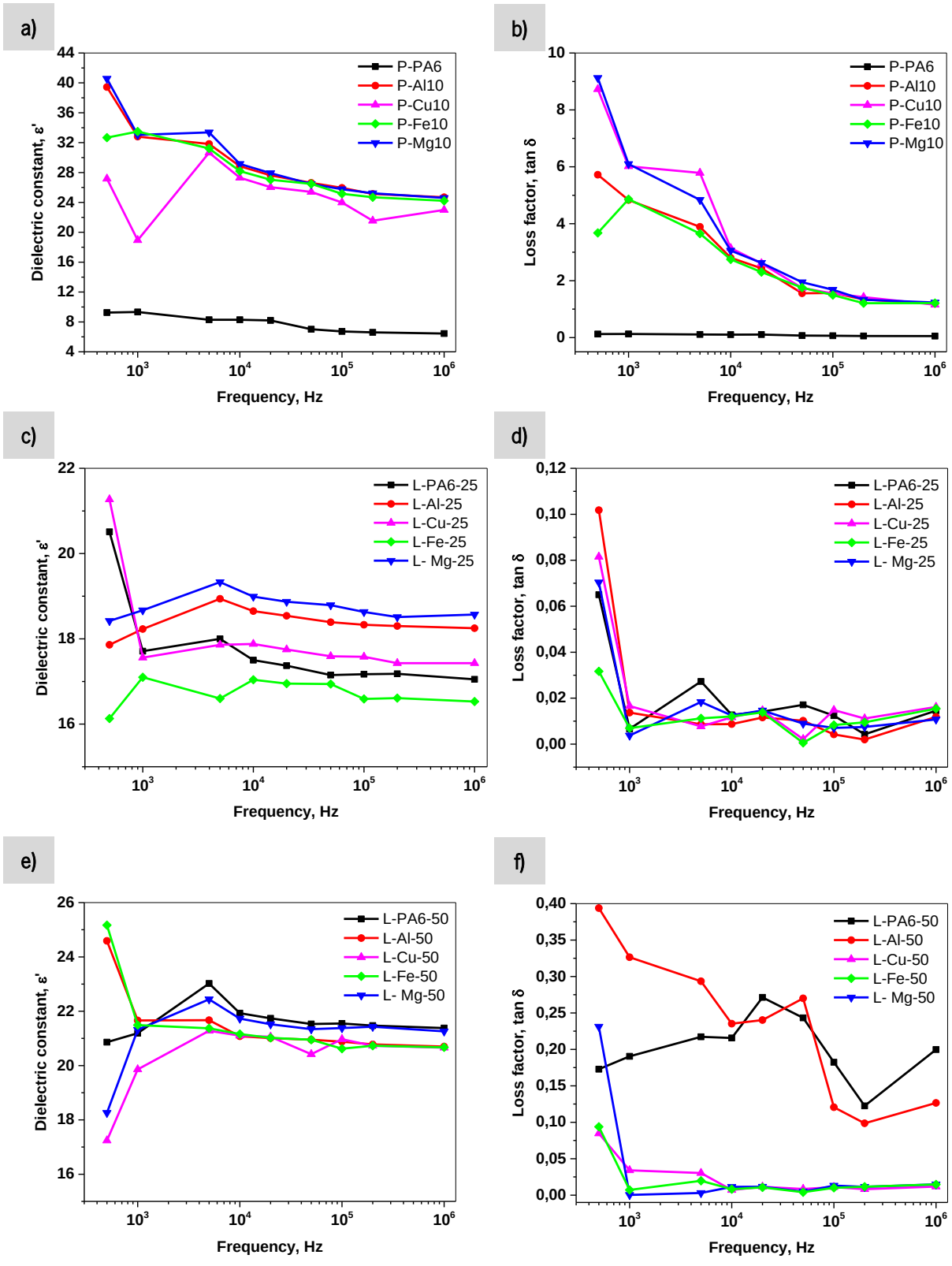

Figure 6.6 | Dielectric properties of: a, b) P-samples obtained from metal-loaded PAMC; and L-samples with c, d) V_f = 0.25 of CFT and e, f) V_f = 0.50 of CFT. Left: dielectric constants. Right: dielectric losses.

6.7. Summary

Multiscale laminate composites based on CFT structures and PA6 matrices additionally reinforced by metal particles were prepared using microencapsulation strategy. The concentration of the metal particles was 13–19 wt.% with respect to the PA6 matrix, and the CFT volume fraction reaching 0.5. The preparation route included reactive microencapsulation of the respective metal particles in PAMC by means of AAROP in suspension. The resulting metal-loaded PAMC were used for powder impregnation of CFT plies that were subsequently consolidated by conventional CM. As far as it is known, such an approach is applied for the first time in the preparation of TPC/CFT laminates with enhanced electrical conductivity. The composites thus obtained displayed a strong increase of the d.c. electrical conductivity in 7 orders of magnitude as well as a tunable real component of the dielectric constant and dissipation factor. This effect was accompanied by 2–3 times increase in the Young modulus and ultimate tensile strength as compared to the anionic PA6 matrix. A factor of prime importance to get such behavior was the good distribution of high loads of metal particles within the PA6 interlayers of the laminates that was achieved by the microencapsulated strategy used in this work. It is believed that this set of properties quite unusual for traditional TPC/CFT laminates can resolve some problems typical for CFT laminate composites and therefore become a useful platform for structural and functional applications mostly in the automotive and electronic industries, where electromagnetic interference shielding, or high *k* materials are required.

6.8. References

[1] Stavrov D, Bersee HEN (2005) Resistance welding of thermoplastic composites-an overview. *Compos Part A Appl Sci Manuf*, 36:39–54. DOI: 10.1016/j.compositesa.2004.06.030

[2] Steenkamer DA, Sullivan JL (1998) On the recyclability of a cyclic thermoplastic composite material. *Compos Part B Eng*, 29:745–752. DOI: 10.1016/S1359-8368(98)00016-X

[3] Chang IY, Lees JK (1988) Recent Development in Thermoplastic Composites: A Review of Matrix Systems and Processing Methods. *J Thermoplast Compos Mater*, 1:277–296. DOI: 10.1177/089270578800100305

[4] Khondker OA, Ishiaku US, Nakai A, Hamada H (2005) Fabrication Mechanical Properties of Unidirectional Jute/PP Composites Using Jute Yarns by Film Stacking Method. *J Polym Environ*, 13:115–126. DOI: 10.1007/s10924-005-2943-y

[5] Svensson N, Shishoo R, Gilchrist M (1998) Manufacturing of Thermoplastic Composites from Commingled Yarns-A Review. *J Thermoplast Compos Mater*, 11:22–56. DOI:

10.1177/089270579801100102

[6] Bernet N, Michaud V, Bourban P-E, Månson J-A. (2001) Commingled yarn composites for rapid processing of complex shapes. *Compos Part A Appl Sci Manuf*, 32:1613–1626. DOI: 10.1016/S1359-835X(00)00180-9

[7] Sakaguchi M, Nakai A, Hamada H, Takeda N (2000) The mechanical properties of unidirectional thermoplastic composites manufactured by a micro-braiding technique. *Compos Sci Technol*, 60:717–722. DOI: 10.1016/S0266-3538(99)00175-X

[8] van Rijswijk K, Bersee HEN, Jager WF, Picken SJ (2006) Optimisation of anionic polyamide-6 for vacuum infusion of thermoplastic composites: choice of activator and initiator. *Compos Part A Appl Sci Manuf*, 37:949–956. DOI: 10.1016/j.compositesa.2005.01.023

[9] van Rijswijk K, Bersee HEN, Beukers A, Picken SJ, van Geenen AA (2006) Optimisation of anionic polyamide-6 for vacuum infusion of thermoplastic composites: Influence of polymerisation temperature on matrix properties. *Polym Test*, 25:392–404. DOI: 10.1016/j.polymertesting.2005.11.008

[10] Harkin-Jones E, Crawford R (1996) Rotational molding of liquid plastic systems: An assessment of material moldability. *Adv Polym Technol*, 15:71–100. DOI: 10.1002/(SICI)1098-2329(199621)15:1<71::AID-ADV6>3.0.CO;2-H

[11] Ying G, Yang G (2009) Manufacturing and physical properties of all-polyamide composites. J Mater Sci, 44:4639–4644. DOI: 10.1007/s10853-009-3708-0

[12] Dencheva N, Sampaio AS, Oliveira FM, Pouzada AS, Brito AM, Denchev Z (2014) Preparation and properties of polyamide-6-based thermoplastic laminate composites by a novel in-mold polymerization technique. J Appl Polym Sci, 131:40083. DOI: 10.1002/app.40083

[13] Guo Z, Sang L, Wang Z, Chen Q, Yang L, Liu Z (2016) Deposition of copper thin films by plasma enhanced pulsed chemical vapor deposition for metallization of carbon fiber reinforced plastics. Surf Coatings Technol, 307:1059–1064. DOI: 10.1016/j.surfcoat.2016.07.029

[14] Lupoi R, O'Neill W (2010) Deposition of metallic coatings on polymer surfaces using cold spray. Surf Coatings Technol, 205:2167–2173. DOI: 10.1016/j.surfcoat.2010.08.128

[15] Zhou XL, Chen AF, Liu JC, Wu XK, Zhang JS (2011) Preparation of metallic coatings on polymer matrix composites by cold spray. Surf Coatings Technol, 206:132–136. DOI: 10.1016/j.surfcoat.2011.07.005

[16] Che H, Vo P, Yue S (2017) Metallization of carbon fibre reinforced polymers by cold spray. Surf Coatings Technol, 313:236–247. DOI: 10.1016/j.surfcoat.2017.01.083

[17] Archambault G, Jodoin B, Gaydos S, Yandouzi M (2016) Metallization of carbon fiber reinforced polymer composite by cold spray and lay-up molding processes. Surf Coatings Technol, 300:78–86. DOI: 10.1016/j.surfcoat.2016.05.008

[18] Kong K, Cheedarala RK, Kim M, Roh H-D, Park Y-B, Park HW (2016) Electrical thermal heating and piezoresistive characteristics of hybrid CuO–woven carbon fiber/vinyl ester composite laminates. Compos Part A, 85:103–112. DOI: 10.1016/j.compositesa.2016.03.015

[19] Denchev Z, Dencheva N (2015) Polyamide Microcapsules and Method to Produce the Same, Portuguese patent PT 107679 A, filled 03.06.2014, published 03.12.2015, C08G 69/18

[20] Dencheva N, Denchev Z, Lanceros-Méndez S, Ezquerra Sanz T (2016) One-step in situ synthesis of polyamide microcapsules with inorganic payload and their transformation into responsive thermoplastic composite materials. Macromol Mater Eng, 301:119–124. DOI: 10.1002/mame.201500194

[21] Brêda C, Dencheva N, Lanceros-Mendez S, Denchev Z (2016) Preparation and properties of metal-containing polyamide hybrid composites via reactive microencapsulation. J Mater Sci, 51:10534–10554. DOI: 10.1007/s10853-016-0274-0

[22] Dencheva NV, Vale DM, Denchev ZZ (2016) Dually reinforced all-polyamide laminate composites via microencapsulation strategy. Polym Eng Sci, 57:806–820. DOI: 10.1002/pen.24456

[23] Mendes SF, Costa CM, Serra RS i, Baldalo AA, Sencadas V, Gomez-Ribelles JL, Jr. RG, Lanceros-Méndez S (2012) Influence of filler size and concentration on the low and high temperature dielectric response of poly(vinylidene fluoride) /Pb(Zr0.53Ti0.47)O3 composites. J Polym Res, 19:9967. DOI: 10.1007/s10965-012-9967-5

[24] Lopes AC, Costa CM, i Serra RS, Neves IC, Ribelles JLG, Lanceros-Méndez S (2013) Dielectric relaxation, ac conductivity and electric modulus in poly(vinylidene fluoride)/NaY zeolite composites. Solid State Ionics, 235:42–50. DOI: 10.1016/j.ssi.2013.01.013

[25] Costa P, Silva J, Lanceros-Méndez S (2016) Strong increase of the dielectric response of carbon nanotube/poly(vinilidene fluoride) composites induced by carbon nanotube type and pre-treatment. Compos Part B Eng, 93:310–316. DOI: 10.1016/j.compositesb.2016.03.010

CHAPTER 7

Broadband electrical conductivity of metal/CNT polyamide 6 composites

7.1. Introduction

Whenever electromagnetic radiation in the domain of broadband dielectric spectroscopy (BDS) is applied to a sample, dielectric dispersion and absorption occur. These two phenomena are due to dipole relaxation arising from the reorientational motions of bound molecular dipoles and to electrical conduction arising from the translational motions of ions or electrons. Depending on the chemical and physical composition of the sample, its BDS response will be dominated by either molecular relaxation or electrical conductivity [1]. This makes BDS a powerful tool to evaluate these two phenomena in polymer-based samples in a non-destructive way.

In general, three main mechanisms of molecular motions are observed in the dielectric spectra of polyamides: two local motions in the lower temperature regime designated as γ- and β-relaxations, and the segmental α-relaxation at higher temperatures related to the glass-rubber transition of the amorphous phase. In addition, at temperatures above the α-relaxation an interfacial polarization designated as Maxwell-Wagner-Sillars (MWS) polarization, can be observed. Its origin is the trapping of free charges at the boundaries between crystalline and amorphous regions [2, 3]. Conductivity phenomena have found to play role in neat polyamides only at relatively high temperatures [4].

As referred previously in Chapter 1, increased conductivity of the thermoplastic matrix is required for electromagnetic interference (EMI) shielding materials. In principle, the electrical conductivity of an insulating material can be increased by adding a conducting component, e.g., carbonaceous fillers [5–9], metallic particles [10, 11], or intrinsically conducting polymers [12, 13]. As the concentration of the conducting component is raised above a critical concentration known as percolation threshold [14], the number of continuous conductive paths through the matrix polymer increases thus allowing conduction of charge carriers.

Among the carbonaceous conductive fillers for polymer composites, the carbon nanotubes (CNT) are most frequently studied since very small amounts of them can cause a significant increase in matrix conductivity. This fact determines the intensive investigation of CNT for EMI shielding polymer-based materials [15–19]. Metal micro- and nanoparticles alone are less frequently used for adjusting the EMI properties of polymer matrices [20, 21], most probably due to impediments in the composite processing based on melt-mixing techniques related to the very high density of most conductive metals. Instead, there is a trend for metallization of carbon fillers by chemical vapor deposition [22], cementation and electroless deposition techniques [23], or by electrochemical deposition [24] using mostly Cu or Ni. All these techniques are relatively complex and costly for an industrial application.

Chapter 5 reports on the preparation of dually loaded polyamide 6 (PA6) microcapsules (DM-samples) by means of activated anionic ring-opening polymerization (AAROP) and their transformation into molded composite plates (DP-samples). Bearing in mind the importance of metal-carbon composites for EMI shielding applications, in the present chapter the frequency and temperature dependence of the conductivity in these composites was discussed in relation to their composition and morphology.

7.2. Samples investigated

The BDS studies in this chapter were performed with compression molded plates produced from metal and CNT-loaded plates (Chapter 2, section 2.3.4.1, samples designate as series P- and DP-). These plates were produced from the respective loaded PA6 microcapsules (PAMC) hybrid powders (Chapter 2, M- and DM-series) synthesized by solution-precipitation AAROP of ε-caprolactam (ECL) performed at fixed reaction conditions as described in sections 2.3.2 and 2.3.3 of Chapter 2. Table 7.1 presents the compositions of the M- and DM-PAMC precursors. All molded plates were prepared by compression molding of the PAMC precursors using a rectangular mold with dimensions 85 × 75 × 1 mm (See section 2.3.4.1 of Chapter 2).

Table 7.1 | Composition of the samples used in the BDS experiments

Sample	Load, wt.% [a]	Composition, vol. % [b]			Real load, wt.% [c]
		Metal	CNT	PA6	
M-PA6	0	0	0	100	0
M-PA6	0	0	100	56.2	0
M-Al5	5	4.18	0	95.8	9.4
M-Cu5	5	1.33	0	98.7	9.6
M-Fe5	5	1.06	0	98.9	7.0
M-CNT5	5	0	4.45	95.6	8.2
DM-Al3-CNT7	3 + 7	1.96	5.71	92.3	14.4
DM-Al5-CNT5	5 + 5	3.84	4.80	91.4	16.7
DM-Al7-CNT3	7 + 3	4.68	2.51	92.8	14.7
DM-Cu5-CNT5	5 + 5	1.03	4.29	94.7	14.8
DM-Fe5-CNT5	5 + 5	0.93	3.38	95.7	11.9

[a] Percentage based on the weight of the ECL monomer in the starting AAROP mixture;

[b] Represents the relation between the volumes of load (metal + CNT) and PA6 in the respective sample;

[c] Determined by thermogravimetric analysis (TGA) according to Eq. 2.13 of Chapter 2.

The fractions of the metals and CNT in the mono-loaded PAMC were fixed between 7–9 wt.%. As to the CNT-loaded hybrid, the respective volume fraction of 4.5 % is ca. three times above its percolation

threshold in PA6 matrices [25], while with the other metals the loading were in the range of 1-4 vol.%, the highest values corresponding to the lightest Al filler. This was far below the percolation threshold for this metal which was not attained even with effective concentrations close to 12 vol.% due to MWS polarization [26].

All the mono- and double-loaded compression molded samples were carefully characterized by scanning electron microscopy, thermal methods (differential scanning calorimetry and TGA), mechanical testing in tension, as well as their electrical properties at room temperature were determined, including σ_{dc}, $\varepsilon' = f(F)$ and $\tan\delta = f(F)$ with the frequency F being in the 10^2–10^6 Hz (see Chapters 3 and 5, respectively). It was decided to study in this chapter the electrical conductivity as a function of both frequency and temperature varying them both in broad intervals, i.e., -150 °C ≤ T ≤ 100 °C and $10^{-1} \leq F \leq 10^6$ Hz. It was expected that these data will shed more light on the type of conductivity in the binary-loaded hybrid plates and its relation to the EMI shielding properties discussed in Chapter 8.

7.3. Broadband electrical conductivity of the binary composites

The logarithmic plots showing the frequency dependence of the electrical conductivity, $\sigma(\omega)$, for the neat PA6 plates and plates prepared from mono-loaded PAMC containing 5 wt.% of either Al or CNT are presented in Figure 7.1. In the neat PA6 (Fig. 7.1a) and in the P-Al5 hybrid (Fig. 7.1b) for temperatures below glass-transition temperature, T_g, $\sigma(\omega)$ follows a linear dependence with frequency. This behavior is characteristic of insulating materials [9, 27], such are the neat PA6 and the P-Al5 hybrid, the latter remaining insulator in spite of the relatively high real Al load of ca. 9.5 wt.% thus confirming previous results on this system.[26] However, when $T > T_g$ (i.e., 50°C), this linearity is upset. The non-linear curve can be due to the segmental α-relaxation related to the glass transition of the amorphous phase [28, 29].

As regards the hybrid plate containing 5 wt.% of CNT (Fig. 7.1b), the $\sigma(\omega)$ curve adopts a characteristic shape assigned to the so-called universal dynamic response [30, 31] described by a law of the type:

$$\sigma(\omega) = \sigma_{dc} + \sigma_{ac} = \sigma_{dc} + A \cdot \omega^s \tag{7.1}$$

where σ_{dc} is the frequency-independent dc conductivity, A is a temperature-dependent parameter, and s is a temperature-dependent exponent where $0 < s < 1$.

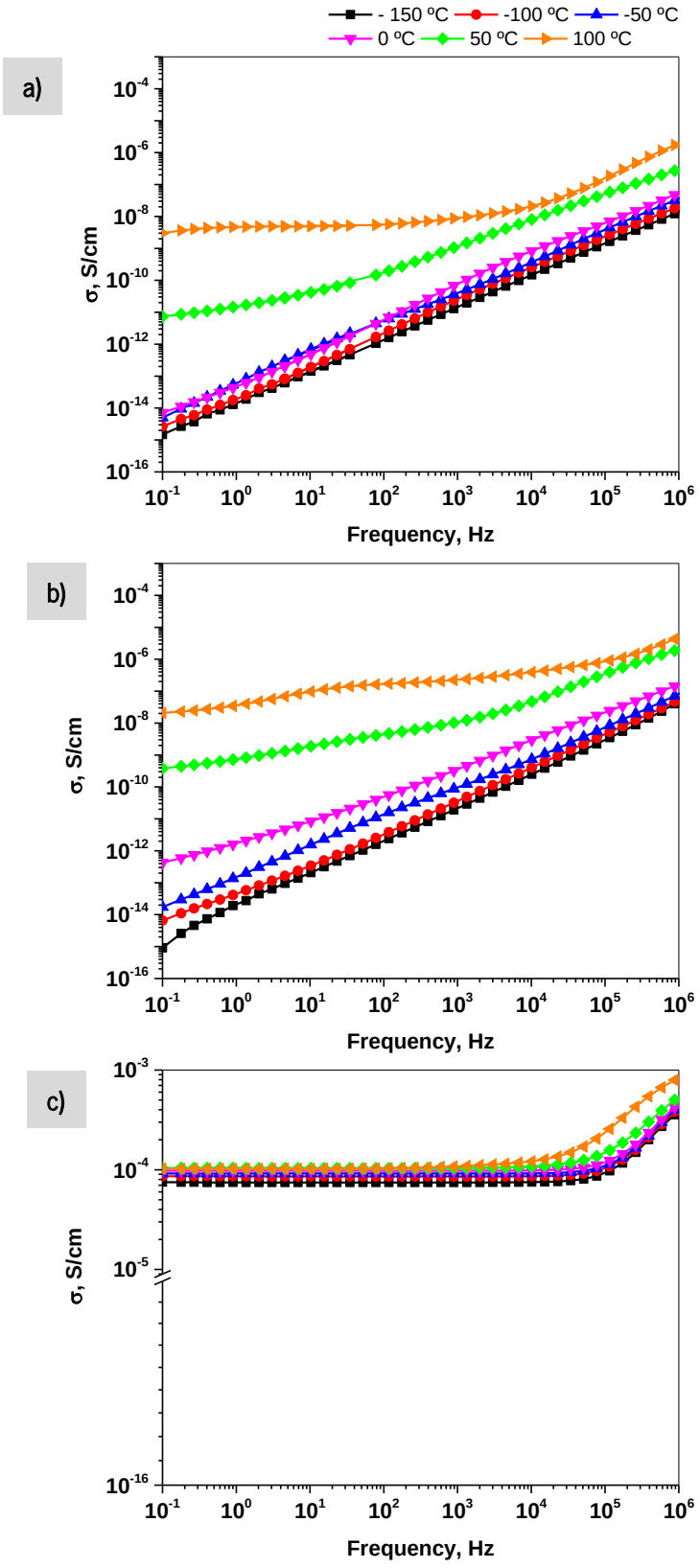

Figure 7.1 | Electrical conductivity as a function of frequency at different temperatures for: a) P-PA6; b) P-Al5; c) P-CNT5 molded samples.

This law introduces a critical frequency, F_c, above which $\sigma(\omega) = \sigma_{ac} \propto \omega^s$. This behavior is a characteristic of translational motion of charges across conducting networks [9, 27, 32], in this case, the one produced by the CNT filler. For the P-CNT5 sample the value of $\sigma(\omega)$ at the lowest measured frequency of 0.1 Hz is considered to be the σ_{dc} [33]. For the insulating samples P-PA6 and P-Al5, the σ_{dc} at 0.1 Hz was considered for comparative analysis. Table 7.2 contains the numeric values for σ_{dc}, F_c and s extracted from the curves in Figure 7.1.

Table 7.2| Parameters describing electrical properties of the PA6 composites

Sample	T, °C	σ_{dc}, S/cm at f = 0.1 Hz	F_c, Hz	s
P-PA6	20	4.77E-14	-	-
	50	7.33E-12	-	-
	100	3.01E-09	-	-
P-CNT5	20	9.97E-05	8.61E+04	0.63
	50	1.04E-04	5.34E+04	0.57
	100	1.02E-04	1.80E+04	0.52
P-Al5	20	7.54E-12	-	-
	50	3.79E-10	-	-
	100	2.08E-08	-	-
P-Cu5	20	2.24E-12	-	-
	50	3.90E-10	-	-
	100	2.37E-08	-	-
P-Fe5	20	2.88E-12	-	-
	50	2.84E-10	-	-
	100	4.32E-08	-	-
DP-Al3-CNT7	20	6.61E-03	-	-
	50	9.90E-03	-	-
	100	1.63E-02	-	-
DP-Al5-CNT5	20	7.14E-04	2.93E+05	0.13
	50	9.43E-04	2.88E+05	0.15
	100	1.28E-03	2.24E+05	0.23
DP-Al7-CNT3	20	1.42E-05	1.13E+04	0.41
	50	1.38E-05	5.64E+03	0.41
	100	1.21E-05	1.92E+03	0.43
DP-Cu5-CNT5	20	2.78E-03	2.79E+05	0.11
	50	2.76E-03	2.79E+05	0.11
	100	3.71E-03	1.94E+05	0.17
DP-Fe5-CNT5	20	4.04E-04	5.71E+04	0.28
	50	4.31E-04	5.48E+04	0.29
	100	4.08E-04	2.54E+04	0.30

As seen from Fig 7.1c and Table 7.2, increasing the temperature of the P-CNT5 sample results in a decrease of F_c from values between 10^5-10^4 Hz (in the -150 – 0°C range) to ca. 10^4 – 10^3 Hz for temperatures equal or higher than 50°C, which is also expected from the theory.

Figure 7.2 and Table 7.2 display the frequency dependence of the electrical conductivity in Al-CNT composites with various compositions at 20°C.

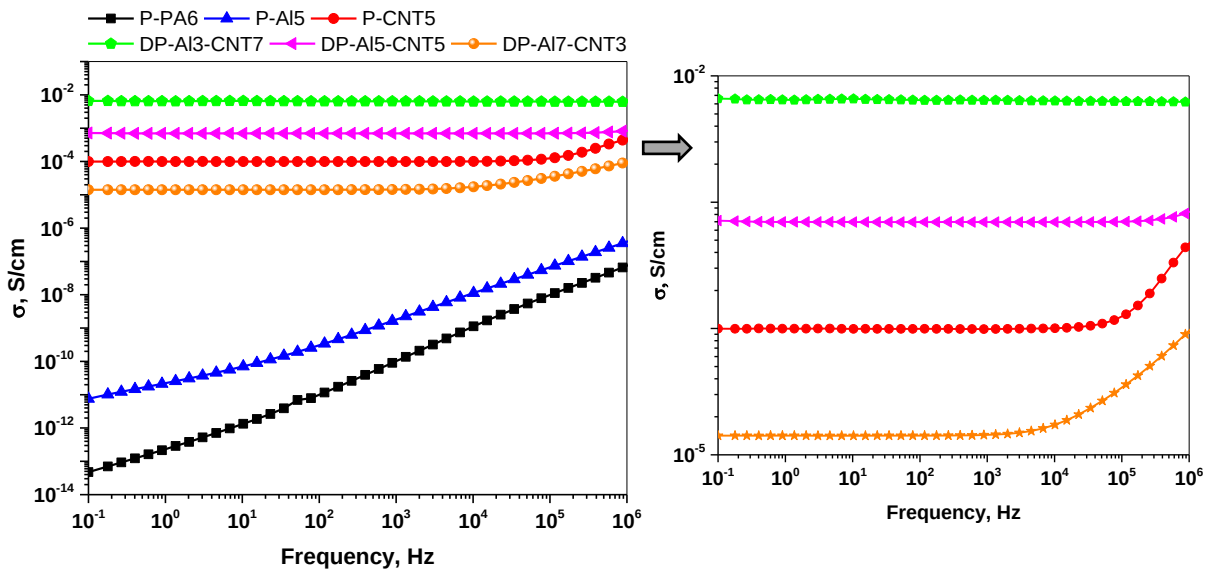

Figure 7.2| Electrical conductivity as a function of frequency for Al-CNT composites with various compositions at 20°C. On the right, a better visualization of the high frequency part of the curves.

First, it can be seen that it is the CNT content that determines the electrical conductivity of the samples, whereas the sample containing only Al behaves as an insulator. The σ_{dc} of the P-CNT5 of 9.8 10^{-5} S/cm is almost one order of magnitude lower than that of the DP-Al5-CNT5 binary hybrid with σ_{dc} = 8.1 × 10^{-4} S/cm. This fact suggests some synergetic effect related to the presence of Al microparticles within the CNT conducting network. Such an effect was observed in other types of CNT- or graphene-containing composite materials [34–39]. The latter work of He et al. [39] explains the increased conductivity in in these systems by the interpenetration of the Ag nanowires and the reduced graphene microsized platelets. In our DP-samples the interpenetration of CNT with metal particles displays a similar synergetic effect. Thus, increasing the CNT component in the DP-Al3-CNT7 sample increases the conductivity to 6.6 × 10^{-3} S/cm whereas in the DP-Al7-CNT3 sample it falls below that of the P-CNT5 sample. Apparently, the transport of charges in the dually filled composites is determined by the

nanosized CNT filler, whereby the presence of Al seems to improve it. Having in mind that the electrical conductivity of the neat, 100 wt.% CNT and Al metal components are in the range of 0.5 – 2.0 × 10^2 S/cm and above 10^5 S/cm respectively, it can be hypothesized that the significantly lower conductivity values obtained in the Al-CNT polyamide hybrids are due to a charge transport through a percolating network [9, 27]. Important factors, in this case, will be the concentration of the filler particles, their size, shape, and distribution in the bulk of the matrix.

Another observation in the samples set in Figure 7.2 is that at 20°C, the F_c is registered below 10^6 Hz for the P-CNT5, DP-Al7-CNT3, and DP-Al5-CNT5 samples. For the DP-Al3-CNT7 sample that contains the highest amount of CNT, the electrical conductivity remains constant through the all frequency range (Fig. 7.2) meaning the F_c value is shifted above 1 MHz.

The next Figure 7.3 displays the electrical conductivity of metal-CNT 5/5 wt.% composites at 20 °C. The numeric data extracted from these curves are summarized in Table 7.2.

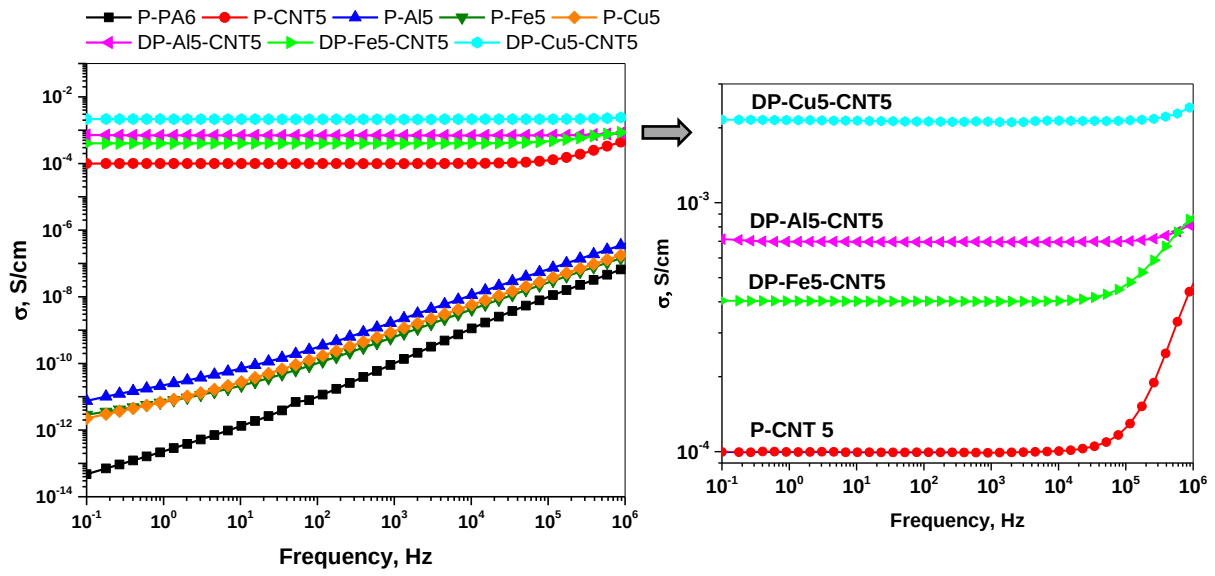

Figure 7.3| Electrical conductivity as a function of frequency for the metal-CNT 5/5 wt.% composites at 20°C. The P-CNT5 sample is presented to enable comparison. The graph on the right presents a better visualization of the high frequency part of the curves.

Again, it is observed that CNT determines the electrical conductivity of the DP-samples since the composites prepared with Fe and Cu particles behave as insulators as the neat matrix and P-Al5 samples (Fig. 7.3, Table 7.2). Moreover, metals as Cu and Fe also display a synergetic effect on the electric conductivity when used in combination with CNT. The Cu metal particles with volume content three times

lower than that of Al lead to higher conductivities of the DP-Cu5-CNT5 composite as compared to the DP-Al5-CNT5 sample. For the DP-Fe5-CNT5 composite with a similar volume fraction of metal, the electrical conductivity values are below those of the DP-Al5-CNT5 system. The explanation of these observations should be related in the first place to the specific electrical conductivity of the different metals. Thus, the electric conductivity of Cu is about 6 times higher than Fe [40], which explains the electrical conductivities of the respective DP-samples. Additionally, some effect on the conductivity of the latter could have the metal particles morphology. Thus, the Cu dendritic particles have sizes of ca. 20 μm (Fig. 3.3b of Chapter 3), which could contribute to closer contact between them and the CNT filler, whereas the Fe particles are predominantly spherical with diameters of 3-5 μm resulting in a worse contact with the CNT filler (Fig. 3.3d of Chapter 3).

Moreover, from Fig. 7.2 and Fig. 7.3 it is observed that the electrical conductivity remains constant until a certain F_c and for $F > F_c$, the conductive samples follow the power law $\sigma_{ac} \propto F^s$. The F^s characterizes the transport in disordered materials and describes the frequency response of the electrical conductivity [32], in that case for the conductive composites. Then, at a certain F, there is a positive deflection of the conductive curve that can be due to the presence of charge carriers with different permittivities and conductivities (MWS relaxation) at the interfaces between phases [25], that are PA6, CNT, and metal. Furthermore, it is seen that the σ_{dc} and F_c increase i) as the amount of the CNT increases in the Al-CNT system (Fig. 7.2), and therefore, for sample DP-Al3-CNT7 the σ_{dc} plateau spreads in the full frequency range; and ii) as the metal conductivity increases in the metal-CNT 5/5 wt.% system (Fig. 7.3). This behavior can be attributed to the formation of a conductive network that depends on the CNT amount and the electrical conductivity of the neat metal particles. Figure 7.4 represents this tendency, where data obtained at different temperatures (Table 7.2) are also included.

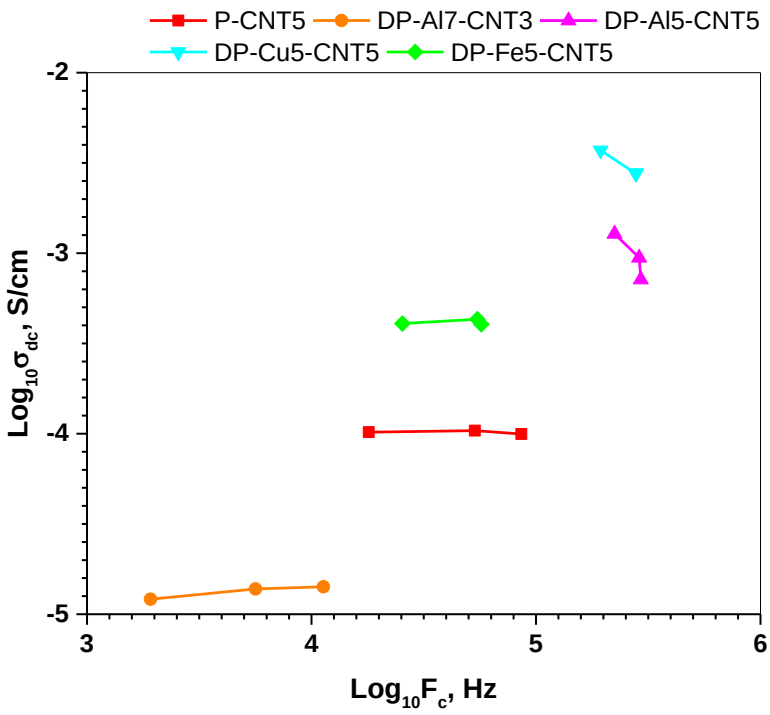

Figure 7.4| Electrical conductivity σ_{dc} as a function of F_c for PA6-based composites, taken at three different temperatures.

Regarding the s-exponent values (Table 7.2), for the P-CNT5 sample 0.52 $< s <$ 0.63 values were measured. As the temperature increases above T_g of ca. 50°C, the s values decrease, suggesting that the mobility of charges through the conductive network is enhanced by higher temperatures. For DP-samples, the s values are lower than the expected ones being in the range of 0.11 (DP-Cu5-CNT5) and 0.41 (DP-Al7-CNT3), whereby the higher the conductivity, the lower the s-exponent. This is probably due to fact that the electrical conductivity of these samples is relatively high and that in the frequency range measured the exponent s cannot display its real value. The measured exponent in the DP-samples is related just to the beginning of the bending-up of the conductivity curve. Nevertheless, the s values of the metal-CNT composites display once again the synergism between the CNT and metal particles in relation of the conductivity. All composites with mixed loads have lower s value than the single CNT loaded sample.

As concerns the F_c (Table 7.2), temperature dependencies were investigated. The F_c as a function of the reciprocal absolute temperature T for the conductive composites is presented in Figure 7.5.

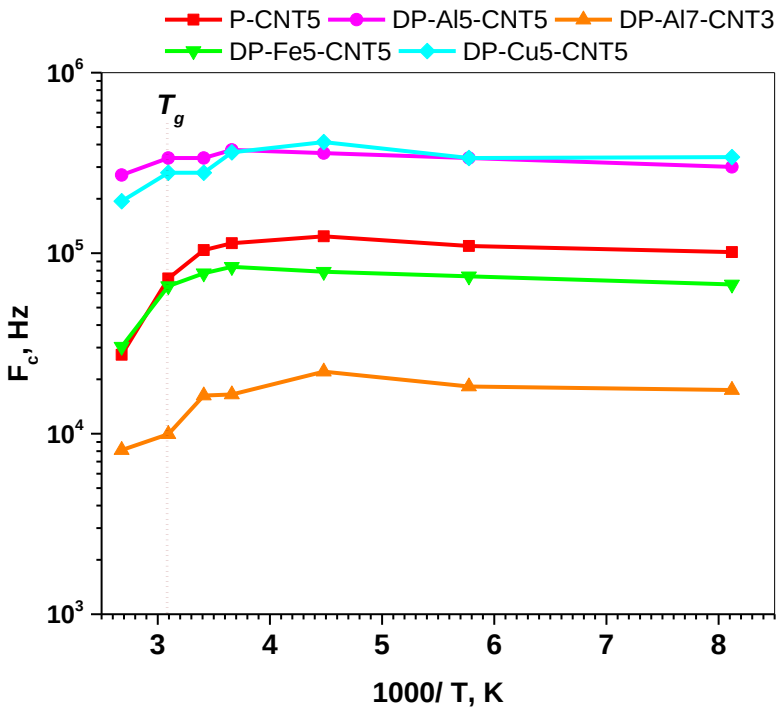

Figure 7.5| F_c as a function of the reciprocal temperature for conductive composites. Selected temperatures: 100, 50, 20, 0, -50, -100, and -150 °C. The dashed line indicates the T_g of the PA6 matrix.

As observed, in general for $T < T_g$, the F_c values seem to be temperature independent. However, at temperatures close or higher than the T_g, the F_c decreases, although slightly. This temperature activation is better expressed in the samples with the inferior F_c values, i.e., DP-Al7-CNT3, DP-Fe5-CNT5, and P-CNT5 whereby in the DP-Al5-CNT5 and DP-Cu5-CNT5 samples the effect is weaker. It can be therefore deduced that the conductance of the percolating network of all the composites studied is affected by the temperature. It should be also noted that the sample DP-Al3-CNT7 does not appear in Figure 7.5. Most probably, due to its conductivity, the respective F_c would appear above 10^6 Hz, i.e., out of the frequency range studied in our experiment.

As a concluding part of the BDS study, the temperature dependencies of σ_{dc} was studied for all PA6-based composites with single metal loads, single CNT load, and the dually loaded metal-CNT samples. Figure 7.6 displays the σ_{dc} of the composites as a function of the reciprocal absolute T at a selected frequency.

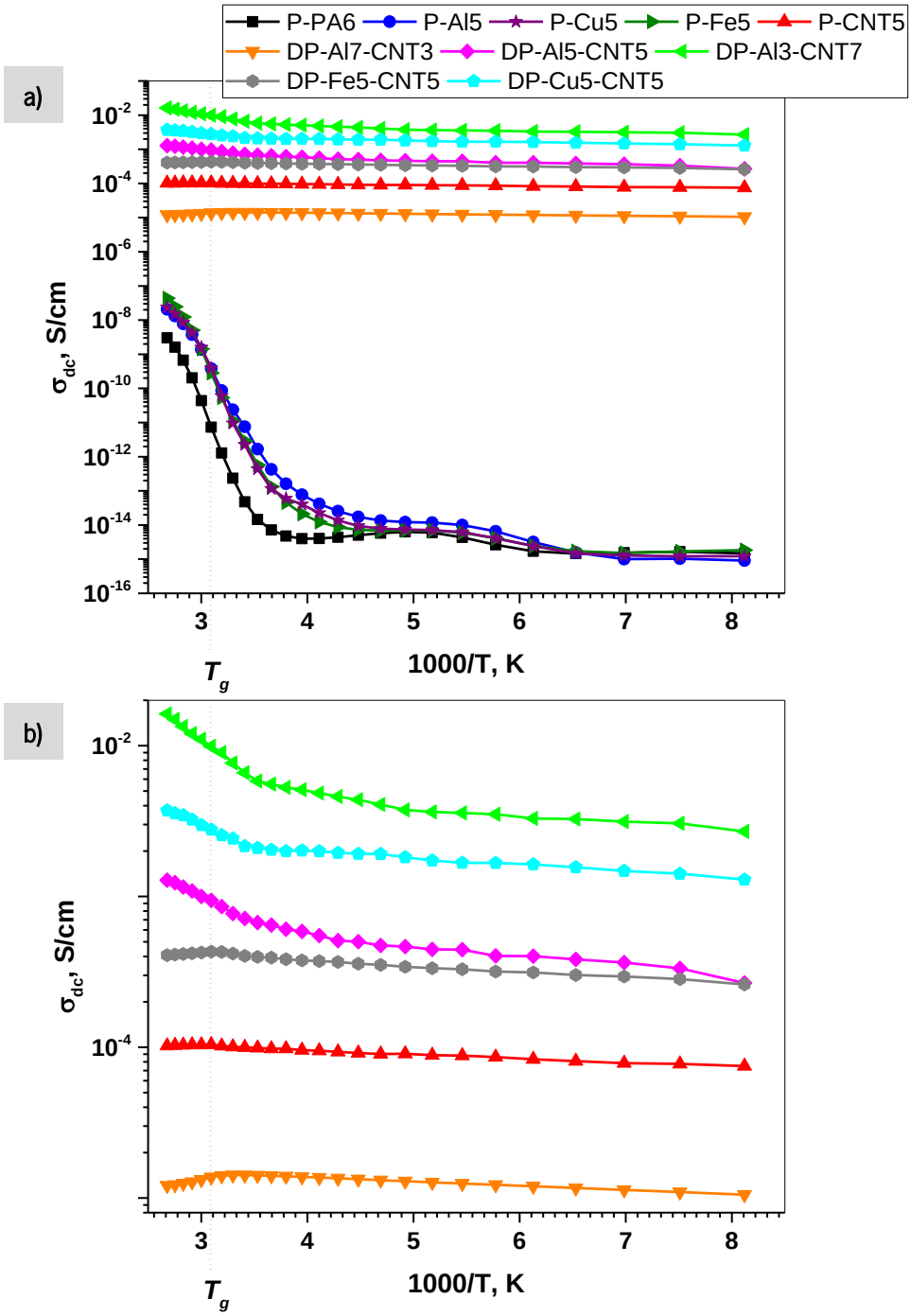

Figure 7.6 | σ_{dc} of the composites as a function of the reciprocal temperature at f = 0.1 Hz: a) P- and DP-samples; b) magnification of a) for DP-samples. The dashed line indicates the T_g of the PA6 matrix.

Figure 7.6a indicates that the *insulating* P-PA6 and P-metal samples display a temperature dependence in the whole temperature interval between -150 – 100 °C showing an increase of σ_{dc} as the temperature increases above T_g of the matrix PA6. This behavior should be related to the increasing mobility of dipoles occurring during heating. At the same time, in the P-CNT-5 and in all dually loaded DP-

samples (*semiconductors*), the σ_{dc} is nearly temperature independent at low temperatures and exhibits a temperature-activated character at higher temperatures. This type of electrical conductivity is characteristic for percolating networks with a fluctuation-induced tunneling conductance (FITC) mechanism that is temperature independent and is frequently found in CNT-containing polymer-based composites.[25, 27, 41].

As seen more distinctly from Figure 7.6b, the temperature dependence can be different, judging from the slope of the high-temperature segments of the curves. As previously shown [42, 43], at $T > T_g$ the temperature dependence of σ_{dc} can be affected by morphological variations of the matrix polymer giving rise to a positive temperature coefficient (PTC) or negative temperature coefficient (NTC), related respectively to an increase or decrease of resistivity of the studied system. Thus, the tree samples designated as DP-Al3-CNT7, DP-Cu5-CNT5, and DP-Al5-CNT5 display a clear NTC effect, while in the DP-Al7-CNT3 and DP-Fe5-CNT5 the opposite PTC is observed. Interestingly, the P-CNT5 sample the high-temperature segment of the curve above T_g does not depend on T.

7.4. Summary

BDS was used for the first time to investigate the frequency- and temperature dependencies of the electrical conductivity in dually loaded metal-CNT composite plates obtained by consecutive reactive microencapsulation and compression molding. Molded samples with monoloads (separate metals or CNT) were also studied at the same conditions to enable comparison.

It was confirmed that while the systems containing 5 wt.% of separate metals remain electrical insulators in the whole range of temperatures and frequencies studied, 5.0 wt.% of CNT leads to semiconductor composite samples with universal dynamic response. The latter is typical for translational motions of charges across conducting networks.

In the dually loaded metal-CNT samples (DP-samples), the significant increase of the dc electrical conductivity by five to eleven orders of magnitude is to be attributed to the coexistence of metal particles embedded within the CNT conducting network. This coexistence changes the values of the critical frequency F_c at which $\sigma(\omega) = \sigma_{ac} \propto \omega^s$. The temperature dependence of F_c and σ_{dc} for all DP-samples is consistent with the FITC mechanism. The FITC could be related with positive or negative temperature coefficient, the latter depending on the type and concentration of the metal component.

7.5. References

[1] Kremer F, Schönhals A (2003) Broadband Dielectric Spectroscopy, 1st ed. Springer-Verlag Berlin Heidelberg

[2] Steeman PAM, Maurer FHJ (1992) Dielectric properties of polyamide-4,6. *Polymer (Guildf)*, 33:4236–4241. DOI: 10.1016/0032-3861(92)90263-V

[3] Xu P, Zhang X (2011) Investigation of MWS polarization and dc conductivity in polyamide 610 using dielectric relaxation spectroscopy. *Eur Polym J*, 47:1031–1038. DOI: 10.1016/j.eurpolymj.2011.02.016

[4] Füllbrandt M, Wellert S, von Klitzing R, Schönhals A (2015) Thermal and corrosion (in)stability of polyamide 6 studied by broadband dielectric spectroscopy. *Polymer (Guildf)*, 75:34–43. DOI: 10.1016/j.polymer.2015.08.016

[5] Connor MT, Roy S, Ezquerra TA, Calleja FJB (1998) Broadband ac conductivity of conductor-polymer composites. *Phys Rev B*, 57:2286–2294. DOI: 10.1103/PhysRevB.57.2286

[6] Lozano K, Bonilla-Rios J, Barrera E V. (2001) A study on nanofiber-reinforced thermoplastic composites (II): Investigation of the mixing rheology and conduction properties. *J Appl Polym Sci*, 80:1162–1172. DOI: 10.1002/app.1200

[7] Barrau S, Demont P, Peigney A, Laurent C, Lacabanne C (2003) DC and AC Conductivity of Carbon Nanotubes–Polyepoxy Composites. *Macromolecules*, 36:5187–5194. DOI: 10.1021/ma021263b

[8] Szymczyk A, Roslaniec Z, Zenker M, García-Gutiérrez MC, Hernández JJ, Rueda DR, Nogales A, Ezquerra TA (2011) Preparation and characterization of nanocomposites based on COOH functionalized multi-walled carbon nanotubes and on poly(trimethylene terephthalate). *eXPRESS Polym Lett*, 5:977–995. DOI: 10.3144/expresspolymlett.2011.96

[9] Linares A, Canalda JC, Cagiao ME, García-Gutiérrez MC, Nogales A, Martín-Gullón I, Vera J, Ezquerra TA (2008) Broad-Band Electrical Conductivity of High Density Polyethylene Nanocomposites with Carbon Nanoadditives: Multiwall Carbon Nanotubes and Carbon Nanofibers. *Macromolecules*, 41:7090–7097. DOI: 10.1021/ma801410j

[10] Psarras GC, Manolakaki E, Tsangaris GM (2002) Electrical relaxations in polymeric particulate composites of epoxy resin and metal particles. *Compos Part A Appl Sci Manuf*, 33:375–384. DOI: 10.1016/S1359-835X(01)00117-8

[11] Mamunya YP, Davydenko VV, Pissis P, Lebedev EV (2002) Electrical and thermal conductivity of polymers filled with metal powders. *Eur Polym J*, 38:1887–1897. DOI: 10.1016/S0014-3057(02)00064-2

[12] Cassignol C, Cavarero M, Boudet A, Ricard A (1999) Microstructure–conductivity relationship in conducting polypyrrole/epoxy composites. *Polymer (Guildf)*, 40:1139–1151. DOI: 10.1016/S0032-3861(98)00349-8

[13] Bhattacharyya S, Saha SK, Mandal TK, Mandal BM, Chakravorty D, Goswami K (2001) Multiple hopping conduction in interpenetrating polymer network composites of poly pyrrole and poly (styrene-co-butyl acrylate). *J Appl Phys*, 89:5547–5551. DOI: 10.1063/1.1356435

[14] Isichenko MB (1992) Percolation, statistical topography, and transport in random media. *Rev Mod Phys*, 64:961–1043. DOI: 10.1103/RevModPhys.64.961

[15] Al-Saleh MH, Sundararaj U (2009) Electromagnetic interference shielding mechanisms of CNT/polymer composites. *Carbon N Y*, 47:1738–1746. DOI: 10.1016/j.carbon.2009.02.030

[16] Al-Saleh MH, Sundararaj U (2012) Microstructure, electrical, and electromagnetic interference shielding properties of carbon nanotube/acrylonitrile–butadiene–styrene nanocomposites. *J Polym Sci Part B Polym Phys*, 50:1356–1362. DOI: 10.1002/polb.23129

[17] Verma P, Saini P, Malik RS, Choudhary V (2015) Excellent electromagnetic interference shielding and mechanical properties of high loading carbon-nanotubes/polymer composites designed using melt recirculation equipped twin-screw extruder. *Carbon N Y*, 89:308–317. DOI: 10.1016/j.carbon.2015.03.063

[18] Jia L-C, Yan D-X, Cui C-H, Jiang X, Ji X, Li Z-M (2015) Electrically conductive and electromagnetic interference shielding of polyethylene composites with devisable carbon nanotube networks. *J Mater Chem C*, 3:9369–9378. DOI: 10.1039/C5TC01822F

[19] Nasouri K, Valipour P (2015) Fabrication of polyamide 6/carbon nanotubes composite electrospun nanofibers for microwave absorption application. *Polym Sci Ser A*, 57:359–364. DOI: 10.1134/S0965545X15030098

[20] Jalali M, Dauterstedt S, Michaud A, Wuthrich R (2011) Electromagnetic shielding of polymer–matrix composites with metallic nanoparticles. *Compos Part B Eng*, 42:1420–1426. DOI: 10.1016/j.compositesb.2011.05.018

[21] Gabriel P, Ana J (2004) Conducting aluminum-filled nylon 6 composites. *Polym Compos*, 22:65–70. DOI: 10.1002/pc.10517

[22] Ogawa F, Masuda C, Fujii H (2018) In situ chemical vapor deposition of metals on vapor-grown carbon fibers and fabrication of aluminum-matrix composites reinforced by coated fibers. *J Mater Sci*, 53:5036–5050. DOI: 10.1007/s10853-017-1921-9

[23] Tzeng S-S, Chang F-Y (2001) EMI shielding effectiveness of metal-coated carbon fiber-reinforced

ABS composites. *Mater Sci Eng A*, 302:258–267. DOI: doi.org/10.1016/S0921-5093(00)01824-4

[24] Pierozynski B (2015) Electrodeposition of Nickel onto 12K Carbon Fibre Tow in a Continuous Manner. *Croat Chem Acta*, 85:1–8. DOI: 10.5562/cca1743

[25] Logakis E, Pandis C, Peoglos V, Pissis P, Pionteck J, Pötschke P, Mičušík M, Omastová M (2009) Electrical/dielectric properties and conduction mechanism in melt processed polyamide/multi-walled carbon nanotubes composites. *Polymer (Guildf)*, 50:5103–5111. DOI: 10.1016/j.polymer.2009.08.038

[26] Brêda C, Dencheva N, Lanceros-Mendez S, Denchev Z (2016) Preparation and properties of metal-containing polyamide hybrid composites via reactive microencapsulation. *J Mater Sci*, 51:10534–10554. DOI: 10.1007/s10853-016-0274-0

[27] Nogales A, Broza G, Roslaniec Z, Schulte K, Šics I, Hsiao BS, Sanz A, García-Gutiérrez MC, Rueda DR, Domingo C, Ezquerra TA (2004) Low Percolation Threshold in Nanocomposites Based on Oxidized Single Wall Carbon Nanotubes and Poly(butylene terephthalate). *Macromolecules*, 37:7669–7672. DOI: 10.1021/ma049440r

[28] Schönhals A, Kremer F (2003) Analysis of Dielectric Spectra. In: Kremer F, Schönhals A (eds) Broadband Dielectric Spectroscopy. Springer Berlin Heidelberg, Berlin, Heidelberg, pp 59–98

[29] Vassilikou-Dova A, Kalogeras IM (2009) Dielectric Analysis. In: Menczel JD, Prime RB (eds) Thermal Analysis of Polymers: Fundametals and Applications, 1st ed. John Wiley & Sons, Inc, USA, pp 497–614

[30] Jonscher AK (1977) The 'universal' dielectric response. *Nature*, 267:673–679. DOI: 10.1038/267673a0

[31] Macdonald JR (2000) Comparison of the universal dynamic response power-law fitting model for conducting systems with superior alternative models. *Solid State Ionics*, 133:79–97. DOI: 10.1016/S0167-2738(00)00737-2

[32] Dyre JC, Schroder TB (2000) Universality of ac conduction in disordered solids. *Rev Mod Phys*, 72:873–892

[33] Kremer F, Różański SA (2003) The Dielectric Properties of Semiconducting Disordered Materials. In: Kremer F, Schönhals A (eds) Broadband Dielectric Spectroscopy. Springer Berlin Heidelberg, Berlin, Heidelberg, pp 475–494

[34] Chatterjee S, Nafezarefi F, Tai NH, Schlagenhauf L, Nüesch FA, Chu BTT (2012) Size and synergy effects of nanofiller hybrids including graphene nanoplatelets and carbon nanotubes in mechanical

properties of epoxy composites. *Carbon N Y*, 50:5380–5386. DOI: 10.1016/j.carbon.2012.07.021

[35] Yang S-Y, Lin W-N, Huang Y-L, Tien H-W, Wang J-Y, Ma C-CM, Li S-M, Wang Y-S (2011) Synergetic effects of graphene platelets and carbon nanotubes on the mechanical and thermal properties of epoxy composites. *Carbon N Y*, 49:793–803. DOI: 10.1016/j.carbon.2010.10.014

[36] Paszkiewicz S, Szymczyk A, Sui XM, Wagner HD, Linares A, Ezquerra TA, Rosłaniec Z (2015) Synergetic effect of single-walled carbon nanotubes (SWCNT) and graphene nanoplatelets (GNP) in electrically conductive PTT-block-PTMO hybrid nanocomposites prepared by in situ polymerization. *Compos Sci Technol*, 118:72–77. DOI: 10.1016/j.compscitech.2015.08.011

[37] Li J, Wong P-S, Kim J-K (2008) Hybrid nanocomposites containing carbon nanotubes and graphite nanoplatelets. *Mater Sci Eng A*, 483–484:660–663. DOI: 10.1016/j.msea.2006.08.145

[38] Valentini L, Bon SB, Lopez-Manchado MA, Verdejo R, Pappalardo L, Bolognini A, Alvino A, Borsini S, Berardo A, Pugno NM (2016) Synergistic effect of graphene nanoplatelets and carbon black in multifunctional EPDM nanocomposites. *Compos Sci Technol*, 128:123–130. DOI: 10.1016/j.compscitech.2016.03.024

[39] He L, Tjong S-C (2014) Electrical behavior and positive temperature coefficient effect of graphene/polyvinylidene fluoride composites containing silver nanowires. *Nanoscale Res Lett*, 9:375. DOI: 10.1186/1556-276X-9-375

[40] Brandes EA, Brook GB (1992) General physical properties. In: Smithells Metals Reference Book (Seventh Edition), Seventh Ed. Butterworth-Heinemann, Oxford, pp 14–43

[41] Sheng P (1980) Fluctuation-induced tunneling conduction in disordered materials. *Phys Rev B*, 21:2180–2195. DOI: 10.1103/PhysRevB.21.2180

[42] J. Meyer (1973) Glass transition temperature as a guide to selection of polymers suitable for PTC materials. *Polym Eng Sci*, 13:462–468. DOI: 10.1002/pen.760130611

[43] Zhang R, Tang P, Li J, Xu D, Bin Y (2014) Study on filler content dependence of the onset of positive temperature coefficient (PTC) effect of electrical resistivity for UHMWPE/LDPE/CF composites based on their DC and AC electrical behaviors. *Polymer (Guildf)*, 55:2103–2112. DOI: 10.1016/j.polymer.2014.02.065

CHAPTER 8

Electromagnetic shielding properties of binary metal/CNT polyamide 6 composites

8.1. Introduction

The attenuation of the electromagnetic (EM) radiation can be achieved through the development of polymer-based composites with electromagnetic interference (EMI) shielding properties. Tailoring the electric conductive properties using proper payloads and ensuring its good dispersion within the polymer matrix, it is possible obtaining these advanced materials. The preliminary results obtained by solid-state nuclear magnetic resonance (ssNMR) (See section 5.8 of Chapter 5) suggested that the mixture of metal/carbon nanotube (CNT) fillers has a shielding effect at low frequencies due to the decrease of the resolution and peak intensity of the NMR signals. However, it is important the use of a simple handling method and in over a wide range of frequencies for studying the EMI shielding properties of composite materials. Thus, the coaxial transmission line method was selected for evaluating such EMI shielding response of the conductive polyamide 6 (PA6)-based composites. The first measurements were made between 30 MHz and 3GHz. Then, systematic experiments were performed for selected molded samples over a frequency range of 3–12.4 GHz to obtain a full profile of the EMI shielding properties of binary PA6 composites containing metal particles and CNT. In addition to the effect of the different loads dispersed in the polymer matrix on the shielding effectiveness (SE), the influence of the thickness on the EMI shielding performance of the molded composites was also evaluated.

8.2. Samples investigated

The EMI shielding measurements were performed by the transmission coaxial line method (See section 1.3.4 of Chapter 1), and the total SE (SE_T), SE by absorption (SE_A), and by reflection (SE_R) were determined as described in section 2.8 of Chapter 2. Mono and dually loaded hybrid plates with metal, CNT and their mixtures were compressed molding from the respective loaded PA6 microcapsules (PAMC) precursors (Chapter 2, M- and DM-series). All molded plates were produced using a mold with dimensions 85 × 75 × 1 mm (See section 2.3.4.1 of Chapter 2). For evaluation of the thickness influence on the EMI shielding properties, selected composites with 2 mm thickness were produced using a mold with dimensions 70 x 70 x 2 mm (See section 2.3.4.1 of Chapter 2). For each composition under analysis, two specimens (load and reference) with specific geometry were cut. For further details and visualization of the specimen's shape and dimensions, see section 2.8 of Chapter 2. Table 8.1 presents the compositions of the P- and DP-samples investigated.

Table 8.1 | Designation and composition of the samples investigated

Sample	Composition, vol.% [a]		
	Metal	CNT	PA6
P-PA6	0	0	100
P-Al5	4.18	0	95.8
P-Cu5	1.33	0	98.7
P-Fe5	1.06	0	98.9
P-CNT3	0	2.65	97.4
P-CNT5	0	4.45	95.6
P-CNT7	0	6.72	93.3
DP-Al3-CNT7	1.96	5.71	92.3
DP-Al5-CNT5	3.84	4.80	91.4
DP-Al7-CNT3	4.68	2.51	92.8
DP-Cu5-CNT5	1.03	4.29	94.7
DP-Fe5-CNT5	0.93	3.38	95.7

[a] Represents the relation between the volumes of metal, CNT, and PA6 in the respective DM-sample.

8.3. EMI shielding efficiency

8.3.1. Experiments from 30 MHz to 3 GHz

The EMI SE plots of the 1 mm thick PA6-based composites loaded with 5 wt.% of CNT or metal payloads are presented in Figure 8.1, within 30 MHz and 3 GHz. In Table 8.2 are summarized the respective numeric EMI SE data obtained at 3 GHz. It is observed that the neat PA6 is completely transparent for EM waves (Fig. 8.1a). With the presence of metal particles, there are no changes in the EMI shielding properties, which means that the PA6/metal composites have poor shielding efficiency. In the P-Al5 sample, it is observed a slight increase in the SE_T value up to 1 dB. This result could indicate the formation of some current path, but the strong Maxwell-Wagner-Sillars (MWS) polarization present in this sample does not allow the mobility of the charge carries, maintaining the insulator properties of the polymer matrix. Having in mind that in the previous chapters have been discussed the insulator properties of such metal-loaded composites, these results were expected. There are no free charge carriers that can interact with the incident EM field, resulting in SE_R (Fig. 8.1b), or electric or magnetic dipoles that could introduce losses into the system resulting in SE_A (Fig. 8.1c).

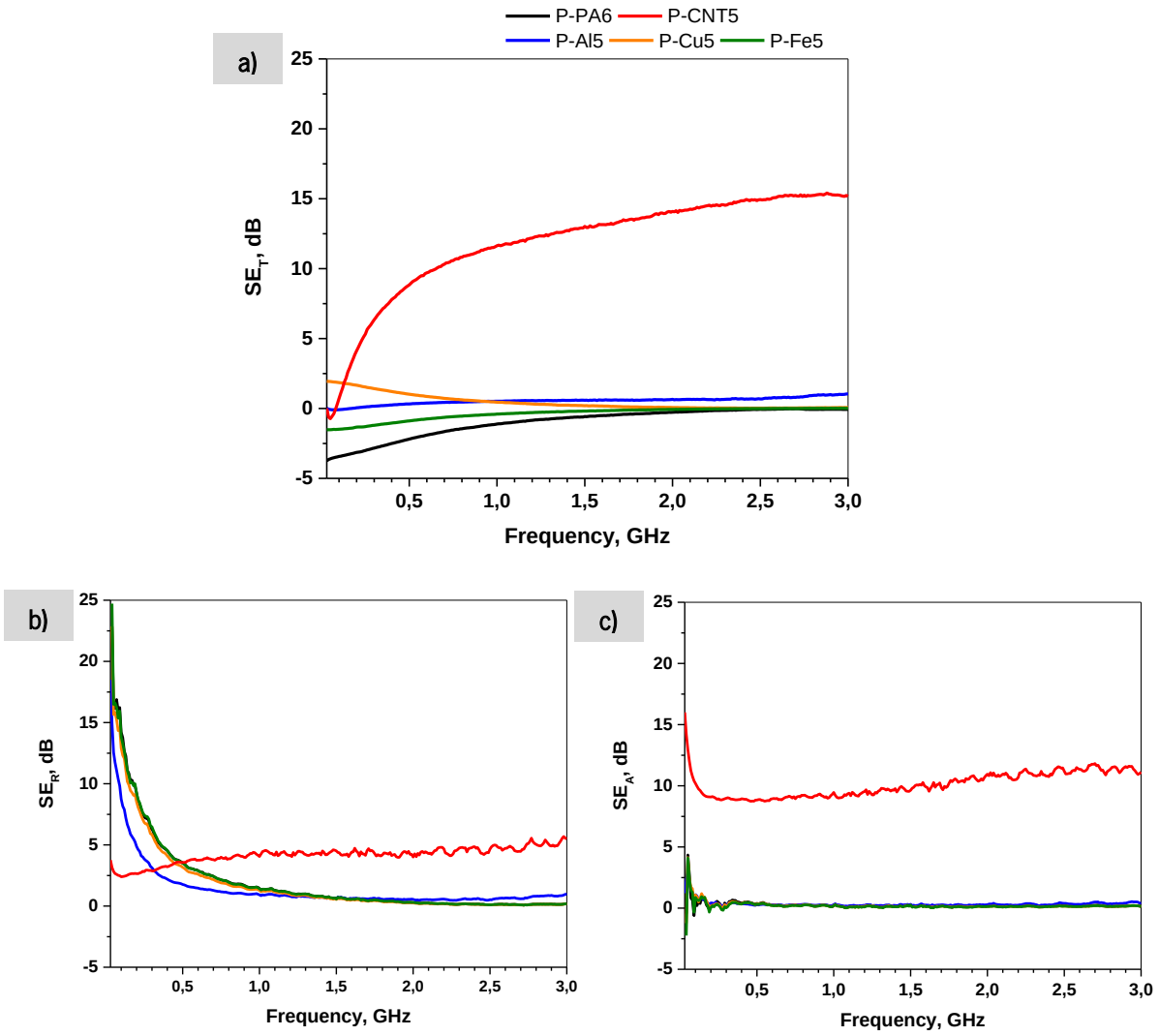

Figure 8.1 | a) Total EMI SE, b) EMI SE by reflection and c) EMI SE by absorption of the PA6-based composites load with 5 wt.% of CNT or metal payloads.

On the other hand, in the presence of CNT, it is observed that the SE is achieved by the incorporation of such carbon allotrope (C-allotrope) within the PA6 matrix (Fig. 8.1a, Table 8.2). Compared with the neat PA6, the total EMI SE value increased significantly to 15.17 dB at 3 GHz in the P-CNT5 sample. The electric conductive properties of this composite (Table 7.2, Figure 7.3 of Chapter 7) lead to the enhanced EMI shielding properties. The high aspect ratio of CNT (Figure 3.2a of Chapter 3) and their good dispersion within the polymer matrix favor the formation of a continuous conducting network, as indicated in the previous chapters (See Chapters 3 – section 3.6, Chapter 5 – section 5.6, and Chapter 7 – section 7.3).

Moreover, the EMI SE by reflection and absorption can be distinguished (Table 8.2, Figure 8.1b, c), in which the shielding mechanism is mainly absorption. This finding is related to the enhanced electric conductivity of the P-CNT5 sample (Table 7.2, Figure 7.3 of Chapter 7). Since there is a conductive network formed by CNT, the EM waves interact with the electron-rich CNT filler leading to the dissipation of the mobile charge carriers, thus increasing the absorption losses. [1–3].

Table 8.2 | EMI SE data for 1 mm thick PA6-based composites at 3 GHz

Sample	SE_T, dB	SE_R, dB	SE_A, dB
P-PA6	0.00	0.19	0.14
P-Al5	1.04	0.97	0.41
P-Cu5	0.07	0.19	0.13
P-Fe5	0.02	0.20	0.14
P-CNT5	15.17	5.51	11.12
DP-Al5-CNT5	20.16	7.99	13.5
DP-Cu5-CNT5	16.61	5.52	11.16
DP-Fe5-CNT5	15.67	5.27	10.77

In order to evaluate the influence of binary loads, that is CNT and metal particles, on the EMI shielding performance, measurements were made for the metal-CNT 5/5 wt.% composites. Figure 8.2 displays the EMI SE plots for these DP-samples. The numeric data related to such samples are summarized in Table 8.2.

As stated in Chapter 7, the improvement of the electric conductive properties of the binary composites is determined by the coexistence of CNT and metal fillers (Table 7.2 and Figure 7.3 of Chapter 7). This synergetic effect should be related to the incorporation of metal particles within the CNT conducting network, which is supposed to improve the charge carrier mobility. The same synergism was expected in the evaluation of the EMI shielding performance of the binary composites. The results in Fig.8.2a and Table 8.2 confirm this expectance showing that the metal-loaded samples are transparent to the EM waves, however the binary composites (DP series) possess higher SE_T than the P-CNT5 composite.

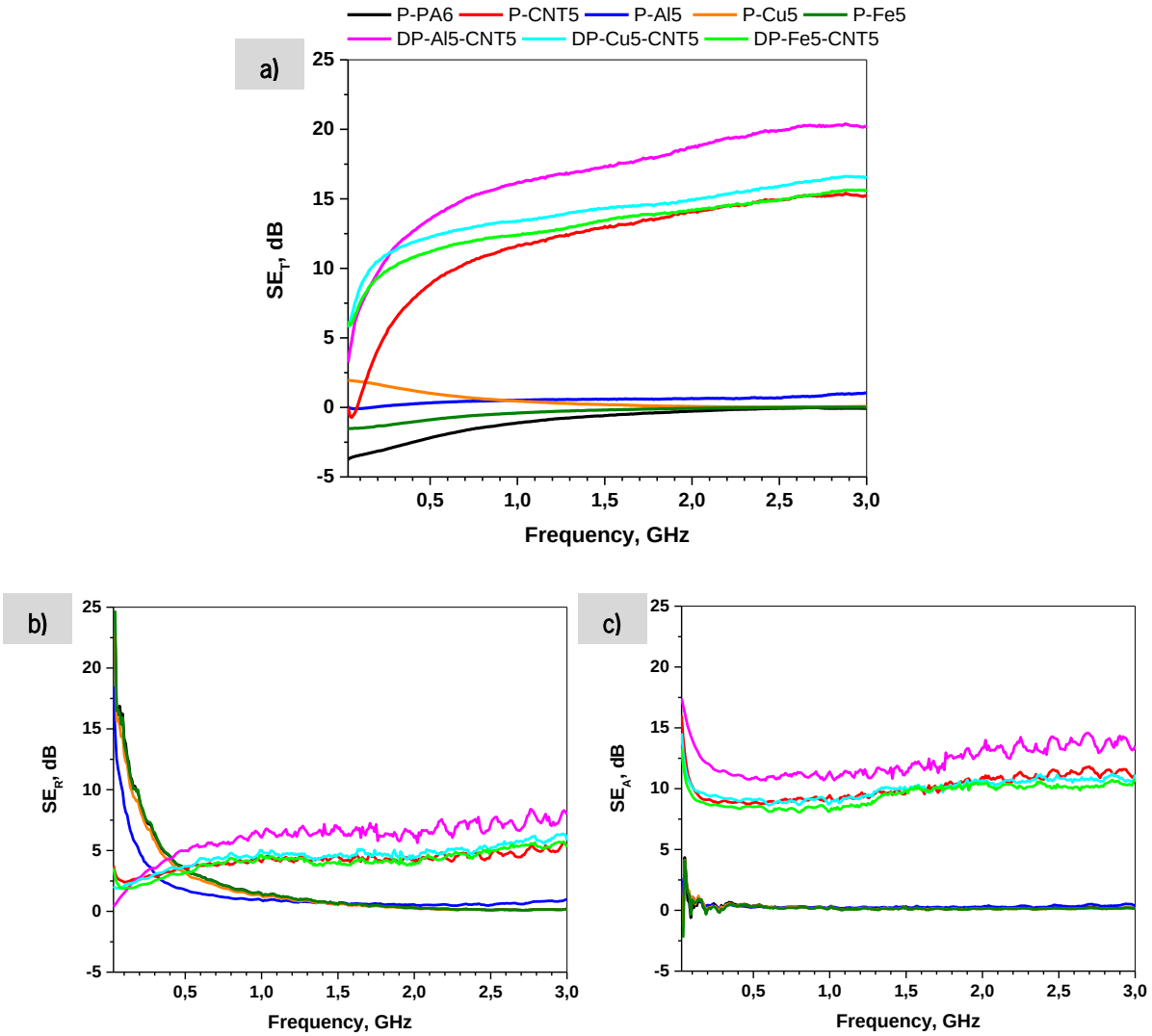

Figure 8.2| a) Total EMI SE, b) EMI SE by reflection and c) EMI SE by absorption of the metal-CNT 5/5 wt.% composites, compared to that loaded with 5 wt.% of CNT or metal particles.

Furthermore, the experimental data show also the influence of the volume fraction, type, and shape of the metal particles used on the composite EMI properties. The volume fraction of Cu and Fe particles in the respective DP-samples is of about three times lower as compared to that of Al (Table 8.1), due to their high densities[4], which does not contribute to the enhancement of the conductive network, and therefore, for a significant increase of EMI SE of these samples. The size and shape of metal particles can also influence the EMI shielding performance. The Cu dendritic particles have sizes of ≈ 20 μm (Figure 3.3b of Chapter 3) and Fe particles are spherical with diameters in the 1–34 μm range (Figure 3.3d of Chapter 3), whereas Al particles are shaped as platelets with maximum sizes of 80–100 μm and thickness of 10 – 15 μm (Figure 3.3a of Chapter 3). Nevertheless, EMI SE values

between 15.67 (DP-Fe5-CNT5) and 20.16 dB (DP-Al5-CNT5) were obtained at 3 GHz, confirming that the use of binary fillers enhances the EMI shielding properties of the PA6-based composites.

Regarding the EMI shielding mechanisms in these composites, Fig. 8.2b-c show, respectively, the dependencies of the SE_R and SE_A components as a function of frequency. It is clear that both SE_R and SE_A increase with frequency and the SE_R values are lower. The absorption is the main shielding mechanism (Fig. 8.2c, Table 8.2), contributing mostly to the increase of the SE_T (Fig. 8.2a). These results agree with the increased charge carriers through the conductive network established by the well-dispersed CNT (Figure 5.3 of Chapter 5) within the polymer matrix, increasing the conductive losses [5], and therefore the absorption occurs.

Moreover, as earlier enunciated with Eq. 1.3 and 1.4 in Chapter 1, the SE_R and SE_A values follow a linear conductivity dependence [2], which means the higher conductivity, the higher the EMI SE. Hence, the data obtained with these experiments confirm that the EMI shielding properties and the electric conductivity of the CNT-loaded, simple or binary, PA6 composites are related and depend on the CNT network formation. The well-dispersed CNT produces the conductive network in which the metal particles are embedded. These embedded metal particles enhance the charge transfer increasing, therefore, the conductivity. In the EMI shielding measurements, the presence of metal particles should result in an energy loss by multiple reflection/absorption within the volume of the sample. In fact, this effect was registered in the EMI shielding measurements up to 3 GHz. As a result, the SE_T values in the DP-samples increase and we can speak of synergism between the CNT and metal fillers in this context.

Having confirmed the improved EMI shielding properties of the PA6-based composites in the presence of binary payloads, systematic measurements were performed for DP-samples over a frequency range of 3–12.4 GHz, as described in section 2.8 of Chapter 2.

8.3.2. Experiments from 3 to 12.4 GHz

Since the coaxial transmission line method is non-destructive, the samples evaluated in this frequency range are the same as those studied in the experiments from 30 MHz to 3 GHz.

The EMI SE plots of the 1 mm thick metal-CNT 5/5 wt.% are presented in Figure 8.3, within 3 and 12.4 GHz. Table 8.3 summarizes the respective numeric data obtained at selected frequencies.

Over the frequency range under analysis, the previous trends related to the influence of metal-CNT composition on the EMI shielding properties of the PA6-based composites remain, since SE_T

values between 17.87 (P-CNT5) and 17.00 – 22.53 dB (DP-Metal5-CNT5) were obtained at 3 GHz (Fig. 8.3a, Table 8.3). The EMI SE values achieved at 12.4 GHz are between 19.56 (P-CNT5) and 19.60–24.33 dB for (DP-Metal5-CNT5) (Table 8.3, Fig. 8.3).

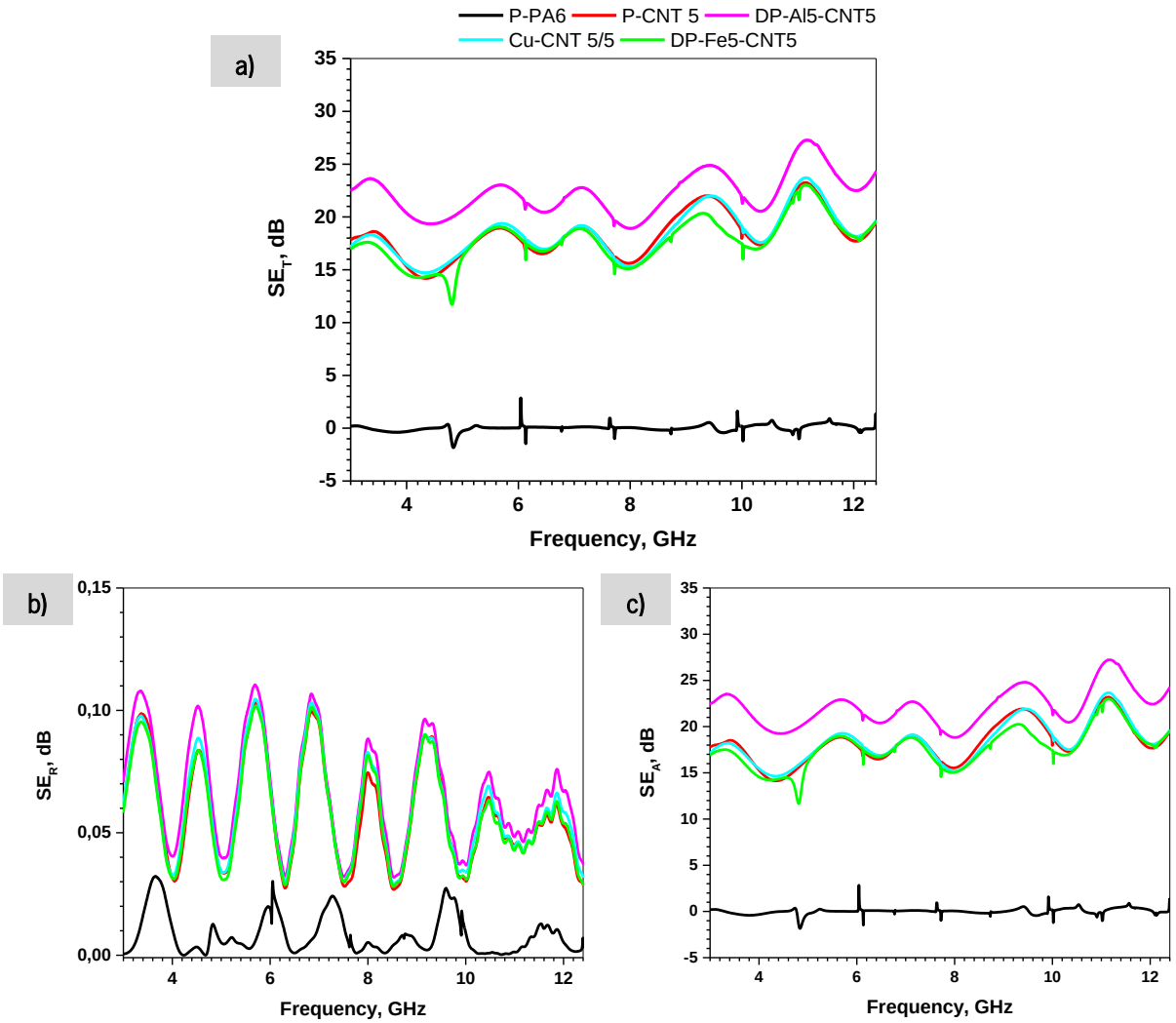

Figure 8.3| a) Total EMI SE, b) EMI SE by reflection and c) EMI SE by absorption of the metal-CNT 5/5 wt.% composites. The P-CNT5 composite is presented to enable comparison.

As mentioned in the analysis of the EMI shielding properties in the 3 MHz – 3 GHz frequency range, the improvement of the EMI shielding properties is determined by the conductive CNT filler (Table 7.2 and Figure 7.3 of Chapter 7). The presence of this C-allotrope leads to the formation of a conductive network, and therefore there is the EM wave attenuation. In the binary composites, their EMI shielding performance also depends on the metal filler within the CNT conductive network.

Table 8.3 | EMI shielding properties for 1 mm thick PA6-based composites at selected frequencies. All the values are given in dB

Sample	EMI shielding	3 GHz	4 GHz	8 GHz	12.4 GHz
	$\boldsymbol{SE_T}$	**0.00**	**0.00**	**0.00**	**0.00**
P-PA6	SE_R	4.82E-04	1.12E-02	3.16E-03	2.90E-03
	SE_A	1.90E-01	3.30E-01	2.30E-02	2.30E-01
	$\boldsymbol{SE_T}$	**7.14**	**6.81**	**6.93**	**11.06**
P-CNT3	SE_R	3.10E-02	2.30E-02	5.60E-02	2.10E-02
	SE_A	7.11	6.79	6.88	11.03
	$\boldsymbol{SE_T}$	**17.87**	**15.30**	**16.20**	**19.56**
P-CNT5	SE_R	6.20E-02	3.10E-02	6.40E-02	2.80E-02
	SE_A	17.81	15.27	16.14	19.53
	$\boldsymbol{SE_T}$	**22.66**	**20.84**	**21.49**	**26.13**
P-CNT7	SE_R	6.50E-02	3.50E-02	7.50E-02	3.30E-02
	SE_A	22.60	20.81	21.42	26.10
	$\boldsymbol{SE_T}$	**15.55**	**14.44**	**14.39**	**16.45**
DP-Al7-CNT3	SE_R	6.30E-02	3.60E-02	7.30E-02	3.10E-02
	SE_A	15.49	14.40	14.32	16.42
	$\boldsymbol{SE_T}$	**22.53**	**20.33**	**19.34**	**24.33**
DP-Al5-CNT5	SE_R	7.20E-02	4.00E-02	7.70E-02	3.70E-02
	SE_A	22.46	20.29	19.34	24.30
	$\boldsymbol{SE_T}$	**24.19**	**21.64**	**22.69**	**28.40**
DP-Al3-CNT7	SE_R	7.10E-02	3.70E-02	7.70E-02	3.50E-02
	SE_A	24.12	21.60	22.61	28.36
	$\boldsymbol{SE_T}$	**17.21**	**15.46**	**15.73**	**19.68**
DP-Cu5-CNT5	SE_R	6.30E-02	3.30E-02	7.10E-02	3.20E-02
	SE_A	17.15	15.43	15.66	19.64
	$\boldsymbol{SE_T}$	**17.00**	**14.58**	**15.62**	**19.60**
DP-Fe5-CNT5	SE_R	6.00E-02	3.10E-02	7.00E-02	2.90E-02
	SE_A	16.94	14.55	15.55	19.57

Besides the influence of the synergetic effect on the conductive properties of such composites, it can be said that the size and shape of the metal also contribute to the EM wave attenuation. According to the results on the electrical conductivity as a function of frequency for the metal-CNT 5/5 wt.% composites at 20°C (Table 7.2 and Figure 7.3 of Chapter 7), the electrical conductivity enhances with Cu particles (2.78E-03 S/cm) compared to the presence of Al particles (7.14E-04 S/cm). Thus, higher EMI SE values should be expected with DP-Cu5-CNT5. However, according to Table 8.3 and Figure 8.3, the DP-Al5-CNT5 sample has a better EMI shielding performance. Hence, it can be said that besides the attenuation of the EM waves due to the conductive losses, some of the EM waves can strike on the laminated and bigger Al surfaces. With this second barrier, the phenomenon of EM waves attenuation repeats. Thus, the EMI shielding is more effective in the DP-Al5-CNT5 composite.

Moreover, it is observed that in this frequency range (3 – 12.4 GHz) all loaded samples show a sinusoidal profile with a slightly increasing tendency with frequency. The sinusoidal shape of the curves can be due to the reflection events through the increased frequency, while the absorption mechanism can explain the increased values. As observed in Fig. 8.3c, the contribution of EM wave absorption (SE_A) for the SE_T is visibly predominant compared to that of the EM reflection (SE_R), which indicates that the absorption is the main EMI shielding mechanism. Moreover, these results confirm that the absorption receives contributions from losses due to conduction [5], as a result of the conductive network established by the well-dispersed CNT. The SE_R decrease with increased frequency (Fig. 8.3b), which agrees with the Eq. 1.2 of Chapter 1, since SE_R is inversely proportional to frequency [2, 6].

The EMI SE in the range of 20–40 dB is considered good for many commercial applications [7, 8]. At 12.4 GHz, our SE_T values between 19.60 and 24.33 dB for all DP-Metal5-CNT5 samples with 1 mm thick composite plates indicate their potential usefulness.

Bearing in mind that from the DP-Metal5/CNT5 series it was the DP-Al5-CNT5 sample that showed the best EMI shielding performance and, also aiming at low price and cost-effective materials, the system Al-CNT with various compositions was chosen for further in-depth studies. Despite the role of CNT on the EMI shielding performance and other related properties, the effect of the amount of this payload should be investigated. Figure 8.4 displays the EMI SE data for the Al/CNT binary composites referred, and the respective numeric data are summarized in Table 8.3.

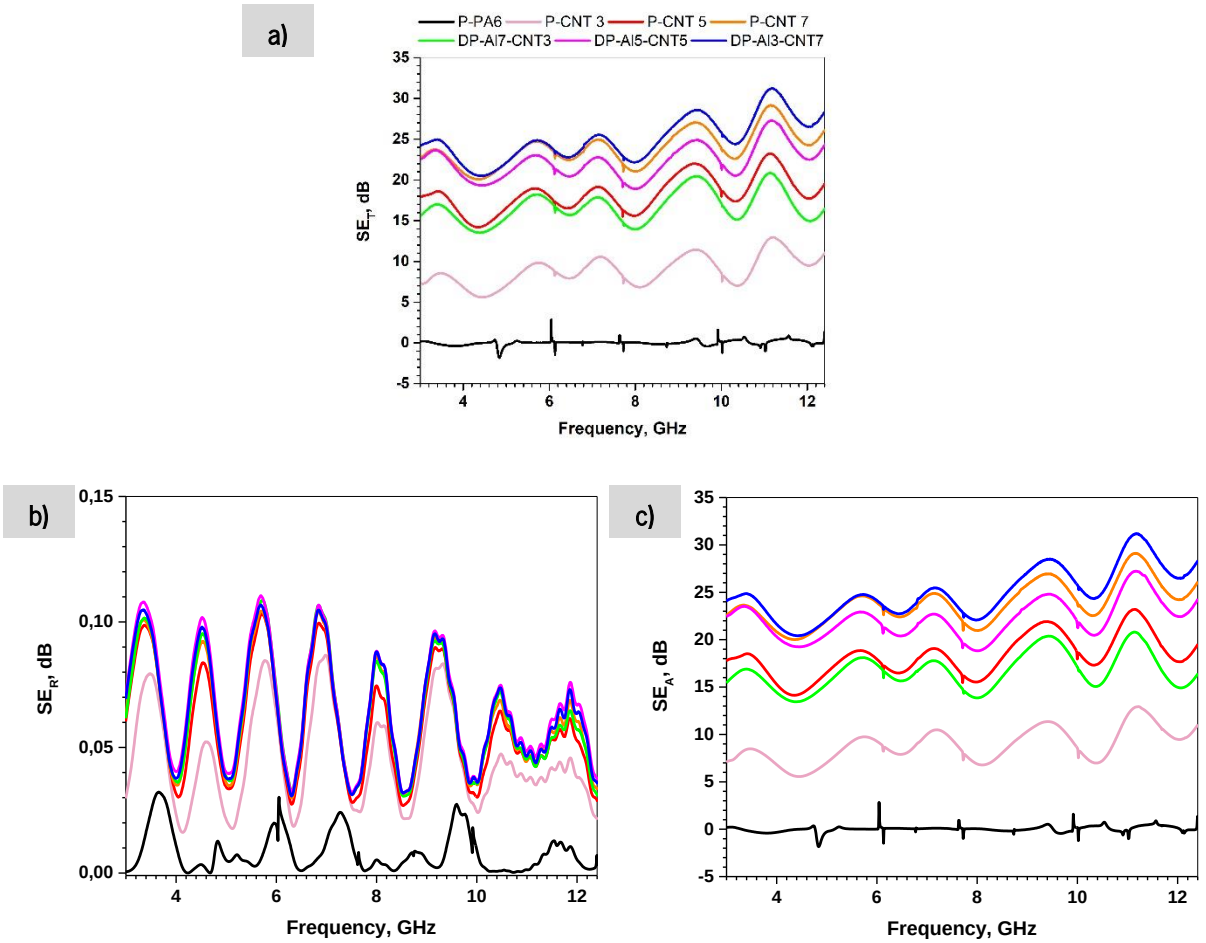

Figure 8.4| a) Total EMI SE, b) EMI SE by reflection and c) EMI SE by absorption of the Al-CNT composites with various compositions. The CNT-loaded composites are presented to enable comparison.

Increasing the amount of CNT, there is an improvement of the EMI shielding properties [3, 9, 10], and it is observed a synergetic effect on the SE when Al particles are combined with CNT within the polymer matrix. At 12.4 GHz, for P-CNT samples, SE_T values between 11.06 (P-CNT3) and 26.13 (P-CNT7) dB were obtained, while values up to 16.45–28.40 dB were reached for binary Al/CNT composites (Fig. 8.4a, Table 8.3), confirming the referred synergetic effect. This result was expected because, as shown in section 7.3 of Chapter 7, at 20 °C, the electrical conductivity enhances from 1.42E-05 S/cm to 6.61E-03 S/cm in the DP-Al7-CNT3 and DP-Al3-CNT7 composites, respectively. This increase in electrical conductivity leads to a higher EM wave attenuation due to the formation of a denser conducting network. For all Al/CNT samples, the absorption is the dominant shielding mechanism, since the SE_A values are always clearly higher than the respective SE_R. Thus, the

increase of the CNT concentration leads to an increase of the dissipating mobile charges carriers and, consequently, higher absorption loss increases [1–3].

In further studies of the Al-CNT system, the influence of the thickness was also evaluated for this set. Selected composites with 2 mm of thickness were prepared and subjected to EMI shielding tests at 3–12.4 GHz in order to compare with the 1 mm thick composite plates. Figure 8.5 shows the plots for such comparison of the EMI shielding properties.

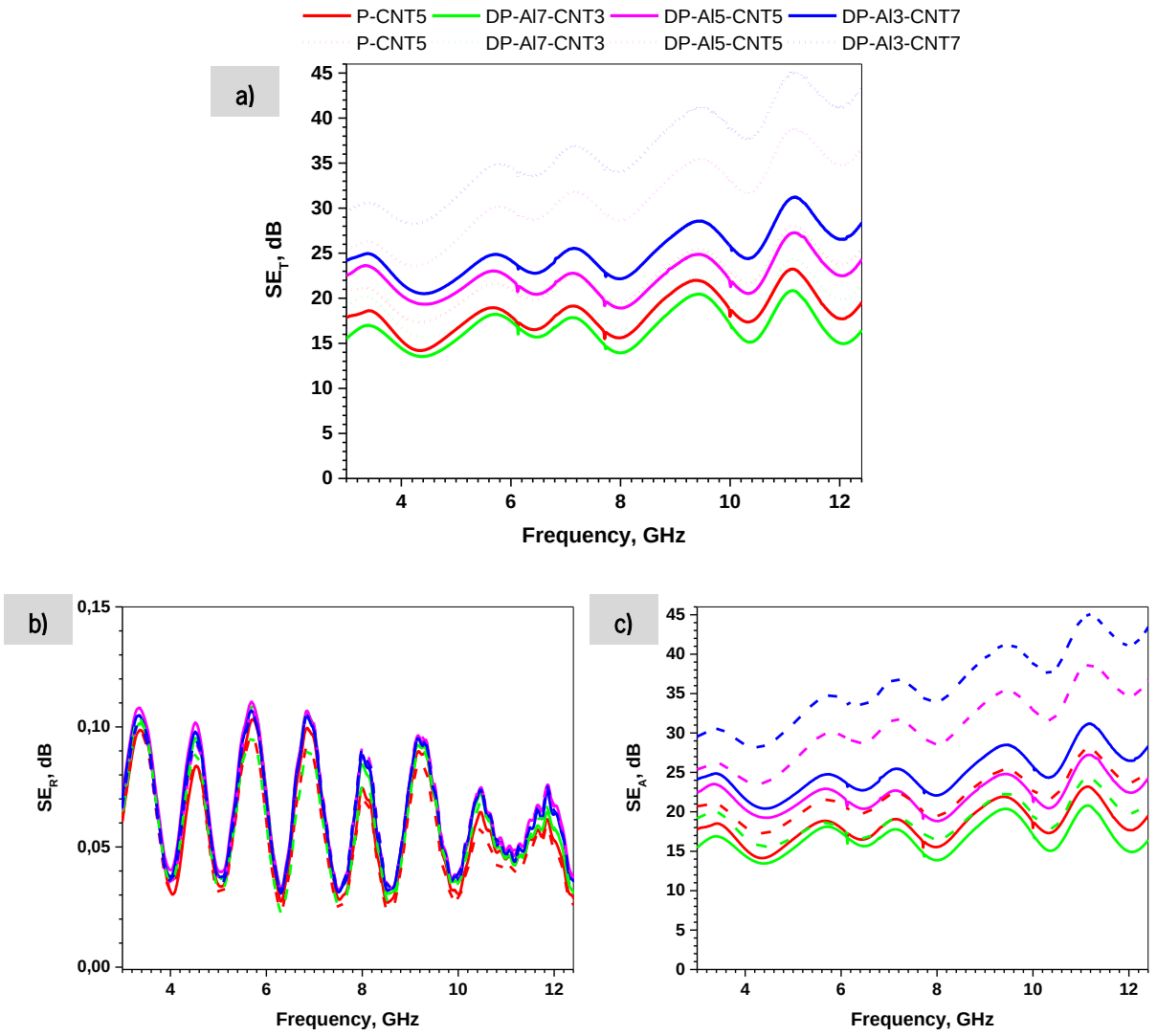

Figure 8.5| Comparison between EMI shielding properties of the 1- and 2-mm thick Al-CNT composites with various compositions. The P-CNT5 composite is presented to enable comparison: a) total EMI SE, b) EMI SE by reflection and c) EMI SE by absorption. 1-mm thick composites: solid lines; 2-mm thick composites: dashed lines.

Table 8.4 summarizes the numeric data obtained at selected frequencies for the 2 mm thick composites. In order to quantify the improvements in the EMI shielding performance related to the thickness influence, the improvement factor (IF) was determined for the SE_T values at 12.4 GHz and the results are presented in Table 8.5.

According to the results obtained, the EMI efficiency increases with increased thickness [2, 11]. These results were expected since the absorption efficiency is proportional to the material thickness as induced by Eq. 1.4 of Chapter 1, while the reflection is independent of the thickness of the shield. For the 2 mm thick DP-Al3-CNT7 sample at a frequency of 12.4 GHz, the SE_T value achieved 43.51 dB, representing an IF of about 53.2 % compared to that 1 mm thick equivalent composition (SE_T = 28.4 dB) (Table 8.5). The higher amount of CNT in the polymer matrix forming a denser conductive network, the insertion of the metal particles in the latter, and the increased thickness of the samples give more possibilities for the interference of the incoming EM waves with the conductive fillers that leads to their attenuation. As observed above, again, the shielding mechanism by absorption plays the main role (Fig. 8.5b, c, Table 8.4). This clear improvement fits the desirable SE value for a commercial EMI shielding material (SE_T > 40 dB)[7, 8].

Table 8.4| EMI shielding properties for 2 mm thick PA6-based composites at selected frequencies. All the values are given in dB

Sample	EMI shielding	3 GHz	4 GHz	8 GHz	12.4 GHz
	$\boldsymbol{SE_T}$	**20.77**	**18.03**	**20.03**	**25.54**
P-CNT5	SE_R	6.20E-02	1.10E-02	3.10E-03	2.90E-03
	SE_A	20.71	18.00	19.97	25.51
	$\boldsymbol{SE_T}$	**19.26**	**16.74**	**16.91**	**21.66**
DP-Al7-CNT3	SE_R	6.60E-02	3.50E-02	6.90E-02	3.10E-02
	SE_A	19.19	16.70	16.85	21.63
	$\boldsymbol{SE_T}$	**25.44**	**23.95**	**29.13**	**36.71**
DP-Al5-CNT5	SE_R	6.70E-02	3.40E-02	8.10E-02	3.70E-02
	SE_A	25.37	23.91	29.05	36.68
	$\boldsymbol{SE_T}$	**29.61**	**28.57**	**34.67**	**43.51**
DP-Al3-CNT7	SE_R	6.80E-02	3.50E-02	8.00E-02	3.60E-02
	SE_A	29.55	28.53	34.60	43.48

Table 8.5| Comparison between EMI SE data of the 1 and 2 mm thick PA6-based composites at 12.4 GHz

Sample	SE_T, dB		IF, %[a)]
	1 mm	2 mm	
P-CNT5	19.56	25.54	30.57
DP-Al7-CNT3	16.45	21.66	31.67
DP-Al5-CNT5	24.33	36.71	50.88
DP-Al3-CNT7	28.40	43.51	53.20

[a)] In respect to 1 mm thick molded sample;

Comparisons between the results obtained in this work and other thermoplastic composite prepared by different methods can be made (Table 8.6). For example, Al/CNT composites are comparable with PE/CNT containing 5 wt.% CNT but the thickness of the latter is a little higher. Also, our composites performed much better than PS/CNT composites containing 4 times higher CNT content. This excellent EMI shielding performance of our composites can be explained with the metal particles contribution on one hand, and with the microencapsulation concept for the synthesis of hybrid thermoplastic composites applied in this thesis - on the other. Using this concept, i.e, the microencapsulation concept, allowed the preparation for the first time of CNT- and metal-CNT loaded PA6 composites with EMI shielding properties. The results obtained in this work can open new opportunities for the preparation of thermoplastic materials with EMI shielding properties since a SE_T ~ 43 dB was achieved for 2 mm thick systems.

Table 8.6 | EMI shielding properties of thermoplastic composites loaded with C-allotropes

Polymer matrix	Filler	Load, wt.%	Processing method	Thickness, mm	Maximum SE_T, dB	Bandwidth range, GHz	Ref.
ABS	MWCNT	15	Solution processing + compression molding	1.1	50	8.2–12.4	[10]
PC	MWCNT	2	Solution processing + compression molding	5.6	23.1	8.2–12.4	[12]
PS	MWCNT	20	Compression molding	2	30	8.2–12.4	[3]
PE	MWCNT	5	Mechanic mixture + compression molding	2.1	46.2	8.2–12.4	[13]
PTT	MWCNT	3	Melt mixing + compression molding	2	38	2.65–3.95	[14]
PA6/PP blend	Sisal fibers + CB	10 + 10	Coating method + extrusion + compression molding	3	40.7	2–18 GHz	[15]
PA6	CF + Ni	15 + 10	Melt pultrusion + injection molding	4	36	0.03–3	[16]

8.4. Summary

The EMI shielding properties of binary PA6 composites containing metal particles and CNT are investigated over a broad frequency range. Using a recognized method, it is confirmed a significant improvement of the EMI shielding properties in the presence of binary fillers from 0 dB for the neat PA6 to 43 dB for the 2 mm thick Al-CNT 3/7 system. The EMI shielding properties are determined by the CNT filler since a conductive network is formed as a result of their good dispersion within the polymer matrix, allowing the charge carriers across it. The synergetic effect related to the presence of metal particles within the CNT conducting network improves the EMI shielding performance of the binary

composites. Further, with increasing CNT content there is an improvement of the SE of the molded samples. Absorption is the dominant EMI shielding mechanism in the systems investigated which agrees with the high dielectric losses previously determined, as a result of the motion of charges through the conducting network. The increase of the thickness to 2 mm revealed an SE improvement of up to 53.2 % for the DP-Al3-CNT7 sample, as compared to the 1 mm thick system. Based on the results presented, it can be concluded that the metal/CNT dually reinforced composites obtained via microencapsulation by AAROP of ECL in solution and CM can produce thermoplastic materials with acceptable to good EMI shielding properties. Within the Al-CNT series, thermoplastic materials with good (43 dB) EMI shielding properties can be obtained adjusting the sample thickness and the metal-to-CNT relation.

8.5. References

[1] Chung DDL (2000) Materials for electromagnetic interference shielding. *J Mater Eng Perform*, 9:350–354. DOI: 10.1361/105994900770346042

[2] Al-Saleh MH, Sundararaj U (2009) Electromagnetic interference shielding mechanisms of CNT/polymer composites. *Carbon N Y*, 47:1738–1746. DOI: 10.1016/j.carbon.2009.02.030

[3] Arjmand M, Apperley T, Okoniewski M, Sundararaj U (2012) Comparative study of electromagnetic interference shielding properties of injection molded versus compression molded multi-walled carbon nanotube/polystyrene composites. *Carbon N Y*, 50:5126–5134. DOI: 10.1016/j.carbon.2012.06.053

[4] ASM (1990) Properties and Selection: Nonferrous Alloys and Special-Purpose Materials - Volume 2. In: Metals Handbook, 1st ed. ASM International, United States of America

[5] Verma P, Saini P, Malik RS, Choudhary V (2015) Excellent electromagnetic interference shielding and mechanical properties of high loading carbon-nanotubes/polymer composites designed using melt recirculation equipped twin-screw extruder. *Carbon N Y*, 89:308–317. DOI: 10.1016/j.carbon.2015.03.063

[6] Han T, Luo R (2018) Effect of carbon nanotubes on the electromagnetic shielding properties of SiC_f/SiC composites. *J Alloys Compd*, 745:90–99. DOI: 10.1016/j.jallcom.2018.02.166

[7] Thomassin J-M, Jérôme C, Pardoen T, Bailly C, Huynen I, Detrembleur C (2013) Polymer/carbon based composites as electromagnetic interference (EMI) shielding materials. *Mater Sci Eng R Reports*, 74:211–232. DOI: 10.1016/j.mser.2013.06.001

[8] Yan D-X, Pang H, Li B, Vajtai R, Xu L, Ren P-G, Wang J-H, Li Z-M (2015) Structured Reduced

Graphene Oxide/Polymer Composites for Ultra-Efficient Electromagnetic Interference Shielding. *Adv Funct Mater*, 25:559–566. DOI: 10.1002/adfm.201403809

[9] Gupta A, Choudhary V (2011) Electromagnetic interference shielding behavior of poly(trimethylene terephthalate)/multi-walled carbon nanotube composites. *Compos Sci Technol*, 71:1563–1568. DOI: 10.1016/j.compscitech.2011.06.014

[10] Al-Saleh MH, Saadeh WH, Sundararaj U (2013) EMI shielding effectiveness of carbon based nanostructured polymeric materials: A comparative study. *Carbon N Y*, 60:146–156. DOI: 10.1016/j.carbon.2013.04.008

[11] Hu M, Gao J, Dong Y, Li K, Shan G, Yang S, Li RK-Y (2012) Flexible Transparent PES/Silver Nanowires/PET Sandwich-Structured Film for High-Efficiency Electromagnetic Interference Shielding. *Langmuir*, 28:7101–7106. DOI: 10.1021/la300720y

[12] Maiti S, Suin S, Shrivastava NK, Khatua BB (2014) A strategy to achieve high electromagnetic interference shielding and ultra low percolation in multiwall carbon nanotube–polycarbonate composites through selective localization of carbon nanotubes. *RSC Adv*, 4:7979–7990. DOI: 10.1039/C3RA46480F

[13] Jia L-C, Yan D-X, Cui C-H, Jiang X, Ji X, Li Z-M (2015) Electrically conductive and electromagnetic interference shielding of polyethylene composites with devisable carbon nanotube networks. *J Mater Chem C*, 3:9369–9378. DOI: 10.1039/C5TC01822F

[14] Kunjappan AM, Poothanari MA, Ramachandran AA, Padmanabhan M, Mathew L, Thomas S (2019) High-performance electromagnetic interference shielding material based on an effective mixing protocol. *Polym Int*, 68:637–647. DOI: 10.1002/pi.5751

[15] He H, Cheng S, Lian Y, Xing Y, He G, Huang Z, Wu M (2015) Electrical conductivity and electromagnetic interference shielding effectiveness of carbon black/sisal fiber/polyamide/polypropylene composites. *J Appl Polym Sci*, 132:42801. DOI: 10.1002/app.42801

[16] Zhang S, Wang X, Wu D (2016) Design and fabrication of long-carbon-fiber-reinforced polyamide-6/nickel powder composites for electromagnetic interference shielding and high mechanical performance. *Polym Compos*, 37:2705–2718. DOI: 10.1002/pc.23465

CHAPTER 9

Conclusions and future perspectives

9.1. Conclusions

High-performance polyamide 6 (PA6) based thermoplastic composites with electromagnetic interference (EMI) shielding effect and high *k* (HK) properties were produced. For their fabrication, a microencapsulation strategy was applied consisting in the preliminary synthesis of dually loaded PA6 microcapsules (PAMC) bearing metal/carbon allotropes (C-allotropes) and their subsequent transformation into composites by compression molding (CM). Four types of micron/nano-sized metal particles, namely: iron, copper, aluminum and magnesium, as well as carbon nanotubes (CNT) and carbon black (CB) were used to synthesize *in situ* dually loaded hybrid PAMC with different metal/C-allotropes formulations by activated anionic ring-opening polymerization (AAROP) of ε-caprolactam (ECL). Composites were produced by CM of the synthesized metal/C-allotrope PA6 precursors. Laminate composites were also prepared by CM of alternating plies of carbon fiber textiles (CFT) and metal-loaded PAMC (Me-PAMC). All PAMC precursors and composites on their basis were subjected to different analyses in order to investigate their structure, thermal, mechanical, electrical and dielectric properties by various methods including scanning electron microscopy (SEM), differential scanning calorimetry (DSC), thermogravimetric analysis (TGA), solid-state ^{13}C nuclear magnetic resonance (^{13}C ssNMR), broadband dielectric spectroscopy (BDS). Particular attention was paid to study the EMI shielding performance of the composites.

The following conclusions may be derived from this Ph.D. research program:

1. Synthesis and characterization of mono- and dually loaded PAMC (M- and DM-samples)

- Loaded PAMC were synthesized by AAROP of ECL in solution, in the presence of up to 19 wt.% of metal particles (Al, Cu, Fe, or Mg, altogether 8 samples), CNT (3 samples), or metal-CNT(CB) mixtures (7 samples). None of the fillers used was organically modified.
- The conversion of ECL to loaded PAMC was in the range of 42–63 wt.%, i.e., the metal and carbon loads used do not hinder or block the anionic polymerization process. The average viscometric molecular weight, M_v, of the PAMC synthesized was estimated to be around 33 000 g/mol.
- The SEM studies demonstrated that all PAMC are porous, with scaffold-like morphology. The size and shape of the mono- or dually loaded PAMC were determined by the morphology of the starting load particles. Thus, empty PAMC displayed almost spherical shapes with d_{max} = 20–30 μm, while the loaded PAMC were less spherical with larger sizes of up to 80–100 μm.

- The DSC traces of mono-loaded PAMC (M-samples) revealed melting temperatures in the range of 206–212 °C, glass-transitions between 35–45 °C, and DSC crystallinity indices varying between 39–53 %. These thermal parameters depend on the type and amount of the fillers applied.
- The TGA traces of the mono-loaded PAMC showed real metal- or CNT-contents between 5–19 wt.%. In general, the thermal resistance of the mono-loaded PAMC is similar or slightly better than the neat PAMC.
- The DSC traces of the dually loaded PAMC (DM-samples) displayed melting/crystallization behavior close to that of the mono-loaded PAMC. According to the TGA traces of the Me/carbon loaded PAMC, these samples seem to be of higher heat resistance, especially the DM-Al5-CNT5 and DM-Fe5-CNT-5 compositions.
- The ^{13}C ssNMR analysis of Me-PAMC (Al, Cu, and Mg) revealed ssNMR crystallinity indices varying between 30–50 %, in which the size and morphology of the metal fillers influence this parameter. Carbon spin-lattice relaxation times in the rotating frame, $^{C}T_{1\rho}$, and carbon spin-lattice relaxation times, $^{C}T_{1}$, in the range of 0.6–42.1 ms and 2.6–23.7 s, respectively, were determined for the Me-PAMC. Thus, the local motion of each nucleus is influenced by the presence of metal particles and their paramagnetic or diamagnetic properties.

2. Structure and properties of composites based on mono-loaded PAMC

- The DSC traces of mono-loaded composites (P-samples) revealed melting temperatures in the range of 206–212 °C, glass-transitions between 44–48 °C, and DSC crystallinity indices varying between 27–40 %. These thermal parameters depend on the type and amount of the fillers applied.
- The TGA traces of the P-series showed that, in general, the thermal resistance of the molded composites is better than the respective PAMC precursors. Maximum degradation temperatures between 322–359 °C and 319–428 °C were obtained, respectively, for M- and P-samples. Besides that, the CNT- and Cu-loaded plates exhibited two degradation processes, in which the second one appears with values in the range of 345–428 °C.
- The tensile properties of the P-samples revealed an improvement factor (IF) of Young's modulus, E, of 84 % for CNT loaded sample and 17–57 % for metal-loaded composites. The improvements are determined by the morphology of the fillers dispersed within the PA6 matrix.
- In the electric conductivity studies, the neat PA6 exhibited an insulator behavior, with d.c electrical conductivity, σ_{dc}, values above 10^{-10} S/m. In the presence of metal fillers, the insulator properties of

the neat matrix remained with σ_{dc} values in the 10^{-09} S/m, as a result of the Maxwell-Wagner-Sillars interfacial polarization. The presence of CNT led to a notable growth of the σ_{dc} to >10^{-1} S/m.

- The dielectric constant, ε', of the P-samples containing metal particles was in the range of 22–25, the P-CNT5 sample exhibited a ε' of 393, i.e., a notable increase of the neat PA6 values ε' = 6.6. Dielectric losses ($\tan\delta$) between 0–1.3 were registered for the insulator materials. On the contrary, the higher electric conductivity of the P-CNT5 sample led to dielectric losses 100 times higher than the neat PA6.

3. Structure and properties of laminate composites based on CFT and mono-loaded PAMC

- The tensile properties of the laminate composites based on CFT (V_f = 0.25) and Me-PAMC (13–19 wt.%) revealed a significant increase of the E and strength at break, σ_{br}, on average by 280–327 % compared to the neat PA6. These improvements are mostly due to the introduction of CFT reinforcements.
- The presence of CFT and the good distribution of metal particles within the interlayer PA6 zones of the laminates contributed to the increase of σ_{dc} to about 10^{-03} S/m.
- The binary laminates exhibited ε' between 17–21 and low $tan\delta$ (in the range of 10^{-02}) indicating a carrier's mobility decrease due to the interfaces established between the metal particles and the CFT.

4. Structure and properties of composites based on dually loaded PAMC

- The DSC traces of the dually loaded composites (DP-samples) are similar to that of the respective PAMC with melting temperatures in the range of 205–215 °C, glass-transitions between 39–54 °C, and DSC crystallinity indices varying between 22-46 %.
- The TGA traces of the DP-samples showed in general better temperature resistance as compared to the respective PAMC. Moreover, the dually loaded DP-Al5-CNT5 and DP-Fe5-CNT5 samples exhibited two degradation processes with maximum rates at 370–380°C and ca. 470°C, respectively. In the pure P-PA6 sample intensive degradation starts right after 300°C.
- The tensile properties of the binary metal-CNT composites revealed an IF of E up to 59 % (DP-Al5-CNT5) with respect to the polymer matrix.
- The electric and dielectric characterization of the binary composites at room temperature allowed verifying that the mixture of metals and C-allotropes in different concentrations or relations led to

tunable conductive and dielectric properties. σ_{dc} values up to 10^{-01} S/m, ε' between 10^{+01}–10^{+03} and $tan\delta$ in the range of 10^{+00}–10^{+03} were measured.

- The further studies on the conduction mechanism of the binary metal/CNT PA6 hybrids by BDS demonstrated that the frequency dependence of the measured conductivity obeys the so-called universal dynamic response since there is a σ_{dc} plateau above a critical frequency, F_c, followed by the ω^s power law with exponent 0.11 < s < 0.63. The σ_{dc} of the binary composites is in the range of 1.21E-05–1.63E-02 S/cm wherein the CNT and the synergetic effect between such C-allotrope and metal particles contributed to the mobility of carriers through the conductive network.

5. EMI shielding properties

- In the ssNMR studies with PAMC containing CNT and Al particles, it was verified partial or total disappearance of the PA6 resonance lines in binary Al-CNT hybrids. These results indicated the potential of the binary composites containing metal particles and C-allotropes as radio wave absorbers.
- The EMI shielding measurements up to 3 GHz with metal-CNT containing plates showed SE_T values of up to 20 dB (1 mm sample thickness) against 15 dB of the P-CNT composites. As the frequency was increased in the 3–12 GHz range, the SE_T reached 28.4 dB (1 mm) and 43.5 dB (2 mm) This performance meets the effectiveness range for commercial applications, which is 20–40 dB.

Summarizing, it was proved that the microencapsulation concept used in this PhD thesis for the preparation of hybrid PAMC based on AAROP of lactams in solution, and their subsequent transformation into composites, can be successfully applied for the development of polyamide composites with good EMI shielding properties.

Examples of possible applications on these new composites could be: i) in smart devices as wearable EM absorbing cloths to protect human beings from the EM pollution; ii) wearable systems for health monitoring and simultaneously EM attenuation; iii) antennas to enhance the EM wave up and decrease the EMI; iv) panels for walls, materials for curtains and booths, and other facilities needed in the medical imaging acquisition area using radio- and microwaves.

9.2. Future perspectives

The EMI shielding performance of the composites based on dually loaded PAMC could be subjected to optimization studies related to the composition of PAMC and the thickness of the final molded articles. Thus, it will be possible to adjust the EMI shielding to each desired application. The substitution of CNT by CB (although even partial) should be tested aiming at more cost-effective composites. Similar optimization studies should be extended to the binary metal-CNT/CFT laminate composites finding the best balance between EMI shielding and mechanical performance.

The almost total absorption of radiofrequencies displayed by some DP-samples in the ssNMR studies of this thesis suggests testing the radio and microwave absorbance of the PA6-based composites prepared by the technology described in this work. The starting PAMC in this case should contain high dielectric constant materials such as $BaTiO_3$, or high permeability materials such as Fe_3O_4. Such composites would be attractive for military stealth applications.

Since materials with EMI shielding properties are of importance in the medical imaging area, the binary PA6-based composites obtained in this work could have potential applications there, e.g., in the development of simultaneous positron emission tomography (PET) and magnetic resonance imaging (MRI) systems. In these systems, the PET detector should be invisible to the MRI and unable to interfere with the RF generated by it. Thus, it could be interesting the use of the novel binary PA6 materials in the design of miniature PET scanner prototypes used to evaluate the shielding of the RF interferences, as well as the reduction of the eddy current effects during the data acquisition.

Finally, it seems reasonable to qualify the novel materials presented in this work in terms of Life Cycle and Environmental Risk Assessment. These studies could give a full picture of the entire environmental impact, energy, and resource usage in the production of the binary PA6-based composites containing metal particles and carbon allotropes. With these results, it could be possible to predict if such materials could meet the certification and standardization tests in areas where EMI shielding materials are required.

You cannot get through a single day without having an impact on the world around you. What you do makes a difference, and you have to decide what kind of difference you want to make.

Jane Goodall